

DESIGN AND FABRICATION OF
A FIBER-INTEGRATED MODE-SELECTIVE
PHOTOPOLYMER GRATING COUPLER

A Thesis Submitted to
the Graduate School of Engineering and Sciences of
Izmir Institute of Technology
in Partial Fulfillment of the Requirements for the Degree of

DOCTOR OF PHILOSOPHY

in Electronics and Communication Engineering

by
Can SÜMER

July 2014
İZMİR

We approve the thesis of **Can SÜMER**

Examining Committee Members:

İMZALI SAYFA İLE DEĞİŞTİRİLECEK

Prof.Dr. M. Salih DİNLEYİCİ

Department of Electrical and Electronics Engineering / Izmir Institute of Technology

İMZALI SAYFA İLE DEĞİŞTİRİLECEK

Prof.Dr. Mustafa M. DEMİR

Department of Materials Science and Engineering / Izmir Institute of Technology

İMZALI SAYFA İLE DEĞİŞTİRİLECEK

Prof.Dr. Alper KİRAZ

Department of Physics / Koç University

İMZALI SAYFA İLE DEĞİŞTİRİLECEK

Assoc.Prof.Dr. Alp KUŞTEPELİ

Department of Electrical and Electronics Engineering / Izmir Institute of Technology

İMZALI SAYFA İLE DEĞİŞTİRİLECEK

Assoc.Prof.Dr. H. Sami SÖZÜER

Department of Physics / Izmir Institute of Technology

10 July 2014

İMZALI SAYFA İLE DEĞİŞTİRİLECEK

Prof.Dr. M. Salih DİNLEYİCİ

Supervisor

Department of Electrical and Electronics Engineering / Izmir Institute of Technology

İMZALI SAYFA İLE DEĞİŞTİRİLECEK

Prof.Dr. M. Salih DİNLEYİCİ

Head of Department of Electrical
and Electronics Engineering

Prof.Dr. R. Tuğrul SENER

Dean of Graduate School of
Engineering and Sciences

ACKNOWLEDGEMENTS

First and foremost, I would like to thank my advisor Prof.Dr. M. Salih Dinleyici, who has been a true guide in all of my academic studies, giving me the right direction at the right time, providing me with the best course-correction to make sure I keep on track. During the eight years of working with him, our teacher and pupil relationship became a joint effort of like-minded colleagues on many occasions. On my account, this has been the most essential aspect of working with him and made this thesis what it is.

Jury members in my progress seminars and also in the defense, Assoc.Prof.Dr. Alp Kuştepelı and Assoc.Prof.Dr. H. Sami Sözüer, with their inimitable knowledge of the Electromagnetic Theory and unique perspective on optics, have led me to alternative approaches and helped me overcome many obstacles throughout the research.

I would like to express my gratitude to Prof.Dr. Mustafa M. Demir not only for taking part in my defense jury, but also for answering each and every one of my questions about polymer processes and materials and most of all, for granting me an all-access pass to his laboratory. He has practically been a second advisor for my dissertation and a wise mentor for a young researcher.

I would like to extend my appreciation to Prof.Dr. Alper Kiraz for taking part in my defense jury, and also for his valuable feedback and support for my thesis.

I would like to thank Vestel Corporate R&D General Manager Murat Sarpel, Vestel Electronics Lead Technologies Group Manager Sedat Şengül and Vestel Electronics Optical Design Group Leader Kıvanç Karlı for letting me take time off for my thesis and experimental studies. They have been supportive of me and my PhD studies from the very beginning of my work at Vestel.

Thanks would never be enough for Prof.Dr. Mehmet Ali Gülgün, Assoc.Prof.Dr. Cleva W. Ow-Yang and Dr. Shawuti Shalima from Sabancı University Faculty of Engineering and Natural Sciences (FENS) for the time and effort they have put in for the measurements and for the insight they have given me for the future of my work. In a most critical time, they took time off their own work for me and reminded me that *research is about collaboration, rather than competition.*

Prof.Dr. Kadir Aslan from Ege University, Prof.Dr. Ayhan Altıntaş from Bilkent University and Prof.Dr. Gönül Turhan Sayan from METU have made my Doctoral education possible via their valuable references and letters of recommendation.

I would like to express my sincere gratitude to following people for introducing me new techniques, devices, ideas, providing me with various equipment, materials, literature and assistance on measurements:

Prof. Pochi Yeh, Assist.Prof.Dr. Şevket Gümüştekin, Assist.Prof.Dr. Sevinç Aydınlık Bechteler, Assoc.Prof.Dr. Barış Bozkurt, Prof.Dr. Serdar Özçelik, Prof.Dr. Salih Okur, Prof.Dr. Lütfi Özyüzer, Dr. İstem Özen (the spirit carries on), Assist.Prof.Dr. Elif Aras Gültürk, Dr. Atilla Özgür Çakmak, Dr. Ahmet Akın Ünal, Dr. Renan Kazazoğlu, Gülay Karaoğlan, Gökhan Erdoğan, Mine Bahçeci, Duygu Oğuz Kılıç, Dr. Başak Özbakış, Dr. Leyla Eral Doğan, Saygın Bildik, Esra Aycan, Ayten Cantaş, Dr. Emre Heves, Özge Tüncel, Hasan Aydın, Nesli Yağmurcukardeş, Dr. Hatice Yavuzdurmaz, Dr. Özge Tunusoğlu, Sarp Satır, Dr. Sinan Karaveli, Dr. Fatma Gül Çelenk, Onur Parlak, Dr. Gülçin Ünal, Dr. Sevnur Serim, Mesut Ünal, Görkem Özvural, Bertan Kılıçcıoğlu, Cihan Kılıçcıoğlu, Göksenin Bozdağ, Alper İnan, Mehmet Salih Kılıç, Fevzi Sümer, and last but certainly not least, Gökçen Coşkuner Ballı and Fevzi Ballı. In particular, I would like to thank whole-heartedly the guy downstairs in 107 for his free help. Can't recall his name, but he wore glasses.

My profound thanks go to Mikael Åkerfeldt. In my mind and memories, each and every stage of this thesis is associated with a distinct Opeth album. I am actually listening to *Watershed* writing these words down.

There are so many things to say about how I could never make up for the time my mother has been missing me during these years. Giving her the news about my successful Ph.D. defense was one of the best moments of my life. She has always been and will always be my anchor on this planet.

I would like to thank Betül and Birol Gökdüman profusely for their endless love, support and encouragement all through the years.

This journey took eight years to conclude and has taken me through: Optics Lab, Vision Lab and Wireless Communication Networks and Multimedia Research Centre (IYTE-WIRELESS) in Electrical Engineering Dept.; Dielectric Lab, Applications of Nanotechnology Lab and Clean Room Facilities in Physics Dept.; Polymer Lab, Physicochemistry Lab and Confocal Microscopy Lab in Chemistry Dept.; Machine Workshop in Mechanical Engineering Dept.; and Center for Materials Research (IYTE-MAM), in addition to Materials Analysis and Characterization Laboratory (MCL) and Clean Room Facilities in Sabancı University FENS, and Optical Design Group Laboratories in Vestel City.

Even though this journey has now concluded, true scientific endeavor can never be complete. The set of findings we call “truth” or “facts” is ever-changing, and scientists are perhaps merely enthusiasts attempting with futility to capture a glimpse of a moment within infinity.

This work was supported in part by TÜBİTAK under projects 107E024, 109E240, 114E006 and by Izmir Institute of Technology under project 2008IYTE10.

ABSTRACT

DESIGN AND FABRICATION OF A FIBER-INTEGRATED MODE-SELECTIVE PHOTOPOLYMER GRATING COUPLER

The aim of this study is to develop a node for an optical add/drop multiplexer, which is capable of packet switching at very high speeds and is controlled by light. The D-Fiber is employed as the transmission medium and the grating formation and polymerization is implemented on the fiber. The optical multiplexer is constructed by cascading two different photonic structures formed on the planar side of the D-Fiber. Multiplexing is performed by forming a temporary (transient) grating; which is the subject of another project in parallel at our laboratory. Right after this grating, will be the structure that is the subject of this thesis, which is the permanent structure fabricated via photopolymerization. The temporary grating breaks the resonance using nonlinear optical effects, coupling the fiber mode into the higher-order mode and the permanent structure extracts the mode out selectively to another fiber. Due to the very fast response of the nonlinear effects, an optical switch capable of transferring optical packets to other waveguides is formed.

Photopolymerization is a method that can be used to fabricate photonic structures such as photonic crystals or permanent gratings, holographically or by direct-writing. The project involves the fabrication of the aforementioned photonic structure via photopolymerization. Even though the main aim of this project is not materials research, extensive effort has been put into optimizing the polymer recipe and characterization of the materials and processing properties.

ÖZET

FİBERE ENTEGRE KİP-SEÇİCİ FOTOPOLİMER IZGARA BAĞDAŞTIRICI TASARIMI VE ÜRETİMİ

Bu çalışmanın amacı, optik ekle/çıkar çoğullayıcılar için yüksek hızlarda paket anahtarlama yapabilen ve ışıkla kontrol edilen bir düğüm geliştirmektir. İletim ortamı olarak D-Fiber kullanılacaktır ve ızgara oluşumu ve polimerizasyon fiber üzerinde gerçekleştirilecektir. Optik çoğullayıcı iki farklı fotonik yapının D-Fiberin düz yanal yüzeyi üzerinde üretilmesiyle oluşturulacaktır. Çoğullama, optik laboratuarda yapılan diğer bir çalışmanın konusu olan geçici ızgara yardımıyla gerçekleştirilecektir. Geçici ızgaranın hemen arkasında, bu çalışmanın konusu olan kalıcı ızgara yer alacaktır ve bu kalıcı ızgara fotopolimerizasyon yöntemi ile üretilecektir. Geçici ızgara doğrusal olmayan optik etki ile rezonansı kırıp fiber modunu yüksek mertebeli moda kuple edecek, kalıcı yapı ise modu diğer bir fibere aktaracaktır. Doğrusal olmayan etkinin çok hızlı tepki süresi sayesinde optik paketleri çok yüksek hızlarda diğer dalga kılavuzlarına aktarabilen bir optik anahtar yapısı elde edilmiş olacaktır.

Fotopolimerizasyon, fotonik kristaller ya da kalıcı ızgaralar gibi yapıların holografik yöntem ya da doğrudan yazma yöntemi ile üretilmesinde kullanılan bir yöntemdir. Bu proje yukarıda bahsedilen fotonik yapının fotopolimerizasyon yöntemi ile üretilmesini içermektedir. Her ne kadar çalışmanın esas amacı malzeme araştırması olmasa da, kullanılan polimer reçetesinin optimize edilmesi ve malzemelerin ve işleme özelliklerinin karakterizasyonu için kapsamlı çalışmalar yapılmıştır.

*I dedicate this to my dear wife Işıl
May her love and joy always brighten my world*

TABLE OF CONTENTS

LIST OF FIGURES	xii
LIST OF TABLES	xviii
CHAPTER 1. INTRODUCTION	1
1.1. Motivation and Background	1
1.2. Aim	2
1.3. Outline	2
CHAPTER 2. PHOTOPOLYMERIZATION	3
2.1. Introduction	3
2.1.1. Photopolymerization	3
2.1.2. Polymer Optical Components	4
2.2. Experimental Studies	6
2.2.1. Initial Recipe	6
2.2.2. Transmission Spectrum	9
2.2.3. Refined Recipe – PVA Matrix	10
2.2.4. Sample Preparation	11
CHAPTER 3. CHARACTERIZATION TECHNIQUES	15
3.1. Brewster Angle Methods	15
3.1.1. Theory	15
3.1.2. Experimental Setup	17
3.2. Diffraction Methods	37
3.2.1. Initial Studies	37
3.2.1.1. Fitting Procedure	39
3.2.1.1.1. Actual Refractive Index Distribution	39
3.2.1.1.2. Analysis	40
3.2.2. Image Correction	41
3.2.3. Near-Field Diffraction Method	45
3.2.4. Direct-Written Waveguides	49

3.3. Grating Characterization	54
3.3.1 Photopolymer Waveguide and Grating Fabrication.....	54
3.3.2. Grating Characterization – Phase Grating (Volumetric Profile).....	55
3.3.2.1. Transmission Optical Microscopy	55
3.3.2.2. Scanning Electron Microscopy	56
3.3.2.3. Confocal Microscopy, Staining, Selective Solubility, Gel Permeation Chromatography.....	57
3.3.3. Grating Characterization – Surface Grating (Surface Profile).....	60
3.3.3.1. Atomic Force Microscopy.....	60
3.3.3.2. Stylus Surface Profilometer	61
 CHAPTER 4. THEORY AND SIMULATIONS	 71
4.1. Theoretical Background	71
4.1.1. Grating Coupler.....	71
4.1.2. Reciprocity and Conservation of Power	76
4.1.3. Design Parameters.....	81
4.2. Sinusoidal Grating – Nufern 780-HP Optical Fiber.....	82
4.2.1. Approximate Grating Steps with Generic Fiber.....	82
4.2.2. Phase Matching Condition	85
4.3. Sinusoidal Grating – Corning HI1060 Optical Fiber	87
4.3.1. Approximate Grating Steps with Realistic Fiber	87
4.4. Gaussian Grating – Corning HI1060 Optical Fiber	91
4.4.1. Realistic Grating Steps with Realistic Fiber	91
4.5. Optimization and Tuning – Final Device at 632.8nm.....	94
4.6. Grating Period Dependence of Coupling Efficiency	99
4.7. Dispersion Relation.....	101
4.8. Wavelength Dependence of Coupling Efficiency.....	104
4.9. Gaussian Grating – Corning HI1060 Optical Fiber at 852nm	105
4.9.1. Optimization and Tuning – Final Device at 852nm.....	108
4.9.2. Dispersion Relation for the 852nm Device.....	111
4.10. Wavelength and Fabrication Tolerances of Coupling Efficiency	112

CHAPTER 5. EXPERIMENTAL REALIZATION.....	115
5.1. In-House D-Fiber Preparation.....	115
5.2. D-Fiber HF Etching.....	119
5.3. Side-Polished Fibers.....	124
5.4. Final Device Fabrication.....	125
5.4.1. Fabrication Steps and Experimental Setup	125
5.4.2. Trial 1 – Single-Fiber Device at 632.8nm.....	127
5.4.3. Trial 2 – Single-Fiber Device at 632.8nm.....	132
5.4.4. Trial 3 – Single-Fiber Device at 852nm.....	136
5.4.5. Trial 4 - Complete Structure at 852nm	137
5.4.6. Trial 5 - Complete Structure at 852nm	140
5.4.7. Trial 6 – Single-Film Device at 852nm.....	143
5.4.8. Trial 7 – Complete Structure with Polarization Analysis	144
 CHAPTER 6. RESULTS AND DISCUSSION.....	 146
 CHAPTER 7. CONCLUSION	 157
 BIBLIOGRAPHY.....	 159
 APPENDICES	
APPENDIX A. POLYMER BATCHES	164
APPENDIX B. IMPROVED BREWSTER METHOD CONFIGURATIONS.....	167
APPENDIX C. SEM IMAGES	176

LIST OF FIGURES

<u>Figure</u>	<u>Page</u>
Figure 1. Monomers undergo a chemical reaction to form polymer chains.	3
Figure 2. Polymer transmission spectra for unprocessed and polymerized samples	9
Figure 3. Transmittance spectra for different number of pulses.	10
Figure 4. Scanning Electron Microscope cross-section image of the film prepared by direct casting	13
Figure 5. Scanning Electron Microscope surface image of the film prepared by direct casting	14
Figure 6. p-polarized external reflection.....	15
Figure 7. The Abelés-Brewster method.....	16
Figure 8. Schematic representation of the initial Brewster measurement setup.....	18
Figure 9. Initial Brewster angle measurements	18
Figure 10. Output variation of 632.8nm He-Ne laser	19
Figure 11. Output variation of 632.8nm He-Ne laser - detail.....	20
Figure 12. Schematic representation of the improved Brewster techniques setup	21
Figure 13. Three-layer model used for reflectance calculations.....	22
Figure 14. Intersection of reflectance curves for different film thicknesses.	25
Figure 15. Region of existence for the second intersection.....	26
Figure 16. Intersection of reflectance curves for different thicknesses.	27
Figure 17. Close study of the intersection point of reflectance curves for the configuration with a single intersection.....	28
Figure 18. Close study of the first intersection point of reflectance curves for the configuration with two intersections.....	29
Figure 19. Close study of the second intersection point of reflectance curves for the configuration with two intersections.....	30
Figure 20. Determining the exact point of intersection for the single-intersection configuration.....	31
Figure 21. Determining the exact point of intersection for the first intersection of two-intersection configuration.....	32
Figure 22. Determining the exact point of intersection for the second intersection of two-intersection configuration.....	32

Figure 23. Reflectance curves of the three thin film-on-glass samples.....	35
Figure 24. Exact point of intersection analysis for the reflectance curves	35
Figure 25. Representation of the combined experimental setup used in the direct-writing and the diffraction pattern measurements.....	37
Figure 26. Theoretical model used in the fit procedures for the diffraction patterns	38
Figure 27. Microscope image and profile of the polymerized region	40
Figure 28. Measured Diffraction Pattern and Best Estimate for the Fit	41
Figure 29. Intensity profiles of plane waves diffracted by fibers immersed in various liquids.....	42
Figure 30. Background elimination and offset correction for recorded patterns.....	43
Figure 31. Intensity profiles of plane waves diffracted by fibers immersed in various liquids.....	43
Figure 32. Intensity profiles of plane waves diffracted by fibers immersed in various liquids.....	44
Figure 33. Defined metrics	45
Figure 34. Investigation of metrics in order to determine the refractive indices.....	45
Figure 35. Intensity profiles of plane waves diffracted by fibers immersed in air and DI water.	46
Figure 36. Intensity profiles of plane waves diffracted by fibers immersed in various liquids.....	47
Figure 37. Measurement and fit for single-mode fiber suspended in air	48
Figure 38. Measurement and fit for single-mode fiber suspended in DI water	49
Figure 39. Cumulative refractive index profiles and transmission optical microscope image of a direct-written photopolymer waveguide.....	50
Figure 40. Recorded diffraction patterns and corresponding pattern cross-sections for single-pass, multiple-pass and triple-pass waveguides	51
Figure 41. Diffraction geometry and approximated profile of the refractive index distribution.....	51
Figure 42. Direct-written photopolymer waveguide structure on polymer film and associated refractive index model.....	52
Figure 43. Reflection optical microscope image of the grating structure.....	55
Figure 44. Top surface confocal microscope image of the grating end region	57
Figure 45. Cross-section confocal microscope image of the grating structure.....	58
Figure 46. Polymer transmission spectra for unprocessed and polymerized samples....	58

Figure 47. AFM analysis of L.GR.050.A	60
Figure 48. AFM analysis of L.GR.050.A (Surface topology)	61
Figure 49. L.GR.010.A grating surface profile - beam speed 0.1mm/sec	62
Figure 50. L.GR.050.A grating surface profile - beam speed 0.5mm/sec	62
Figure 51. L.GR.140.A grating surface profile - beam speed 1.4mm/sec	63
Figure 52. L.GR.280.A grating surface profile - beam speed 2.8mm/sec	63
Figure 53. Gaussian function fit for single step of grating L.GR.050.A	64
Figure 54. Gaussian function fit for single step of grating L.GR.140.A	64
Figure 55. Gaussian function fit for single step of grating L.GR.280.A	65
Figure 56. Gaussian coefficients vs. direct-writing beam speed	65
Figure 57. Waveguide L.WG.005.B2 surface profile.....	66
Figure 58. Waveguide L.WG.010.B1 surface profile.....	66
Figure 59. Waveguide L.WG.050.B2 surface profile.....	67
Figure 60. Waveguide L.WG.140.A2 surface profile.....	67
Figure 61. Peak height vs. direct-writing beam speed for waveguides	68
Figure 62. Corrugation amplitude vs. direct-writing beam speed for gratings.....	68
Figure 63. L.GR.010.B grating surface profile.....	69
Figure 64. L.GR.050.B2 grating surface profile.....	70
Figure 65. Grating coupler with model parameters shown for the structure	71
Figure 66. Defined approximate/sinusoidal grating structure and corresponding Fourier series approximation	82
Figure 67. Modes supported by Nufern 780-HP fiber excited at 632.8nm wavelength	83
Figure 68. Modes supported by the input and output fibers	83
Figure 69. Modes supported by the whole structure.....	84
Figure 70. An example of coupling between input and output waveguide modes.....	84
Figure 71. Coupling efficiency between input and output modes with respect to waveguide separation.....	86
Figure 72. Coupling distance for coupling between each mode in two guides	87
Figure 73. Modes supported by Corning HI1060 fiber excited at 632.8nm wavelength.....	88
Figure 74. Modes supported by the input and output guides.....	88
Figure 75. Modes supported by the whole structure.....	89
Figure 76. Coupling efficiency with respect to waveguide separation with	

sinusoidal gratings for Corning HI1060 excited at 632.8nm.....	90
Figure 77. Device lengths necessary to reach the calculated efficiencies wrt waveguide separation	90
Figure 78. L.GR.010.A grating surface profile.....	91
Figure 79. Gaussian function fit for single step of grating L.GR.280.A	92
Figure 80. Gaussian grating structure and corresponding Fourier series approximation used in the calculations.....	92
Figure 81. Coupling efficiency with respect to waveguide separation with Gaussian gratings for Corning HI1060 excited at 632.8nm.....	93
Figure 82. Device lengths necessary to reach the calculated efficiencies w.r.t. waveguide separation.....	93
Figure 83. Coupling efficiency with respect to waveguide separation – detail.....	94
Figure 84. Device lengths necessary to reach the calculated efficiencies – detail	95
Figure 85. Mode field propagations at waveguide separation of 22 μ m	96
Figure 86. Mode field propagations at waveguide separation of 23 μ m	97
Figure 87. Mode field propagations at waveguide separation of 23 μ m and device length of 0.8354mm.....	98
Figure 88. Coupling efficiency with respect to grating period for all modes.....	100
Figure 89. Coupling efficiency with respect to grating period for all modes – detail ..	101
Figure 90. ω vs. β relation when the used fiber is excited at 632.8nm wavelength	102
Figure 91. ω vs. β relation when the fiber is excited at 632.8nm – scaled	102
Figure 92. ω vs. β relation for the fiber with grating when excited at 632.8nm wavelength – scaled	103
Figure 93. Intersection of ω vs. β relation for the bare fiber and grating induced fiber – scaled.....	104
Figure 94. Operation wavelength dependence of 632.8nm device.....	105
Figure 95. Modes supported by Corning HI1060 fiber excited at 852nm wavelength	106
Figure 96. Modes supported by the input and output fibers	106
Figure 97. Modes supported by the whole structure.....	107
Figure 98. Coupling efficiency with respect to waveguide separation with Gaussian gratings for Corning HI1060 excited at 852nm.....	107
Figure 99. Device lengths necessary to reach the calculated efficiencies w.r.t. waveguide separation.....	108

Figure 100. Coupling efficiency with respect to waveguide separation – detail.....	109
Figure 101. Device lengths necessary to reach the calculated efficiencies – detail	109
Figure 102. Mode field propagations at waveguide separation of 55 μ m	110
Figure 103. ω vs. β relation for the bare fiber and fiber with grating when excited with 852nm laser – scaled.	112
Figure 104. Operation wavelength dependence of coupling efficiency	113
Figure 105. Waveguide separation dependence of coupling efficiency	114
Figure 106. Device length dependence of coupling efficiency	114
Figure 107. Chemical etch of standard fibers for D-Fiber manufacturing	116
Figure 108. Output power throughout etching for standard fiber.....	117
Figure 109. Transmitted power versus the etching time.....	117
Figure 110. Chemically etched standard fibers	118
Figure 111. Setup used for HF etching of D-Fibers	119
Figure 112. Measurement of the output power throughout HF etching of D-Fiber	120
Figure 113. SEM analysis of D-Fiber etched with HF:H ₂ O=1:6 for 38 min.....	121
Figure 114. SEM analysis of D-Fiber etched with HF:H ₂ O=1:6 for 48 min.....	121
Figure 115. SEM analysis of D-Fiber etched with HF:H ₂ O=1:6 for 63 min.....	122
Figure 116. SEM analysis of raw (unprocessed) D-fiber sample	122
Figure 117. D-Fiber model based on SEM studies and fiber specifications.....	123
Figure 118. HF-etch depth vs. etch time for D-Fiber	124
Figure 119. Side-polished optical fibers manufactured by Phoenix Photonics.	124
Figure 120. Schematic representation of the experimental setup	126
Figure 121. Experimental setup	126
Figure 122. Modes supported by Corning HI1060 fiber excited at 632.8nm.....	127
Figure 123. Launched optical fiber mounted on the motorized xyz-stage	127
Figure 124. Launching the fiber and exciting the first two modes.....	128
Figure 125. Polymer coating, doctor blade and cure	129
Figure 126. Recording the fiber output post-cure, prior to direct-writing.....	129
Figure 127. Photopolymerization by direct-writing	130
Figure 128. Monitoring the fiber output following the fabrication of grating via direct-writing polymerization	130
Figure 129. CCD fiber output images of before and after grating direct-writing.....	131
Figure 130. Polymer coating and cure	133
Figure 131. CCD fiber output images of prior to and after grating direct-writing.....	134

Figure 132. Cross-sectional analysis of the input and output mode profiles	135
Figure 133. Fiber output profiles without and with grating implementation.....	135
Figure 134. Reflection microscope image of the fiber with the fabricated grating	136
Figure 135. Original and modified structures of the glass fiber holder	138
Figure 136. Modified fiber holder	138
Figure 137. Final device fabrication – mounting the output fiber	139
Figure 138. Final device	140
Figure 139. Schematic representation of final form of the experimental setup.....	141
Figure 140. Final form of the experimental setup	141
Figure 141. Schematic representation of the revised fiber holder	142
Figure 142. Revised fiber holder	142
Figure 143. OSA measurements performed before and after direct-writing	143
Figure 144. OSA measurements performed before and after device fabrication	144
Figure 145. Representation and photograph of the rotating polarizer+CCD system....	145
Figure 146. Fundamental mode and second-order mode supported by the device.....	148
Figure 147. Structure of the optical fiber used in the experiments.....	148
Figure 148. Degenerate LP_{01} modes supported by HI1060 at 632.8nm	149
Figure 149. Degenerate LP_{11} modes supported by HI1060 at 632.8nm	150
Figure 150. Degenerate $LP_{01}E_H$ + degenerate LP_{11} combinations.....	151
Figure 151. Degenerate $LP_{01}E_V$ + degenerate LP_{11} combinations.....	151
Figure 152. Degenerate modes propagating through the device output	153
Figure 153. Total output field pattern before grating implementation	155

LIST OF TABLES

<u>Table</u>	<u>Page</u>
Table 1. Summary of photopolymerization literature.....	5
Table 2. Constituents of the initial polymer recipe.....	7
Table 3. Polymer constituents and their weight ratios.....	8
Table 4. Polymer constituents and molar ratios in the refined recipe.....	11
Table 5. Sensitivity analysis of the method.	33
Table 6. Accuracy analysis of the method for the first intersection	33
Table 7. Accuracy analysis of the method for the second intersection.....	34
Table 8. Experimental results	36
Table 9. Properties of the fabricated waveguides	55
Table 10. Properties of the fabricated gratings	55
Table 11. Specifications of the final device at 632.8nm.....	99
Table 12. Specifications of the final device at 852nm.....	111
Table 13. Specifications of Nufern 780-HP optical fiber (Nufern, 2011).	115
Table 14. Specifications of Corning HI1060 optical fiber (Corning, 2010).....	125
Table 15. Output power of bare fiber – Trial 1	128
Table 16. Polymer recipe constituents and their respective molar ratios	128
Table 17. Output power of unprocessed polymer coated fiber – Trial 1	129
Table 18. Output power at various process stages – Trial 1	130
Table 19. Output power of the bare fiber – Trial 2.....	132
Table 20. Output power of unprocessed polymer coated fiber – Trial 2	133
Table 21. Output power at various process stages – Trial 2	134
Table 22. Output power at various process stages – Trial 3	137
Table 23. Output power at various process stages – Trial 4.....	139
Table 24. Output power at various process stages – Trial 5	142
Table 25. Relative mode power ratios obtained via OSA measurements.....	143
Table 26. Output power at various process stages – Trial 6	144
Table 27. Relative mode power ratios obtained via OSA measurements.....	144
Table 28. Output power at various process stages – Final Trial.....	145
Table 29. Single-fiber devices fabricated throughout the study	146
Table 30. Complete devices fabricated throughout the study.....	147

Table 31. Measured and calculated degenerate modes of unetched fiber.....	152
Table 32. Measured and pattern-fitted degenerate modes before grating fabrication ..	154
Table 33. Measured and pattern-fitted degenerate modes after grating fabrication	155

CHAPTER 1

INTRODUCTION

1.1. Motivation and Background

The development in optical communication networks has been driving the technology towards packet switched all-optical networks and it is foreseen that triple play –namely audio, video and data– will be carried together on these networks via IP protocol. These networks require components capable of performing routing, add/drop multiplexing, address identification and related functions in optical domain. Despite the abundance of theoretical work in the area, the quantity and the quality of devices actually realized are yet poor.

Grating couplers are one of the key components of optical networks. Being a passive component allows for the fundamental nodes of many all-optical devices to be fabricated by utilizing grating couplers, including wavelength filters, all-optical switches, etc. (Huang and Haus, 1989), (Yesayan and Piche, 2004), (Yokota, et.al., 2008).

D-Fiber is a special kind of optical fiber with an outer form of the cladding layer resembling the capital letter D, where the flat planar side-surface of the fiber allows for the implementation of various structures on the fiber and facilitates fiber-integration of optical devices like sensors, etc. (Smith, 2005), (Lowder, 2008).

Photopolymerization is a popular research area and a practical tool for the fabrication of optical components; the focus is particularly common in creation of holographic memory systems (Garcia, et.al, 2002), (Sabel, et.al, 2013). The main reasons for the popularity are the low-cost materials, simple handling and easy production. Apart from holographic techniques, direct-writing is an alternative method for fabrication of optical components, which provides more control and precision in production and also allows for the fabrication of three-dimensional components (Sullivan, et.al, 2007).

1.2. Aim

The aim of this work is to design, realize and demonstrate a node capable of all-optical switching in packet-speeds.

The D-Fiber is employed as the transmission medium and the grating formation and polymerization is also implemented on the fiber. The optical multiplexer is constructed by cascading two different photonic structures formed on the planar side surface of the D-Fiber. Multiplexing is performed by forming a temporary (transient) grating; which is the subject of another project in parallel at our laboratory. Right after this grating, will be the structure that is the subject of this thesis, which is the permanent structure, fabricated via photopolymerization. The temporary grating breaks the resonance using nonlinear optical effects, coupling the fiber mode into the higher-order mode and the permanent structure extracts the mode out selectively to another fiber. Due to the very fast response of the nonlinear effects, an optical switch capable of transferring optical packets to other waveguides is formed.

1.3. Outline

This dissertation is organized as follows: Chapter 2 presents the materials and chemical aspects regarding the device fabrication. In Chapter 3, optical and physical characterization methods studied throughout the thesis are described. Chapter 4 describes the theoretical and simulation studies regarding the device; and in Chapter 5, device fabrication and experimental studies are presented; and in Chapter 6, the results of the fabricated device performances are discussed.

CHAPTER 2

PHOTOPOLYMERIZATION

2.1. Introduction

A *polymer* is a very large molecule, composed of repeating structural units (Callister Jr., 2003). Commonly known polymers include synthetic polymers like plastics, PVC, PET, nylon, synthetic rubber; and natural biopolymers (produced by living organisms) like DNA and cellulose. For most polymers, the molecules are in the form of long and flexible chains. The backbone of each chain is a string of carbon atoms; many times each carbon atom singly bonds to two adjacent carbon atoms on either side. These long molecules are composed of structural entities called *mer* units, which are successively repeated along the chain; hence the word *polymer*, meaning “many mers”. The term *monomer* is sometimes used and it refers to a stable molecule from which a polymer is synthesized.

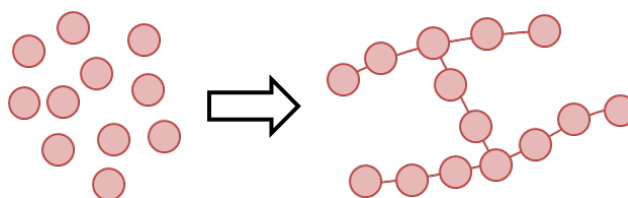


Figure 1. Monomers undergo a chemical reaction to form polymer chains.

Polymerization is the process in which monomer molecules undergo a chemical reaction to bond one another to form the polymer structure. As a result, macromolecular (polymer) chains are formed. These chains are generally linear, but they can also be branched, or cross-linked as well.

2.1.1. Photopolymerization

Photopolymerization is the reaction of monomers to produce polymers by light-induced initiation (excitation of a photoinitiator) and subsequent polymerization

(Verhoeven, 1996), (Wang and Elisseff, 2004). In other words, photopolymerization requires light in order to take place. This provides significant advantages in terms of the controllability of the reaction and the complexity of the desired patterns. In essence, the pattern of the polymerized regions follows the pattern of the exposed light employed in the photopolymerization.

Photopolymerization is a popular research area and it can be used to fabricate photonic structures such as photonic crystals or gratings structures (Jia, et.al, 2004). Photopolymers attract great deal of attention of researchers due to a relatively large refractive index modulation ($\Delta n \sim 10^{-2}$) and low cost (Lawrence, et.al, 2001) (Hesselink, et.al, 2004) (Dhar, 2006). Polymerization can be performed using pulsed (Zammit, et.al, 1997) (Garcia, et.al, 2002) or continuous-wave lasers operating in the visible or infrared wavelengths (Kim, et.al, 2005). Photonic structures can be fabricated holographically, by interfering the light beams on the polymer (Garcia, et.al, 2002), (Kim, et.al, 2005) (Martin, et.al, 1997) or by direct-writing, by exposing the polymer directly to the laser beam (Zammit, et.al, 1997). Wavelength and the energy of the beams emitted by the laser vary depending on the type of the polymer used. In holographic method, exposure of the photopolymer material to an interference pattern initiates a photopolymerization reaction that occurs preferentially in regions of constructive interference. After exposure, the photopolymer contains a periodic pattern as a spatial variation of chemical composition and corresponding variation of refractive index (Kim, et.al, 2005). As for the direct-writing method, the refractive index variation of the chemical composition after the exposure follows the intensity of the laser beam incident on the material. In direct-writing, precise control of the beam position, scanning speed and beam focus gains importance, whereas holographic method requires accurate control of the angle of incidence of beams.

2.1.2. Polymer Optical Components

The majority of photopolymer optical components stem from research aimed at obtaining memory units based on polymer materials, fabricated via holographic technique (Neipp, et.al., 2003) (Das, et.al., 2009). On the other hand, direct-writing method makes possible the fabrication of planar lightwave circuits on thin film polymer layers (Dinleyici and Sümer, 2011) (Liu, et.al, 2007).

In 2002, Ma, Jen and Dalton (Ma, et.al, 2002) compiled various polymers that could be employed in optical communication systems and investigated their properties and applications. The study provides a variety of examples for polymer waveguide devices such as interconnects, directional couplers, multiplexers, switches, tunable filters and amplifiers. In addition, the study highlights several integrated planar lightwave circuits including tunable optical add/drop multiplexers, photonic crystal waveguides, etc. In 2007, Jeong, (Jeong, et.al, 2007) used laser light from a DPSS laser to obtain photopolymerization and formed photonic structures. In 2000, Trentler, (Trentler, et.al, 2000) also used a DPSS laser system to obtain photopolymerization and presented the new materials they have developed for the technique. Similarly, Schilling, (Schilling, et.al, 1999) presented new polymers for photopolymerization and their respective performances in 1999. Another similar work is that of Li in 2004 (Li, et.al, 2004), where nanosecond-pulses were used to fabricate a holographic grating structure using photopolymerization.

Some of the studies reported in the literature regarding photopolymers are summarized in the following table, which presents a set of published outcomes that provides a perspective for evaluating the future findings of photopolymerization studies throughout this project.

Table 1. Summary of photopolymerization literature

Date	Photopolymer	Pulsed / CW	Source	Intensity	Exposure duration	Resolution / Δn	Ref
1997	Acryamide based	50nsec	Ar-ion@514nm	6mW/cm ²	60sec	3000lines/mm	1
1999	Acrylate based	CW	Nd:YAG@532nm	8mW	200sec	0.0012	2
2000	Vinyl based	CW	Nd:YAG@532nm	4mW/cm ²	1500sec	-	3
2001	Acryamide based	CW	Ar-ion@514nm	2mW/cm ²	20sec	2000lines/mm	4
2002	Acryamide based	8nsec	Nd:YAG@532nm	0.07-6.7mJ/cm ²	6000 pulses	0.0025	5
2005	Acryamide based	CW	633nm	8mW/cm ²	200sec	0.0020	6
2007	Acryamide	CW	DPSS@532nm	3mW/cm ²	-	1940lines/mm	7

In the above table, the references cited are: 1 (Martin, et.al, 1997), 2 (Schilling, et.al, 1999), 3 (Trentler, et.al, 2000), 4 (Lawrence, et.al, 2001), 5 (Garcia, et.al, 2002), 6 (Kim, et.al, 2005), 7 (Park, et.al, 2007).

In addition to the research activities focused on photopolymers and photopolymerization, there are also examples of studies obtaining photonic structures with polymers using methods other than photopolymerization. In 1998, Eldada reported the optical add/drop multiplexer realized using the Bragg Grating Mach-Zender Interferometer structures fabricated on planar polymer materials (Eldada, et.al, 1998). In the article dated 2005, Keil, et.al., report the polymer material they processed using conventional photolithography and reactive ion etching (RIE) techniques, and the multiplexer they fabricated for Fiber-to-the-Home (FTTH) applications (Keil, et.al, 2005). Also in 2005, Y.Leng, et.al. reported the fabrication and characterization of polymer waveguide structures fabricated by direct-dispensing and the surface-relief grating structures fabricated by laser ablation technique (Leng, et.al, 2005).

Volumetric refractive index modulation and surface modification effects of polymerization need to be taken into account during the design and fabrication of photopolymer optical devices (Liu, et.al, 2007). Photopolymerization achieved through laser direct-writing exhibits a non-local behavior, in that the induced material modification is not limited to the area exposed to the laser beam (Gleeson and Sheridan, 2009). The first-harmonic diffusion model demonstrated by Gallego et al. estimates the performance of holographic gratings fabricated in photopolymer materials with respect to the thickness of the polymer film layer (Gallego, et.al, 2005). Accordingly, the rate of polymerization increases with increased film thickness; so does the rate of monomer diffusion during photopolymerization. The two-way diffusion model introduced by Babeva et al. accounts for not only the diffusion mechanism taking place during the photopolymerization process, but also the post process stabilization of the material subsequent to laser direct-writing (Babeva, et.al., 2010). The study reveals an inverse correlation between the direct-writing beam intensity and the surface relief profile as a result of the photopolymerization.

2.2. Experimental Studies

2.2.1. Initial Recipe

For the polymer synthesis and photopolymerization studies, the work of Jeong, dated 2007, was taken as the model for the photopolymerization and the polymer recipe

(Jeong, et.al, 2007). In the original study, the photopolymerizable polymer was employed in writing holographic diffraction gratings with spatial frequency of approximately 1940lines/mm. As the name implies, the selected photopolymer composition is an epoxy-resin photopolymer, meaning that the epoxy-resin exists in the polymer composition to act like a skeleton for the whole polymer, providing a mechanical base for the material, thus keeping it intact.

The polymer material in the model study is composed of the following:

Table 2. Constituents of the initial polymer recipe

Material	Function
PPGDGE (Polypropylenediglycidylether)	For the synthesis of epoxy-resin
PEI (Polyethyleneimine)	For the synthesis of epoxy-resin
AA (Acrylamide)	Photopolymerizable monomer
TEA (Triethanolamine)	Co-initiator
YE (Yellowish Eosin)	Sensitizer

All reagents were used as received without any purification (PEI was prepared as an acetone solution, as explained below). As stated previously, PPGDGE and PEI are used in the synthesis of the epoxy-resin and are mixed with 1:1 molar ratio. In addition, the PPGDGE/PEI mixture must be cured at room temperature for 12h. Acrylamide is the monomer to form the backbone of the polymer chain, TEA is the co-initiator of the chain reaction and YE is the sensitizer, increasing the light sensitivity of the composition. When the light is incident on the mixture of co-initiator and the monomer, the applied energy divides the initiator into a two free radicals symmetrically or asymmetrically. This highly active free radical attacks the double bond of the monomer and activates the monomer. This process continues as a chain reaction and polymer chains are formed by back-to-back addition of monomer molecules to each other.

The batches of the photopolymerizable material are prepared based on the weight ratios stated in the model study:

Table 3. Polymer constituents and their weight ratios

Material	Reference amount	Type
TEA	218mg	Liquid
PEI + PPGDGE	242mg	PPGDGE: Liquid
		PEI: Very viscous
AA	218mg	Powder
YE	0.22mg	Powder

As stated in Table 3, PEI is a very viscous material which is soluble in acetone, so it was prepared as an acetone solution to be able to mix with remaining constituents. After studying the model and the assessment of the material properties, preparation of the polymer material was set as the following: TEA, PPGDGE, AA and YE were mixed by the given ratios in a separate beaker, while the PEI solution was prepared in another. Later, the two mixtures were added together and left to mix for 1h in an isolated beaker.

Photopolymer films were prepared by spin-coating (at different speeds between 500rpm and 3000rpm) the reactant solutions on 0.75mm-thick glass substrates. The coated samples were placed in fume hood for 12h for the PPGDGE/PEI cure and also to let the remaining acetone dry. The samples were stored in the dark to prevent polymerization of acrylamide during the epoxy cure at room temperature. The samples appear as light pink films on glass slides, while the shade of the pink depends on the thickness.

It should be remembered that the purpose of employing photopolymerization in this study is to fabricate a grating assisted coupler that would couple the higher order modes from one fiber to the neighboring one. Hence, during the course of the studies up to this point, the agenda of the photopolymerization studies were set as follows:

- 1) “Flood” exposure to investigate the change in the refractive index of the material, depending on the laser power, exposure time, film thickness and other possible effective parameters.
- 2) Expose a strip region and investigate the dependence of the resolution, beam-to-pattern relationship and depth to the exposure parameters.
- 3) Minimize the strip and investigate the limits (how small, how deep, spatial period, etc.).

Up to this point, flood exposure was qualitatively investigated and material modification was observed; exposed samples appear light yellow, whereas raw samples appear pink, as stated above. Obtaining a quantitative measure for the modification will be presented within the upcoming chapter related to the measurement techniques.

2.2.2. Transmission Spectrum

After preparation of the polymer thin film samples, it was possible to obtain the transmission spectra of the unprocessed and polymerized samples. The measurements are given in Figure 2:

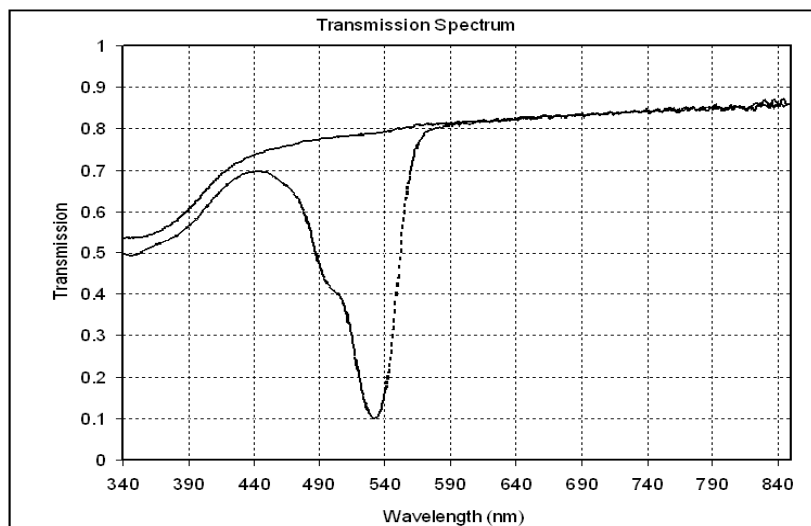


Figure 2. Polymer transmission spectra for unprocessed (dashed) and polymerized (solid) samples (Source: Dinleyici and Sümer, 2011)

This set of measurements proved to be very useful in verifying the precision of the synthesis and the photopolymerization. When compared with the transmission measurements of a similar acrylamide-based polymer from the literature, the results suggest the accuracy of the polymerization process (Garcia, et.al, 2002):

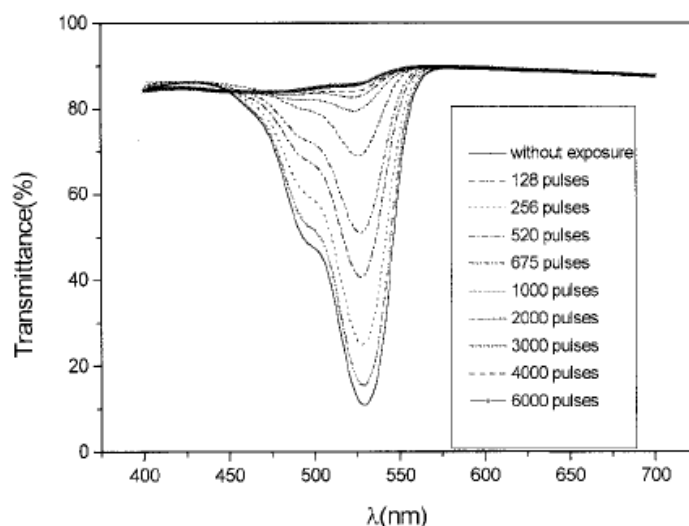


Figure 3. Transmittance spectra for different number of pulses at a pulse fluence of $1.74\text{mJ}/\text{cm}^2$ and a pulse repetition rate of 3Hz (Source: Garcia, et.al, 2002).

2.2.3. Refined Recipe – PVA Matrix

Using the epoxy-resin formulation for the matrix of the polymer formulation, total of five different batches were prepared and some recurring problems were noted regarding the preparation and handling of polyethyleneimine (PEI). First of all, PEI is a highly viscous and sticky material, leading to problems in the preparation stages of the mixtures resulting in low yields and more importantly, problems in obtaining the desired amounts and ratios in the matrix formulations. Besides the material being sticky, the ambiguities with the amounts are also mainly due to the PEI solution being prepared with acetone, which is a highly volatile material. Acetone continues to vaporize following the mixing of all the ingredients and this leads to a continuously changing viscosity of the mixture while spin-coating the samples. Since the thickness of the spun films is directly related to the viscosity of the cast material, the result is a variety of thicknesses for subsequent samples, even if the spin rate is kept constant.

This constitutes a major problem in terms of the goals of this project, i.e., even though the photopolymerization reaction is not affected by the matrix, the thickness of the films is a parameter which should be controlled very precisely but use of PEI/acetone solution prevents this.

In order to overcome the problems regarding the viscosity and handling of PEI, alternative formulations were investigated and in light of (Garcia et.al. 2002), using a Polyvinyl Alcohol (PVA) matrix was decided. In this new recipe, the

photopolymerizable monomer, co-initiator and the sensitizer are the same as the initial recipe, whereas the PPGDGE/PEI epoxy-resin is replaced by the PVA matrix prepared in the form of an aqueous solution. All the remaining batches of samples were prepared based on the molar ratios stated in the model study:

Table 4. Polymer constituents and molar ratios in the refined recipe

Material	Ratio	Calculated amount in 15ml aqueous solution	Type
H ₂ O	-	(15g)	Liquid
PVA	10% w/v H ₂ O	1.5g	Powder
TEA	0.199M	0.445g	Liquid
AA	0.446M	0.475g	Powder
YE	2.5x10 ⁻⁴ M	2.4mg	Powder

Using a PVA matrix provides several advantages over using the PPGDGE/PEI matrix. First of all, since the PVA is prepared in its aqueous solution from its powder form, using the correct amount of the material becomes possible. In addition, since the solution is prepared in water, water being much less volatile than acetone makes the preparation and handling more efficient.

With the new recipe, polymer material was prepared by adding TEA, AA and YE by the given amounts into the aqueous solution of PVA and the solution was left to stir for 24h, in order to allow for the complete solution of PVA in water. Once the solutions were ready, samples were prepared using glass substrates with varying configurations (explained below) and left in the fume hood for 24h for PVA cure. The samples were stored in the dark to prevent polymerization of Acrylamide during the PVA cure at room temperature. The samples appear as light pink films on glass slides, with the shade of the pink depending on film thickness.

2.2.4. Sample Preparation

First of all, throughout the sample preparation process, the use of 0.75mm-thick glass (silica) slides was abandoned because of difficulties in handling and sample positioning in the optical setup. Instead, 1.25mm glass (silica) slides were brought in as substrates, which provided ease in handling and durability of the samples.

The refined recipe provides the availability to prepare samples in different configurations. The first type of the prepared samples were the same as the previous batches, i.e., the polymer material was spin coated on glass substrates at 1000rpm and 2500rpm. Samples prepared with this method had film thicknesses around 5 μ m, which resulted in problems in the observability and measurements. In addition, even though spin coating distributes the polymer solution evenly throughout the surface, a near-perfect smooth surface could not be obtained using this method due to adhesivity problems.

The second variety of samples was prepared as thin films sandwiched between glass substrates with spacers of known thickness. Optical fibers with and without jackets were used as spacers, which resulted in film thicknesses of 125 μ m and 200 μ m. This set of samples have in fact demonstrated the significance of the surface quality of the thin films, revealing polymerization patterns that were previously hidden in the artifacts and noise patterns originating from the surface irregularities of the film.

The third kind of samples were prepared by direct casting (direct deposition) the polymer solution on glass substrates where the substrates were placed on level surfaces, solution was allowed to disperse evenly throughout the entire 25mm x 75mm substrate and left in the fume hood for 24h for the PVA matrix cure. This method resulted in film thicknesses of 86 μ m:

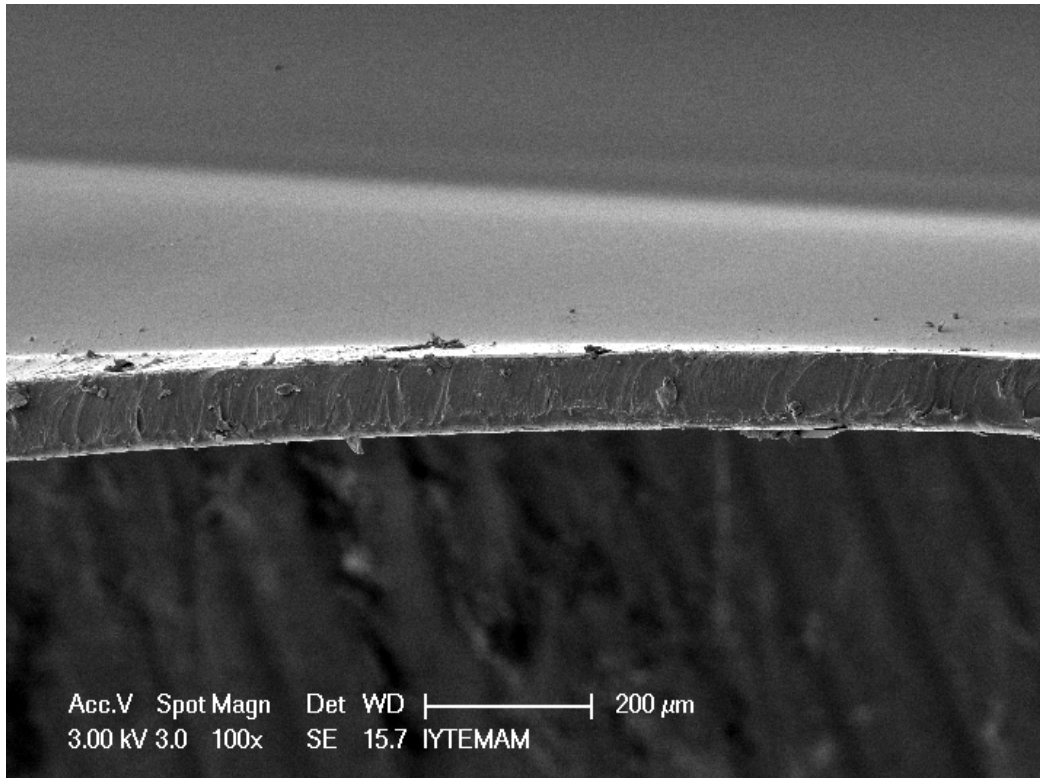


Figure 4. Scanning Electron Microscope (SEM) cross-section image of the film prepared by direct casting (The film section seen in the image is separated from the silica substrate normally underneath the polymer)

The direct deposition method actually yields to very good quality of film surface and this was directly observed in SEM analyses:

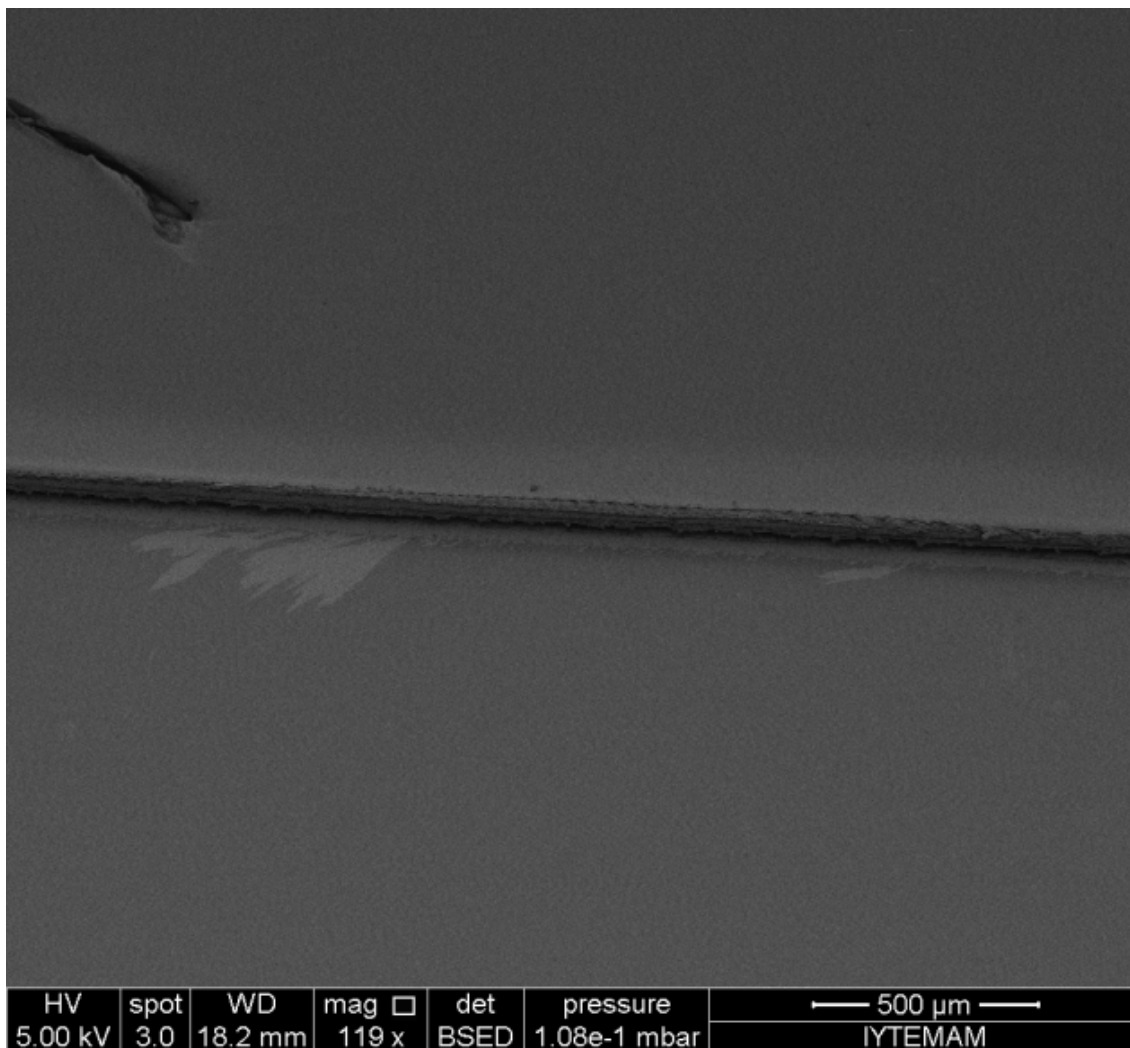


Figure 5. Scanning Electron Microscope (SEM) surface image of the film prepared by direct casting (Polymer thin film layer is seen on the top half and the glass substrate is seen on the bottom half of the image).

The quantitative analyses regarding the exact refractive index and the change induced on the material by photopolymerization are presented in the following chapter.

CHAPTER 3

CHARACTERIZATION TECHNIQUES

3.1. Brewster Angle Methods

3.1.1. Theory

The reflection of light from an interface of different indices of refraction is represented by the Fresnel equations. The reflection coefficient of p-polarized light is given by (Saleh and Teich, 2007):

$$r_p = \frac{n_2 \cos \theta_1 - n_1 \cos \theta_2}{n_2 \cos \theta_1 + n_1 \cos \theta_2} \quad (3.1)$$

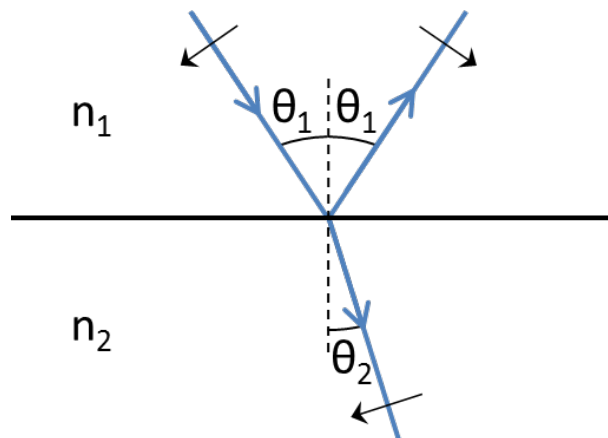


Figure 6. p-polarized external reflection

When p-polarized light is incident on an interface from a medium of refractive index n_1 to a medium of index of n_2 (external reflection), the reflection coefficient decreases from a positive value of $(n_2 - n_1)/(n_2 + n_1)$ at normal incidence, until it vanishes at an angle $\theta_1 = \theta_B$ called the Brewster angle. Light is not reflected at the Brewster angle, which can be expressed as (Saleh and Teich, 2007):

$$\theta_B = \tan^{-1} \frac{n_2}{n_1} \quad (3.2)$$

The *Brewster angle method* is one of the most popular techniques for determining the refractive index of optical materials (Schutzmann, et.al, 2005). It is simple to set up and use. Bulk material is illuminated with p-polarized light and the angle of incidence is scanned for the minimum reflectance angle. The minimum reflectance angle is the Brewster angle for the material and the refractive index is found simply by taking the tangent (given that the ambient medium is air, i.e., $n_1=1$). However, in the case of thin film analysis, the estimation of the film refractive index is not straightforward since the reflection response is the convolution of the substrate–film system. On this regard, *Abele’s–Brewster method* (Abeles, 1963) should be used. When the angle of incidence of p-polarized light is equal to Brewster angle for the ambient–film interface, the reflectance from covered and uncovered substrate are equal regardless of the film thickness, since the contribution of the reflected light from the ambient–film interface is zero. Therefore, in the Abele’s–Brewster method, the experimental data of the ambient–film–substrate system has to be compared with the ambient–substrate system. The intersection of reflectance curves of covered and uncovered regions represent the Brewster angle of the film, from which the refractive index can be estimated using Equation (3.2).

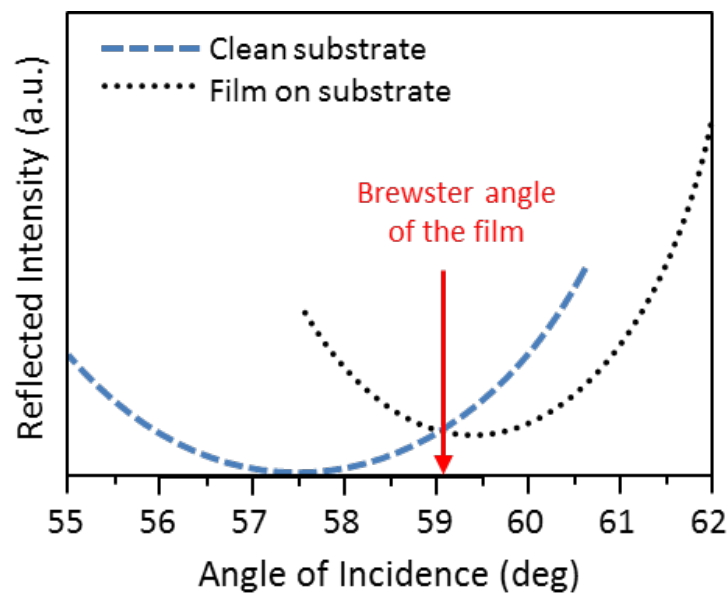


Figure 7. The Abelés-Brewster method.

The Abele's–Brewster method could be enhanced using computer simulations and employing data fitting for the measured values. The reflectance $R(\theta)$ for p-polarized light of an ambient–film–substrate system has the form (Born and Wolf, 1999):

$$R(\theta) = \left| \frac{r_{01} + r_{12}e^{-2i\beta}}{1 + r_{01}r_{12}e^{-2i\beta}} \right|^2 \quad (3.3)$$

where, r_{01} and r_{12} are Fresnel reflection coefficients at the ambient–film and film–substrate interfaces, respectively, and β is given by:

$$\beta = \frac{2\pi}{\lambda_0} n_1 d \cos \theta_t = \frac{2\pi}{\lambda_0} d \sqrt{n_1^2 - n_0^2 \sin^2 \theta} \quad (3.4)$$

where λ_0 is the free-space wavelength, d is the film thickness, θ is the angle of incidence in the ambient, θ_t the angle of refraction, and n_0 and n_1 are the refractive indices of ambient and film, respectively. To estimate the refractive indices, the substrate refractive index (n_2) and the film thickness (d) must be known. The substrate index could be obtained by a bulk Brewster angle measurement. Film thickness measurements are possible using a mechanical profilometer. It should be noted that using a profilometer could be a destructive procedure for some materials and it may have to be avoided. Using Scanning Electron Microscopy (SEM) is an alternative for thickness measurements and visual surface quality assessments. However, it should also be kept in mind that depending on the material of the films, the sample may have to be coated with a conductor material and the sample may not be viable for further use.

3.1.2. Experimental Setup

In order to obtain the refractive indices of the polymerized and unpolymerized samples, measurements regarding Brewster angle techniques were pursued and the technique was investigated further. The initial setup used in the measurements can be seen in the following figure:

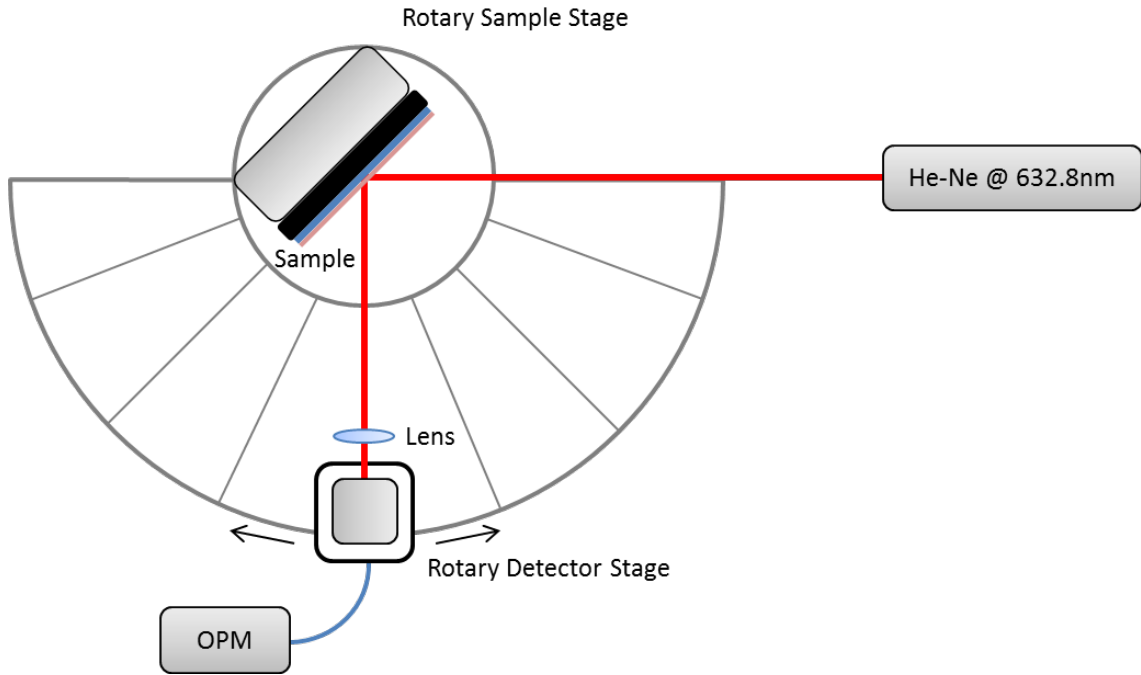


Figure 8. Schematic representation of the initial Brewster measurement setup

This setup employs a 632.8nm He-Ne laser and has an angular resolution of 0.5° , which corresponds to a refractive index difference of approximately 0.027 between incident angles of 50° and 60° . The following dataset was obtained in the measurements:

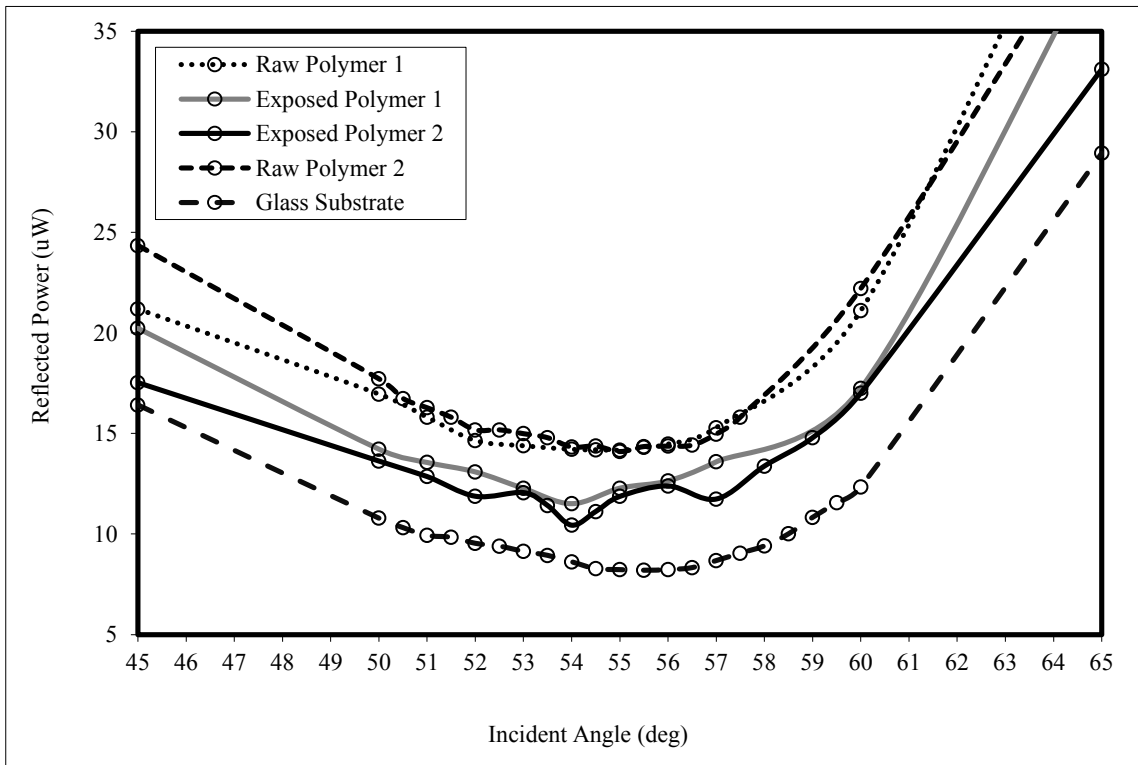


Figure 9. Initial Brewster angle measurements

Using this setup, the refractive indices of BK7 glass substrates, raw (unpolymerized) and exposed (polymerized) samples were measured and a refractive index of 1.455 ± 0.013 for BK7, 1.428 ± 0.013 for raw samples and 1.376 ± 0.013 for exposed samples were estimated.

However, discrepancies in reproducibility of the measurements have led to investigations of the setup itself. Long-term measurements of 632.8nm He-Ne laser were performed using Newport 1830-C Optical Power Meter via RS232 connection and Newport 818-BB-21 Photodiode with HP 34401A Digital Multimeter via GPIB connection to the computer. Later, it was found more effective to use GPIB connection for both instruments. As a result, the following output characteristics were obtained for the 632.8nm laser:

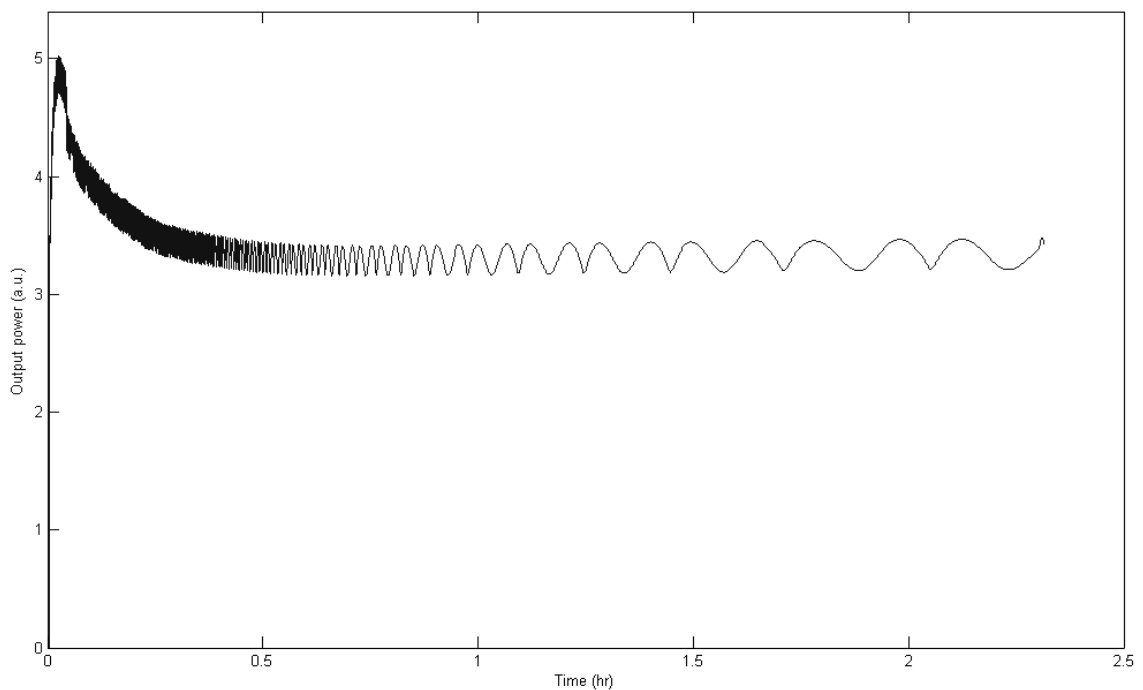


Figure 10. Output variation of 632.8nm He-Ne laser, with both short-term and long-term components

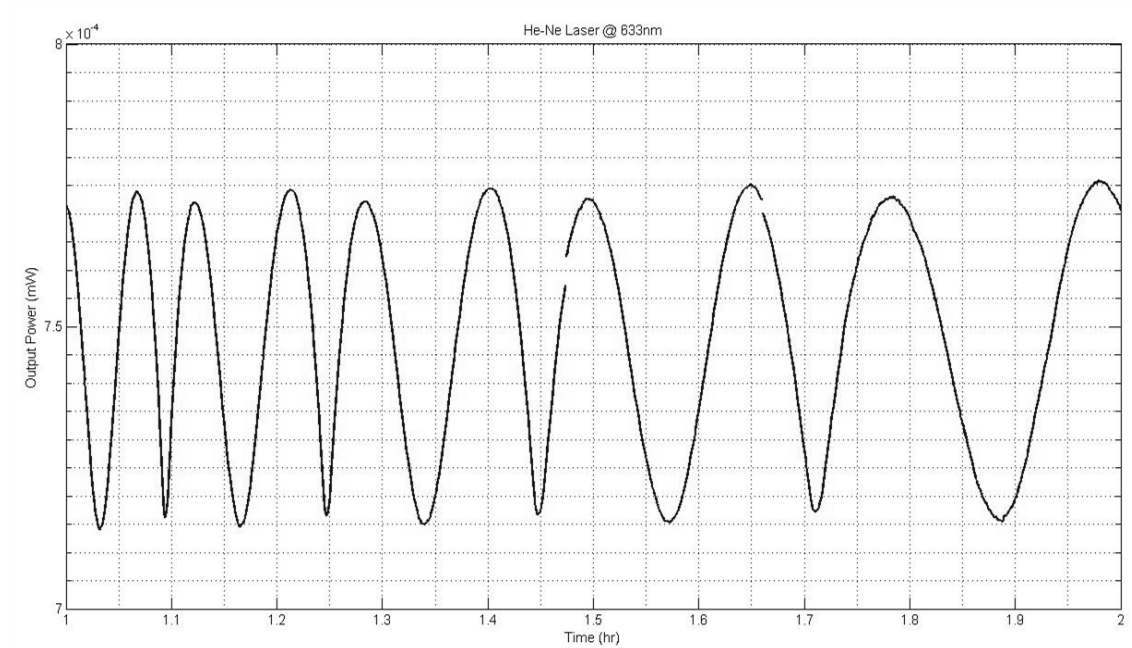


Figure 11. Output variation of 632.8nm He-Ne laser - detail

As seen in the above figure, the output of the laser varies both in short and long range measurements and this explains the problems with the reproducibility of the measurements. In addition, with the output of the laser varying as such, sensitive measurements required for the Brewster technique are not possible. In order to overcome this problem, the measurement setup was modified to enable measuring the laser output prior to reflection from the sample surface. This allows for the normalization of the output with respect to the variations in laser the laser input. In the improved setup, Newport 818-BB-21 Photodiode with HP 34401A Digital Multimeter via GPIB connection was used to measure the laser output and Newport 1830-C Optical Power Meter via RS232 connection was used to collect the reflection data:

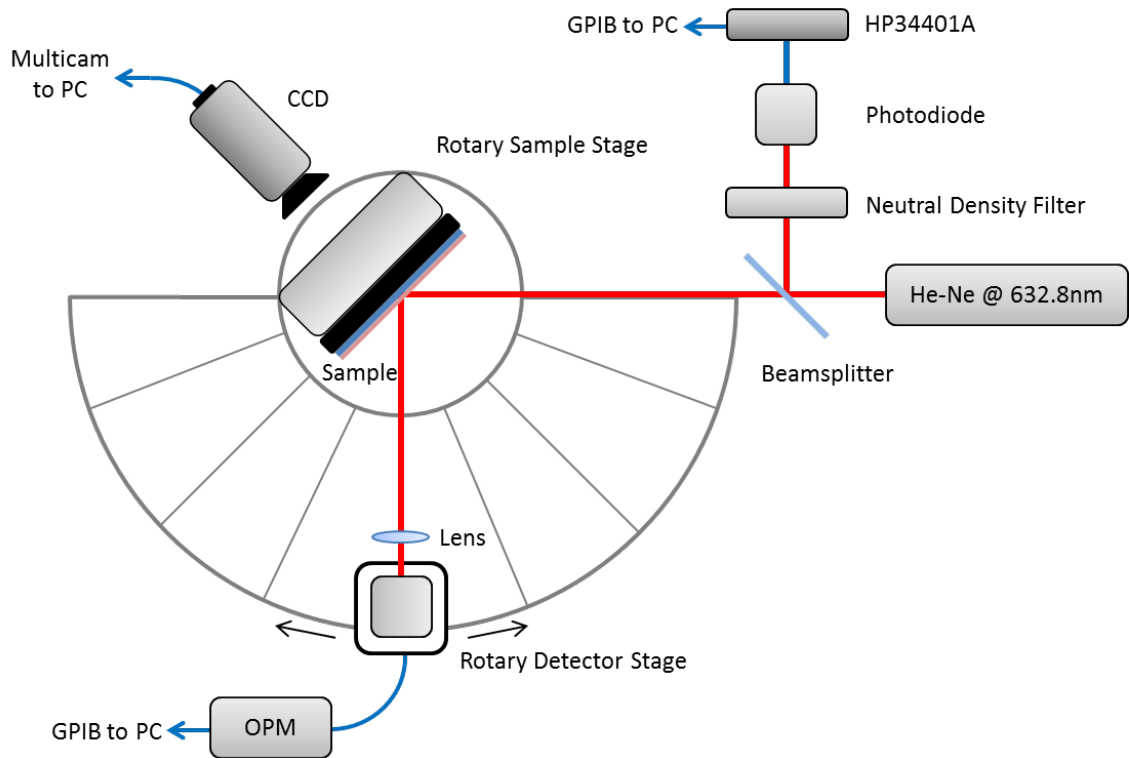


Figure 12. Schematic representation of the improved Brewster techniques setup

Using the improved setup, owing to the computer connections and the ability to program the measurements with MATLAB, the recorded data for each angle was obtained by averaging a series of values in order to overcome the noise and other undesired fluctuations. The data obtained using this setup have proven to be useful in obtaining reproducible i.e., more accurate measurements of angular reflection. As a result, a refractive index value of **1.455** was measured for the raw polymer material at 632.8nm wavelength.

3.1.3. An Improved Method

In parallel to reflection measurements, modeling and simulations of the reflection were also studied in order to perform a data-fit of the measured data to the calculated values and thus to provide a better measurement technique for the thin film refractive index. Consider the following three-layer model:

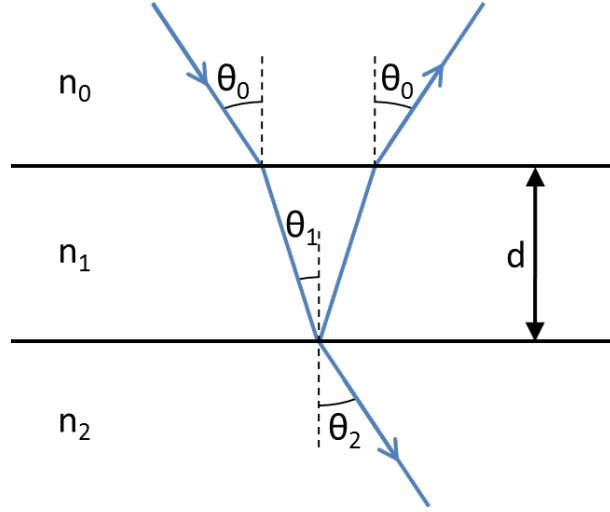


Figure 13. Three-layer model used for reflectance calculations

Where n_0 , n_1 and n_2 represent the ambient, polymer thin film and substrate refractive indices, respectively, d is the film thickness, θ_0 and θ_1 are the angles of incidence for the incoming beam and the refracted beam in the polymer layer and θ_2 is the angle of refraction in the substrate region. From (Born and Wolf, 1999), the reflectivity of a homogeneous dielectric film located between two homogeneous media for p-polarized light can be expressed as:

$$R(\theta) = \left| \frac{r_{01} + r_{12}e^{-2i\beta}}{1 + r_{01}r_{12}e^{-2i\beta}} \right|^2 \quad (3.5)$$

where r_{01} and r_{12} are Fresnel reflection coefficients at the ambient–film and film–substrate interfaces, respectively, and β is given by:

$$\beta = \frac{2\pi}{\lambda_0} n_1 d \cos \theta_1 = \frac{2\pi}{\lambda_0} d \sqrt{n_1^2 - n_0^2 \sin^2 \theta_0} \quad (3.6)$$

where λ_0 is the free-space wavelength. The Fresnel coefficients for the interfaces are given by (Saleh and Teich, 2007):

$$r_{01} = \frac{n_1 \cos \theta_0 - n_0 \cos \theta_1}{n_1 \cos \theta_0 + n_0 \cos \theta_1} \quad (3.7)$$

$$r_{12} = \frac{n_2 \cos \theta_1 - n_1 \cos \theta_2}{n_2 \cos \theta_1 + n_1 \cos \theta_2} \quad (3.8)$$

Using Snell's Law:

$$n_0 \sin \theta_0 = n_1 \sin \theta_1 \quad (3.9)$$

and trigonometric identities, Equations (3.7) and (3.8) can be re-written as:

$$r_{01} = \frac{n_1 \cos \theta_0 - n_0 \sqrt{1 - \left(\frac{n_0}{n_1} \sin \theta_0\right)^2}}{n_1 \cos \theta_0 + n_0 \sqrt{1 - \left(\frac{n_0}{n_1} \sin \theta_0\right)^2}} \quad (3.10)$$

$$r_{12} = \frac{n_2 \sqrt{1 - \left(\frac{n_0}{n_1} \sin \theta_0\right)^2} - n_1 \sqrt{1 - \left(\frac{n_0}{n_2} \sin \theta_0\right)^2}}{n_2 \sqrt{1 - \left(\frac{n_0}{n_1} \sin \theta_0\right)^2} + n_1 \sqrt{1 - \left(\frac{n_0}{n_2} \sin \theta_0\right)^2}} \quad (3.11)$$

For mathematical convenience, reflectance expression given in Equation (3.5) can be re-written without using the exponential terms (Born and Wolf, 1997) as:

$$R(n_0, n_1, n_2, \theta_0, d, \lambda_0) = \frac{r_{01}^2 + r_{12}^2 + 2r_{01}r_{12} \cos 2\beta}{1 + r_{01}^2 r_{12}^2 + 2r_{01}r_{12} \cos 2\beta} \quad (3.12)$$

Where, $\beta = \beta(n_0, n_1, \theta_0, d, \lambda_0)$, $r_{01} = r_{01}(n_0, n_1, \theta_0)$ and $r_{12} = r_{12}(n_0, n_1, n_2, \theta_0)$ are as given in Equations (3.6), (3.10) and (3.11), respectively.

Now consider the case where the incoming beam's angle of incidence is exactly the Brewster angle for the ambient-film interface, i.e., $\theta_0 = \tan^{-1}(n_1/n_0) = \theta_B$. For this case, it can easily be seen that:

$$r_{01}(\theta_0 = \theta_B) = 0 \quad (3.13)$$

$$r_{12}(\theta_0 = \theta_B) = \frac{n_1 n_2 - \frac{n_1}{n_2} \sqrt{n_0^2 n_2^2 + n_1^2 n_2^2 - n_0^2 n_1^2}}{n_1 n_2 + \frac{n_1}{n_2} \sqrt{n_0^2 n_2^2 + n_1^2 n_2^2 - n_0^2 n_1^2}} \quad (3.14)$$

and,

$$\beta(\theta_0 = \theta_B) = \frac{2\pi}{\lambda_0} dn_1^2 \frac{1}{\sqrt{n_0^2 + n_1^2}} \quad (3.15)$$

Substituting Equations (3.13), (3.14) and (3.15) in the reflectance equation (3.12) yields the expression for the reflectance when the angle of incidence equals the Brewster's angle for the ambient-film interface:

$$R(\theta_0 = \theta_B) = r_{12}^2 \quad (3.16)$$

Which is a function of n_0 , n_1 and n_2 , i.e., $R(\theta_0 = \theta_B) = R(n_0, n_1, n_2)$. This means that when the angle of incidence is equal to the Brewster's angle for the ambient-film interface, the value of the reflectance does *not* depend on the thickness of the film. To put mathematically, if $\theta_0 = \theta_B$, then:

$$\frac{\partial R}{\partial d} = \frac{\partial r_{12}^2}{\partial d} = 0 \quad (3.17)$$

The interpretation of the above equation implies the following: For a set of reflectance measurements performed on different three-layer samples with the same material in the thin film layer, the measured reflectance value at the Brewster angle will always be the same, regardless of the film thickness. Consequently, by a set of measurements performed on samples with different thicknesses, the refractive index of the film can be found without any necessity to know the actual thickness of the film layers themselves. This property was also observed by (Pawluczyk, 1990) and partially analyzed by (Surdutovich, et.al, TSF, 1999) and (Surdutovich, et.al, AO, 1999). In this section, mathematical fundamentals of the property presented above are utilized for further investigation; in addition, significance of the method is demonstrated based on consequent derivations, numerical analysis and experimental studies.

It should be noted here that, for the three-layer configuration presented in Figure 13, if $\theta_0 = \theta_B$, obtaining a zero reflection coefficient for any given film thickness requires either $n_2 = n_0 = 1$ or $n_1 = n_2$ in Equation (3.14), which implies the structure to be either a film layer sandwiched by ambient on both sides, or, to be a two-layer structure. This result makes the condition presented in (Surdutovich, et.al, AO, 1999) to

be incorrect, i.e., if $\theta_0 = \theta_B$, it is *not* possible to reduce the reflection coefficient of a film-covered substrate to zero for any film thickness.

Reflectance curves of various samples with film layer thicknesses varying between $0.5\mu\text{m}$ and $300\mu\text{m}$ have been calculated for the laser wavelength of 633nm , illustrating the uniqueness of the intersection point.

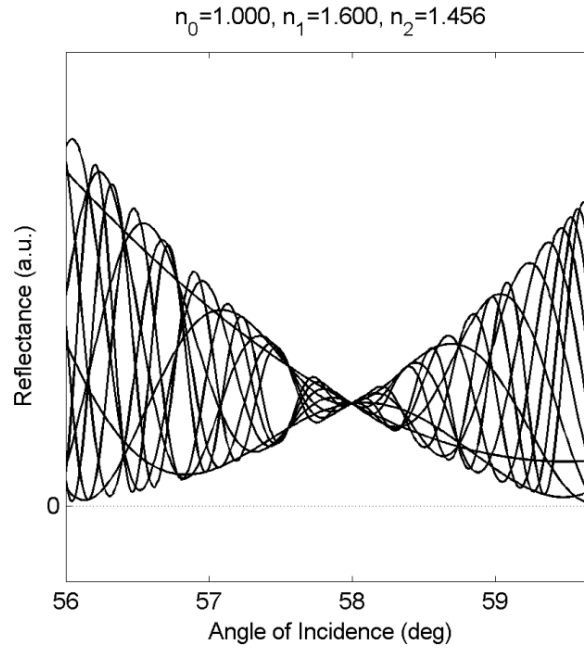


Figure 14. Intersection of reflectance curves for different film thicknesses. Intersection angle corresponds to the Brewster angle for $n_0 - n_1$ interface.

Although measuring only two samples with different thicknesses would be sufficient to determine the refractive index of the film, a higher number of measurements leads to higher precision in determining the exact angular point of intersection, overcoming possible experimental errors and noise factors.

Moreover, if the same dielectric thin film is coated on another substrate with a different refractive index, the angular location of the intersection point remains the same. The difference is only the value of reflectance at the point of intersection. This variation can be pictured as the intersection point shifting upwards or downwards on the reflectance graph with shift direction depending on the substrate refractive index. What this means is, with this method neither the thickness of the film layer, nor the refractive index of the substrate needs to be known in order to calculate the refractive index of the film. As stated previously, once the angle of intersection for the reflectance curves is determined, the refractive index of the film layer can easily be calculated, since the

angle of intersection corresponds to the Brewster angle for the ambient-film interface.

That is:

$$\tan \theta_{int} = \frac{n_1}{n_0} \Rightarrow n_1 = n_0 \tan \theta_{int} \quad (3.18)$$

In addition, further investigation shows that a *second* intersection of the reflectance curves occurs due to r_{12} becoming zero at the angle of incidence calculated by:

$$\theta_0 = \sin^{-1} \left(\frac{n_1 n_2}{n_0 \sqrt{n_1^2 + n_2^2}} \right) \quad (3.19)$$

if a three-layer structure as in Figure 13 satisfies either of the below conditions:

$$n_1 \leq \frac{n_2}{\sqrt{n_2^2 - 1}} \quad (3.20)$$

$$n_2 \leq \frac{n_1}{\sqrt{n_1^2 - 1}} \quad (3.21)$$

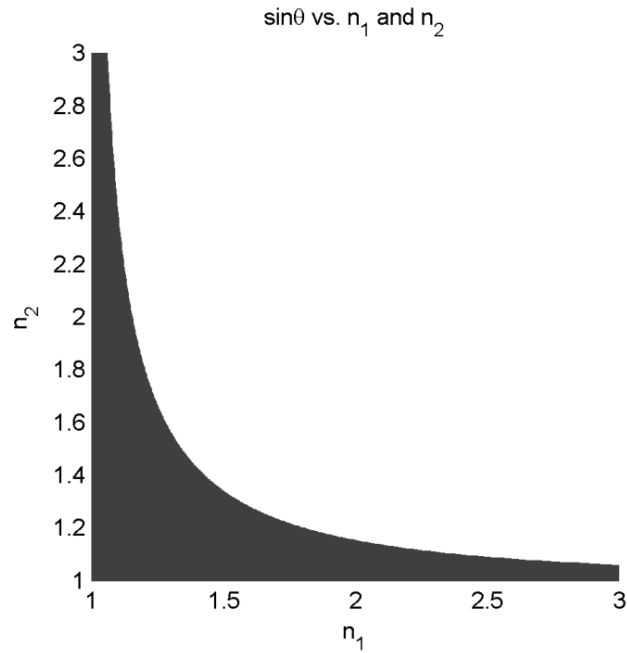


Figure 15. Region of existence (shaded area) for the second intersection.

This second intersection, an example of which is depicted in Figure 16, occurs because either of the conditions (3.20) or (3.21) makes the Brewster angle for the second intersection smaller than the critical angle for the interface, allowing it to exist within the measurable range.

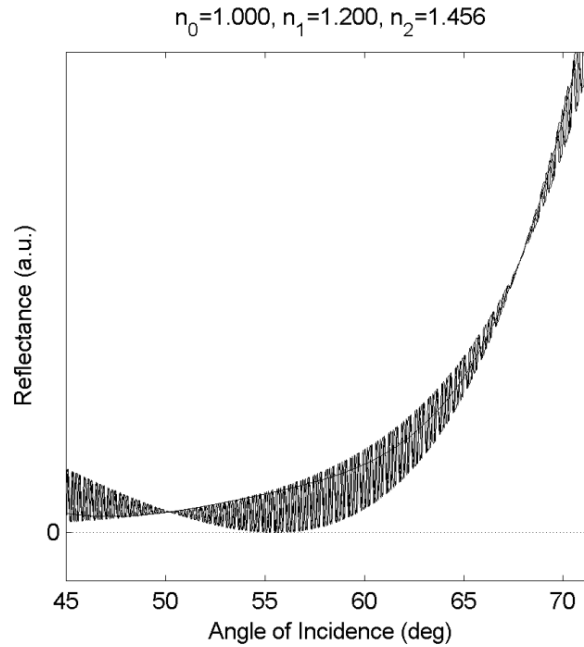


Figure 16. Intersection of reflectance curves for different thicknesses. Intersection angles correspond to the Brewster angles for $n_0 - n_1$ and $n_1 - n_2$ interfaces.

3.1.3.1 Substrate Refractive Index

If two intersection points exist for the reflectance curves of an ambient-film-substrate configuration, it can be shown that the substrate refractive index can be determined using the angular data alone. If the intersection angles of the curves are obtained using the measurements, it is possible to determine the substrate refractive index without having to know neither the refractive index (n_1) nor the thickness (d) of the thin film layer. It can be shown that, using Equations (3.18) and (3.19) and assuming the ambient is air ($n_0 = 1$) the substrate refractive index can be found using:

$$n_2 = \frac{\alpha\beta}{\sqrt{\alpha^2 - \beta^2}} \quad (3.22)$$

where $\alpha = \tan(\theta_{i1})$, $\beta = \sin(\theta_{i2})$ and θ_{i1} and θ_{i2} are the first and second intersection points, respectively ($\theta_{i1} < \theta_{i2}$).

3.1.3.2 Sensitivity

The sensitivity of the method was investigated by studying the reflectance curves at the intersections in detail. Sensitivity was defined by the angular width of the uncertainty region and determined by the loss of linearity in the envelope enclosing multiple reflectance curves. The angular width was taken as the error margin determining the ambiguity of the results achievable by the method.

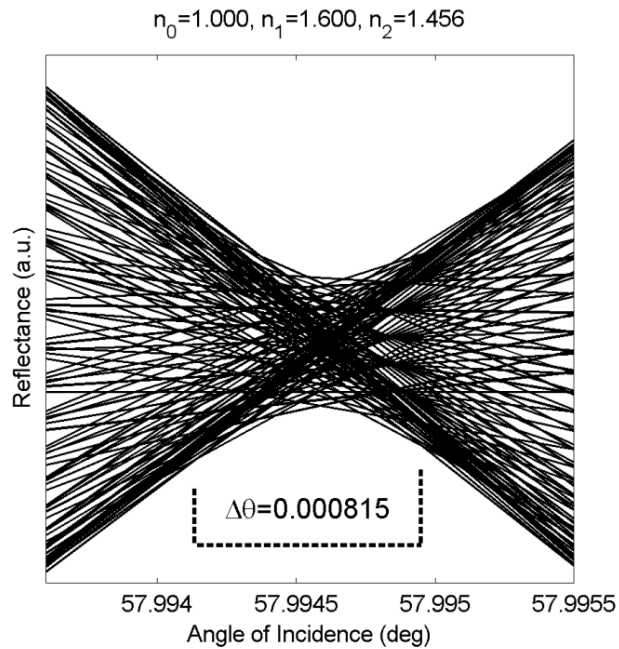


Figure 17. Close study of the intersection point of reflectance curves for the configuration with a single intersection

For the configuration including a single intersection of reflectance curves as illustrated in Figure 14, the close study of the intersection point indicates an angular uncertainty of $\Delta\theta = 0.000815^\circ$, as shown in Figure 17. Accordingly, for the single intersection configuration, the maximum error in the refractive index measurement corresponds to $\Delta n = 1.4224 \times 10^{-5}$.

For the configuration including two intersections as illustrated in Figure 16, the angular width of uncertainty for the first intersection was determined as $\Delta\theta = 0.00163^\circ$

which corresponds to a maximum error in refractive index of $\Delta n = 2.8449 \times 10^{-5}$ (see Figure 18).

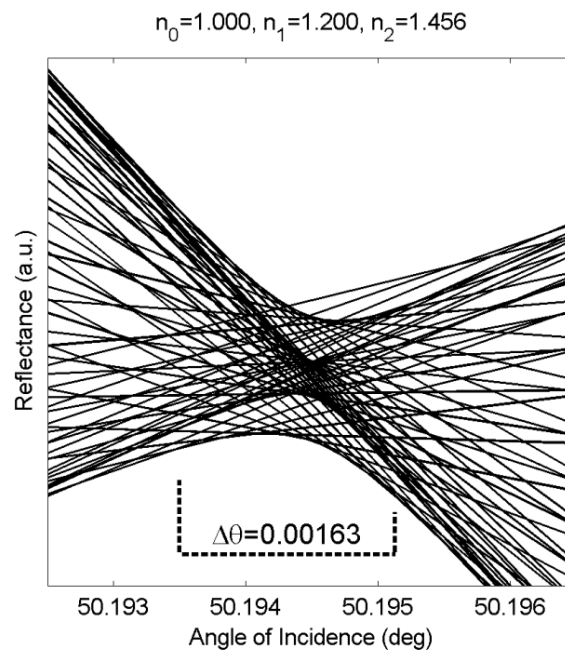


Figure 18. Close study of the first intersection point of reflectance curves for the configuration with two intersections.

For the same configuration, the angular width uncertainty for the second intersection was determined as $\Delta\theta = 0.0014^\circ$, corresponding to a maximum error in substrate refractive index of $\Delta n = 2.0541 \times 10^{-3}$ (see Figure 19).

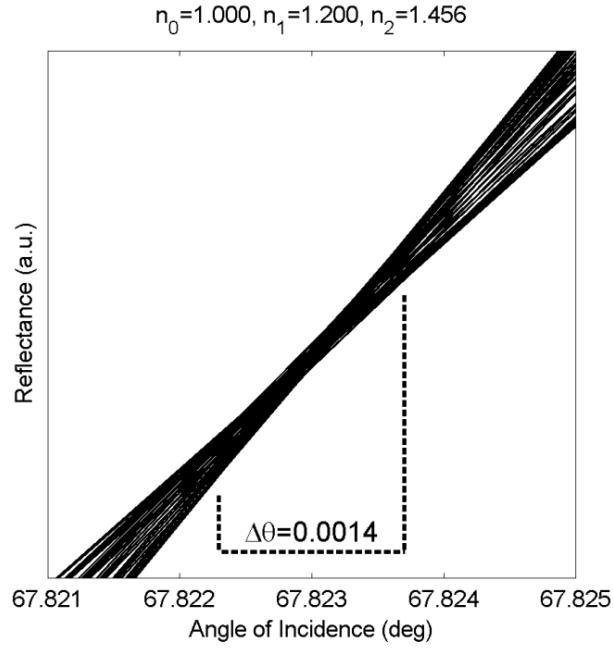


Figure 19. Close study of the second intersection point of reflectance curves for the configuration with two intersections.

3.1.3.3 Accuracy

Accuracy analysis of the method was performed by studying the exact location of intersection points in the reflectance curves. Intersection locations were determined by tracing the linear sections of the envelopes enclosing the reflectance curves and corresponding refractive indices were calculated. For thin film refractive index n_1 , relative errors of the analytically determined refractive indices were calculated with respect to the actual refractive indices. In configurations with two intersection points, substrate refractive indices n_2 were also obtained using the intersection points θ_{i1} and θ_{i2} with Equation (3.22) and relative errors were calculated with respect to the actual substrate refractive indices.

The analysis of the intersection point for the configuration with a single intersection point given in Figure 17 is presented in Figure 20. Results indicate a relative error rate of $1.5464 \times 10^{-5} \%$ in determining the thin film refractive index.

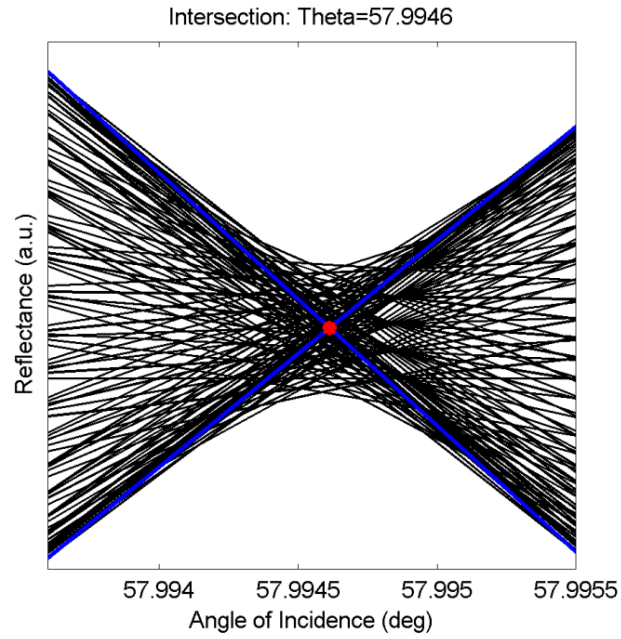


Figure 20. Determining the exact point of intersection for the single-intersection configuration.

For the configuration with two intersections presented in Figure 18 and Figure 19, the analysis of the exact intersection points indicate a relative error rate of $2.9897 \times 10^{-5} \%$ and $1.2772 \times 10^{-5} \%$ in determining the thin film and substrate refractive indices, respectively (See Figure 21 and Figure 22).

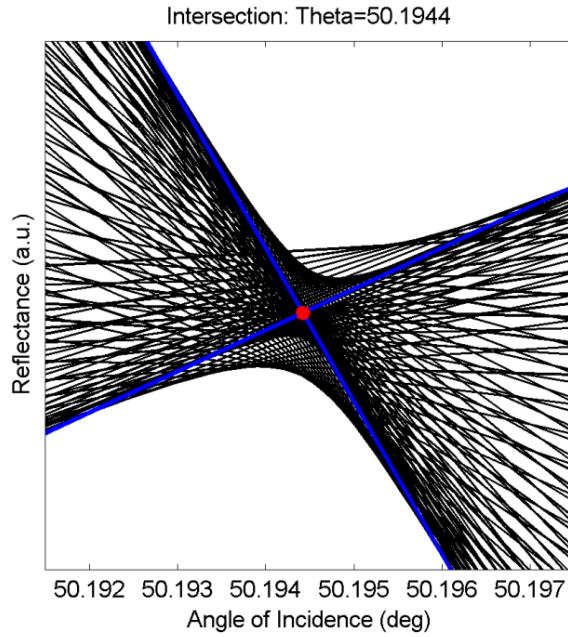


Figure 21. Determining the exact point of intersection for the first intersection of two-intersection configuration.

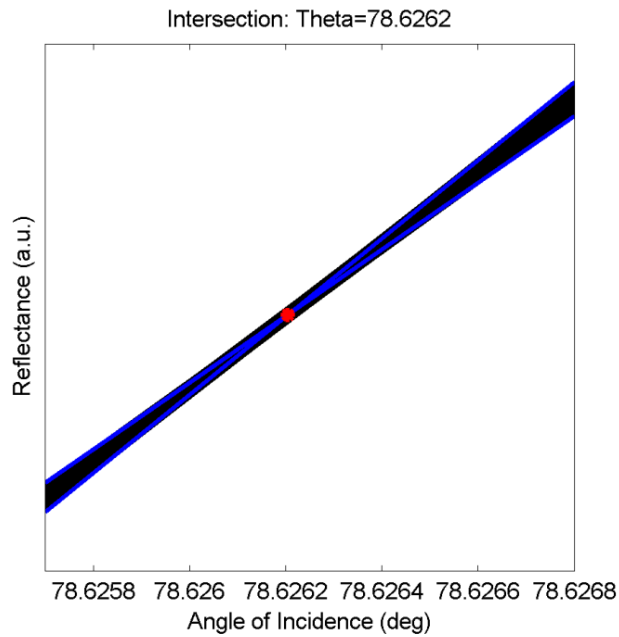


Figure 22. Determining the exact point of intersection for the second intersection of two-intersection configuration.

The results presented above, as well as calculations for additional configurations are presented together in the next section. The complete set of calculations used in the sensitivity and accuracy analyses for all of the configurations listed in the related tables are presented in APPENDIX B.

3.1.3.4 Numerical Results

Results of the sensitivity analysis are presented in Table 5.

Table 5. Sensitivity analysis of the method.

Configuration			Calculation			
n_0	n_1	n_2	$\Delta\theta_{i1}$	n_1 sensitivity	$\Delta\theta_{i2}$	n_2 sensitivity
1.000	1.200	1.456	0.001630°	2.8449×10^{-5}	0.001400°	2.0541×10^{-3}
1.000	1.600	1.456	0.000815°	1.4224×10^{-5}	-	-

Results show a refractive index sensitivity of up to 0.000014 for the measurement of the thin film layer, which is beyond any of the sensitivity figures reported earlier regarding the Brewster angle based methods. It also shows a sensitivity for the measurement of substrate refractive index of 0.002054.

Results of the accuracy analyses for the thin film refractive index (RI) based on the first intersection and the substrate refractive index based on the second intersection are presented in Table 6 and Table 7, respectively. In both tables, determined values for the intersection angles are only shown up to the third digit and error figures are only shown up to the fourth digit for convenience.

Table 6. Accuracy analysis of the method for the first intersection

Configuration			Calculation		
n_0	n_1	n_2	θ_{i1}	Absolute RI error	Relative error
1.000	1.200	1.456	50.194°	9.8055×10^{-7}	$8.1713 \times 10^{-5} \%$
1.000	1.200	1.700	50.194°	3.5876×10^{-7}	$2.9897 \times 10^{-5} \%$
1.000	1.245	1.483	51.228°	4.2595×10^{-6}	$3.4214 \times 10^{-4} \%$
1.000	1.245	1.513	51.228°	1.1016×10^{-7}	$8.8487 \times 10^{-6} \%$
1.000	1.455	1.522	55.499°	1.2927×10^{-7}	$8.8846 \times 10^{-6} \%$
1.000	1.581	1.483	57.686°	7.4596×10^{-7}	$4.7183 \times 10^{-5} \%$
1.000	1.600	1.456	57.994°	2.4741×10^{-7}	$1.5464 \times 10^{-5} \%$
1.000	1.875	1.513	61.927°	1.4585×10^{-8}	$7.7789 \times 10^{-7} \%$
1.000	1.900	1.700	62.241°	1.0293×10^{-7}	$5.4174 \times 10^{-6} \%$

For the configurations listed in Table 6, the existence of the second intersection of reflectance curves was checked via Equations (3.20) and (3.21). For configurations with a second intersection, angular values of second intersection θ_{i2} were calculated

and corresponding substrate refractive indices were calculated using θ_{i1} values from Table 6 and Equation (3.22).

Table 7. Accuracy analysis of the method for the second intersection.

Configuration			Calculation		
n_0	n_1	n_2	θ_{i2}	Absolute RI error	Relative error
1.000	1.200	1.456	67.822°	6.3753×10^{-7}	$4.3787 \times 10^{-5} \%$
1.000	1.200	1.700	78.626°	1.2002×10^{-6}	$7.0603 \times 10^{-5} \%$
1.000	1.245	1.483	72.464°	6.4601×10^{-6}	$4.3561 \times 10^{-4} \%$
1.000	1.245	1.513	74.021°	8.0807×10^{-6}	$5.3409 \times 10^{-4} \%$

For the thin film measurement, results of the accuracy analysis show a minimum accuracy of 4.25×10^{-6} in refractive index value, corresponding to a relative error rate of $3.42 \times 10^{-4} \%$. In determining the substrate refractive index, results show a minimum accuracy of 8.08×10^{-6} in refractive index value, corresponding to an error rate of $5.34 \times 10^{-4} \%$. In addition to the minimum accuracy, the thin film measurement results also indicate that it is possible to reach a maximum accuracy of 1.45×10^{-8} using the method, corresponding to a minimum relative error of $7.77 \times 10^{-7} \%$.

3.1.3.5 Experimental Results

For the experimental verification of the improved method, the angular reflectance measurement system illustrated in Figure 12 was used. In the study, angular reflectance characteristics of three samples of AA/PVA thin film covered glass substrates with film thicknesses 75 μm , 80 μm and 90 μm were measured and the obtained results are presented in Figure 23. It is known from earlier studies that the polymer has a refractive index of 1.455 at 632.8nm wavelength.

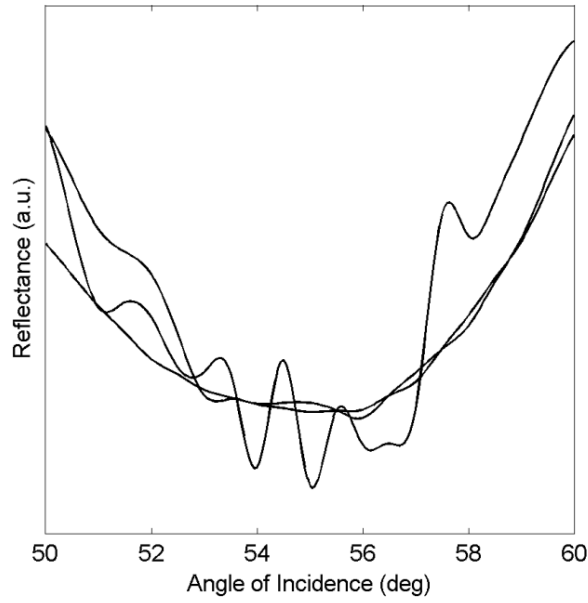


Figure 23. Reflectance curves of the three thin film-on-glass samples.

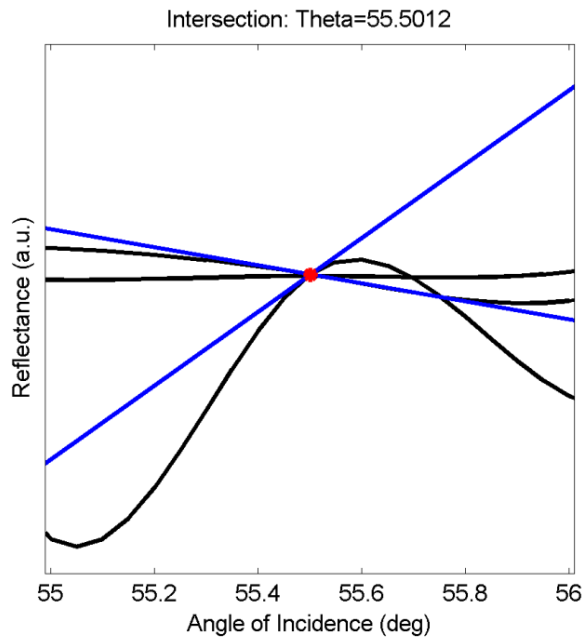


Figure 24. Exact point of intersection analysis for the reflectance curves

The close study of the reflectance curves presented in Figure 24 reveals the intersection point at $\theta_i = 55.5012^\circ$, corresponding to an absolute refractive index error of 7.1707×10^{-5} and a relative error of $4.9283 \times 10^{-3} \%$. The three-layer configuration under investigation and the overall results are reviewed in Table 8.

Table 8. Experimental results

Configuration			Measurement results		
n_0	n_1	n_2	θ_t	Absolute RI error	Relative error
1.000	1.455	1.522	55.501°	7.1707×10^{-5}	$4.9283 \times 10^{-3} \%$

Considering the absolute and relative error values achieved through the experimental results, it can be seen and concluded that there is significant improvement in the accuracy of the method. Even though only three samples were involved in the experimental studies, the results obtained demonstrate the remarkable improvement brought on to the Brewster angle based techniques by the improved method. Increasing the number of samples used in the measurements would further improve the achieved results and bring the experimental results closer to the calculated accuracy levels presented in Table 6.

While the experimental results indicate that the measured three-layer structure leads to a single intersection of reflectance curves, this result is also confirmed by cross-checking conditions (3.20) or (3.21) with the obtained results.

In summary, the improved method has been shown to have a theoretical thin film refractive index sensitivity of 0.000014 and substrate refractive index sensitivity of 0.002054. To our knowledge, this is the highest sensitivity reported regarding Brewster angle based thin film measurement methods. Furthermore, experimental studies of the method have led to an absolute error in thin film refractive index measurement of 0.000072 and a relative error of 0.0049 %, where both error values are subject to further improvement by increasing the number of samples employed in the measurements.

Even though the level of accuracy obtainable with the method is quite impressive, the volumetric structure of the refractive index change should also be studied. Therefore, the thin film measurements obtainable with the improved Brewster angle method do not entirely satisfy the needs of the study. In order to obtain the volumetric refractive index information of direct-written photopolymer structures, a study of the refractive index measurement techniques based on diffraction methods have been performed.

3.2. Diffraction Methods

3.2.1. Initial Studies

The main aim of this approach in determining the refractive indices was to measure the *difference* in the refractive indices of polymerized and unpolymerized samples, which was a value that could not have been detected using the Brewster method measurements. The approach is based on the work of Sabatyan and Tavassoly, which investigates the diffraction of a plane wave from a phase object. In (Sabatyan and Tavassoly, 2007) the technique was used to determine the refractive indices of optical fibers and in (Sabatyan and Tavassoly, 2009) it was used to determine the refractive indices of a number of liquids into which optical fibers with known shape, core and cladding refractive indices were immersed. The technique is based on measuring the normalized intensity distribution of the Fresnel diffraction pattern of a monochromatic plane wave diffracted from a phase object.

Using the setup illustrated below, direct-writing photopolymerization have been performed on samples prepared by direct casting method to write line (i.e., waveguide) structures and the diffraction patterns for these samples were recorded.

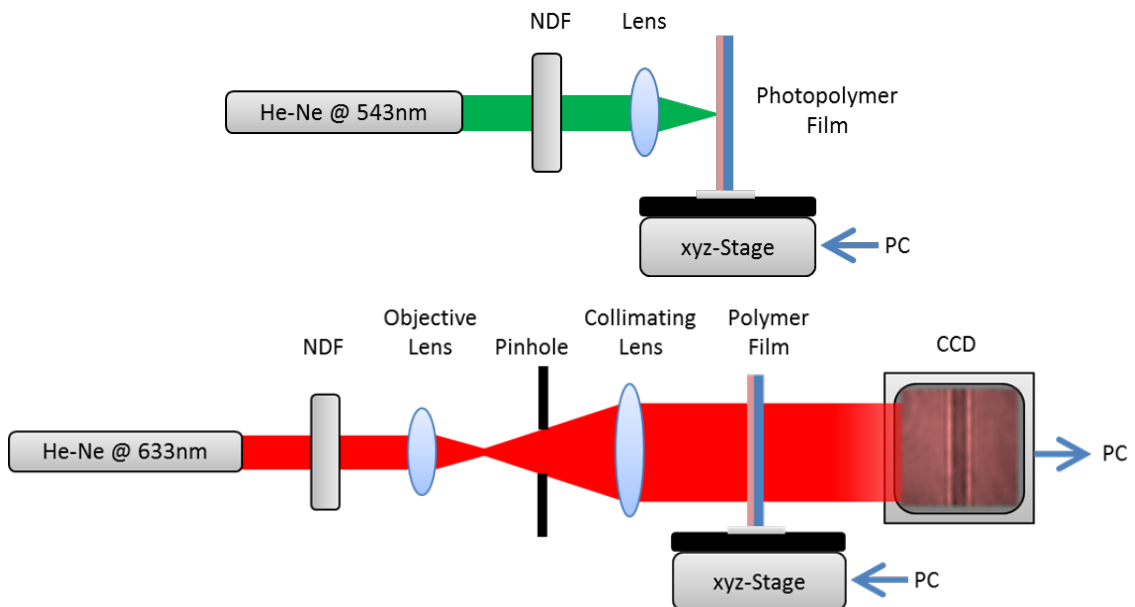


Figure 25. Representation of the combined experimental setup used in the direct-writing (linear pattern photopolymerization) (top) and the diffraction pattern measurements.

In order to determine the difference in the refractive indices of the polymerized and unpolymerized regions, line patterns recorded using the CCD sensor were extracted. The cylindrical structure (originating from the optical fiber) in the study of Sabatyan and Tavassoly was replaced by a new geometry. The following structure was employed as the theoretical model for the polymerized patterns in fit procedures:

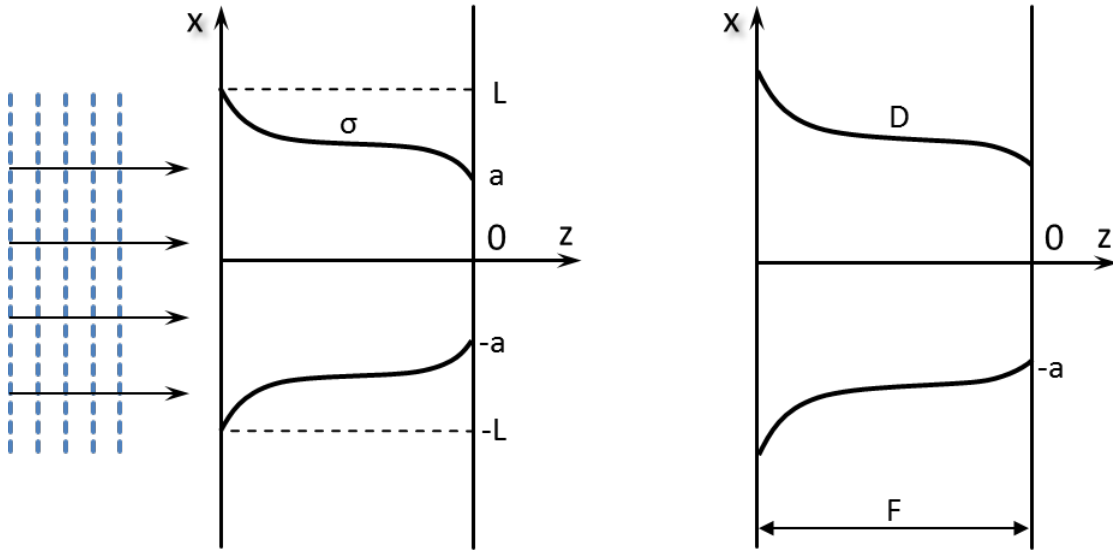


Figure 26. Theoretical model used in the fit procedures for the diffraction patterns

In the above figure, a monochromatic plane wave is incident on the polymerized region on the left-hand-side, and on the right-hand-side of the figure the depth profile of the refractive index difference is shown. The pattern is approximated as a strip with variable phase for Fresnel approximation. For the structure defined as above, amplitude of the diffracted wave is calculated using:

$$\begin{aligned}
 U(r) = & \frac{\pi}{\lambda d} \int_0^F \int_{-a}^L \cos F_1 + i \sin F_1 dx dz \\
 & + \frac{\pi}{\lambda d} \int_0^F \int_{-a}^a \cos F_2 + i \sin F_2 dx dz \\
 & + \frac{\pi}{\lambda d} \int_0^F \int_a^L \cos F_3 + i \sin F_3 dx dz
 \end{aligned} \tag{3.23}$$

With

$$F_1 = k(i\Delta + \delta) \left[z \exp\left(\frac{-z^2}{D^2}\right) \exp\left(\frac{-(x+a)^2}{\sigma^2}\right) \exp\left(\frac{-a^2}{\beta^2}\right) \right] + \alpha(x-r)^2 \quad (3.24)$$

$$F_2 = k(i\Delta + \delta) \left[z \exp\left(\frac{-z^2}{D^2}\right) \exp\left(\frac{-(x)^2}{\sigma^2}\right) \right] + \alpha(x-r)^2 \quad (3.25)$$

$$F_3 = k(i\Delta + \delta) \left[z \exp\left(\frac{-z^2}{D^2}\right) \exp\left(\frac{-(x-a)^2}{\sigma^2}\right) \exp\left(\frac{-a^2}{\beta^2}\right) \right] + \alpha(x-r)^2 \quad (3.26)$$

where, d is the observation plane distance, D is the depth variance of the Gaussian function, L is the half-limit of integration on the film surface, λ is the wavelength, σ is the Gaussian shaped edge half-length of the polymerized region, a is the flat middle region half-length of the polymerized region and Δ is the refractive index difference between the polymerized and unpolymerized regions. The intensity is calculated simply as $I = U \cdot U^*$. The normalized intensity distribution across the Fresnel diffraction pattern is obtained by plotting the intensity I versus x .

3.2.1.1. Fitting Procedure

3.2.1.1.1. Actual Refractive Index Distribution

In order to obtain an initial estimate for the shape of the refractive index distribution, color gradient of the laser written lines was obtained using microscope images. In doing so, it is assumed that the color gradient follows the refractive index distribution exactly. The accuracy of such an assumption is open to debate and should be kept in mind in interpreting the results. A sample microscope image of the polymerized region and the gradient obtained from the image is given in Figure 27:

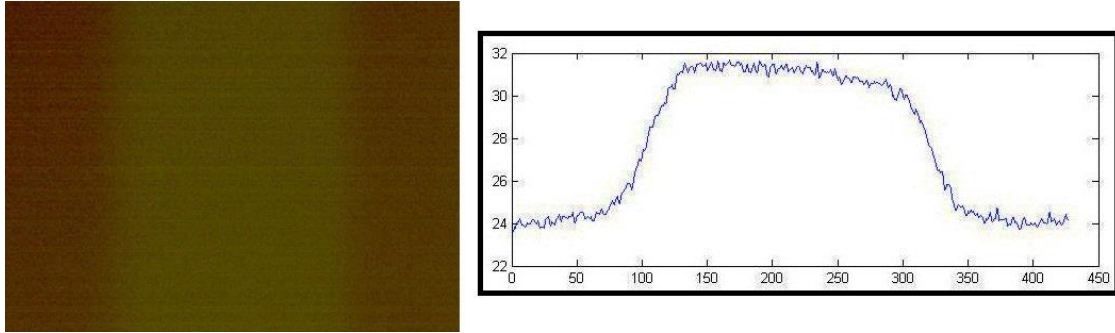


Figure 27. Microscope image and profile of the polymerized region

3.2.1.1.2. Analysis

In order to come up with a suitable fitting procedure, certain parameters in the main equation were investigated to set metrics for the intensity distribution graphs. Effects of variation in certain parameters on the resulting distribution were observed by isolating the investigated parameter. The investigated parameters are:

- a – flat middle part half-length of the polymerized region
- β – variance of the Gaussian function within the middle region of the polymerized region
- d – observation plane distance
- Δ – refractive index difference between the polymerized and unpolymerized regions
- σ – Gaussian shaped edge half-length of the polymerized region

In light of the simulations performed, the following results were deduced for the parameters varying within the scale of interest:

- Parameter ‘ a ’ expands the pattern as it increases, which is to be expected. It is a fundamental parameter for the general fitting of the pattern and estimation of the width of the polymerized strip.
- Parameter ‘ β ’ does not make any significant contribution to the diffraction pattern within the scale of interest. Microscope images of the region confirm virtually flat shape of polymerized region throughout the direct-written line.
- Parameter ‘ d ’ does not directly affect the fitting in the sense to find the polymerization parameters. Rather, it is used as a verifying factor of the whole measurement system. Measurements of the diffraction pattern at different

observation distances and comparing the measured and the calculated patterns leads to the verification of the obtained fitting.

- Parameter ' σ ' is one of the two crucial parameters affecting the fine details of the diffraction pattern. Based on the microscope images, a fit for the exact shape of the Gaussian edges was attempted.
- Parameter ' Δ ' is the other crucial parameter and the main goal of the fit process. It affects the amplitudes of the obtained diffraction patterns, rather than the fine details and the wave shapes observed on the patterns.

Based on the analysis of the parameters and repeated fit studies, an exact match of the diffraction pattern was not achieved; rather, a best estimate of the parameters was obtained as follows: $a=0.29\text{mm}$, $\beta=7.0$, $\sigma=0.13$ and $\Delta=0.00015$. Corresponding diffraction patterns are given below:

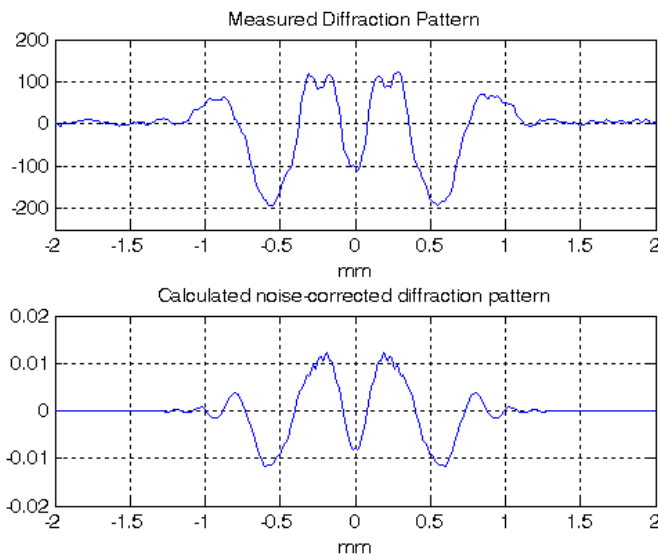


Figure 28. Measured Diffraction Pattern and Best Estimate for the Fit

3.2.2. Image Correction

At this point, even though the obtained results could be considered a close fit, the characterization and calibration of the measurement setup and the simulation algorithm itself was decided to be necessary. In order to normalize the measurements and for the obtained results to correspond to actual values, measurements of materials with known refractive indices and known geometries were performed. As a first step,

taking into account the model study, stripped single-mode fibers were used phase objects for plane waves propagating in various materials. This method has the advantage of involving very well-known fiber geometries and fiber-layer refractive indices, even though the refractive indices of the materials used as surrounding media tend to deviate depending on their purity and ambient temperature.

In the initial measurements performed for system characterization and calibration, plane waves formed using a 632.8nm laser were diffracted by stripped fibers suspended in air ($n=1.000$), deionized water ($n=1.333$), benzene ($n=1.501$) and benzene-methanol ($n=1.329$) mixture and the diffraction patterns were recorded using a CCD array at 550mm distance:

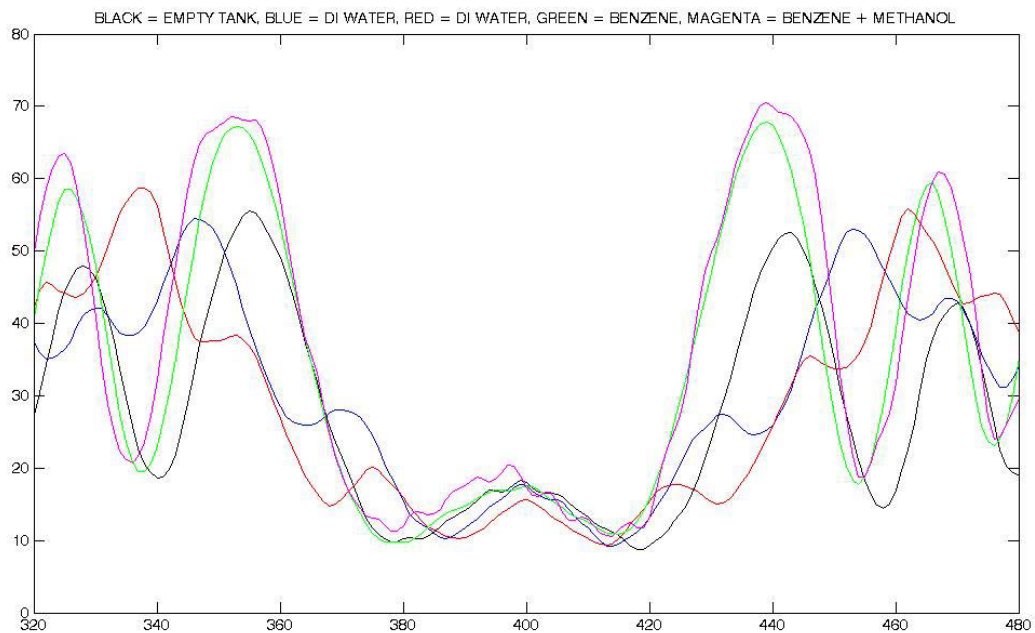


Figure 29. Intensity profiles of plane waves diffracted by fibers immersed in various liquids.

In recording the profiles, more than 50 separate measurements were taken for each material, background elimination was performed to minimize the errors due to noise and recording system, offset levels were corrected in order to get the optimum results and finally, profiles for different materials were aligned to a common level:

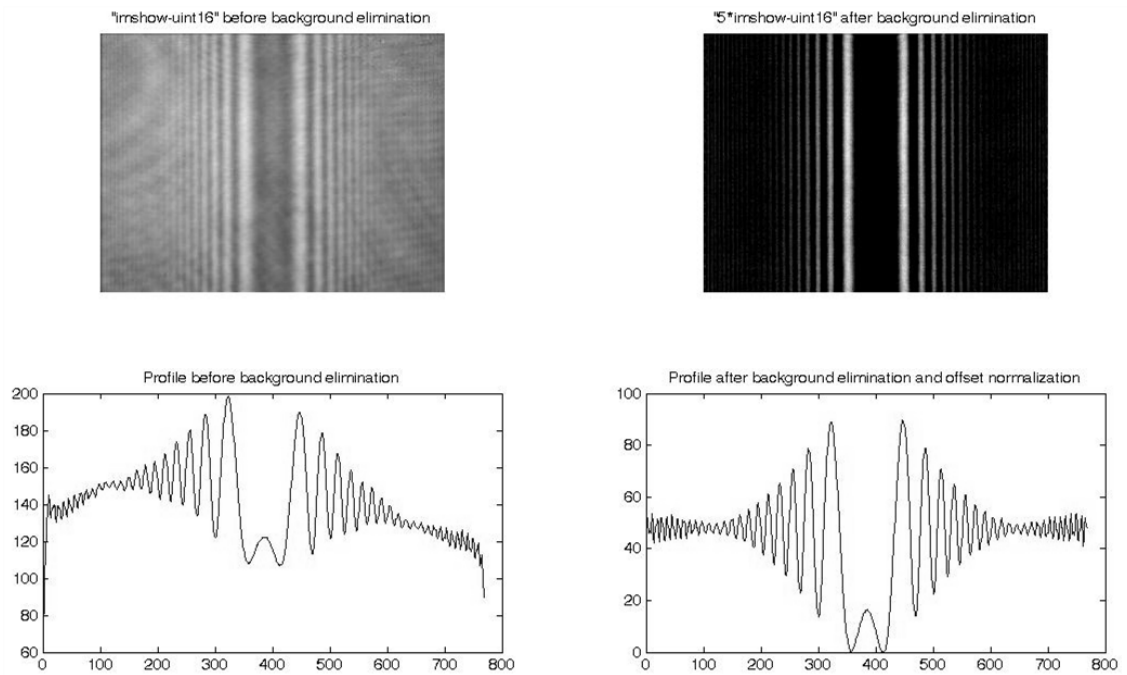


Figure 30. Background elimination and offset correction for recorded patterns

In following measurements, plane waves formed using laser output at the same wavelength were diffracted by jacketed fibers suspended in air ($n=1.000$), deionized water ($n=1.333$), PVA ($n=1.510$) and ethanol ($n=1.362$) and the diffraction patterns were recorded using a CCD array at 270mm distance:

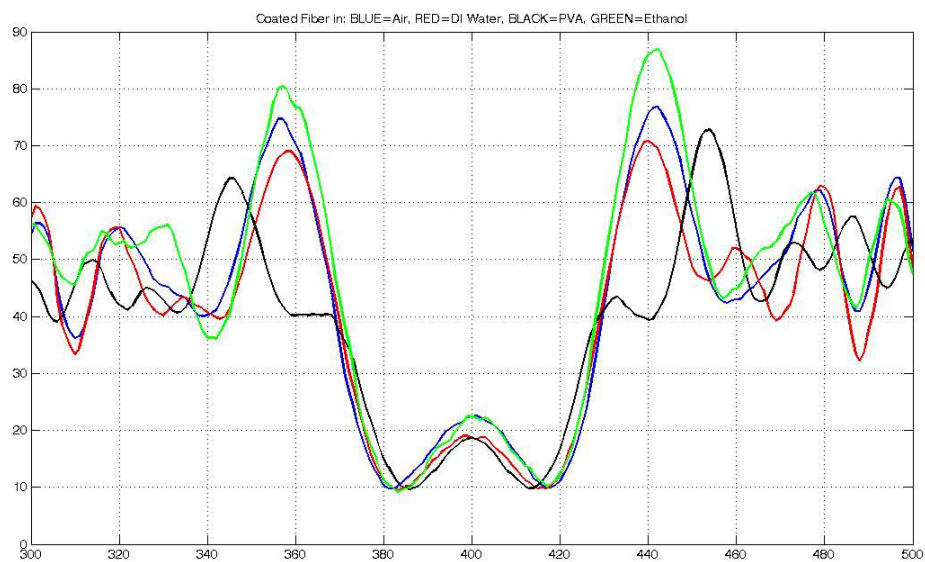


Figure 31. Intensity profiles of plane waves diffracted by fibers immersed in various liquids.

Later, plane waves formed using the 632.8nm laser were diffracted by stripped fibers suspended in air ($n=1.000$), benzene ($n=1.501$), toluene ($n=1.496$), deionized water ($n=1.333$), methanol ($n=1.329$), index-matching fluid (IMF) ($n=1.520$) and ethanol ($n=1.329$) and the diffraction patterns were recorded using a CCD array at a distance of 270mm:

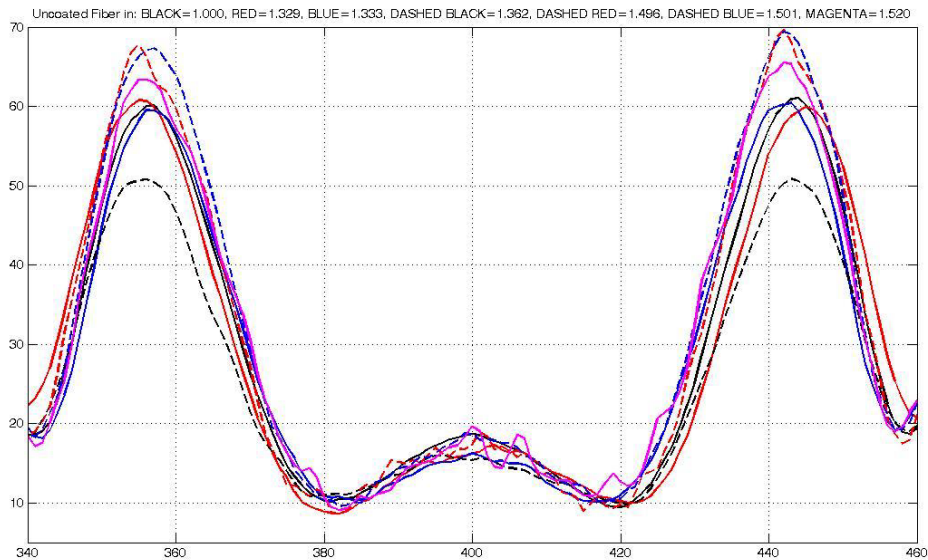


Figure 32. Intensity profiles of plane waves diffracted by fibers immersed in various liquids.

Throughout these studies, in order to check for an alternative method in matching the recorded intensity profiles with the refractive indices of surrounding media, metrics were determined and the relationship between these metrics and the refractive indices were investigated:

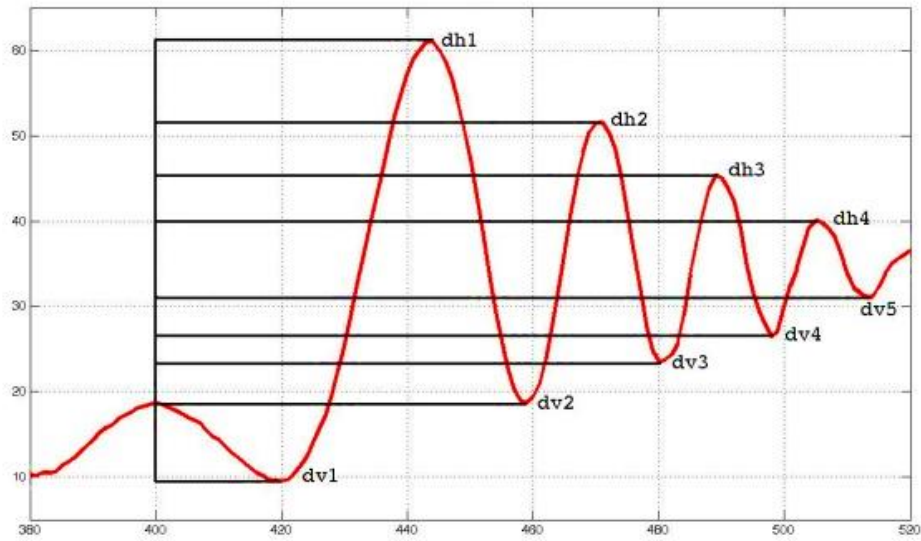


Figure 33. Defined metrics

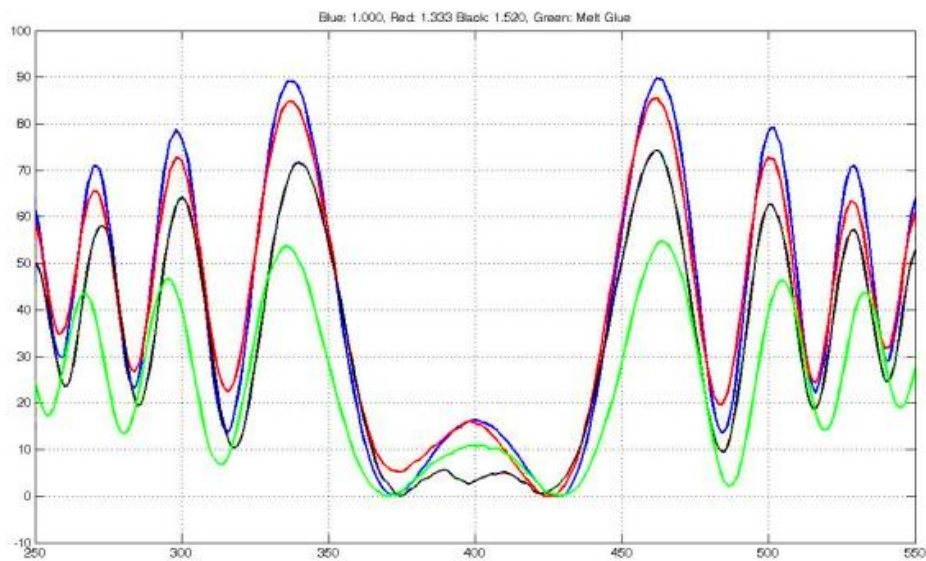


Figure 34. Investigation of metrics in order to determine the refractive indices

3.2.3. Near-Field Diffraction Method

In light of these studies, it was found that the determined metrics did not behave in a linear fashion with respect to the changes in refractive index and also that no direct proportionality existed among the metrics themselves. Therefore, it was concluded that fitting method was the best method of choice at this point. In addition, it was also

determined that the previous recording distance was not adequate to be able to measure the slight change in the refractive index and near-field measurements were necessary. So, near-field measurements were initiated. Accordingly, plane waves formed using a 632.8nm laser were diffracted by stripped fibers suspended in air ($n=1.000$) and deionized (DI) water ($n=1.333$) and the diffraction patterns were recorded using a CCD array at 25mm distance:

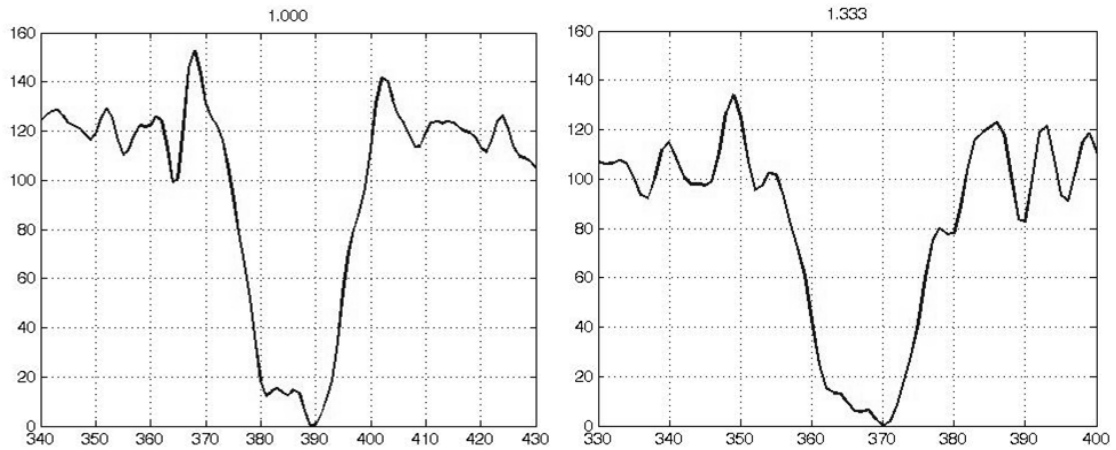


Figure 35. Intensity profiles of plane waves diffracted by fibers immersed in air (left) and DI water.

Then, plane waves formed using a 632.8nm laser were diffracted by stripped fibers suspended in methanol ($n=1.329$), deionized (DI) water ($n=1.333$), acetone ($n=1.357$), ethanol ($n=1.362$) and isopropanol ($n=1.377$) and the diffraction patterns were recorded using a CCD array at 26mm distance:

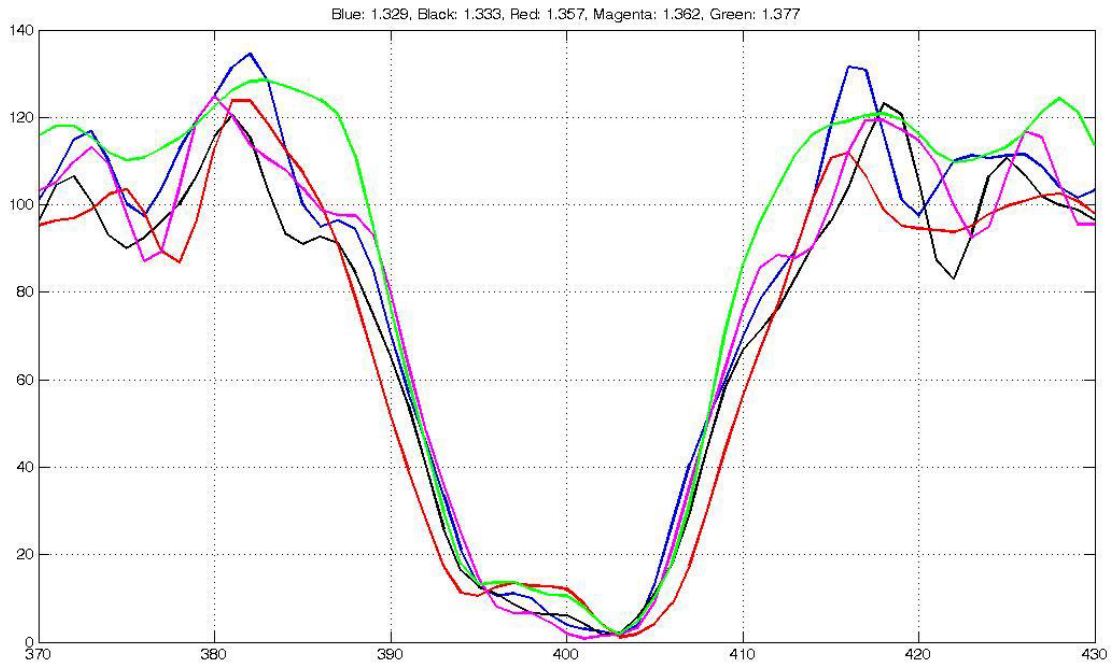


Figure 36. Intensity profiles of plane waves diffracted by fibers immersed in various liquids

Fitting studies were performed on the recorded diffraction patterns. For instance, for a stripped single-mode fiber suspended in air, for which the diffraction pattern were recorded at 26mm distance, using near-field diffraction measurements cladding radius was determined to be $127.5\mu\text{m}$, core radius to be $5.4\mu\text{m}$, cladding refractive index $n=1.4536$, core refractive index $n=1.4531$ and air refractive index to be $n=1.00233$:

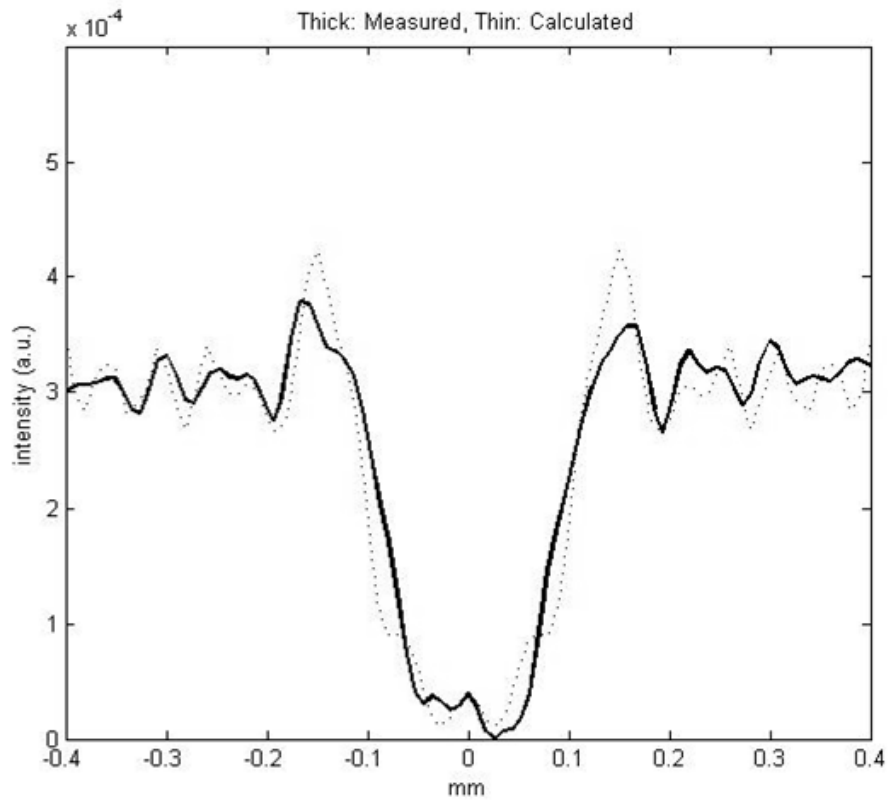


Figure 37. Measurement and fit for single-mode fiber suspended in air

Similarly, using near-field diffraction measurements of a single-mode fiber suspended in deionized water at 26mm distance, cladding radius was determined to be $127.7\mu\text{m}$, core radius to be $5.4\mu\text{m}$, cladding refractive index $n=1.4536$, core refractive index $n=1.4531$ and deionized (DI) water refractive index to be $n=1.33375$:

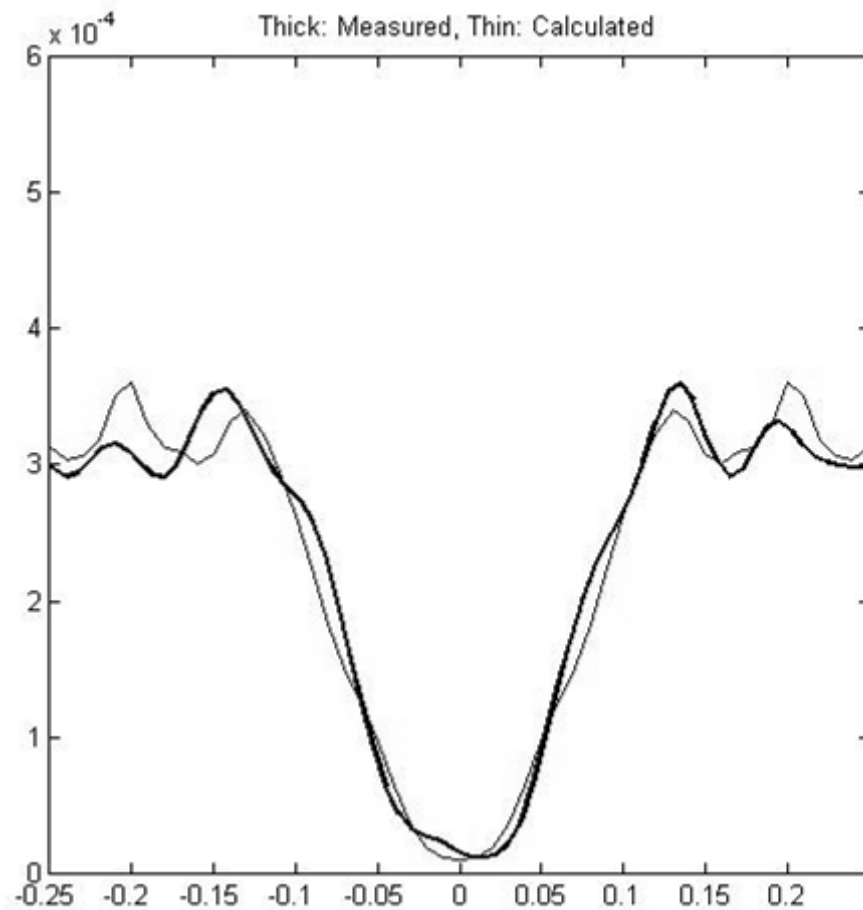


Figure 38. Measurement and fit for single-mode fiber suspended in DI water

After establishing the grounds for the near-field method, the measurements and fitting studies were once more concentrated on direct-written photopolymer waveguides.

3.2.4. Direct-Written Waveguides

Using laser direct-writing on the same photopolymer film sample, three different waveguide structures were fabricated and used as phase objects for diffracting plane waves. The waveguides were written by scanning the focused laser beam (using the setup depicted previously) at the same velocity, but with different number of scan repetitions; namely, single-pass, triple-pass and multiple-pass. Since the scan velocity and the beam intensity are kept constant in all three structures, the difference is in the exposure of the polymerized regions.

As for the previous direct-written structures, transmission optical microscope images were used for the initial evaluation of the structures:

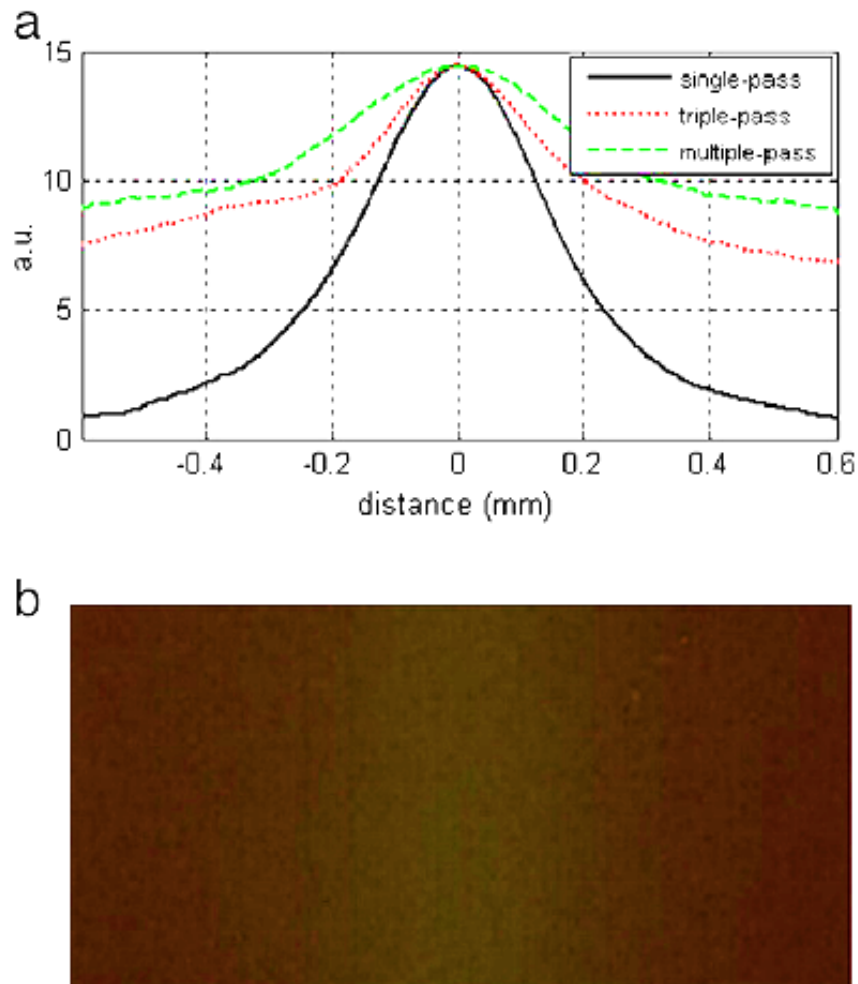


Figure 39. a) Cumulative refractive index profiles and b) Transmission optical microscope image of a direct-written photopolymer waveguide (Source: Dinleyici and Sümer, 2011)

It should be noted that the profiles obtained by transmission of incandescent microscope backlight are *not* true refractive index profiles of the waveguide cross-section, but could be considered as cumulative refractive index profiles. The recorded intensity distributions of the diffraction patterns are given below:

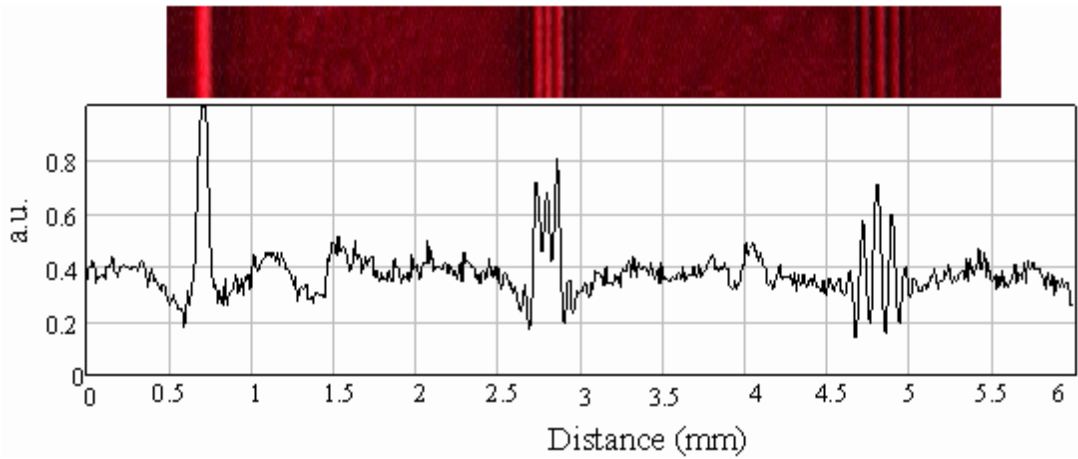


Figure 40. Recorded diffraction patterns and corresponding pattern cross-sections for single-pass (left), multiple-pass (middle) and triple-pass (right) waveguides (Source: Dinleyici and Sümer, 2011)

For the simulation and fitting of the recorded diffraction patterns, the index profiles are expected to be of Gaussian in nature, due to the writing procedure, i.e., exposure, laser beam profile and due to the material diffusion properties, i.e., nonlocal diffusion of photopolymerization. Hence, the refractive index profile is approximated with two Gaussian functions, one in the central section (associated with parameter β) and the other in the tail section (associated with parameter σ):

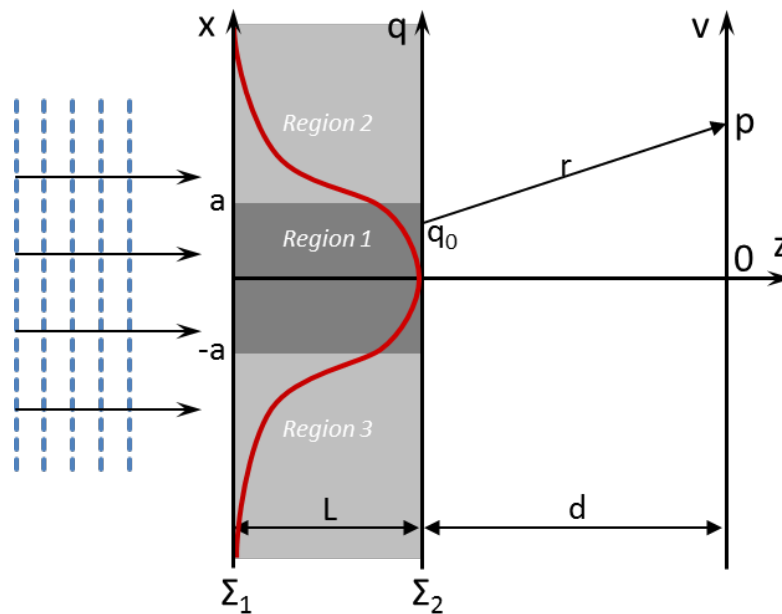


Figure 41. Diffraction geometry and approximated profile (red line) of the refractive index distribution

In addition to the transverse distribution described above, the refractive index distribution profile is also approximated with a Gaussian function (associated with the term D) in the *depth* direction of the polymer film. With these definitions, the direct-written region and the simulated model of the refractive index distribution on the polymer film can be illustrated as follows:

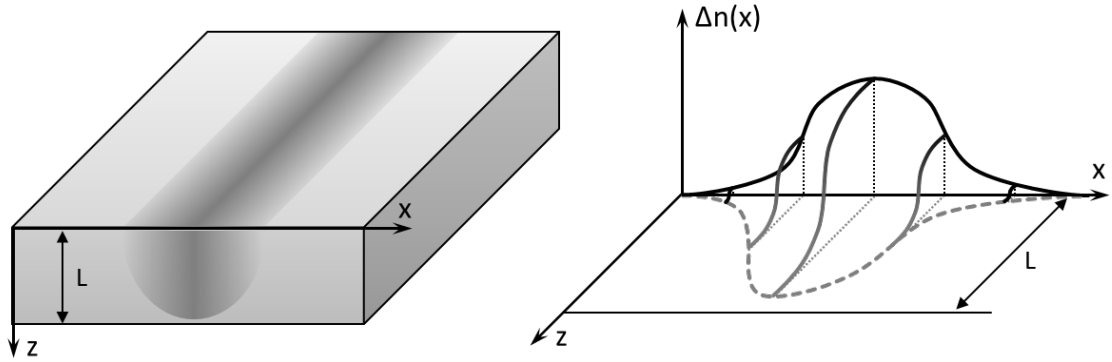


Figure 42. Direct-written photopolymer waveguide structure on polymer film (left) and associated refractive index model

Using this geometry, the simulated diffraction pattern (which is to be fitted with the recorded patterns) can be calculated as follows: On the observation plane ‘ v ’ in Figure 41, the diffraction integral for the complex amplitude of the field is given as (Sabatyan and Tavassoly, 2007):

$$U(p) = \int \frac{A(q)\Gamma(q,p)}{r} \exp(ikr) dq \quad (3.27)$$

Where, $A(q)$ is the complex amplitude at the Σ_2 plane, k is the wave vector and $\Gamma(q,p)$ is the inclination factor, which is assumed to be unity because of the faint and smooth refractive index modulation (Dinleyici and Sümer, 2011). The intensity at p is given by $I(p) = U(p)U^*(p)$. The distance between a point on Σ_2 plane and the observation point p is approximated by $r(p) \cong d + (p - q)/2d$. In order to match the assumed refractive index profile, it is divided into two regions on each side. In each region, the refractive index profile is modeled by a piece-wise combination of Gaussian functions as shown in Figure 41. Then, the diffraction integral for the middle section (Region 1: $-a \leq q \leq a$) is given as (Dinleyici and Sümer, 2011):

$$U_1(p) = K_1 \int_{-a}^a \exp i \left[\Delta n k T_F \exp \left(\frac{-x^2}{\beta^2} \right) + \frac{\pi}{\lambda d} (q - p)^2 \right] dq \quad (3.28)$$

And in the side/tail sections, for nonnegative a (Region 2: $q \geq a$):

$$U_2(p) = K_2 \int_a^{\infty} \exp i \left[\Delta n k T_F \exp \left(\frac{-(x - a)^2}{\sigma^2} \right) \exp \left(\frac{-a^2}{\beta^2} \right) + \frac{\pi}{\lambda d} (q - p)^2 \right] dq \quad (3.29)$$

For negative a (Region 3: $q \leq a$):

$$U_3(p) = K_3 \int_{-\infty}^{-a} \exp i \left[\Delta n k T_F \exp \left(\frac{-(x + a)^2}{\sigma^2} \right) \exp \left(\frac{-a^2}{\beta^2} \right) + \frac{\pi}{\lambda d} (q - p)^2 \right] dq \quad (3.30)$$

Then the total field at ‘ p ’ is given by:

$$U(p) = U_1(p) + U_2(p) + U_3(p) \quad (3.31)$$

And intensity:

$$I_p = |U_p|^2 \quad (3.32)$$

In the above expressions for U_1 , U_2 and U_3 , $\Delta n(x)kT_F$ is the retardation term associated with the propagation in the depth direction of the film at position x . With the assumption of the distribution in the depth direction being of Gaussian nature, total phase retardation is obtained as (Dinleyici and Sümer, 2011):

$$T_F = \int_0^L \exp \left(\frac{-z^2}{D^2} \right) dz \Rightarrow D \frac{\sqrt{\pi}}{2} \operatorname{erf} \left(\frac{L}{D} \right) \quad (3.33)$$

where L the film thickness and D is the waveguide depth parameter. The above integral results in a constant value (T_F) and hence the total diffraction intensity distribution can be obtained by applying the procedure for every point on the observation plane.

Using the above theoretical approach, diffraction patterns for the three waveguide structures were fitted with theoretical patterns, and distribution parameters were found for the single-pass waveguide as $\beta=0.13\text{mm}$, $\sigma=0.055\text{mm}$ and $D=0.25\text{mm}$; for the triple-pass waveguide as $\beta=0.11\text{mm}$, $\sigma=0.02\text{mm}$ and $D=0.56\text{mm}$; and for the multiple-pass waveguide as $\beta=0.7\text{mm}$, $\sigma=0.075\text{mm}$ and $D=0.4\text{mm}$. For all three fit calculations, the parameters for peak index modulation and observation distance parameters were kept constant. Under these calculations, the peak refractive index modulation was found as **0.0013**.

With the same chemical photopolymerization formula, peak refractive index distributions of up to 0.0028 have been reported (Garcia, et.al, 2002) and the difference of the obtained value is accounted for by the slight difference in the direct-writing laser wavelength and laser power.

3.3. Grating Characterization

3.3.1 Photopolymer Waveguide and Grating Fabrication

With the polymer film batch labeled “L” (see APPENDIX A) numerous waveguide and grating structures were fabricated on photopolymer films with thickness of $90\mu\text{m}$ prepared using the polymer recipe given earlier. This batch was of key importance in terms of the characterization of the material properties and processes. The variations of the samples and types of structures fabricated are given below:

Table 9. Properties of the fabricated waveguides

Direct-writing laser beam speed	Waveguide length
2.8mm/s	12mm
1.4mm/s	
0.5mm/s	
0.1mm/s	
0.05mm/s	

Table 10. Properties of the fabricated gratings

Direct-writing laser beam speed	# of steps	Grating period	Grating length
2.8mm/s	49	250 μ m	12mm
1.4mm/s			
0.5mm/s			
0.1mm/s	30		

3.3.2. Grating Characterization – Phase Grating (Volumetric Profile)

3.3.2.1. Transmission Optical Microscopy

Initial observation and inspection of the structures formed on photopolymer thin films were performed using the reflection optical microscope and material modification was confirmed:

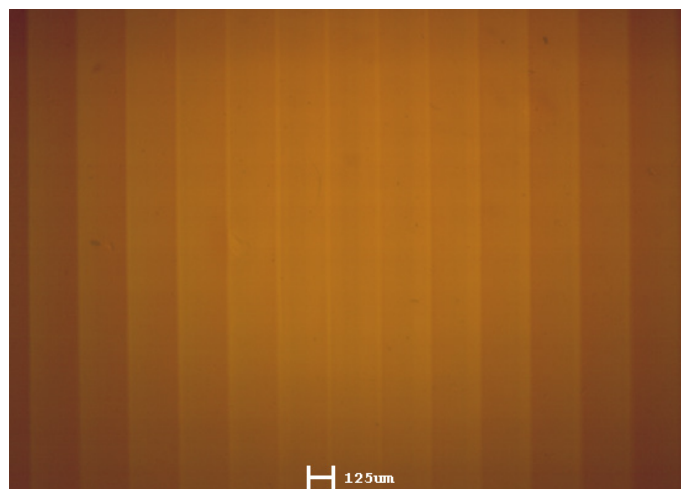


Figure 43. Reflection optical microscope image of the grating structure

As described earlier, previous work on the characterization of volumetric refractive index profile of direct-written photopolymer structures were based on transmission optical microscopy images of recorded samples. The subsequent diffraction technique characterization of the volumetric profiles were based on these images of the cumulative refractive index profiles (See Figure 39)

3.3.2.2. Scanning Electron Microscopy

In order to obtain the exact volumetric profile of the refractive index instead of the cumulative profile, Scanning Electron Microscopy (SEM) investigation of the direct-written structures were attempted at Sabancı University Materials Analysis and Characterization Laboratory (SU-MCL). The intended measurements were low-voltage incremental microscopy analyses of both transverse cross-section and surface of waveguides and gratings.

In the analysis, polymer samples were investigated without any conductive coating in the SEM analysis in order to preserve any electrical conductivity information inherent in the samples due to the polymerized and unpolymerized regions. The observation was started from lowest possible electron gun voltages that allowed image acquisition at the current vacuum pressure. The gun energy was increased in small increments in order to obtain a specific voltage where the Fermi level differences between the polymerized and unpolymerized would lay on opposite levels with respect to the gun energy. This would result in an observable contrast in the obtained SEM image for the two regions, in the sense that each region would appear darker/lighter than the other, hence leading to visual differentiation of the two phases (i.e. refractive indices) on the sample (Gülgün, 2011).

Unfortunately, no tangible results were obtained as a result of SEM analyses. The polymerized and unpolymerized regions could not be differentiated, neither any volumetric information nor any feature related to photopolymerization was observed. Since the polymerized regions were actually visually observable, the results of the SEM analysis were attributed to the electrical properties of the two regions being very close to one another. This conclusion is supported by the fact that artificial polymer regions, i.e. positioning and alignment markers deposited on the film surface prior to SEM analysis were clearly observed in the analysis even though such markers did not cause

any disruptions in the surface topology; markers' being observable was in fact due to the electrical difference between the film and the marker polymer.

3.3.2.3. Confocal Microscopy, Staining, Selective Solubility, Gel Permeation Chromatography

Following the SEM measurements, confocal microscopy was performed on the samples using the confocal microscope at Izmir Institute of Technology Chemistry Department Polymer Research Laboratory.

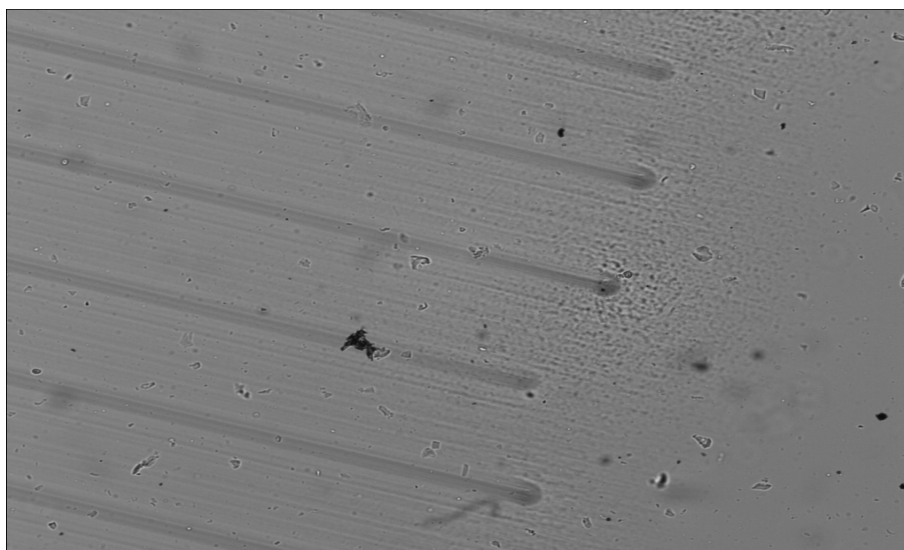
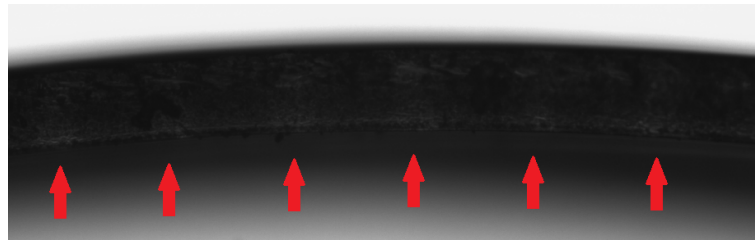
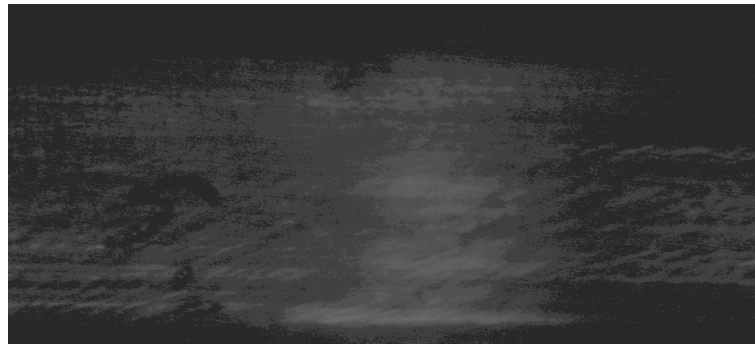


Figure 44. Top surface confocal microscope image of the grating end region



(a)



(b)

Figure 45. Cross-section confocal microscope image of the grating structure (a) 6 visible grating steps are shown (b) Close-up of a single step cross-section

However, the wavelength of light source employed in the device that could give usable results was 532nm, which is right at the center of the active region of Acrylamide:

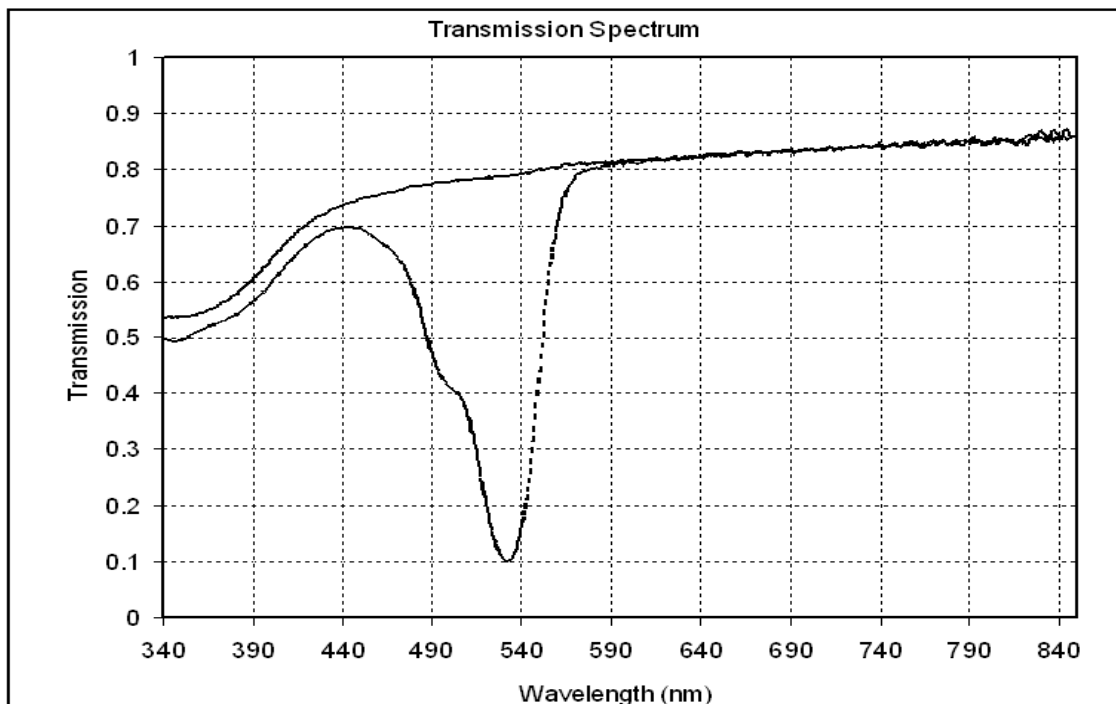


Figure 46. Polymer transmission spectra for unprocessed (dashed) and polymerized samples (Source: Dinleyici and Sümer, 2011)

Therefore, the confocal microscopy measurements were destructive and no usable results were obtained. Furthermore, during the brief window of measurements while the sample features were still intact, yet still being altered, the images obtained contained a large amount of noise which affected the observations considerably.

Besides the imaging experiments, polymer staining was also one of the techniques attempted with recommendation of Dr. M.Ali Gülgün from Sabancı University, Faculty of Engineering and National Sciences in order to obtain the volumetric refractive index profile (Gülgün, 2011). Accordingly, samples surfaces were coated with iodine by direct exposure to iodine vapor, in hope for the coating to attach to the unlinked bonds on the surface, revealing the polymerized region. However due to the complex structure of the polymer recipe, i.e., including AA, PVA, TEA, and YE, iodine stain covered the whole sample surface, without showing any selectivity. Iodine staining was abandoned, so were the trials involving Ruthenium Tetroxide and Osmium which are common stains employed in PVA staining.

In addition, with recommendation of Dr. Virginia Martin Torres from Spanish National Research Council, Institute of Physical Chemistry, selective solubility tests were performed on photopolymer film samples containing polymerized patterns (Torres, 2001). The idea of this method is to take advantage of the possible difference in solubility of the polymerized and unpolymerized regions both present at the film samples. Even though this is a destructive method by definition, if the right solvent is used, unpolymerized material could be dissolved into the solvent, which would expose the polymerized region in the same physical pattern it is formed in the volume of the film.

Initial observations of tests involving ethanol and methanol indicate that unreacted sensitizer (Yellowish Eosin) present in the film dissolves out of the polymer film. The surface topology of the samples seemed to be intact, while none of the changes in the diffractive/phase properties of the films could be determined.

In addition, recommendation of Dr. Manuel Ortuño Sanchez from University of Alicante, University Institute of Physics Applied to Sciences and Technologies, Gel Permeation Chromatography was another considered technique that could be used to obtain the volumetric refractive index of the laser-written lines (Sanchez, 2011). The method evaluates the fractions of polymers/monomers with different molecular weights. The required equipment is currently not present in Izmir Institute of Technology to our

knowledge and the applicability of the method to the problem at hand and the search for the possibility of using equipment available in other institutions have been inconclusive.

3.3.3. Grating Characterization – Surface Grating (Surface Profile)

3.3.3.1. Atomic Force Microscopy

Surface profiles of the direct-written samples were investigated with Atomic Force Microscopy using the AFM equipment at the Center for Materials Research (IYTE-MAM), however the maximum window that could be observed using the microscope was $13\mu\text{m} \times 13\mu\text{m}$ and no meaningful result was obtained.

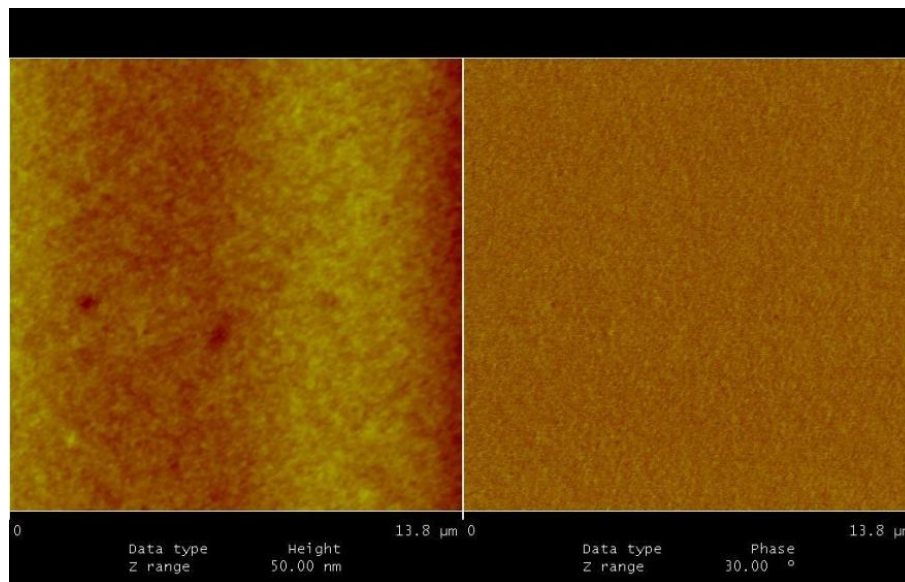


Figure 47. AFM analysis of L.GR.050.A performed at IYTE-MAM Left: Surface topology Right: Phase information

Later, a second AFM measurement was performed on the samples using the AFM equipment at Izmir Institute of Technology Physics Department. Despite the maximum observable window being larger in this microscope ($40\mu\text{m} \times 40\mu\text{m}$), the desired features could not be measured.

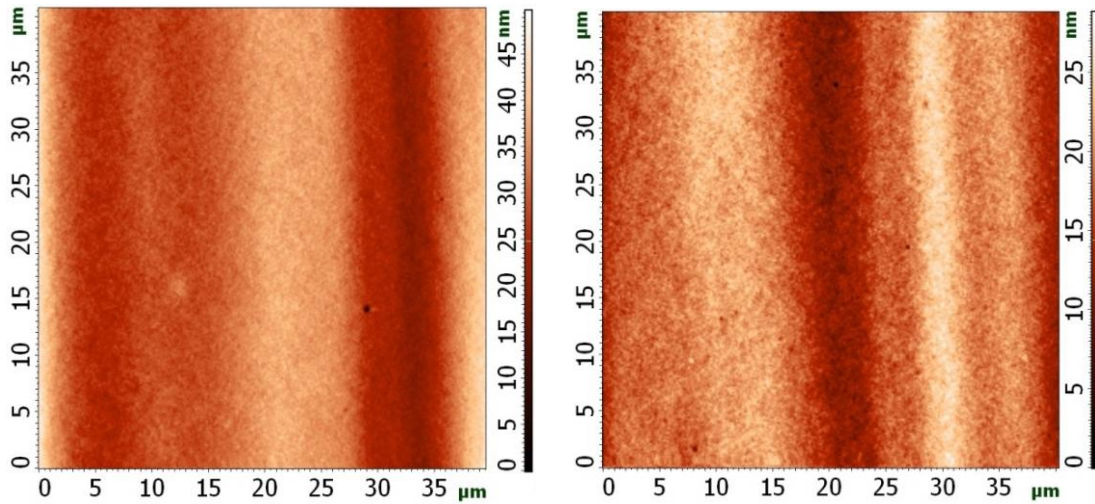


Figure 48. AFM analysis of L.GR.050.A (Surface topology)

A survey of the AFM equipment available in Turkey has shown that the AFM with the largest observable window was in Sabancı University with a maximum range of $125\mu\text{m} \times 125\mu\text{m}$. Even though using the aforementioned equipment could potentially give somewhat meaningful results, the overall yield of using that particular microscope was weighed against the cost and efficiency of the measurements and as a result AFM measurements were abandoned.

3.3.3.2. Stylus Surface Profilometer

The surface profiles of the laser-written structures were investigated using stylus surface profilometers at both Izmir Institute of Technology Physics Department Cleanroom Facility and Sabancı University Faculty of Engineering and Natural Sciences Cleanroom Laboratory.

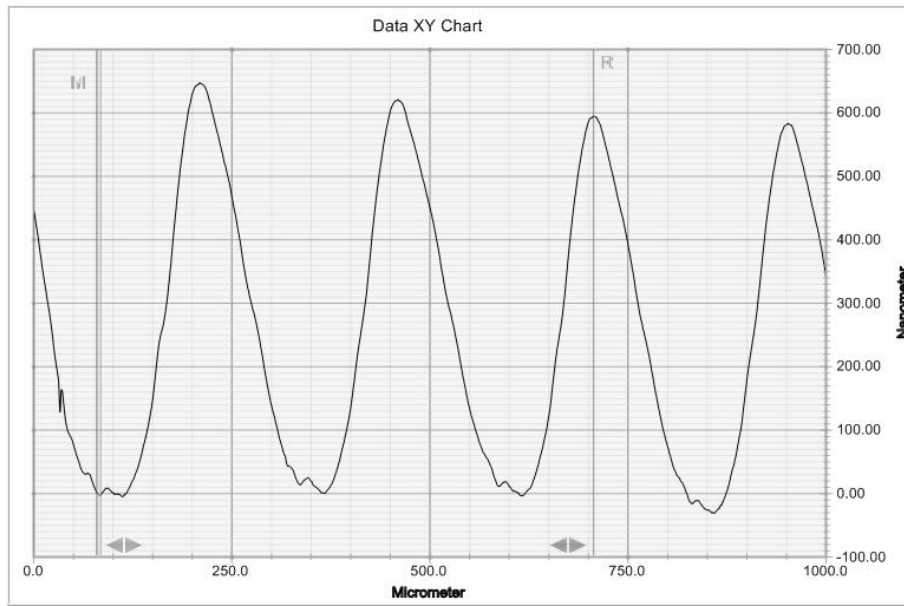


Figure 49. L.GR.010.A grating surface profile - beam speed 0.1mm/sec

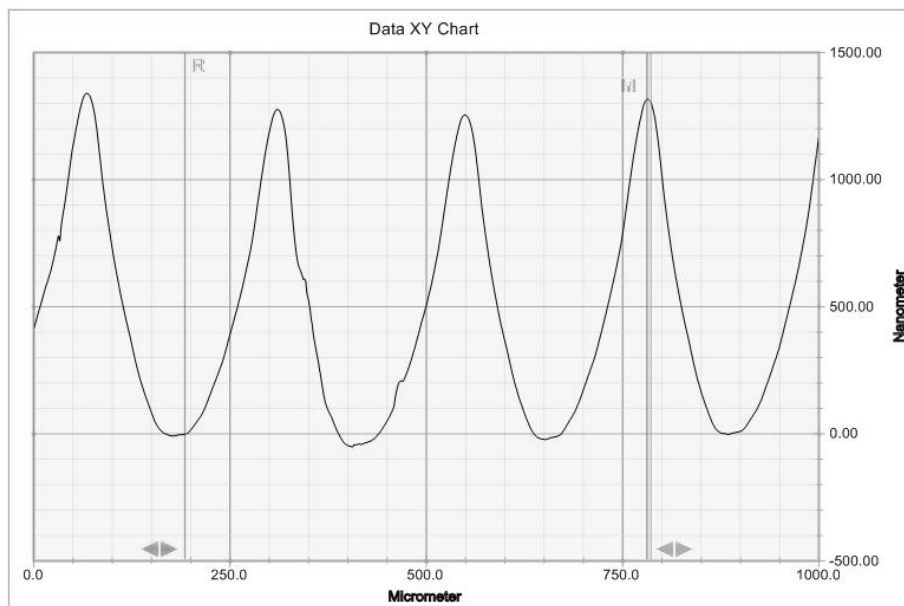


Figure 50. L.GR.050.A grating surface profile - beam speed 0.5mm/sec

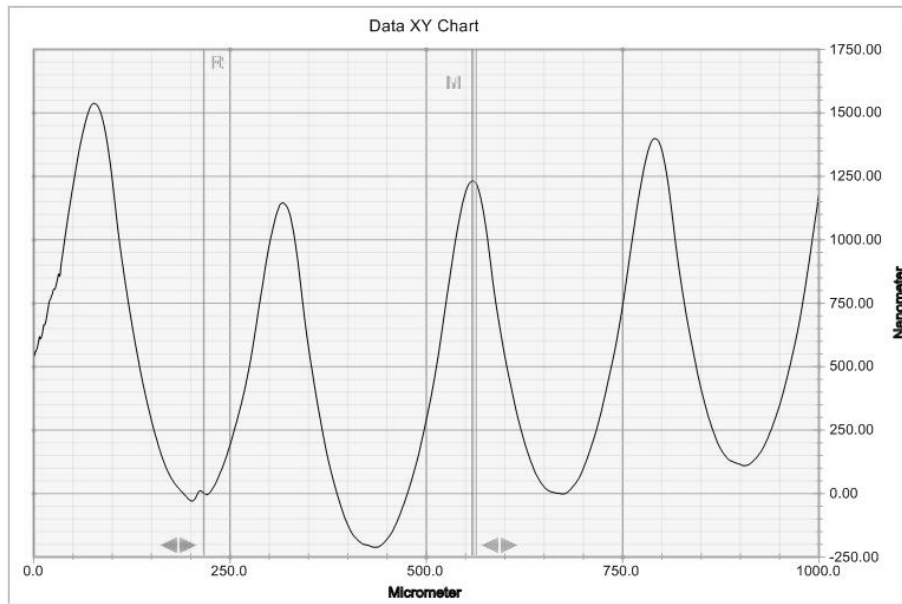


Figure 51. L.GR.140.A grating surface profile - beam speed 1.4mm/sec

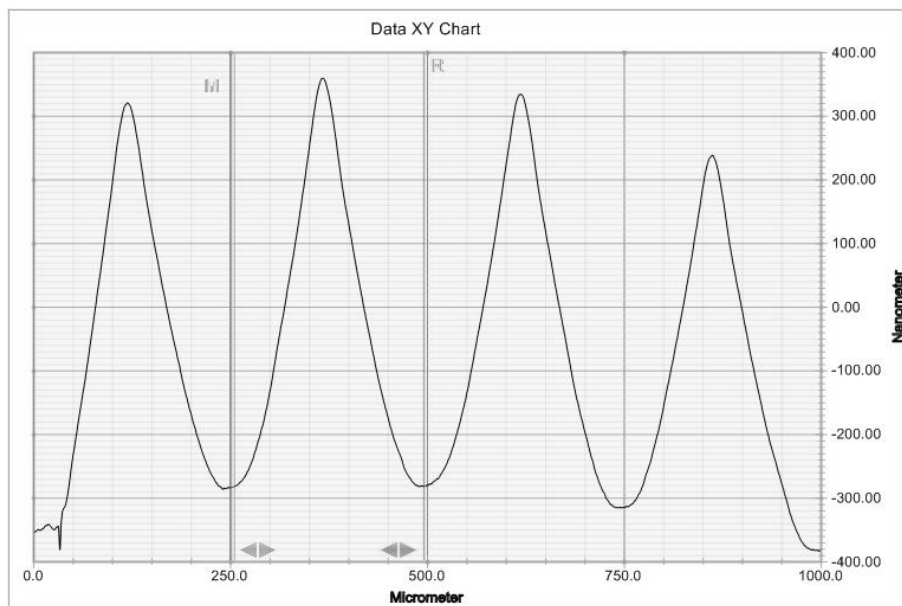


Figure 52. L.GR.280.A grating surface profile - beam speed 2.8mm/sec

Initial analysis of the surface profile measurements verified the consistency of the direct-writing setup in terms of the period of the grating steps which was set to be $250\mu\text{m}$. The heights of the corrugations formed due to photopolymerization are in the order of $1\mu\text{m}$. The measured surface profiles of each of the grating steps were approximated as a combination of two Gaussian functions of form $A \cdot \exp(-x^2/b^2)$.

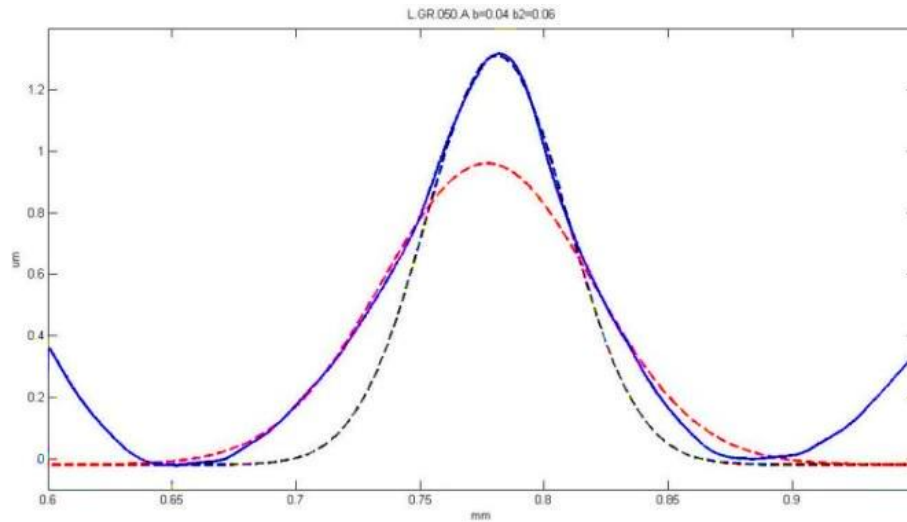


Figure 53. Gaussian function fit for single step of grating L.GR.050.A [Beam speed: 0.5mm/sec, b: 0.040 (black), b2: 0.060 (red)]

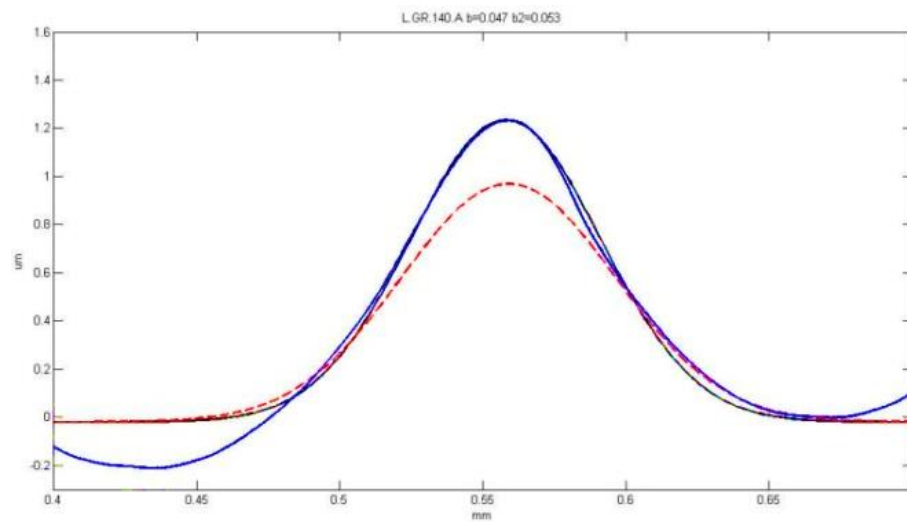


Figure 54. Gaussian function fit for single step of grating L.GR.140.A [Beam speed: 1.4mm/sec, b: 0.047 (black), b2: 0.053 (red)]

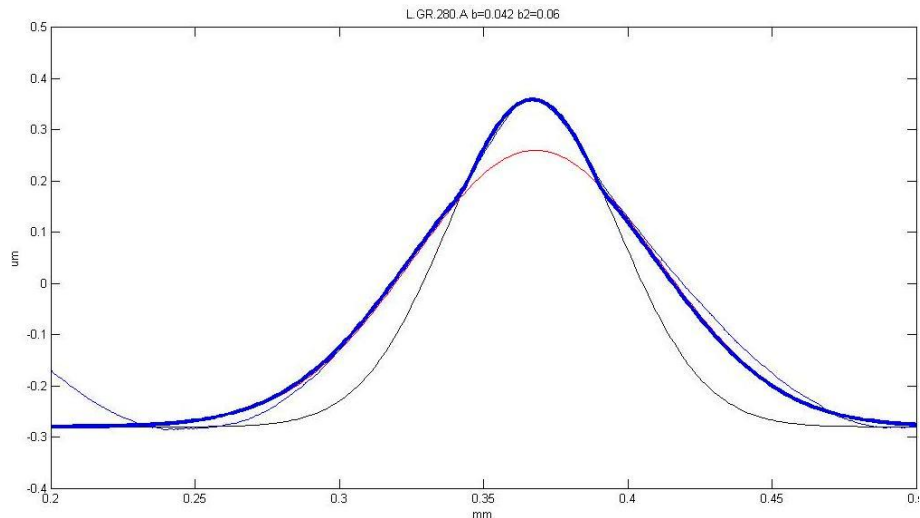


Figure 55. Gaussian function fit for single step of grating L.GR.280.A [Beam speed: 2.8mm/sec, b: 0.042 (black), b2: 0.060 (red)]

Using the analyses, the beam-speed dependences of the Gaussian parameters are summed up in the following graph:

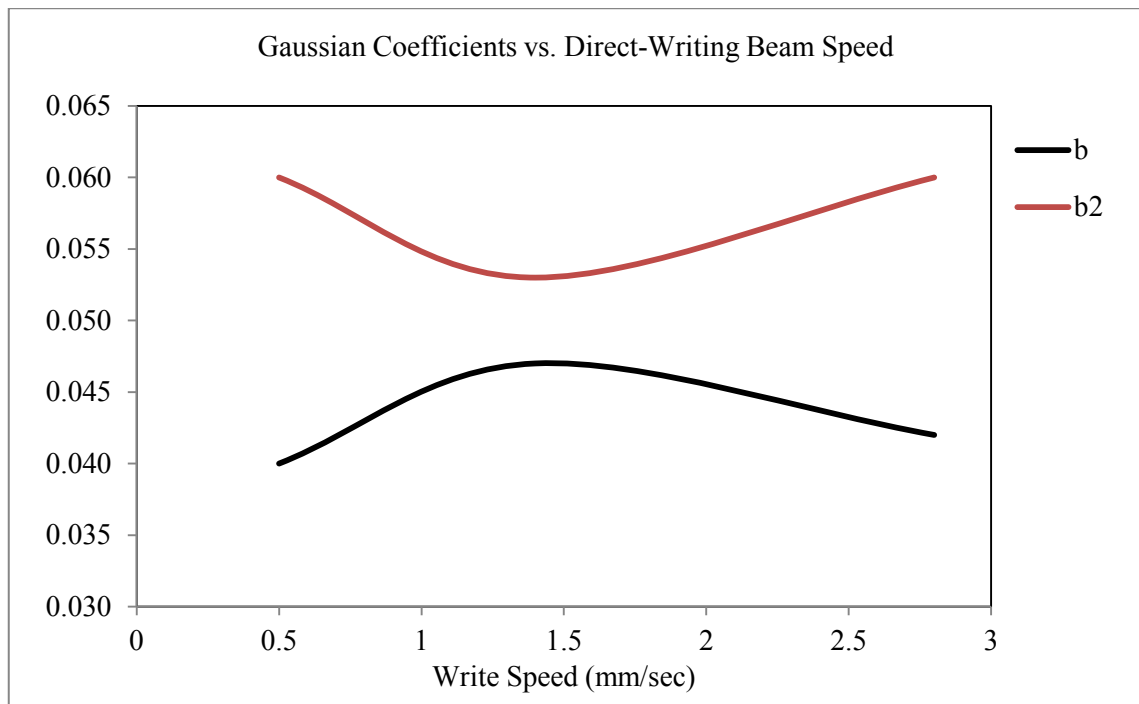


Figure 56. Gaussian coefficients vs. direct-writing beam speed

Surface profile measurements of the individual direct-written waveguides also revealed a Gaussian-type shape of the volume shrinkage on the sample surfaces:

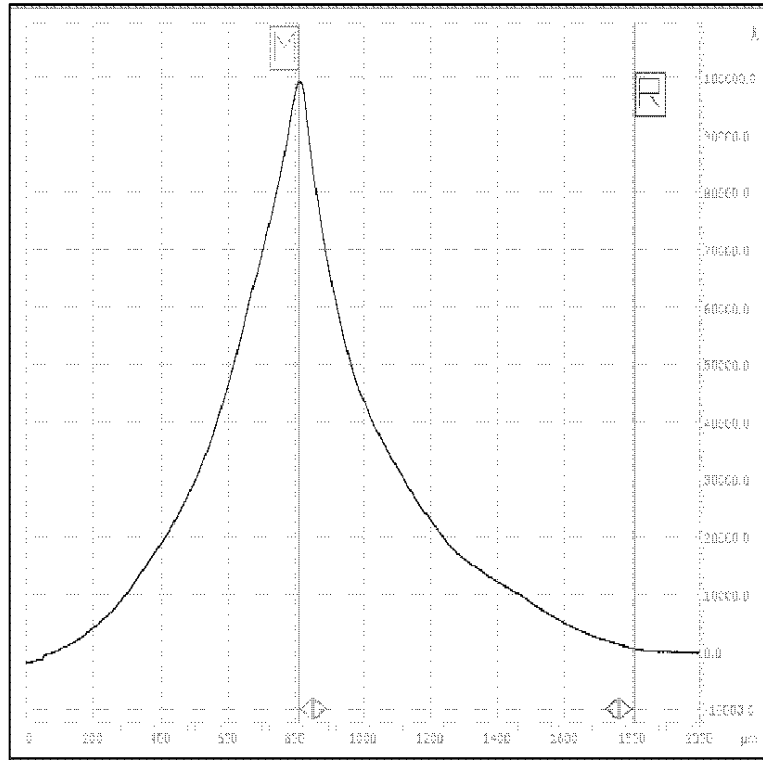


Figure 57. Waveguide L.WG.005.B2 surface profile - direct-writing beam speed [0.05mm/sec - M-R cursors $\Delta x=996\mu\text{m}$, $\Delta y=9.891\mu\text{m}$]

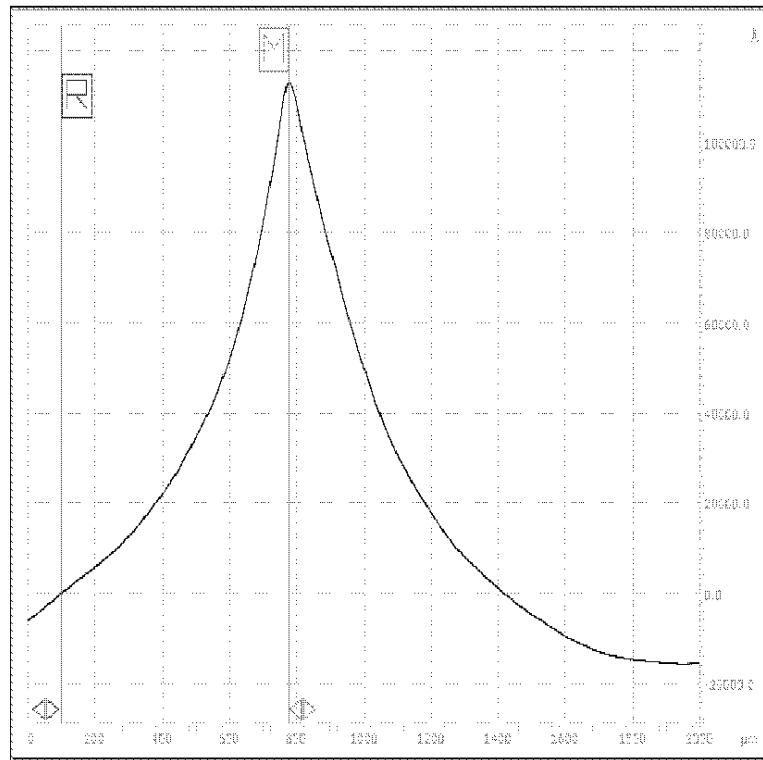


Figure 58. Waveguide L.WG.010.B1 surface profile - direct-writing beam speed [0.1mm/sec - M-R cursors $\Delta x=676\mu\text{m}$, $\Delta y=11.306\mu\text{m}$]

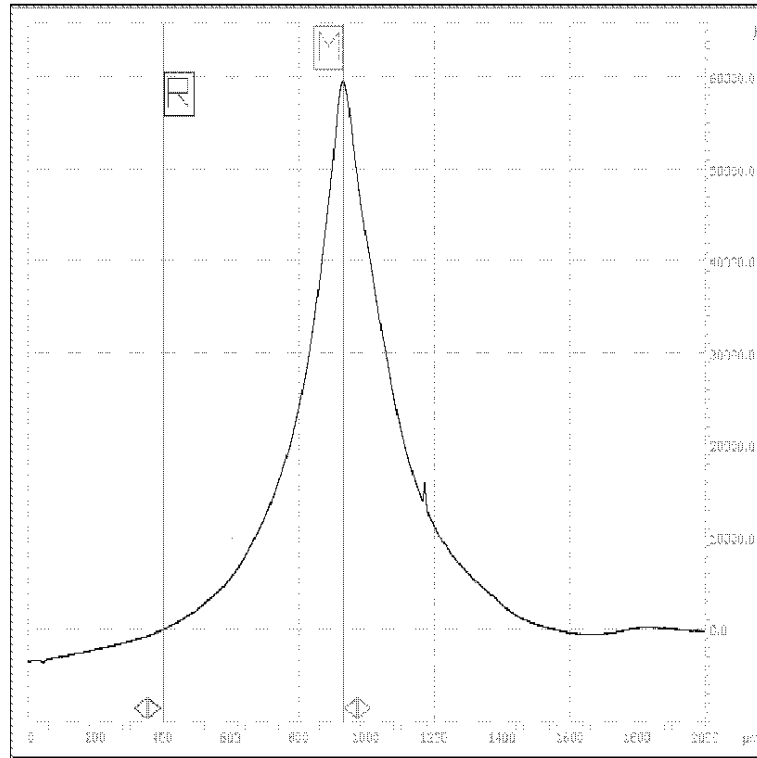


Figure 59. Waveguide L.WG.050.B2 surface profile - direct-writing beam speed [0.5mm/sec - M-R cursors $\Delta x=533\mu\text{m}$, $\Delta y=5.952\mu\text{m}$]

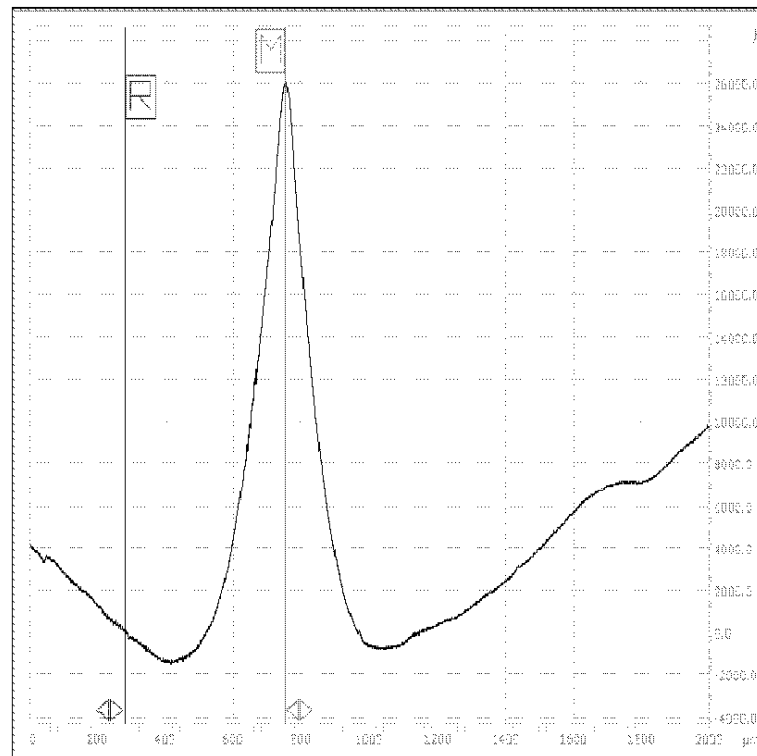


Figure 60. Waveguide L.WG.140.A2 surface profile - direct-writing beam speed [1.4mm/sec - M-R cursors $\Delta x=472\mu\text{m}$, $\Delta y=2.593\mu\text{m}$]

Using these measurements, the relation between direct-writing beam speed and the peak height of the surface relief for direct-written waveguides and peak amplitude of the surface corrugation for direct-written gratings were obtained:

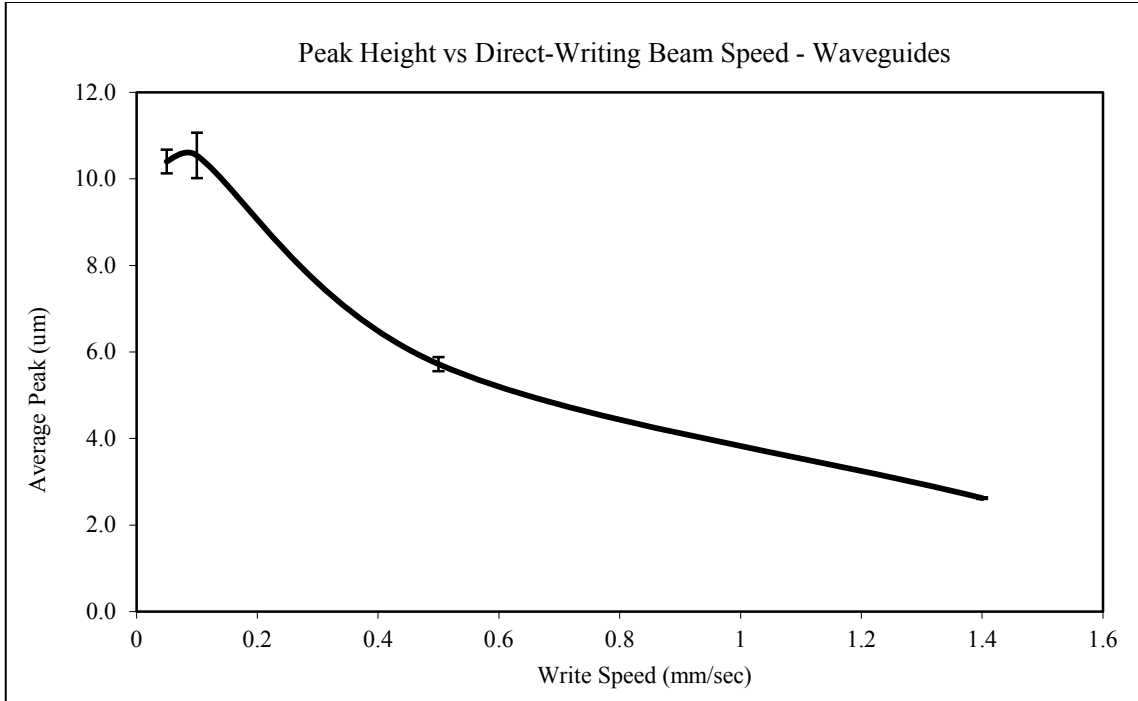


Figure 61. Peak height vs. direct-writing beam speed for waveguides

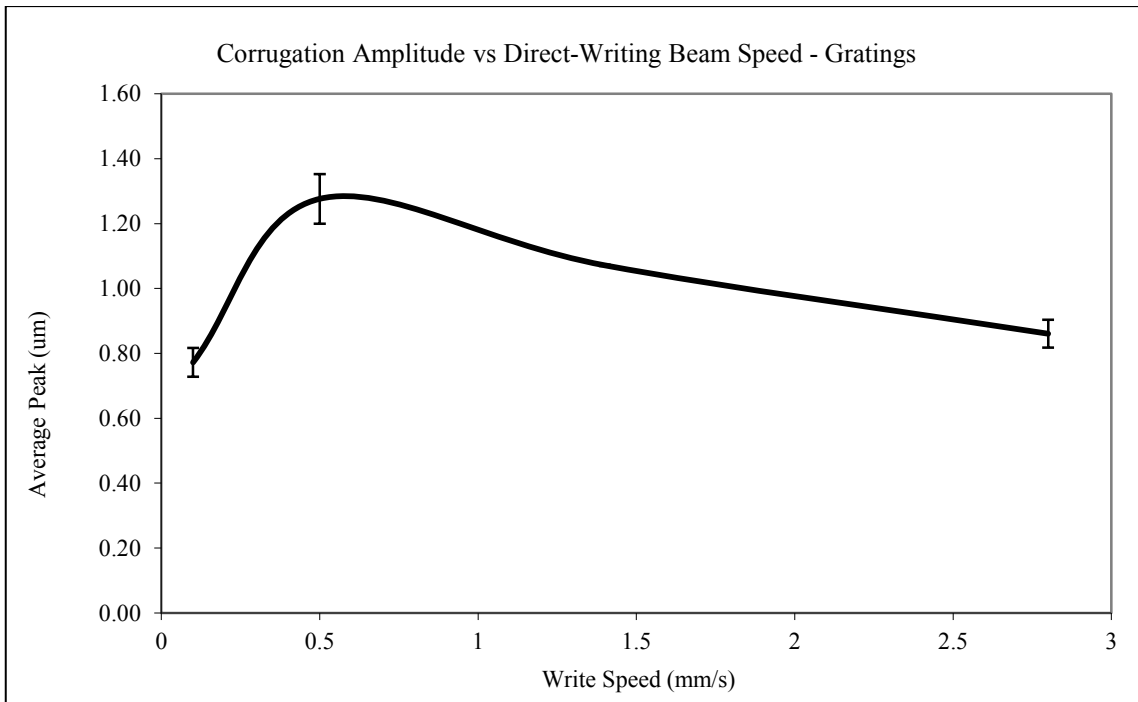


Figure 62. Corrugation amplitude vs. direct-writing beam speed for gratings

Comparing the surface characteristics of waveguides and gratings (which can actually be thought of to be composed of repeated waveguides side by side) reveals interesting facts about the measured height and the actual height of the surface relief in gratings. Accordingly, in the gratings, while the corrugations caused by the surface relief follow the grating period, the corrugations themselves also exhibit an inherent height offset. Therefore, once the first grating step is written on the photopolymer film at the beginning of the grating, the following step right after the first step is then written on the surface which is already altered due to the writing of the previous grating step. This property was verified by a set of profile measurements covering both the corrugations of the grating and the beginning of the grating region on the sample surface:

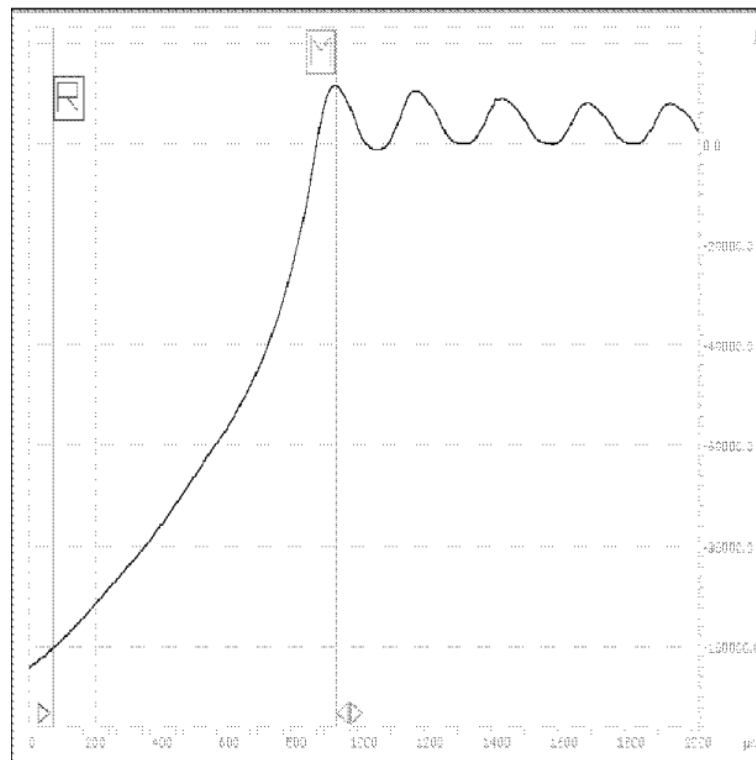


Figure 63. L.GR.010.B grating surface profile - direct-writing beam speed 0.1mm/sec - M-R cursors $\Delta x=845\mu\text{m}$, $\Delta y=11.177\mu\text{m}$.

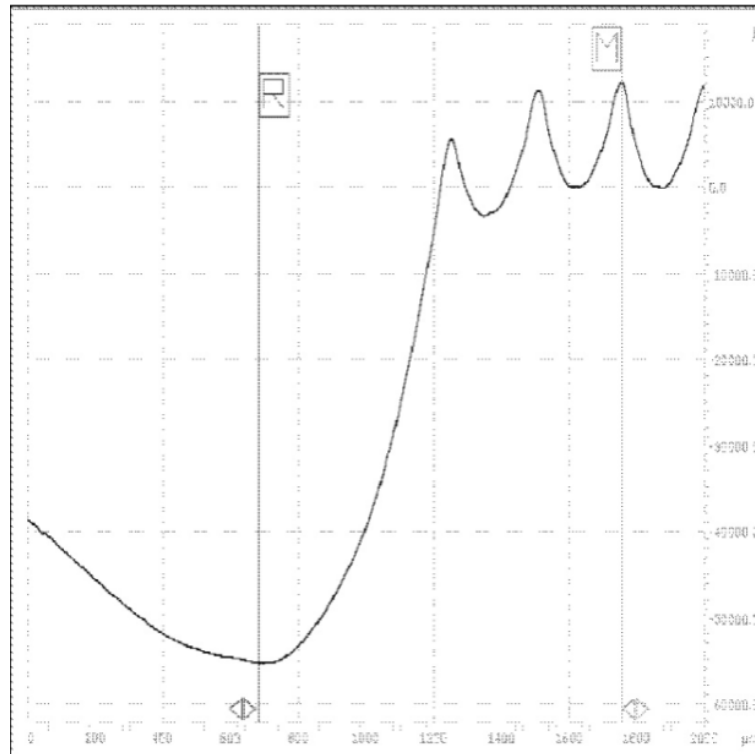


Figure 64. L.GR.050.B2 grating surface profile - direct-writing beam speed 0.5mm/sec - R cursor-first peak $\Delta x \approx 500 \mu\text{m}$, M-R $\Delta y = 6.218 \mu\text{m}$

As seen in the above measurements, the offset value of the surface relief depends on the velocity of the direct-writing laser beam. Also comparing the measurements for the relief offset with the previous measurements for the individual steps and waveguides shows that offset behavior measured above has been found to be in strong agreement with the findings of the previous surface profile measurements.

CHAPTER 4

THEORY AND SIMULATIONS

4.1. Theoretical Background

4.1.1. Grating Coupler

The theoretical background of the grating coupler is based on the studies of Yariv and Yeh (Yariv and Yeh, 2006). In that view, the theoretical work related to the selective directional coupling of two modes in fibers with a periodic structure in between, are presented here, with reference to the below figure:

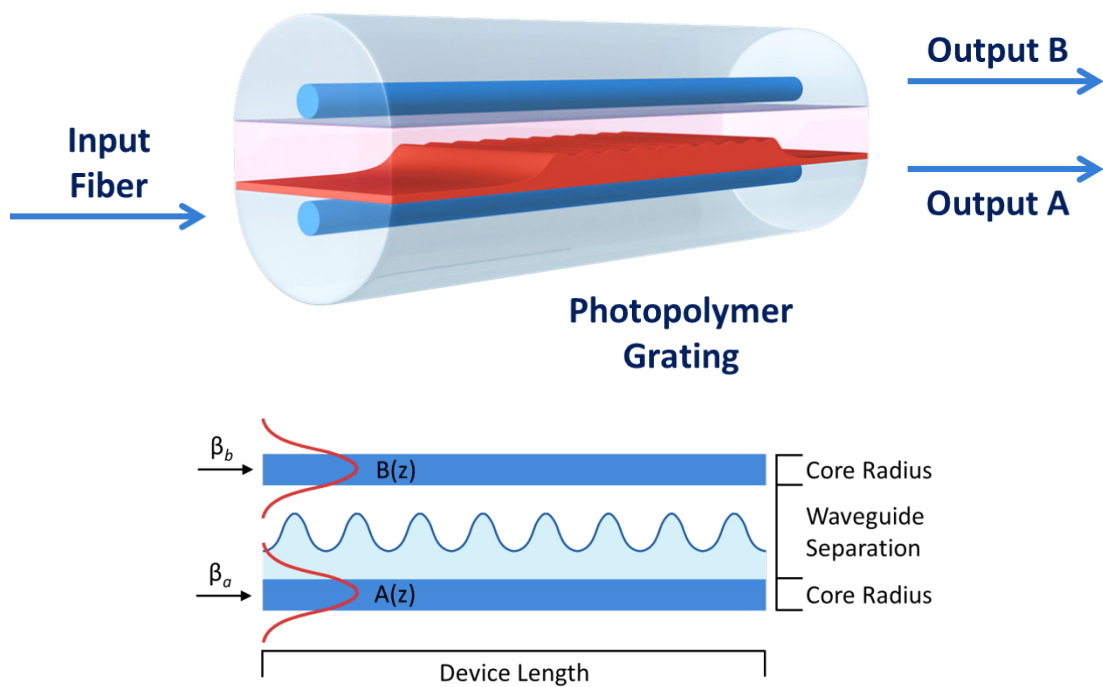


Figure 65. Grating coupler with model parameters shown for the structure

The normal modes of propagation for unperturbed fibers can be written as:

$$\mathbf{E}(x, y, z, t) = \mathbf{E}_m(x, y)e^{i(\omega t - \beta_m z)} \quad (4.1)$$

Where β_m is the propagation constant of the m^{th} mode and $\mathbf{E}_m(x, y)$ is the wavefunction of the normal mode. Assuming that $(\nabla \cdot \mathbf{E}) = 0$, the LP modes in step-index fibers satisfy the approximation to the wave equation (which is obtained via re-writing Maxwell's equations in terms of \mathbf{E} only):

$$\left(\frac{\partial^2}{\partial x^2} + \frac{\partial^2}{\partial y^2} + \omega^2 \mu \epsilon_a(x, y) - \beta_m^2 \right) \mathbf{E}_m(x, y) = 0 \quad (4.2)$$

With the above assumptions, the orthogonality of the modes is expressed as:

$$\int \mathbf{E}_n^*(x, y) \cdot \mathbf{E}_m(x, y) dx dy = \frac{2\omega\mu}{|\beta_m|} \delta_{mn} \quad (4.3)$$

Where, δ_{mn} is the Kronecker delta function for the guided modes and the Dirac delta function for the unguided, i.e., radiation modes. When the unperturbed mode given in Equation (4.1) is excited in the medium in the presence of the dielectric perturbation $\Delta\epsilon(x, y, z)$, an additional polarization wave is formed:

$$\Delta\mathbf{P} = \Delta\epsilon(x, y, z)\mathbf{E}_1(x, y)e^{i(\omega t - \beta_1 z)} \quad (4.4)$$

The polarization wave acts as a distributed radiating source and causes energy exchange between modes \mathbf{E}_1 and \mathbf{E}_2 . The electric field vector of the electromagnetic wave can be expressed as a linear combination of normal modes of the unperturbed medium as:

$$\mathbf{E} = \sum_m A_m(z)\mathbf{E}_m(x, y)e^{i(\omega t - \beta_m z)} \quad (4.5)$$

Substituting Equation (4.5) into the wave equation and using Equation (4.2), we get:

$$\begin{aligned} \sum_m \left(\frac{d^2}{dz^2} A_m - 2i\beta_m \frac{d}{dz} A_m \right) \mathbf{E}_m(x, y) e^{i(\omega t - \beta_m z)} \\ = -\omega^2 \mu \sum_n \Delta\epsilon(x, y, z) A_n \mathbf{E}_n(x, y) e^{i(\omega t - \beta_n z)} \end{aligned} \quad (4.6)$$

Under slowly varying amplitude approximation, Equation (4.6) yields:

$$\begin{aligned}
-2i \sum_m \beta_m \left(\frac{d}{dz} A_m \right) \mathbf{E}_m(x, y) e^{-i\beta_m z} \\
= -\omega^2 \mu \sum_n \Delta\epsilon(x, y, z) A_n \mathbf{E}_n(x, y) e^{-i\beta_n z}
\end{aligned} \tag{4.7}$$

Taking the scalar product of Equation (4.7) with $\mathbf{E}_k^*(x, y)$, integrating over x and y , and using the orthogonality of the modes, we get:

$$\langle k|k \rangle \frac{d}{dz} A_k = \frac{\omega^2 \mu}{2i\beta_k} \sum_n \langle k|\Delta\epsilon|n \rangle A_n(z) e^{i(\beta_k - \beta_n)z} \tag{4.8}$$

Where,

$$\langle k|k \rangle = \int E_k^* \cdot E_k dx dy = \frac{2\omega\mu}{|\beta_k|} \tag{4.9}$$

$$\langle k|\Delta\epsilon|n \rangle = \int \mathbf{E}_k^* \cdot \Delta\epsilon(x, y, z) \mathbf{E}_n dx dy \tag{4.10}$$

Using Fourier series expansion and substituting the above expressions, Equation (4.8) is re-written as:

$$\frac{d}{dz} A_k = -i \frac{\beta_k}{|\beta_k|} \sum_m \sum_n C_{kn}^{(m)} A_n(z) e^{i(\beta_k - \beta_n - m2\pi/\Lambda)z} \tag{4.11}$$

Where $C_{kn}^{(m)}$ is defined as:

$$C_{kn}^{(m)} = \frac{\omega}{4} \langle k|\epsilon_m(x, y)|n \rangle = \frac{\omega}{4} \int \mathbf{E}_k^* \cdot \epsilon_m(x, y) \mathbf{E}_n dx dy \tag{4.12}$$

Incorporating Equation (4.11) and assuming that only the two modes $\mathbf{E}_1(x, y)e^{i(\omega t - \beta_1 z)}$ and $\mathbf{E}_2(x, y)e^{i(\omega t - \beta_2 z)}$ are involved in coupling, the coupled equations become:

$$\frac{d}{dz} A_1 = -i \frac{\beta_1}{|\beta_1|} C_{12}^{(m)} A_2(z) e^{i\Delta\beta z} \tag{4.13}$$

$$\frac{d}{dz}A_2 = -i\frac{\beta_2}{|\beta_2|}C_{21}^{(-m)}A_1(z)e^{i\Delta\beta z} \quad (4.14)$$

Where,

$$\Delta\beta = \beta_1 - \beta_2 - m\frac{2\pi}{\Lambda} \quad (4.15)$$

With $C_{12}^{(m)}$ and $C_{21}^{(-m)}$ are coupling coefficients given by Equation (4.12).

Let A , B and z represent the input guide, output guide and the propagation direction, respectively, and $A(z)$ and $B(z)$ the mode amplitudes as functions of z ; for co-directional coupling, the coupled mode equations (4.13) and (4.14) become:

$$\frac{d}{dz}A_1 = -i\kappa A_2(z)e^{i\Delta\beta z} \quad (4.16)$$

$$\frac{d}{dz}A_2 = -i\kappa^* A_1(z)e^{-i\Delta\beta z} \quad (4.17)$$

Where the coupling constant is given as:

$$\kappa = \frac{\omega^2\mu}{2\sqrt{|\beta_1\beta_2|}}\mathbf{p}_1^*\epsilon_m\mathbf{p}_2 \quad (4.18)$$

With unit vectors \mathbf{p}_1 and \mathbf{p}_2 representing the polarization states of the plane waves. Coupled mode equations obey the law of conservation of energy, meaning:

$$\frac{d}{dz}(|A_1|^2 + |A_2|^2) = 0 \quad (4.19)$$

In the case of coupling of modes with a phase mismatch, in order to solve the coupled mode equations, we multiply both sides of the equation by $e^{-i\Delta\beta z}$, which leads:

$$e^{-i\Delta\beta z}\frac{d}{dz}A_1 = -i\kappa A_2(z) \quad (4.20)$$

Performing the differentiation and replacing A_2 using the coupled equations we get following the second order ODE:

$$\frac{d^2}{dz^2} A_1 - i\Delta\beta \frac{d}{dz} A_1 + |\kappa|^2 A_1 = 0 \quad (4.21)$$

The general solution of the above differential equation can be written as:

$$\begin{aligned} A_1(z) &= e^{i(\frac{\Delta\beta}{2})z} \left[\left(\cos sz - i \frac{\Delta\beta \sin sz}{2s} \right) A_1(0) - i\kappa \frac{\sin sz}{s} A_2(0) \right] \\ A_2(z) &= e^{-i(\Delta\beta/2)z} \left[-i\kappa^* \frac{\sin sz}{s} A_1(0) + \left(\cos sz + i \frac{\Delta\beta \sin sz}{2s} \right) A_2(0) \right] \end{aligned} \quad (4.22)$$

Where,

$$s^2 = \kappa^* \kappa + \left(\frac{\Delta\beta}{2} \right)^2 \quad (4.23)$$

With $A_1(0)$ and $A_2(0)$ being the amplitudes of the modes at $z = 0$. Applying the above formulation for the device to be designed, when the electric field of the optical propagation is given as:

$$\mathbf{E}(x, y, z) = A(z) \boldsymbol{\varepsilon}_a(x, y) e^{-i\beta_a z} + B(z) \boldsymbol{\varepsilon}_b(x, y) e^{-i\beta_b z} \quad (4.24)$$

We replace A_1 with A as the input signal and A_2 with B as the output signal to get the length-dependent general solutions of the amplitudes in the presence of a periodic structure between the waveguides as:

$$A(z) = e^{i(\Delta\beta/2)z} \left[\left(\cos sz - i \frac{\Delta\beta \sin sz}{2s} \right) A(0) - i\kappa \frac{\sin sz}{s} B(0) \right] \quad (4.25)$$

$$B(z) = e^{-i(\Delta\beta/2)z} \left[-i\kappa^* \frac{\sin sz}{s} A(0) + \left(\cos sz + i \frac{\Delta\beta \sin sz}{2s} \right) B(0) \right] \quad (4.26)$$

Where,

$$s^2 = \boldsymbol{\kappa}^* \boldsymbol{\kappa} + \left(\frac{\Delta\beta}{2}\right)^2 \quad (4.27)$$

$$\boldsymbol{\kappa} = \frac{\omega}{4} \int \boldsymbol{\varepsilon}_a^*(x, y) \epsilon_m(x, y) \boldsymbol{\varepsilon}_b(x, y) \quad (4.28)$$

$$\Delta\beta = \beta_a - \beta_b - m \frac{2\pi}{\Lambda} = 0 \quad (4.29)$$

Finally, setting $B(0) = 0$ for single-beam incidence, we obtain the solutions as:

$$A(z) = e^{i(\Delta\beta/2)z} \left[\left(\cos sz - i \frac{\Delta\beta \sin sz}{2s} \right) A(0) \right] \quad (4.30)$$

$$B(z) = e^{-i(\Delta\beta/2)z} \left[-i\boldsymbol{\kappa}^* \frac{\sin sz}{s} A(0) \right] \quad (4.31)$$

4.1.2. Reciprocity and Conservation of Power

The total power carried by the modes is proportional to $A^*A + B^*B$. To verify the conservation of power, the derivative of the power with respect to propagation direction z must be examined. Taking the derivative, we get:

$$\begin{aligned} \frac{d}{dz} (A^*A + B^*B) &= A'^*A + A^*A' + B'^*B + B^*B' \\ &= -i\kappa_{ab}A^*B e^{i2\delta z} + i\kappa_{ab}^*AB^* e^{-i2\delta z} \\ &\quad - i\kappa_{ba}AB^* e^{-i2\delta z} + i\kappa_{ba}^*A^*B e^{i2\delta z} \\ &= -i(\kappa_{ab} - \kappa_{ba}^*)A^*B e^{i2\delta z} \\ &\quad + i(\kappa_{ab}^* - \kappa_{ba})AB^* e^{-i2\delta z} \end{aligned} \quad (4.32)$$

The derivative equals zero if $\kappa_{ab} = \kappa_{ba}^*$. So, to prove the conservation of power, it is necessary to show that $\kappa_{ab} = \kappa_{ba}^*$.

For the two fibers forming the directional coupler structure, let $\boldsymbol{\varepsilon}_a(x, y)\exp[i(\omega t - \beta_a z)]$ and $\boldsymbol{\varepsilon}_b(x, y)\exp[i(\omega t - \beta_b z)]$ be the unperturbed modes.

When the two guides are separated by a finite distance, the electric field of wave propagation in the coupled-waveguide structure can be written as:

$$\begin{aligned} \mathbf{E}(x, y, z, t) = & A(z)\boldsymbol{\varepsilon}_a(x, y)\exp[i(\omega t - \beta_a z)] \\ & + B(z)\boldsymbol{\varepsilon}_b(x, y)\exp[i(\omega t - \beta_b z)] \end{aligned} \quad (4.33)$$

If the distance between the fibers is infinite, then the modes are unperturbed and $A(z)$ and $B(z)$ do not depend on z since both terms in the right and side of the above equation satisfy the wave equation individually. If we let $n^2(x, y)$ be the refractive index distribution of the coupler, defined as:

$$n^2(x, y) = \begin{cases} n_a^2, & \text{core } a \\ n_b^2, & \text{core } b \\ n_c^2, & \text{elsewhere} \end{cases} \quad (4.34)$$

For mathematical convenience, the above terms can be redefined as:

$$\begin{aligned} \Delta n_a^2(x, y) &= \begin{cases} n_a^2 - n_c^2, & \text{core } a \\ 0, & \text{elsewhere} \end{cases} \\ \Delta n_b^2(x, y) &= \begin{cases} n_b^2 - n_c^2, & \text{core } b \\ 0, & \text{elsewhere} \end{cases} \\ n_s^2(x, y) &= n_c^2 \end{aligned} \quad (4.35)$$

Then, the refractive index distribution of the device can be written as:

$$n^2(x, y) = n_s^2(x, y) + \Delta n_a^2(x, y) + \Delta n_b^2(x, y) \quad (4.36)$$

Where, $n_s^2(x, y)$ is the refractive index distribution in the region outside the two fiber cores, $\Delta n_a^2(x, y)$ is the presence of fiber A and $\Delta n_b^2(x, y)$ is the presence of fiber B. With the above definitions, the refractive index profiles of the two waveguides are given as:

$$\begin{aligned} n_a^2(x, y) &= n_s^2(x, y) + \Delta n_a^2(x, y) \\ n_b^2(x, y) &= n_s^2(x, y) + \Delta n_b^2(x, y) \end{aligned} \quad (4.37)$$

Then, the individual fiber modes $\boldsymbol{\varepsilon}_a(x, y)$ and $\boldsymbol{\varepsilon}_b(x, y)$ satisfy the equation:

$$\begin{aligned} \left(\frac{\partial^2}{\partial x^2} + \frac{\partial^2}{\partial y^2} + \frac{\omega^2}{c^2} [n_s^2(x, y) + \Delta n_\alpha^2(x, y)] \right) \boldsymbol{\varepsilon}_\alpha(x, y) \\ = \beta_\alpha^2 \boldsymbol{\varepsilon}_\alpha(x, y), \quad \alpha = a, b \end{aligned} \quad (4.38)$$

Hence, the presence of fiber B causes a perturbation of $\Delta n_b^2(x, y)$ on the propagation of $\boldsymbol{\varepsilon}_a(x, y) \exp[i(\omega t - \beta_a z)]$ and likewise, the presence of fiber A causes a perturbation of $\Delta n_a^2(x, y)$ on $\boldsymbol{\varepsilon}_b(x, y) \exp[i(\omega t - \beta_b z)]$. By utilizing operators and using Dirac notation, the above equation can be rewritten as:

$$(L + \Delta n_\alpha^2)|\alpha\rangle = \beta_\alpha^2|\alpha\rangle, \quad \alpha = a, b \quad (4.39)$$

Where L is a linear operator representing $\nabla_\xi^2 + \omega^2 [n_s^2(x, y)]/c^2$, with $\nabla_\xi^2 = \partial^2/\partial x^2 + \partial^2/\partial y^2$. Using this notation, the coupling constants:

$$\begin{aligned} \kappa_{ab} &= \frac{\omega}{4} \varepsilon_0 \iint \boldsymbol{\varepsilon}_a^* \Delta n_a^2(x, y) \boldsymbol{\varepsilon}_b \, dx \, dy \\ \kappa_{ba} &= \frac{\omega}{4} \varepsilon_0 \iint \boldsymbol{\varepsilon}_b^* \Delta n_b^2(x, y) \boldsymbol{\varepsilon}_a \, dx \, dy \end{aligned} \quad (4.40)$$

are rewritten as:

$$\begin{aligned} \kappa_{ab} &= \langle a | \Delta n_a^2 | b \rangle \frac{\omega \varepsilon_0}{4} \\ \kappa_{ba} &= \langle b | \Delta n_b^2 | a \rangle \frac{\omega \varepsilon_0}{4} \end{aligned} \quad (4.41)$$

Using orthogonality of the modes ($\langle a | b \rangle = 0$), from Equation (4.38):

$$\begin{aligned} \langle b | (L + \Delta n_a^2) | a \rangle &= \beta_a^2 \langle b | a \rangle = 0 \\ \langle a | (L + \Delta n_b^2) | b \rangle &= \beta_b^2 \langle a | b \rangle = 0 \end{aligned} \quad (4.42)$$

Then,

$$\begin{aligned}
-\langle b|L|a\rangle &= -\langle b|La\rangle = -\int b^*La \\
-\langle a|L|b\rangle &= -\langle a|Lb\rangle = -\int a^*Lb
\end{aligned}
\tag{4.43}$$

Which yields,

$$-\langle a|L|b\rangle^* = -\int a(Lb)^* = -\langle Lb|a\rangle
\tag{4.44}$$

And using the orthogonality, leads to:

$$-\langle b|La\rangle = -\langle Lb|a\rangle
\tag{4.45}$$

Which means that L is an Hermitian operator. Orthogonality of the modes enables us to write:

$$\langle a|H|b\rangle = 0
\tag{4.46}$$

Replacing H:

$$\langle a|(L + \Delta n_b^2)|b\rangle = 0
\tag{4.47}$$

Leads to:

$$-\langle a|L|b\rangle = \langle a|\Delta n_b^2|b\rangle
\tag{4.48}$$

Since L is an Hermitian operator, we can write:

$$\begin{aligned}
\langle a|(\Delta n_b^2)|b\rangle &= -\langle a|L|b\rangle \\
&= -\langle La|b\rangle \\
&= -\langle b|L|a\rangle^*
\end{aligned}
\tag{4.49}$$

In Equation (4.46), if we replace for the other eigenvalue equation:

$$\langle b|(L + \Delta n_a^2)|a\rangle = 0 \quad (4.50)$$

we get:

$$\langle b|L|a\rangle = -\langle b|(\Delta n_a^2)|a\rangle \quad (4.51)$$

When we plug Equation (4.51) into Equation (4.49) above, we can extend the equations as:

$$\begin{aligned} \langle a|\Delta n_b^2|b\rangle &= -\langle a|L|b\rangle \\ &= -\langle La|b\rangle \\ &= -(\langle b|L|a\rangle)^* \\ &= -(-\langle b|(\Delta n_a^2)|a\rangle)^* \\ &= (\langle b|(\Delta n_a^2)|a\rangle)^* \end{aligned} \quad (4.52)$$

From Equation (4.51), assuming the media are non-absorbing ($\Delta n_a^2 = \text{Re}\{\Delta n_a^2\}$ and $\Delta n_b^2 = \text{Re}\{\Delta n_b^2\}$) and using Equation (4.49) we write:

$$\begin{aligned} \langle b|\Delta n_a^2|a\rangle &= -\langle b|L|a\rangle \\ &= -(\langle a|L|b\rangle)^* \\ &= -(-\langle a|\Delta n_b^2|b\rangle)^* \\ &= \langle b|\Delta n_b^2|a\rangle \end{aligned} \quad (4.53)$$

Which leads to, using Equation (4.52):

$$\begin{aligned} (\langle b|\Delta n_a^2|a\rangle)^* &= \langle a|\Delta n_a^2|b\rangle \\ &= \langle a|\Delta n_b^2|b\rangle \\ &= (\langle b|\Delta n_b^2|a\rangle)^* \\ \Rightarrow \langle a|\Delta n_a^2|b\rangle &= (\langle b|\Delta n_b^2|a\rangle)^* \end{aligned} \quad (4.54)$$

When we replace the above expression in the coupling coefficients given in Equation (4.41), we get:

$$\begin{aligned}
 \kappa_{ab} &= \langle a | \Delta n_a^2 | b \rangle \frac{\omega \varepsilon_0}{4} \\
 &= (\langle b | \Delta n_b^2 | a \rangle)^* \frac{\omega \varepsilon_0}{4} \\
 \kappa_{ba} &= \langle b | \Delta n_b^2 | a \rangle \frac{\omega \varepsilon_0}{4}
 \end{aligned} \tag{4.55}$$

which finally leads to:

$$\kappa_{ab} = \kappa_{ba}^* \tag{4.56}$$

4.1.3. Design Parameters

Theoretical model was implemented into MATLAB environment and simulations were carried onwards. Two types of optical fiber, Nufern 780-HP and Corning HI1060 were employed in the calculations. Calculations and simulations were performed for configurations based on previous studies and initially for the case where the fiber was launched using 632.8nm laser and later for 852nm laser.

Throughout the design and simulation studies, based on the fabrication capabilities and the material properties, the design parameters of the device were determined as follows:

- Optical fiber structure (fiber used in the device fabrication)
- Grating period (distance between the grating steps)
- Shape of the individual grating steps (double-Gaussian model parameters)
- Distance between the input and output fibers (waveguide separation)
- Total device length

4.2. Sinusoidal Grating – Nufern 780-HP Optical Fiber

4.2.1. Approximate Grating Steps with Generic Fiber

The first configuration studied is the one where the grating structure written in between the optical fibers is of pure sinusoidal form. This structure is an approximation of the Gaussian structure to be used in the final design and convenient for fast simulations. Structure of the simulated configuration and the results obtained are presented below.

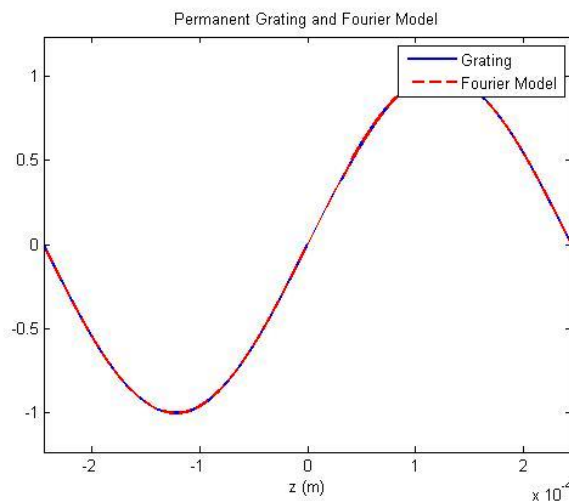


Figure 66. Defined approximate/sinusoidal grating structure and corresponding Fourier series approximation

Specifications of Nufern 780-HP optical fiber are (Nufern, 2011):

- Core refractive index: $n_{\text{Core}}=1.4591$
- Cladding refractive index: $n_{\text{Clad}}=1.4537$
- Core radius: $a=4\mu\text{m}$

Based on calculations using the fiber specifications, the optical fiber supports 3 modes (**LP₀₁**, **LP₁₁** and **LP₀₂**) when excited at 632.8nm wavelength:

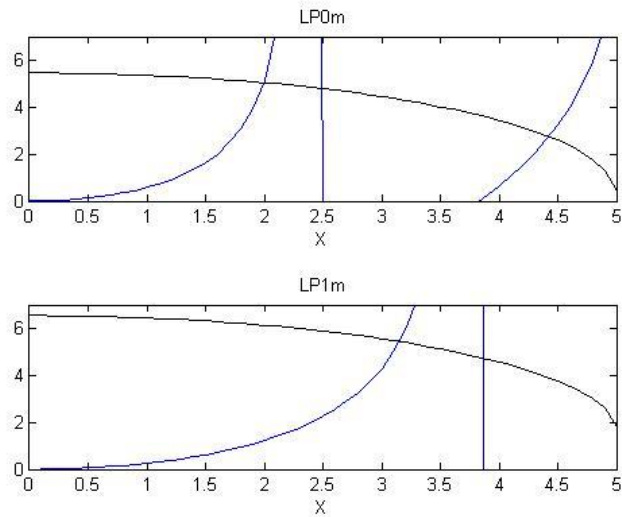


Figure 67. Modes supported by Nufern 780-HP fiber excited at 632.8nm wavelength

Propagation constants of the supported modes are calculated as:

- $\beta_{01} = 1.447452009555042 \times 10^7$
- $\beta_{11} = 1.446166260645392 \times 10^7$
- $\beta_{02} = 1.444081208785489 \times 10^7$

Based on these values, the fields of the modes supported by the input and output fibers are obtained:

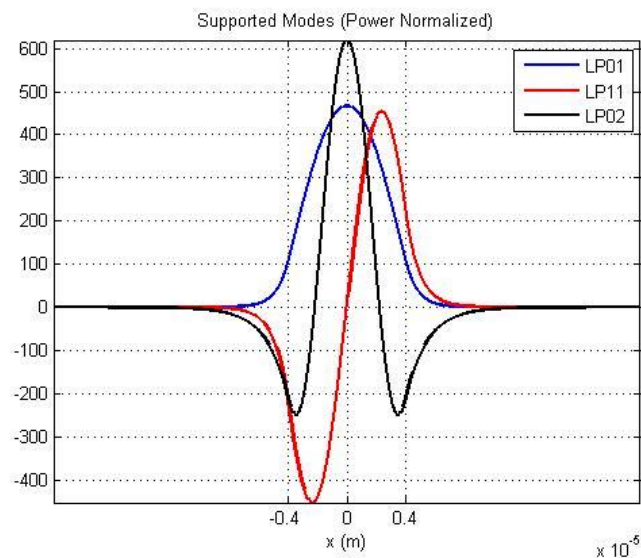


Figure 68. Modes supported by the input and output fibers

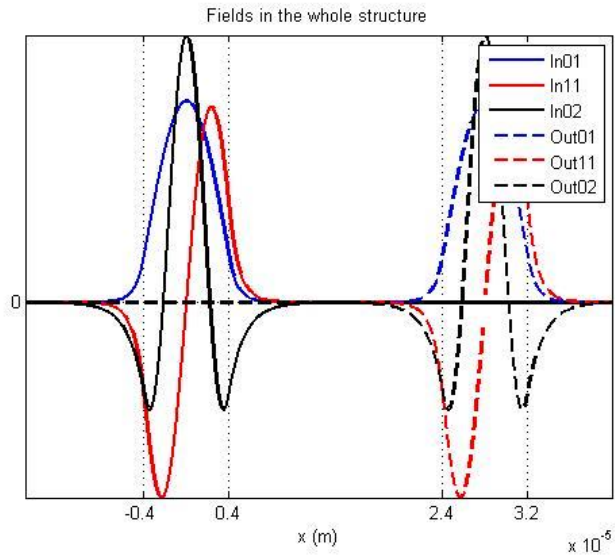


Figure 69. Modes supported by the whole structure

Propagation of each mode throughout the structure, as well as the coupling between each and every mode was calculated with respect to propagation distance:

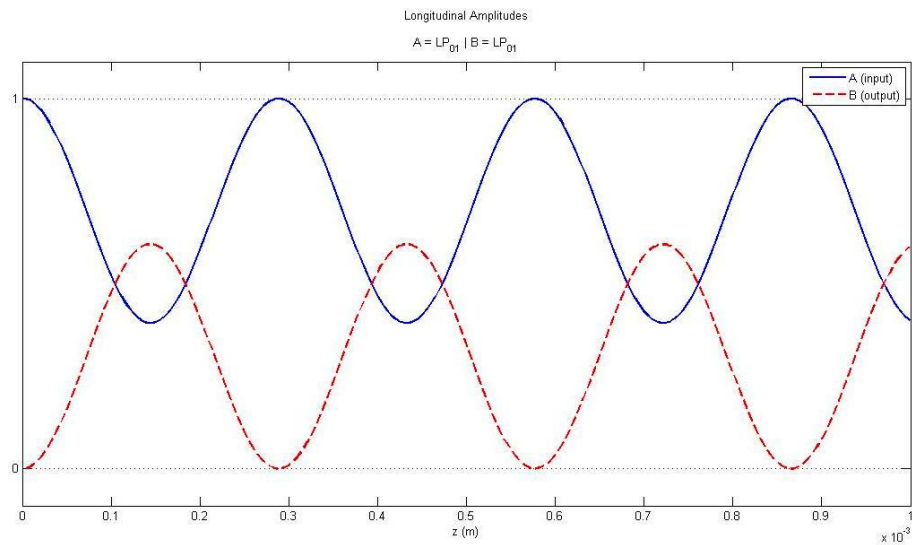


Figure 70. An example of coupling between input and output waveguide modes

The distance between the waveguides is selected as the first optimization parameter. It should be remembered that, the design target is the coupling between the second input mode (LP_{11}) and fundamental output mode (LP_{01}) being maximum. In addition, coupling between input fundamental mode (LP_{01}) and remaining output modes is desired to be minimized or totally cut off.

4.2.2. Phase Matching Condition

In such a structure where a periodic perturbation is employed, the modes to be coupled in the input and output waveguides need to be phase-matched and hence a certain phase-matching condition should be met, i.e., the device should be designed accordingly. Let λ_0 be the wavelength of light and n_a and n_b be the effective indices of modes; then the phase difference between the two modes is represented as:

$$\Delta\beta = \beta_a - \beta_b - m \frac{2\pi}{\Lambda} = n_a \frac{2\pi}{\lambda_0} - n_b \frac{2\pi}{\lambda_0} - m \frac{2\pi}{\Lambda} = 0 \quad (4.57)$$

Where $\lambda = \lambda_0$. Then, in order to obtain co-directional coupling, the grating period should satisfy the phase matching condition:

$$\Lambda = m \frac{\lambda_0}{|n_a - n_b|}, \quad m = 1, 2, 3 \dots \quad (4.58)$$

For this configuration, it was calculated that phase matching between input second mode (LP₁₁) and output fundamental mode (LP₀₁) requires a grating period of 488.6 μ m. Implementing this condition into the device design, the results obtained are presented below:

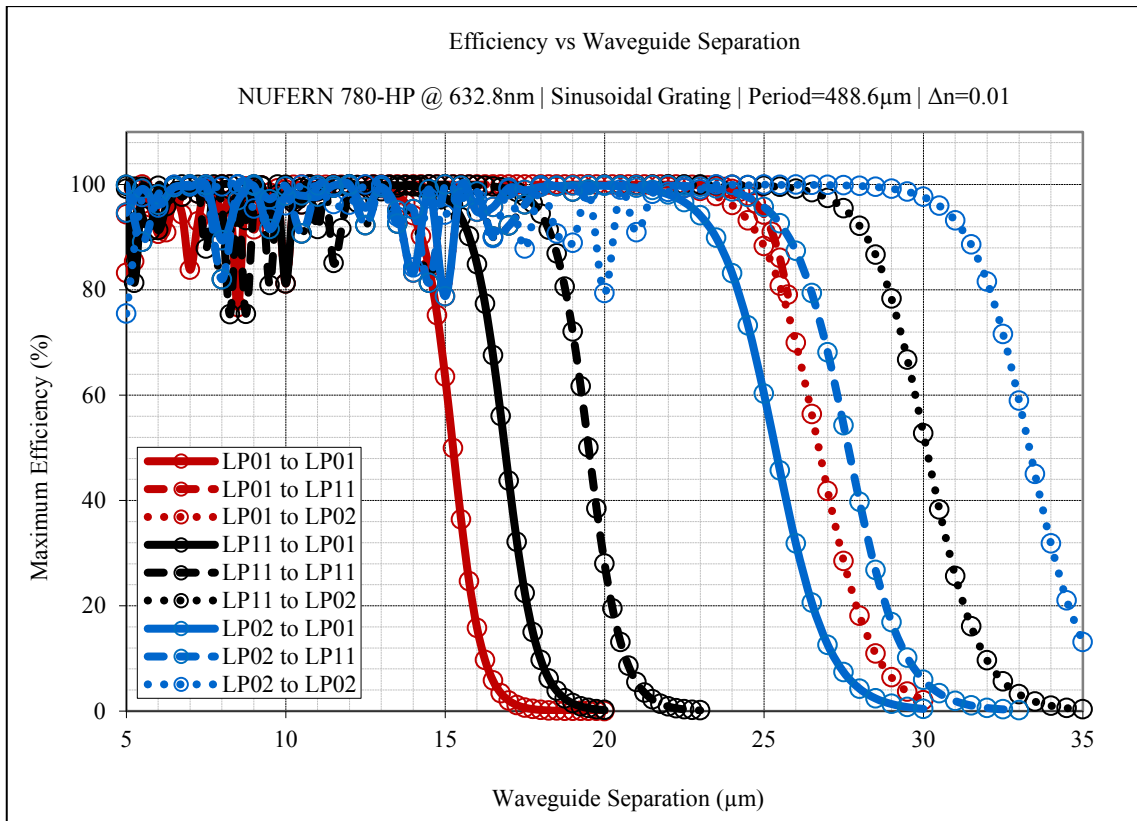


Figure 71. Coupling efficiency between input and output modes with respect to waveguide separation

The device lengths necessary to reach the calculated efficiencies given above are given in the below figure. Calculation of such distances is important in that it allows an evaluation of the actual possibility of realizing the physical device, due to the physical limitations of the experimental setup.

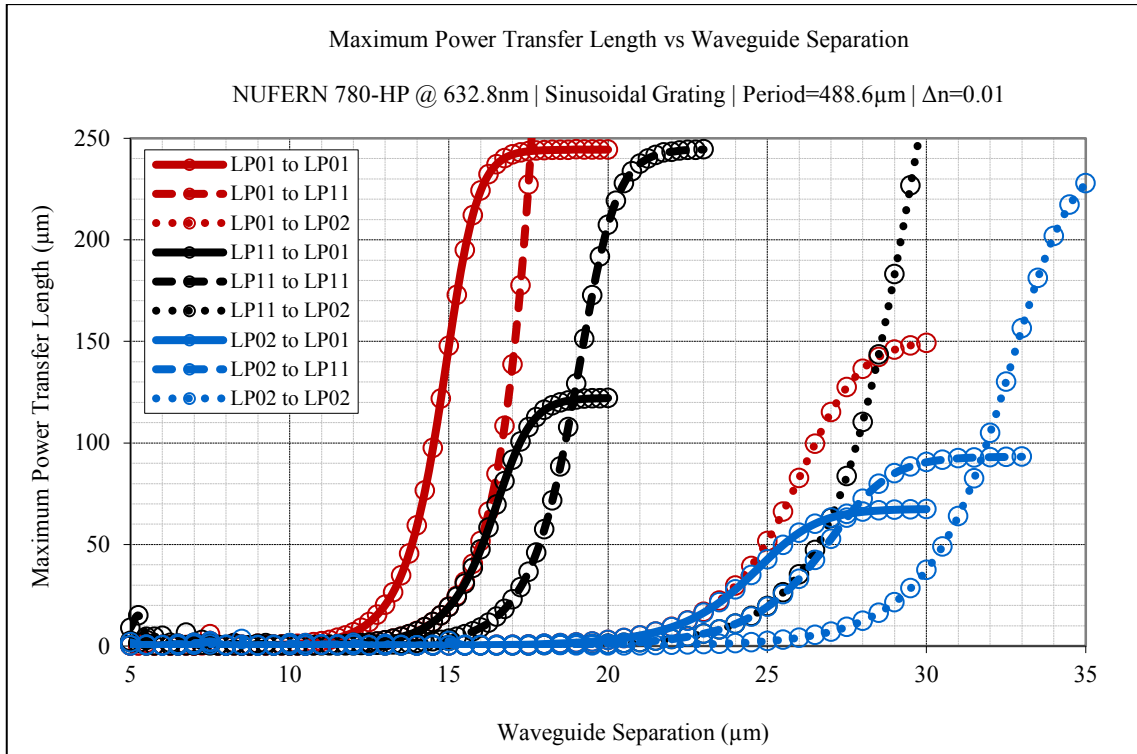


Figure 72. Coupling distance for coupling between each mode in two guides

4.3. Sinusoidal Grating – Corning HI1060 Optical Fiber

4.3.1. Approximate Grating Steps with Realistic Fiber

Following the calculations employing Nufern 780-HP optical fiber, a second series of simulations were performed employing Corning HI1060 optical fiber, which was set to be employed in D-fiber fabrication by flattening of the side surface (see Section 5.3). The specifications of Corning HI1060 fiber are (Corning, 2010):

- Core refractive index: $n_{\text{Core}}=1.4572$
- Cladding refractive index: $n_{\text{Clad}}=1.4507$
- Core radius: $a=2.65\mu\text{m}$

Based on calculations using the fiber specifications, the optical fiber supports 2 modes (**LP₀₁** and **LP₁₁**) when excited at 632.8nm wavelength:

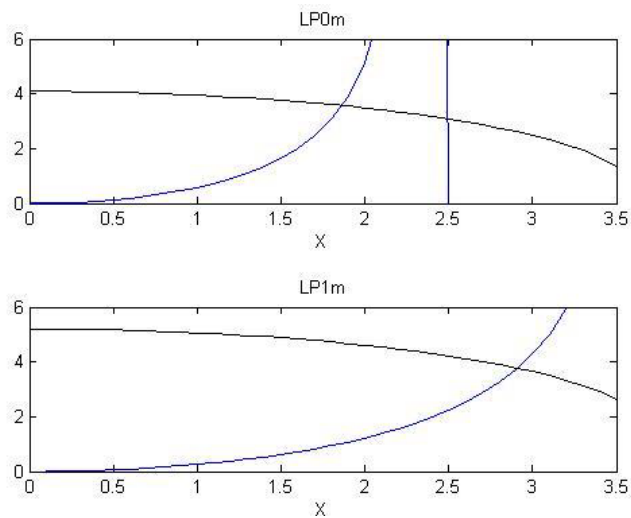


Figure 73. Modes supported by Corning HI1060 fiber excited at 632.8nm wavelength

Propagation constants of the supported modes are calculated as:

- $\beta_{01} = 1.444714490226709 \times 10^7$
- $\beta_{11} = 1.442255268723464 \times 10^7$

Based on these values, the fields of the modes supported by the input and output waveguides are obtained:

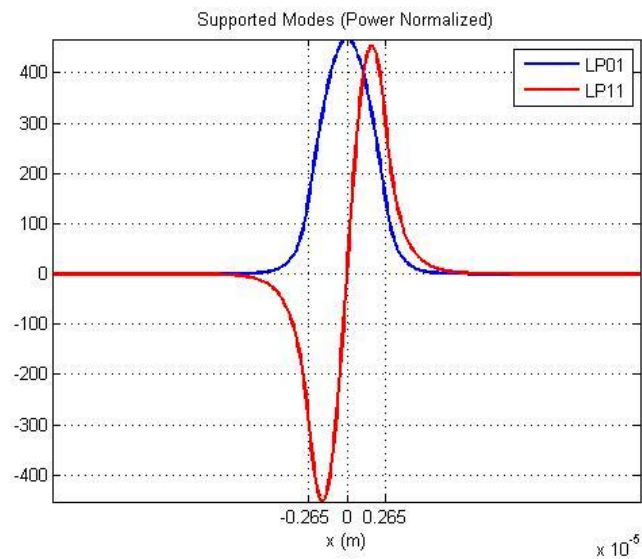


Figure 74. Modes supported by the input and output guides

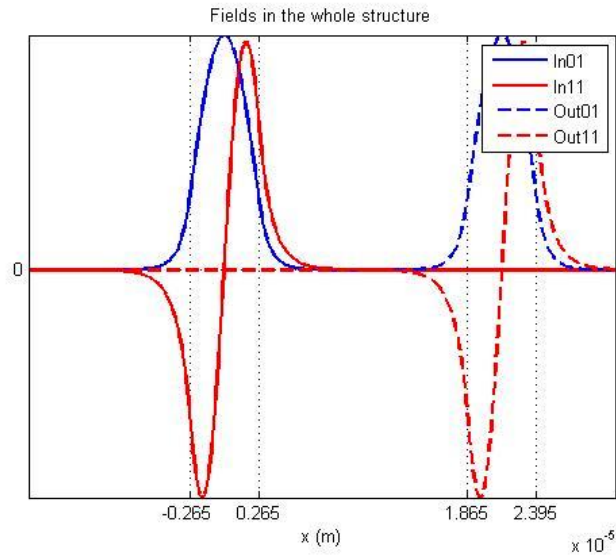


Figure 75. Modes supported by the whole structure

As with the previous calculations for Nufern fiber, propagations of all modes through the structure were calculated and the coupling efficiency between each and every mode was obtained with respect to propagation distance. Also for this set of conditions, the coupling is desired to be maximized between input second mode (LP_{11}) and output fundamental mode (LP_{01}) and coupling from all the remaining modes is desired to be minimized or completely cut off.

Using the formulation and the expressions presented in the previous section, the grating period satisfying the phase matching condition between input second mode (LP_{11}) and output fundamental mode (LP_{01}) is calculated as **255.49 μm** . Under this condition, the results obtained are presented below:

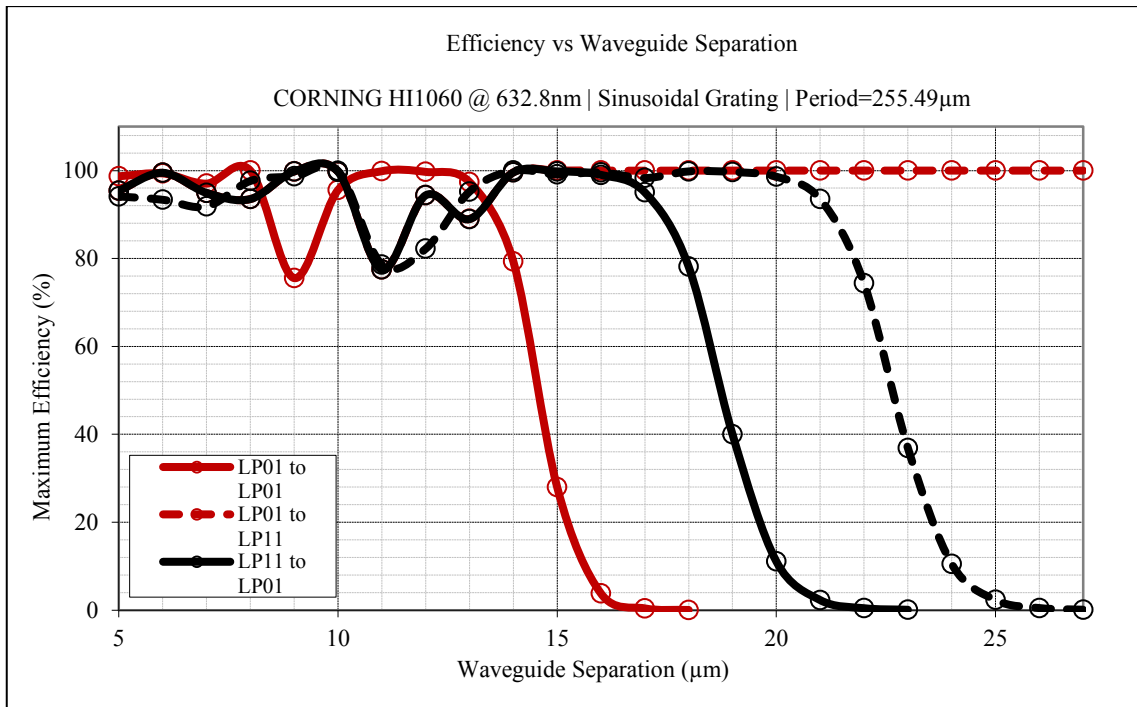


Figure 76. Coupling efficiency with respect to waveguide separation with sinusoidal gratings for Corning HI1060 excited at 632.8nm.

In addition, device lengths necessary to reach the calculated efficiencies are:

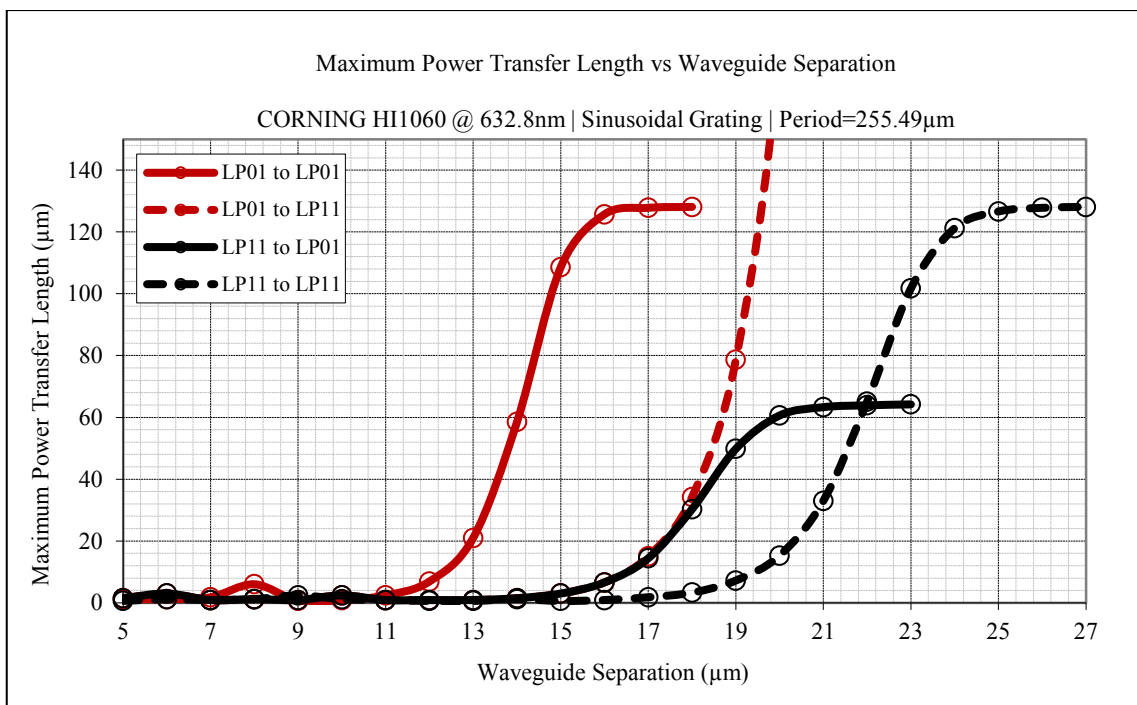


Figure 77. Device lengths necessary to reach the calculated efficiencies wrt waveguide separation; sinusoidal grating, Corning HI1060 excited at 632.8nm

4.4. Gaussian Grating – Corning HI1060 Optical Fiber

4.4.1. Realistic Grating Steps with Realistic Fiber

Calculations and simulations up to this point, where the realistic optical fiber was employed together with an approximate grating structure, point to the possibility of obtaining a selective mode coupling with the designed structure. From this point on, calculations and simulations have been performed using the actual Gaussian-type grating structure together with Corning HI1060 optical fiber, which was set to be used in the final device.

The physical properties of the grating structure that could be fabricated in-house had been studied earlier; individual steps of the permanent photopolymer grating structure were characterized and mathematically modelled:

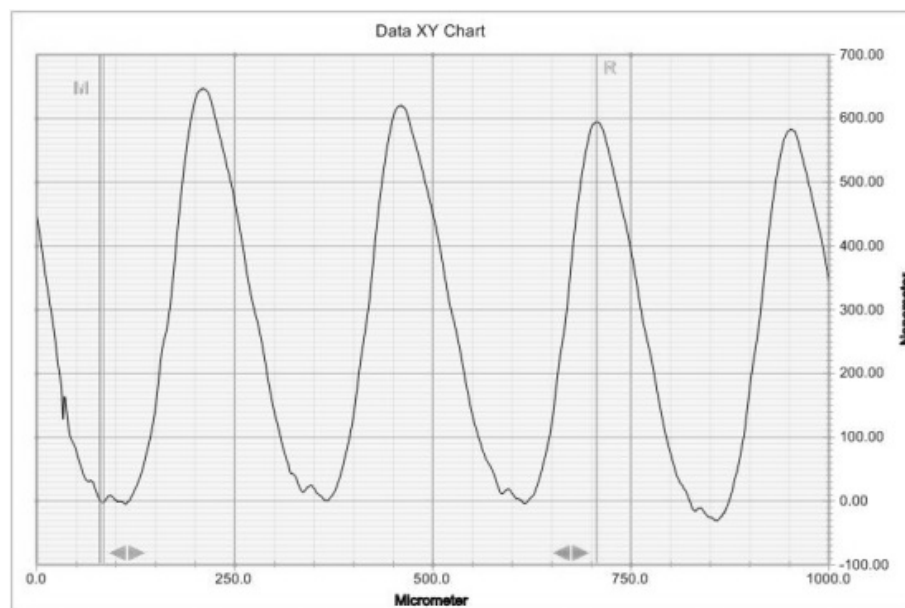


Figure 78. L.GR.010.A grating surface profile - beam speed 0.1 mm/sec

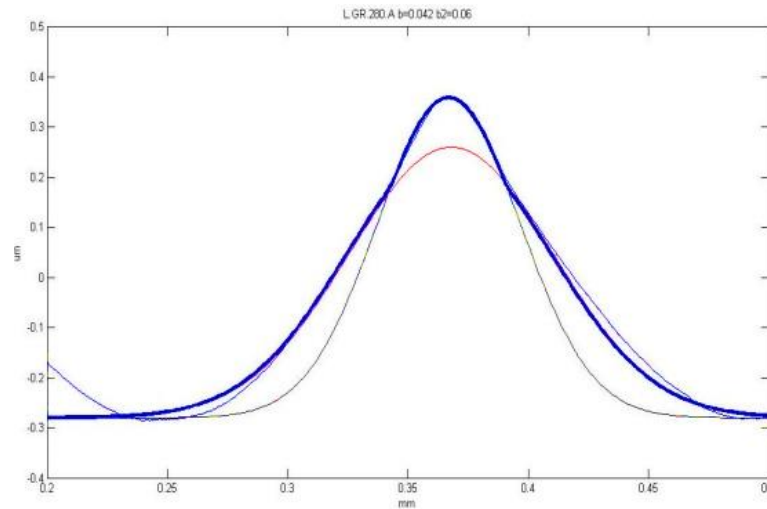


Figure 79. Gaussian function fit for single step of grating L.GR.280.A [$b=0.042$ (black), $b_2=0.060$ (red)]

Accordingly, the previously defined grating structure was implemented in MATLAB environment used into the calculations as in the previous configurations:

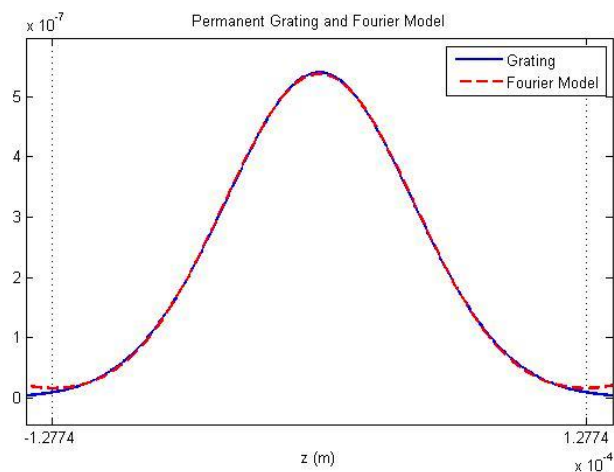


Figure 80. Gaussian grating structure and corresponding Fourier series approximation used in the calculations

The specifications of Corning HI1060 optical fiber and the supported modes were discussed earlier. Similar to previous configurations, the maximum coupling target and the phase matching condition are identical (LP_{11} to LP_{01} , $255.49\mu\text{m}$) and propagation of the mode fields were calculated for this setting as well.

The results obtained with respect to the distance between the waveguides are presented below:

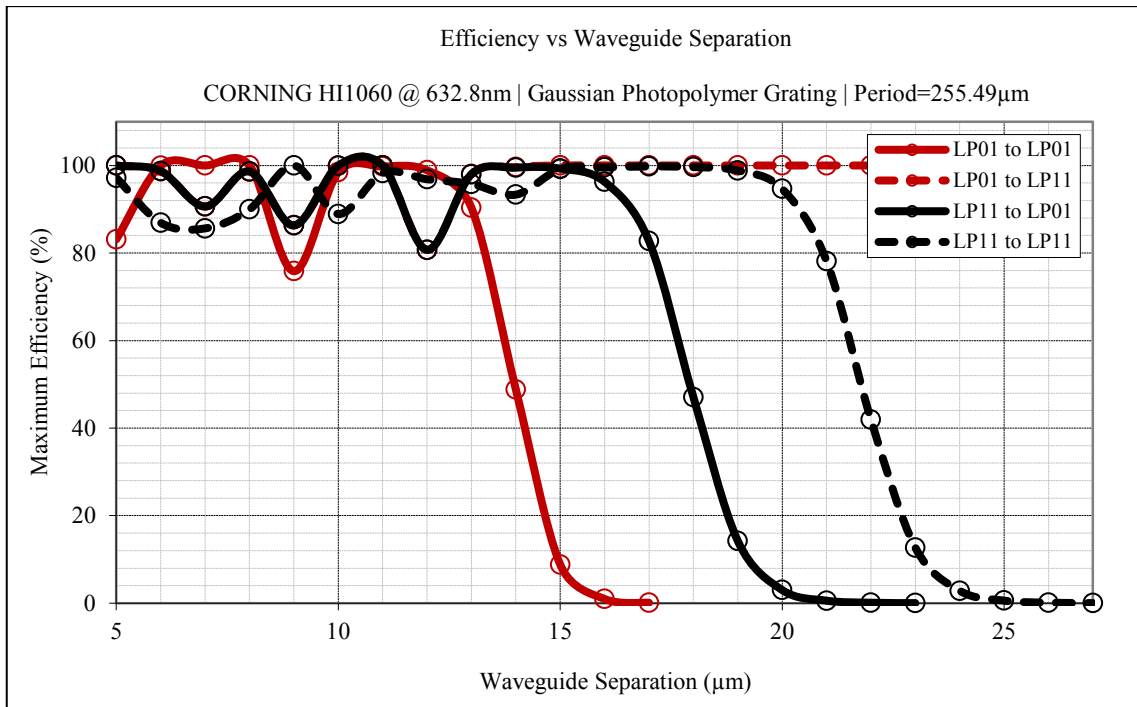


Figure 81. Coupling efficiency with respect to waveguide separation with Gaussian gratings for Corning HI1060 excited at 632.8nm.

And the related necessary device lengths to reach the calculated efficiencies above are:

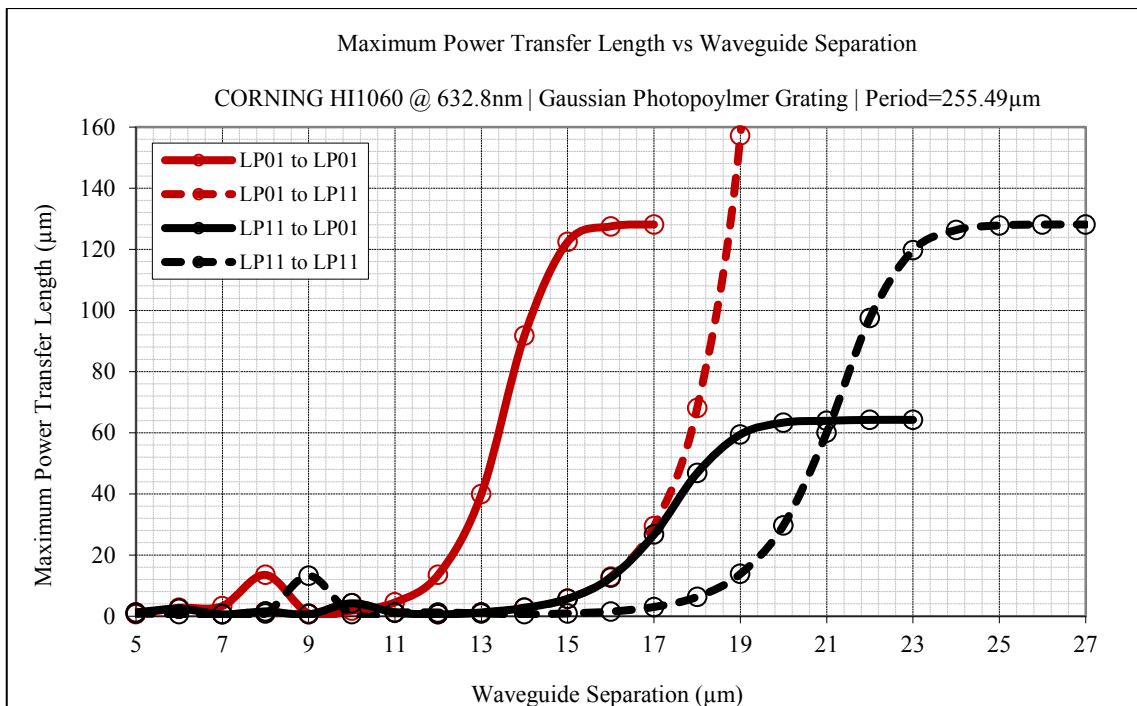


Figure 82. Device lengths necessary to reach the calculated efficiencies w.r.t. waveguide separation with Gaussian gratings for Corning HI1060 at 632.8nm.

4.5. Optimization and Tuning – Final Device at 632.8nm

Taking the results obtained so far as a base for the design, it seems to be the logical move to start the optimization by fixing the waveguide separation, i.e., the distance between the optical fibers. In the above graph showing the coupling efficiencies w.r.t. waveguide separation, red curves represent efficiencies to be minimized and black curves represent vice versa; details are given in the legend. Waveguide separation optimization has been performed as follows:

- In order to ensure the complete cancellation of coupling from input LP₀₁ to output LP₀₁, the distance between the waveguides should be at least 18 μ m.
- In order not to completely lose the power coupled from input LP₁₁ to output modes, the distance between the waveguide should be at most 24 μ m.

Which yields:

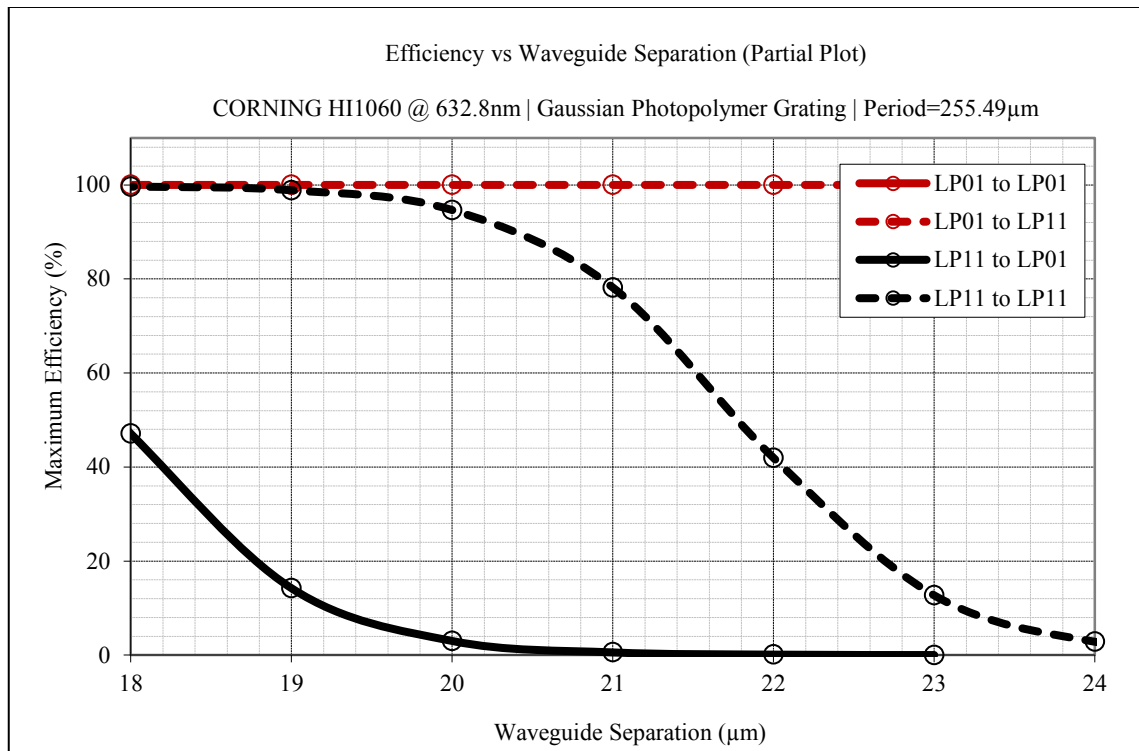


Figure 83. Coupling efficiency with respect to waveguide separation – detail.

At this point, a choice should be made as to whether prioritize output LP₀₁ or output LP₁₁. If the output LP₀₁ is favored, then the waveguide separation should set to around 18 μ m, which may make the selectivity cumbersome. In addition, it can be seen

on the field propagations that the beat length of modes is very short for this configuration; which makes the selectivity/tuning even more critical. So the choice of favoring output LP₁₁ is therefore made.

In order to fix the waveguide distance to enable selective coupling, the complementary part of the efficiency plot, which represents the necessary device lengths needed to reach the calculated efficiencies –which actually is the half beat-length-, should be examined.

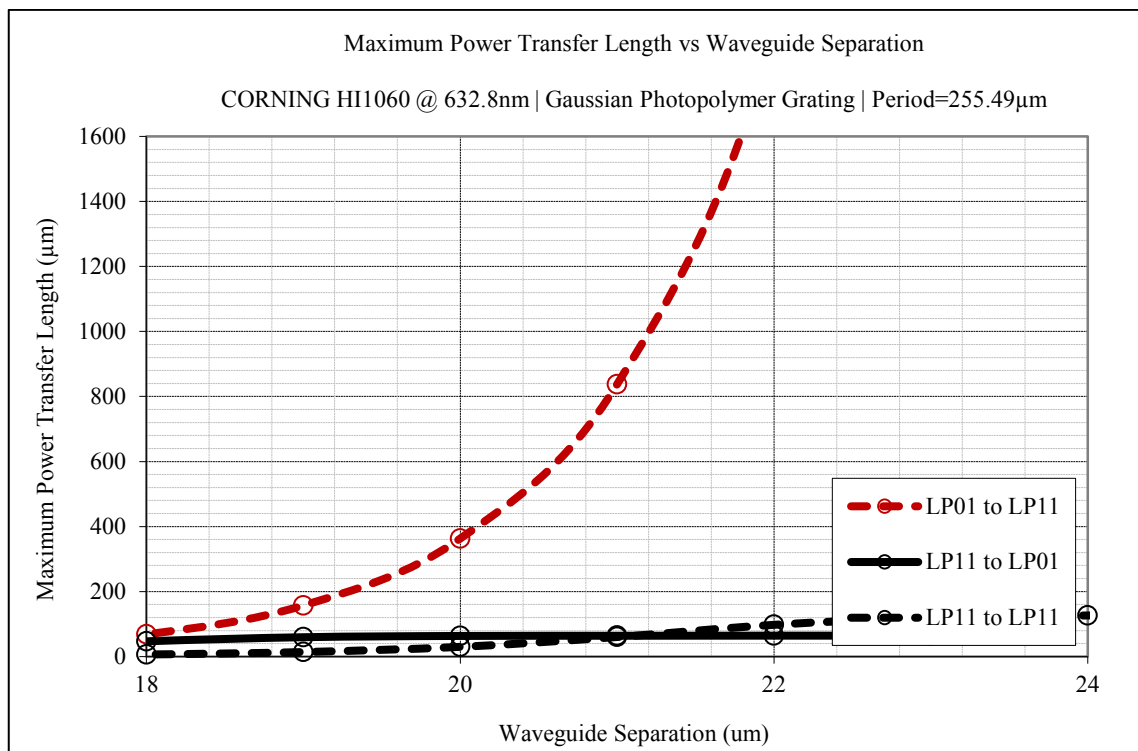


Figure 84. Device lengths necessary to reach the calculated efficiencies – detail

As mentioned above, the beat-length of the mode fields across the waveguides being close to each other causes a problem in selectivity of coupling. Therefore,

- Designated waveguide separation should be as away from the 18μm as possible (which also supports the favoring of output LP₁₁).
- However, going all the way to the 24μm border almost completely zeroes-out the desired mode power (2% coupling efficiency at 24μm) and therefore 24μm waveguide separation is not an option.

In the light of the above conditions, let's look at the mode field propagations at waveguide separation d=22μm:

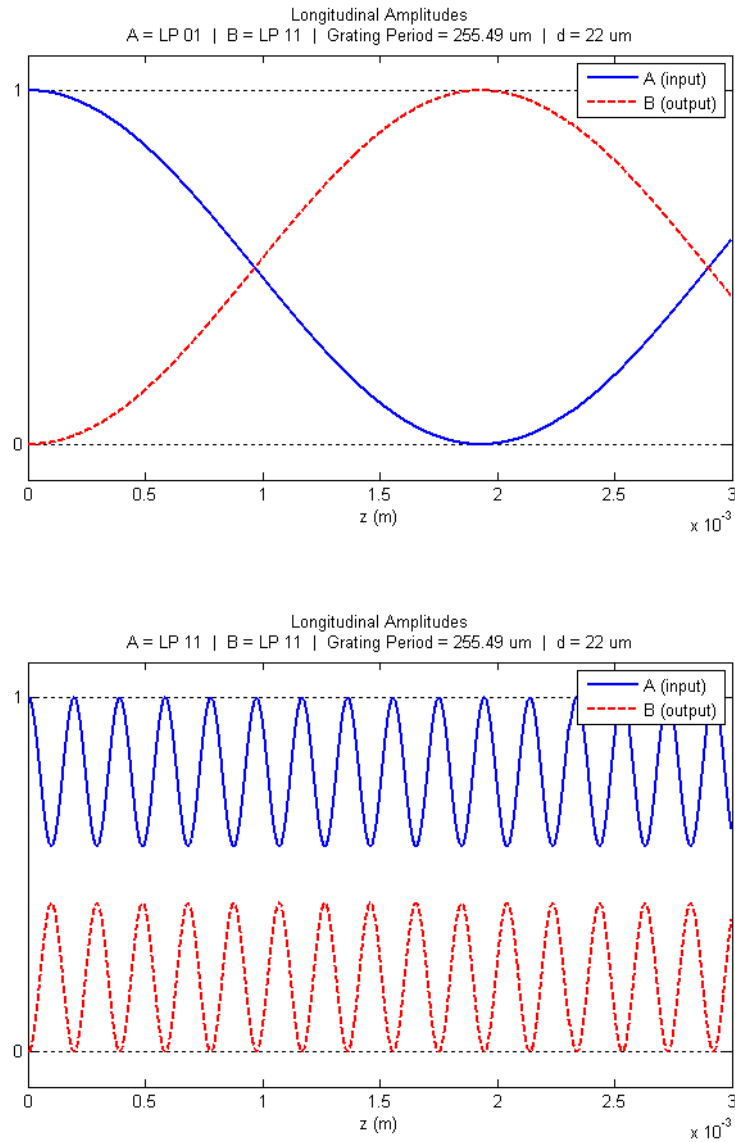


Figure 85. Mode field propagations at waveguide separation of 22 μm

In this setting, the maximum power transfer ratio for LP₀₁-to-LP₁₁ is 100% at a transfer length of 1.932mm, whereas the ratio for LP₁₁-to-LP₁₁ is 41.94% at 97.5 μm , which is not realistic in terms of physical fabrication. In addition, the transfer speed (beat length) of input LP₀₁ is quite rapid and a slower transfer would be favored in order to achieve selectivity via tuning the total device length when potential fabrication tolerances are taken into account. Therefore, the analysis of the mode field propagation at a waveguide separation of 23 μm is performed:

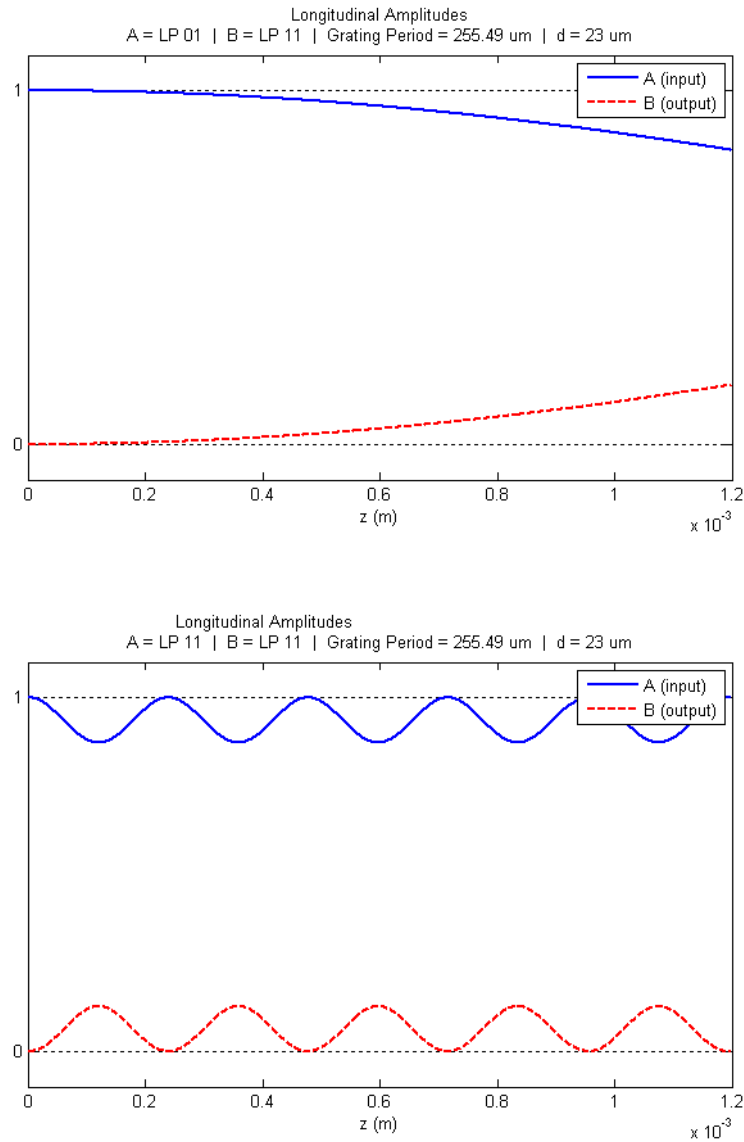


Figure 86. Mode field propagations at waveguide separation of 23μm

In this case, even though the difference between the maximum power transfer ratios of two modes is not high, the slow transfer rate (longer beat length) of LP₀₁-to-LP₁₁ poses an advantage in terms of obtaining mode selectivity by tuning the device length. It should be kept in mind that, as long as it is within the physical fabrication capability range, the longer the device, the more ease in realization.

In the above simulation, device length is set to 1.2mm and it can be clearly seen that this is not an advantageous device length in terms of LP₁₁-to-LP₁₁ coupling, in that the beat period coincides with the device output, causing the exact opposite of the desired outcome. A careful and more precise study yields the optimum device length of L=0.8354mm, which can be seen below:

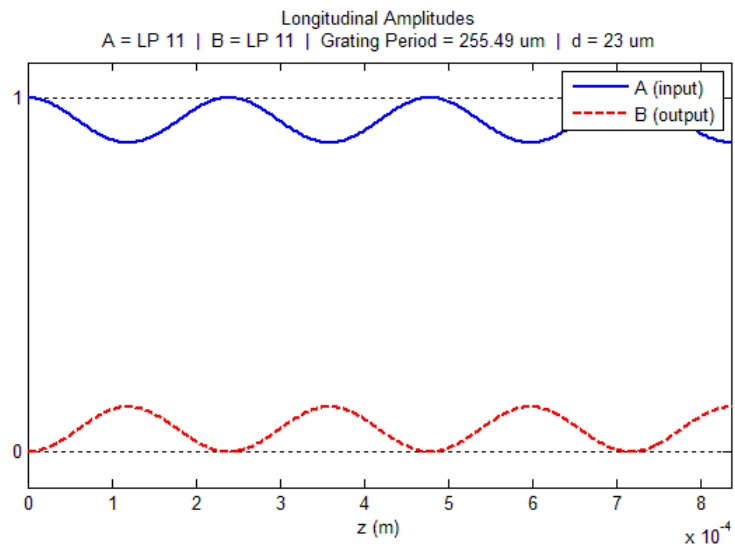
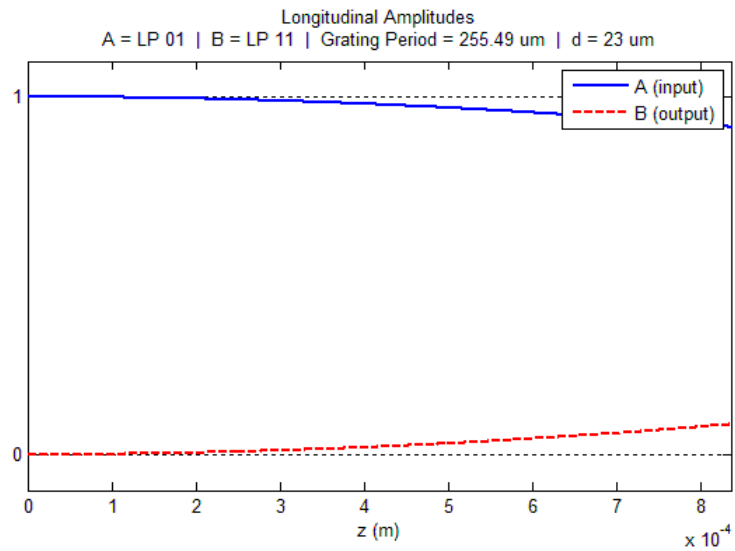


Figure 87. Mode field propagations at waveguide separation of $23\mu\text{m}$ and device length of 0.8354mm

This constitutes the final form of the designed device, where the specifications are presented in the below table:

Table 11. Specifications of the final device at 632.8nm

Input fiber	Type	Corning HI1060
	Core index	1.4572
	Clad index	1.4507
	Core radius	2.65 μm
Signal wavelength		632.8nm
Supported modes		LP ₀₁ , LP ₁₁
Waveguide separation		23 μm
Device length		0.83mm
Calculated coupling efficiency	LP ₀₁ to LP ₀₁	0.00%
	LP ₀₁ to LP ₁₁	8.44%
	LP ₁₁ to LP ₀₁	0.02%
	LP ₁₁ to LP ₁₁	12.70%

4.6. Grating Period Dependence of Coupling Efficiency

Although the grating period has been determined using the phase matching condition, further study was also performed to investigate the effect of the grating period on coupling efficiency. Taking the final device properties determined in the previous part as the starting point and setting the grating period as the new optimization parameter, the coupling efficiencies between each and every mode in the structure for grating period varying between 50 μm and 500 μm are obtained as follows:

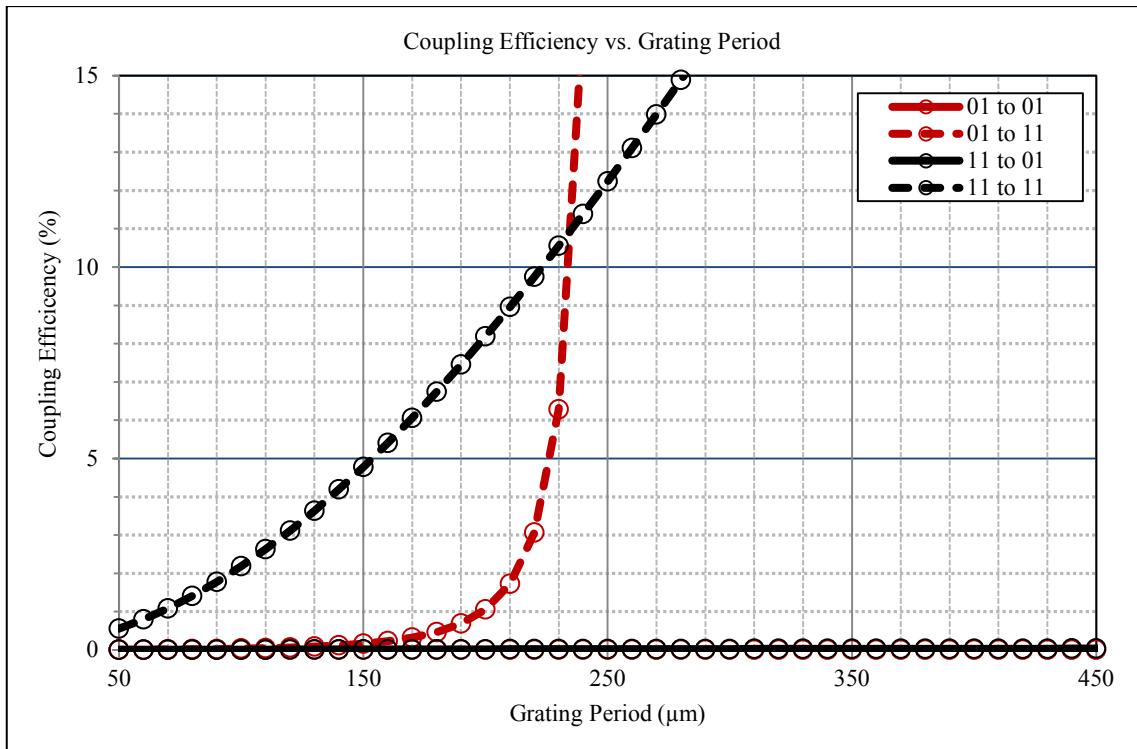


Figure 88. Coupling efficiency with respect to grating period for all modes

Analyzing the above plot, it must be kept in mind that previous optimization process involved setting the device length according to the appropriate beat length of the target mode. This means that the efficiency characteristics seen in the above plot contain both the maximum coupling and the beat length simultaneously. Therefore it would not be accurate to judge only by the high LP_{11} -to- LP_{11} coupling calculated for low periods alone.

Recalling the process during the optimization, even though the target coupling efficiency was seen to be high in the plots, a selective coupling was not possible due to the beat lengths of the modes. A similar case applies here as well. Therefore, the area which must be focused on is the vicinity of $255\mu\text{m}$ grating period, where the phase matching condition in Yariv and Yeh's theoretical study is satisfied (Yariv and Yeh, 2006). When we study this area closer, we get:

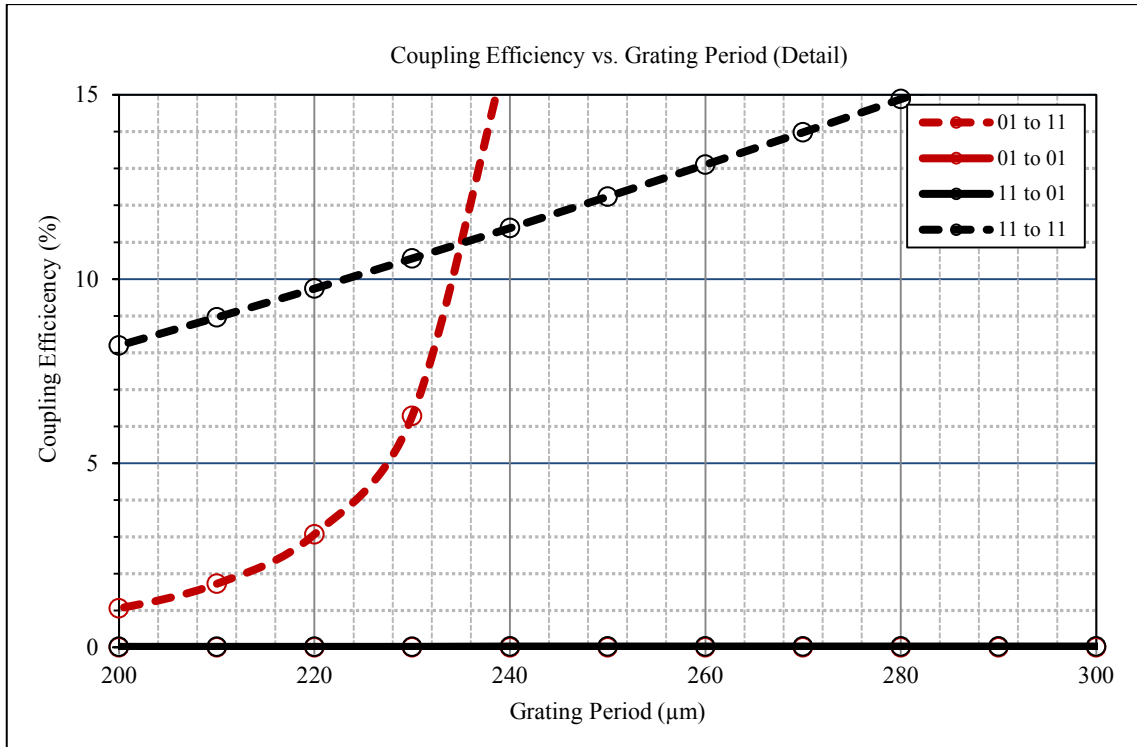


Figure 89. Coupling efficiency with respect to grating period for all modes – detail

As explained above, phase matching condition dictating a grating period of $255\mu\text{m}$ maximizes input LP_{11} to output LP_{01} coupling efficiency, however mathematically and due to device symmetry it also maximizes input LP_{01} to output LP_{11} coupling efficiency. For the current state of device configuration, the final step of previous optimization involving tuning of the device length effectively minimizes the efficiency of the power coupled from LP_{01} mode and leads to the selective coupling of modes.

4.7. Dispersion Relation

The dispersion relation, namely, ω vs. β relation of the grating structure was also studied. Following the studies of (Saleh and Teich, 2007) and (Sun, et.al, 1997) and calculating according to the properties of the designed device, when the used fiber is excited at 632.8nm wavelength the ω vs. β relation is obtained as presented below:

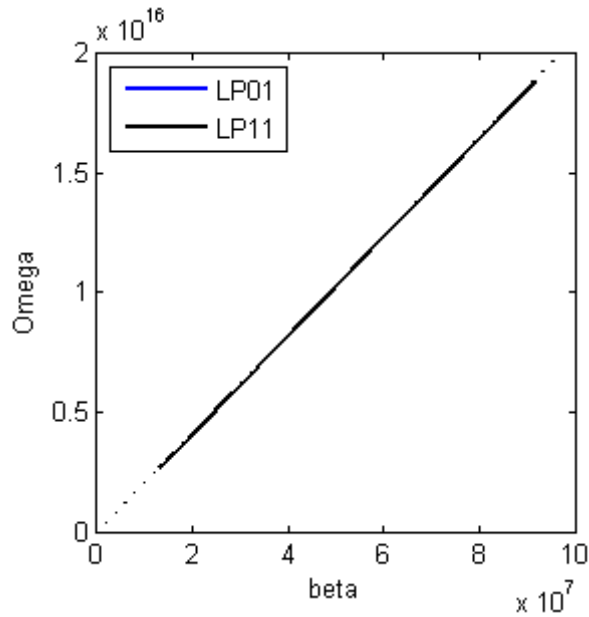


Figure 90. ω vs. β relation when the used fiber is excited at 632.8nm wavelength

As can be seen above, the so-called “light lines” according to Saleh’s terminology, i.e., physical limits of guided light propagation, are very close to the actual mode lines due to the scale of the obtained curves. Hence, an up scaling of the plot was applied which allowed observing the modes:

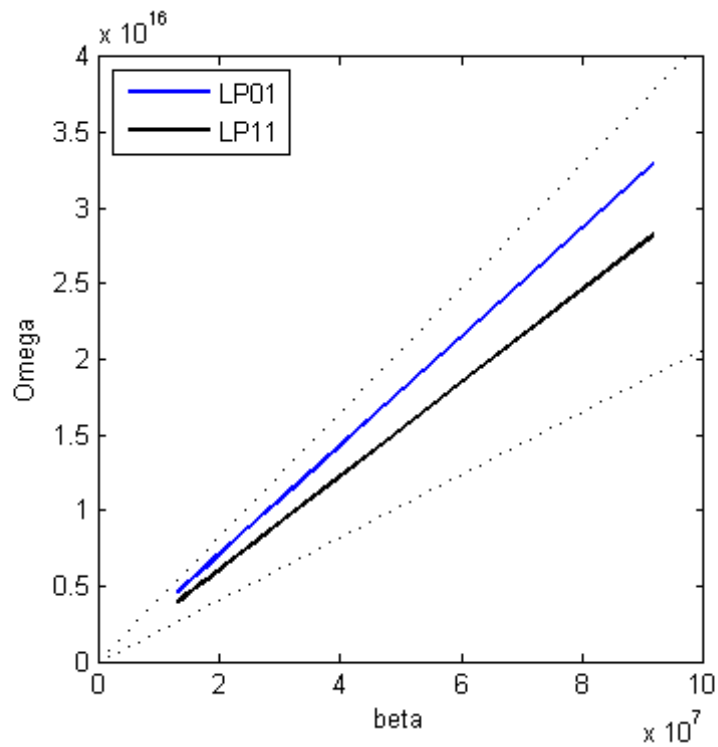


Figure 91. ω vs. β relation when the fiber is excited at 632.8nm – scaled

The same characteristics are also obtained for the fiber with the perturbation caused by the grating taken into account:

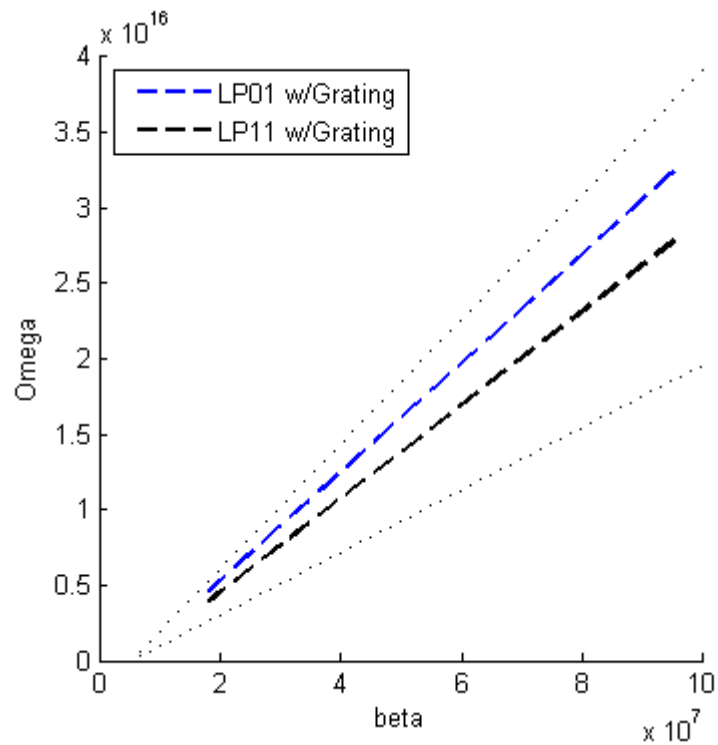


Figure 92. ω vs. β relation for the fiber with grating when excited at 632.8nm wavelength – scaled

When the dispersion characteristics of the fiber with the effect of the grating are included in the plot, the plots are obtained very close to distinguish, similarly due to the actual scale of the curves.

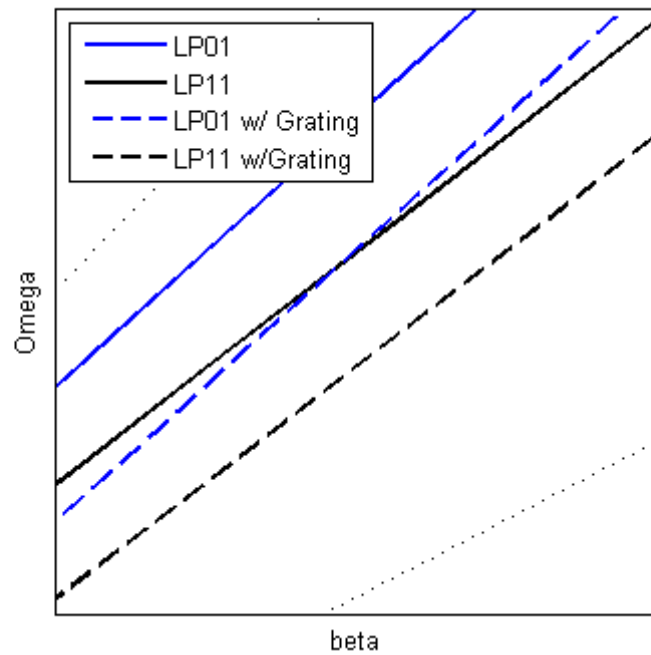


Figure 93. Intersection of ω vs. β relation for the bare fiber and grating induced fiber – scaled

Therefore, in order to distinguish the plots and find the exact point of intersection, a detailed non-scaled plot is obtained. According to the detailed intersection investigation, the dispersion characteristics of LP₀₁ mode of the native fiber intersects that of the grating induced fiber's LP₁₁ mode at $\beta=1.4422552 \times 10^7$, which is also equal to the propagation constant of the LP₁₁ mode of the native fiber. This result is in fact the outcome expected to get from this investigation, confirming the design obtained using the theoretical and simulation studies to be accurate.

4.8. Wavelength Dependence of Coupling Efficiency

This particular study was performed to anticipate the response of the device to deviations in the output wavelength that the 632.8nm laser may exhibit. The results are presented in the following figure.

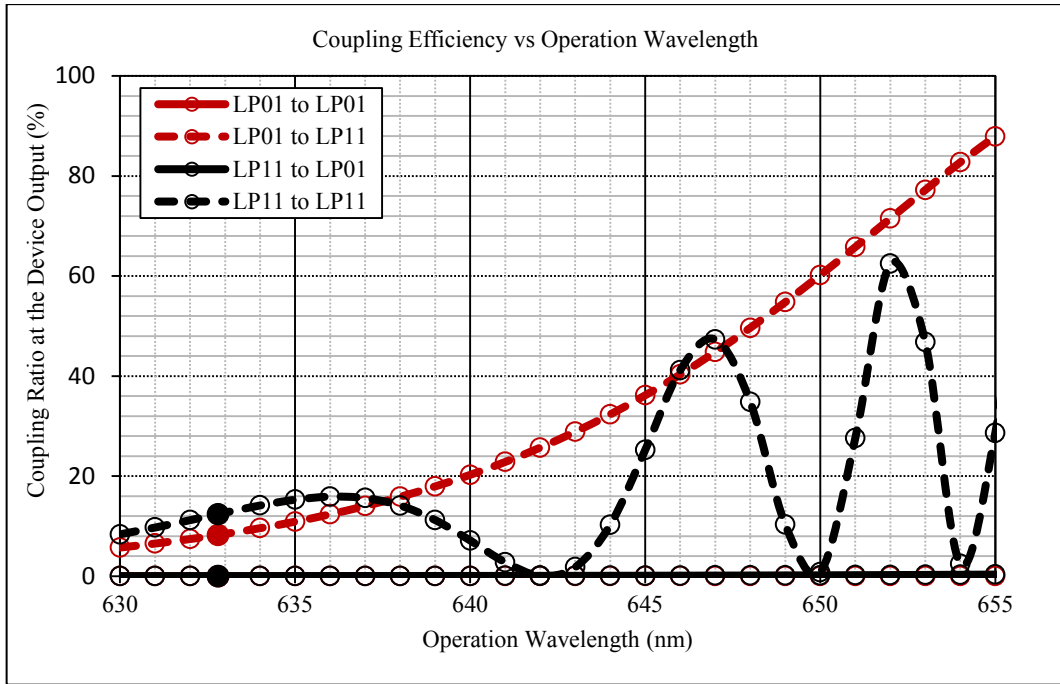


Figure 94. Operation wavelength dependence of 632.8nm device

Results show that the difference of desired and undesired coupling efficiencies is located at a local maximum for the operation wavelength of 632.8nm, as the theoretical results suggest.

Following these calculations, to utilize a second laser source in the experimental studies, namely, the 852nm laser with ± 1 nm tunability, a new device was designed for operation at 852nm wavelength. The studies regarding this device are presented in the following sections.

4.9. Gaussian Grating – Corning HI1060 Optical Fiber at 852nm

For the 852nm device, a similar methodology was used as in the design of the previous 632.8nm device. The fiber modes supported by Corning HI1060 optical fiber at the laser wavelength of 852nm were calculated. Using the fiber specifications presented in the previous sections, calculations indicate that the optical fiber supports 2 modes (LP_{01} and LP_{11}) when excited at 852nm wavelength:

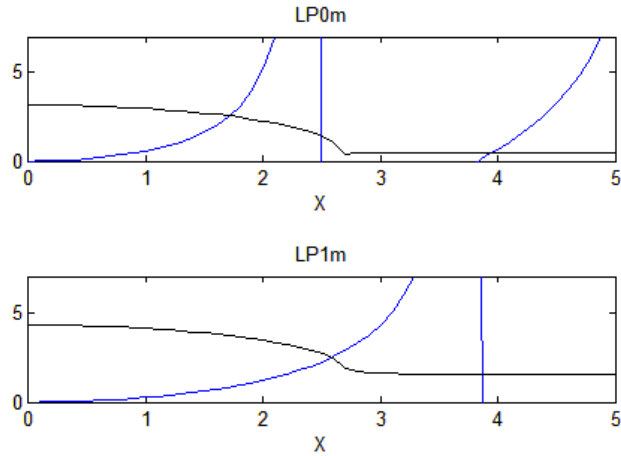


Figure 95. Modes supported by Corning HI1060 fiber excited at 852nm wavelength

Propagation constants of the supported modes are calculated as:

- $\beta_{01} = 1.072689136168106 \times 10^7$
- $\beta_{11} = 1.070206616371683 \times 10^7$

Based on these values, the fields of the fiber modes supported by the input and output fibers were obtained:

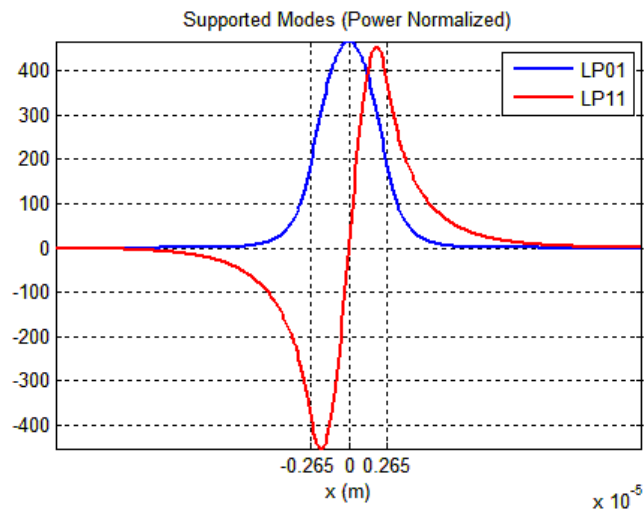


Figure 96. Modes supported by the input and output fibers

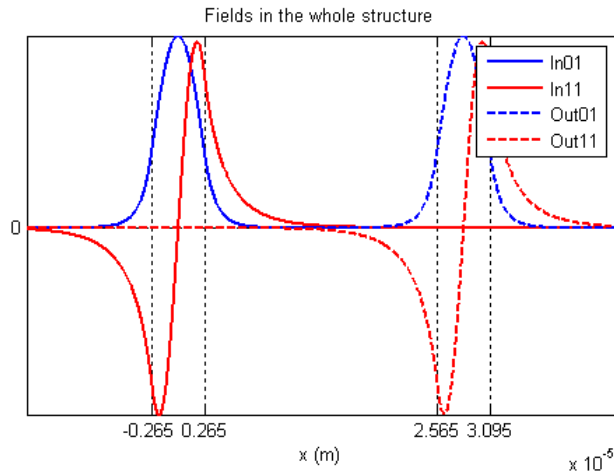


Figure 97. Modes supported by the whole structure

As in the previous design procedures, waveguide distance was selected as the initial optimization parameter to achieve maximum coupling between the second input mode (LP₁₁) and fundamental output mode (LP₀₁), while minimizing the coupling from the input fundamental mode (LP₀₁). The grating period meeting the phase matching condition between input second mode (LP₁₁) and output fundamental mode (LP₀₁) is calculated as **253.09 μ m**. Using this condition, the results obtained are presented below:

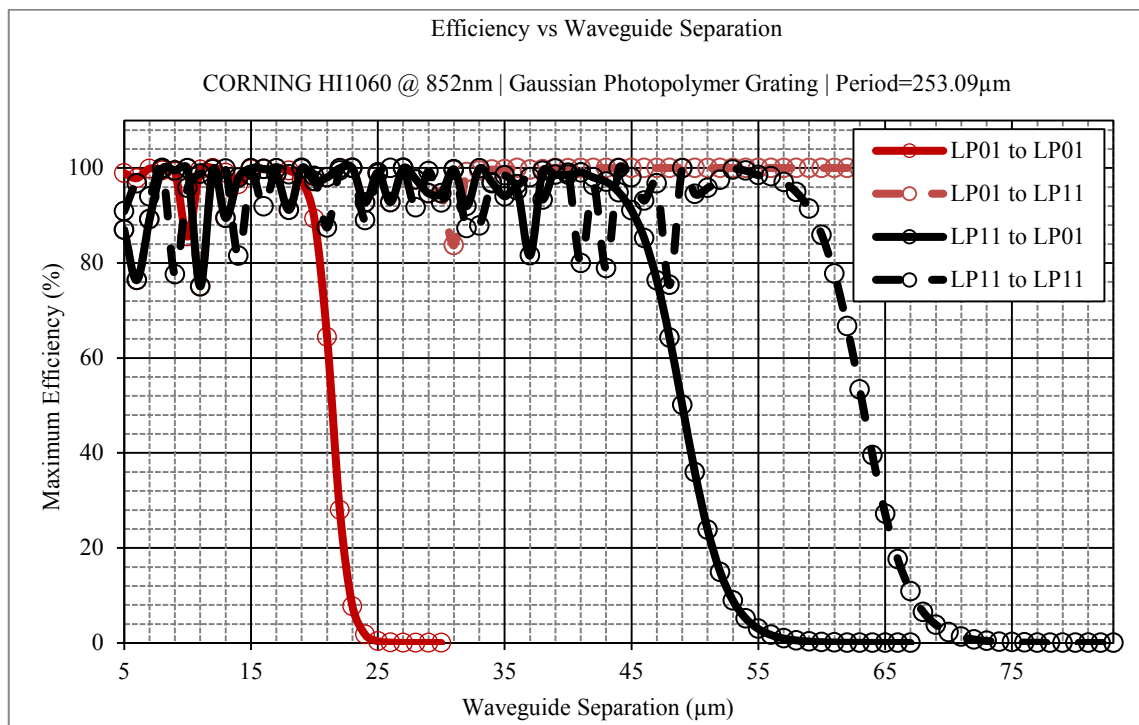


Figure 98. Coupling efficiency with respect to waveguide separation with Gaussian gratings for Corning HI1060 excited at 852nm.

Related necessary device lengths to reach the maximum efficiencies are calculated as given below:

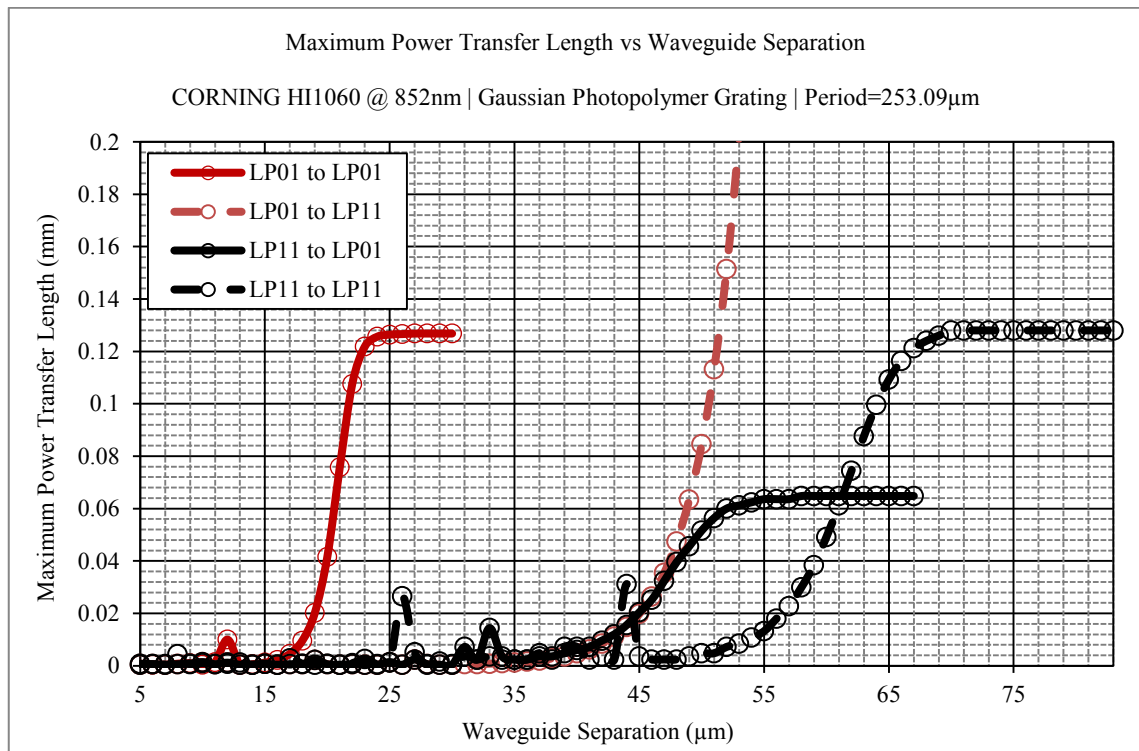


Figure 99. Device lengths necessary to reach the calculated efficiencies w.r.t. waveguide separation with Gaussian gratings for Corning HI1060 excited at 852nm

4.9.1. Optimization and Tuning – Final Device at 852nm

In the tuning and finalization of the 852nm device, the same approach as that of the 632.8nm device was employed. Accordingly, the waveguide separation, i.e., the distance between the fibers was selected as the first optimization parameter. That said, taking the waveguide separation as the first optimization parameter, detailed analysis of the 51 μm – 59 μm region in Figure 98 leads the following:

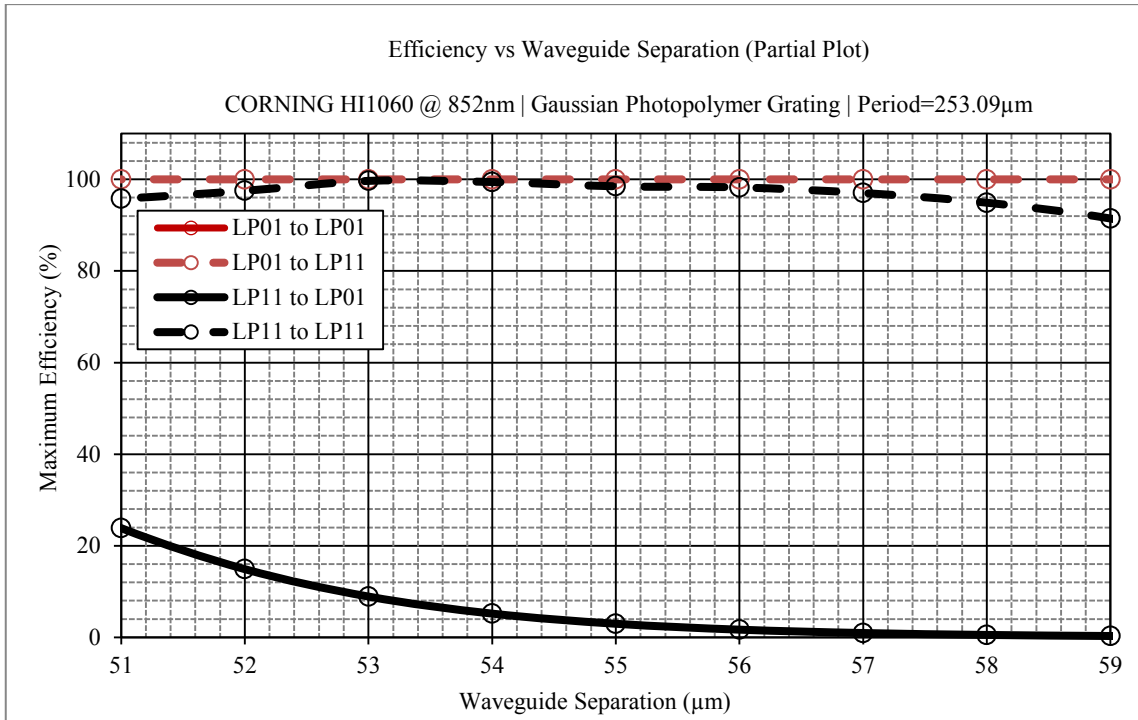


Figure 100. Coupling efficiency with respect to waveguide separation – detail.

Analysis of the device lengths necessary to reach the calculated efficiencies above for the same region yields:

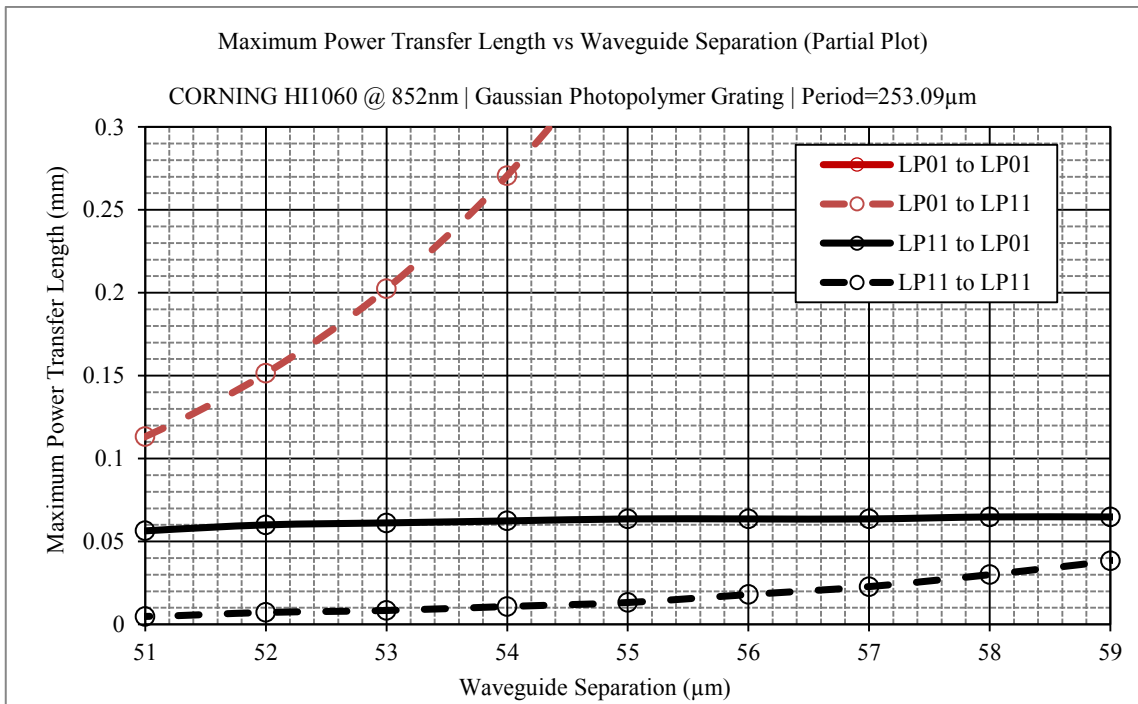


Figure 101. Device lengths necessary to reach the calculated efficiencies – detail

Based on the results obtained above, it was decided to set the waveguide separation to be $55\mu\text{m}$ and the first optimization parameter has been fixed. Moving forward from this point, the next optimization parameter was selected as the device length. In order to be able to fix the device length, the beat lengths of fiber mode fields as they propagate through the device were calculated:

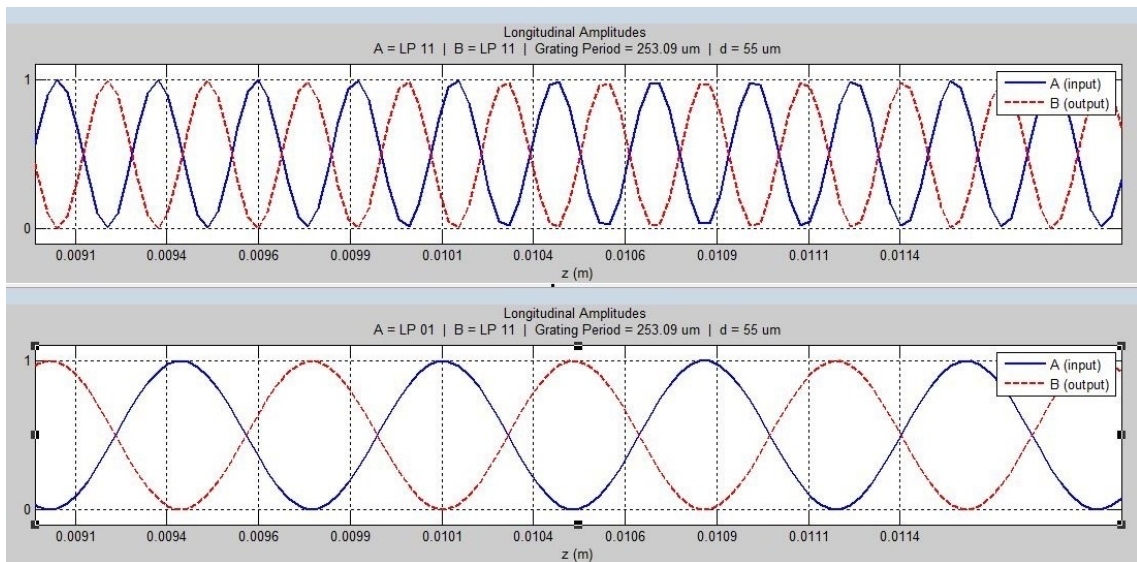


Figure 102. Mode field propagations at waveguide separation of $55\mu\text{m}$

In this configuration, bearing in mind the manufacturability and taking into account both the beat lengths of the modes and the device lengths necessary to achieve the maximum coupling efficiencies, the device length was set as 10.88mm , leading to exactly 44 direct-written grating steps; this yields the following specifications for the final device:

Table 12. Specifications of the final device at 852nm

Input fiber	Type	Corning HI1060
	Core index	1.4572
	Clad index	1.4507
	Core radius	2.65 μ m
Signal wavelength		852nm
Supported modes		LP ₀₁ , LP ₁₁
Waveguide separation		55 μ m
Device length		10.88mm
Calculated coupling efficiency	LP ₀₁ to LP ₀₁	0.00%
	LP ₀₁ to LP ₁₁	2.08%
	LP ₁₁ to LP ₀₁	1.99%
	LP ₁₁ to LP ₁₁	68.64%

This device designed to operate at 852nm theoretically delivers 68% coupling efficiency from the input LP₁₁ mode with only 2% from the input LP₀₁ mode.

4.9.2. Dispersion Relation for the 852nm Device

In order to verify the design of the 852nm device theoretically, the dispersion relation study was also performed for this device as well. Accordingly, the dispersion characteristics, namely, ω vs. β relation for the device designed with Corning HI1060 fiber excited at 852nm were calculated, in the same methodology as for the previous 632.8nm device:

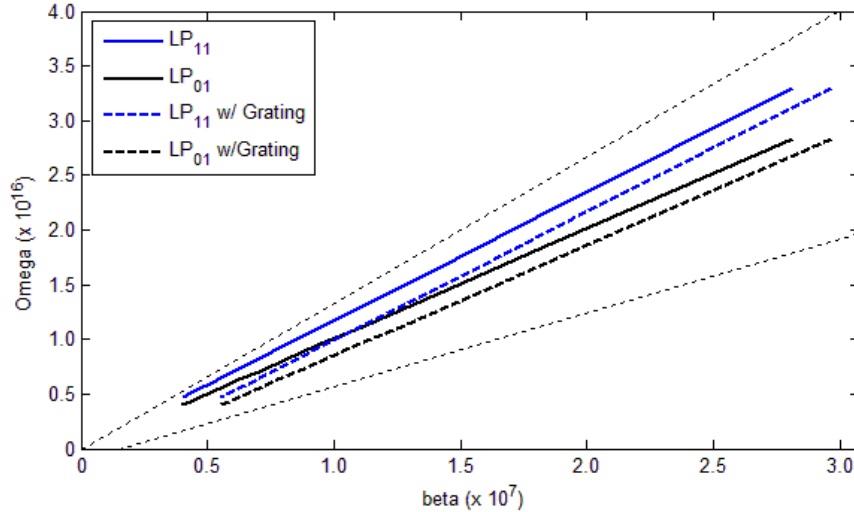


Figure 103. ω vs. β relation for the bare fiber and fiber with grating when excited with 852nm laser – scaled.

The results show that the dispersion relation of LP₀₁ mode of the native fiber intersects that of the grating induced fiber's LP₁₁ mode at $\beta=1.4422552 \times 10^7$, which is also equal to the propagation constant of the LP₁₁ mode of the native fiber and therefore verifies the device design.

4.10. Wavelength and Fabrication Tolerances of Coupling Efficiency

The laser source available in the laboratory which would be employed in the experimental studies of the above device is a ± 1 nm tunable source around the center wavelength of 852nm. Due to the tunability of the laser, wavelength dependence of coupling efficiency of the device was investigated to evaluate whether it would be possible to exploit this property of the source. Thus, the coupling efficiency of the final device, with specifications presented in Table 12, was calculated with respect to variations in operation wavelength. The results are presented below:

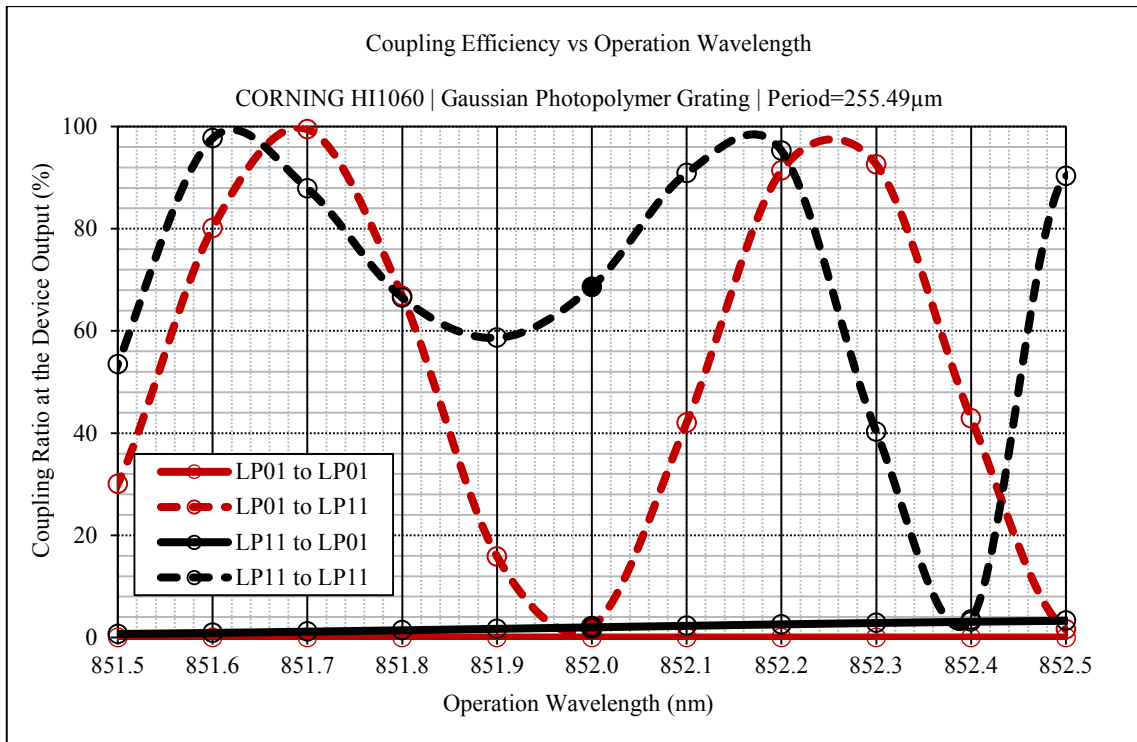


Figure 104. Operation wavelength dependence of coupling efficiency

Furthermore, with the fabrication experience of the 632.8nm device, certain additional simulations were performed regarding the performance of the 852nm device under unideal fabrication conditions. In other words, taking into account potential tolerances in device fabrication, a preliminary analysis of device performance was executed to cover the possible outcomes of an imperfect fabrication.

The variation of the coupling efficiency of the final device with respect to waveguide separation is presented in the next figure.

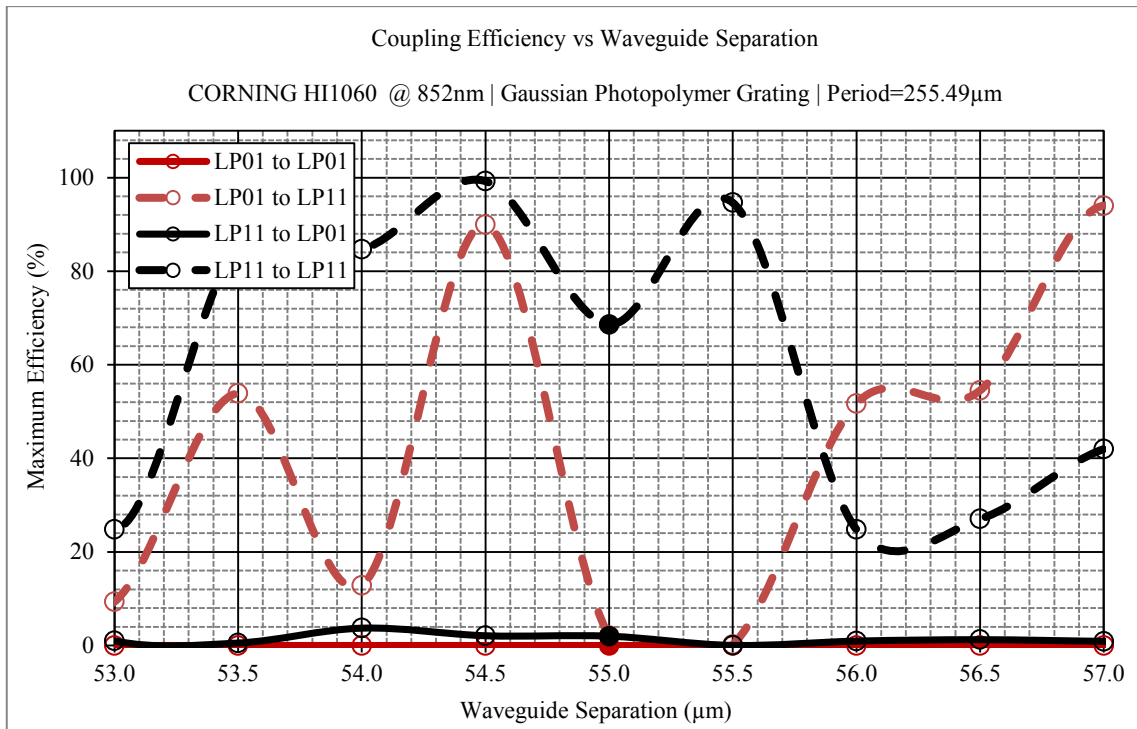


Figure 105. Waveguide separation dependence of coupling efficiency

Moreover, the variation of the coupling efficiency of the final device with respect to device length is presented in the next figure.

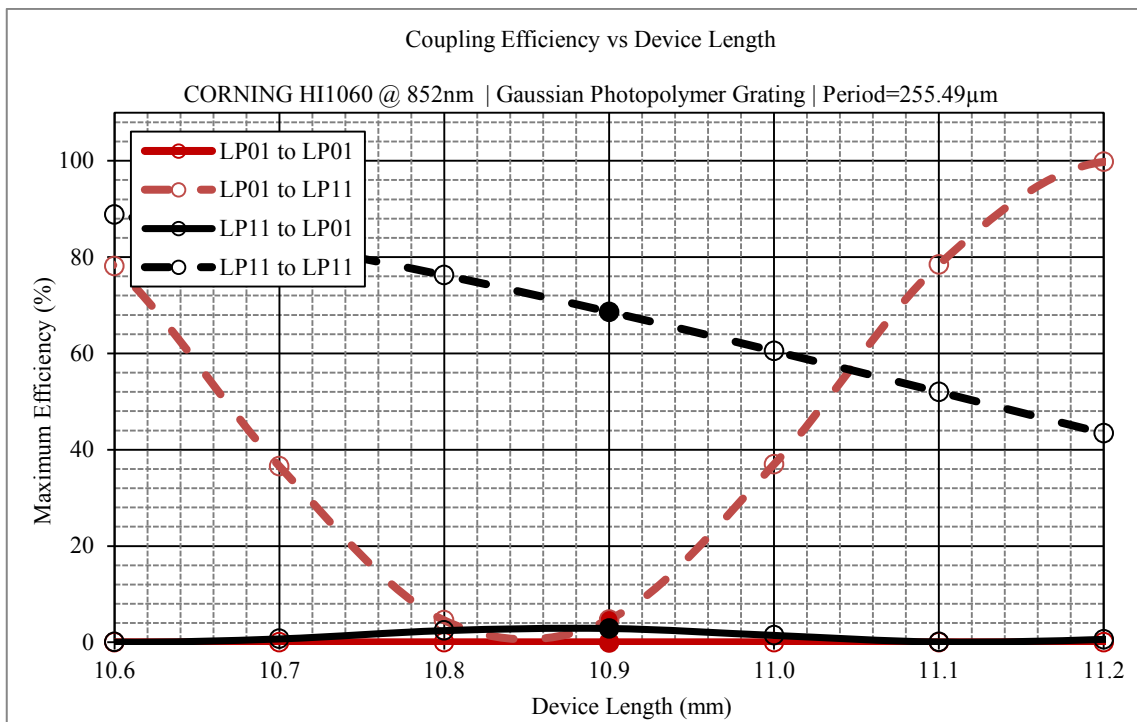


Figure 106. Device length dependence of coupling efficiency

CHAPTER 5

EXPERIMENTAL REALIZATION

5.1. In-House D-Fiber Preparation

In the initial stages of the study, the grating coupler had been planned on being assembled on prefabricated complete D-Fibers. While there was no problem in the fiber supply from the sole manufacturer of fiber in the previous years, as in the initial stages of the project, the US-based company has reported that the fibers were no longer available for the countries outside US due to national security reasons. Thereupon, alternative methods of obtaining the required fiber structure, which could involve manufacturing the D-Fiber using the facilities and in-house equipment, were investigated.

One method for obtaining the D-Fiber consists of choosing an appropriate standard fiber and etching one side of the fiber in order to obtain a planar surface similar to that of the D-Fiber. The fiber used in this procedure should support both single-mode and two-mode operation. Lab facilities houses an 808nm CW microchip laser, a 632.8nm He-Ne laser, 543nm He-Ne laser and a 852nm diode laser with ± 1 nm tunability. Thus, it was concluded that a fiber which supports device fabrication for both 632.8nm and 852nm operation wavelength would be an appropriate choice for the study. Given these requirements, a suitable product available in the market is the 780-HP fiber produced by Nufern (Source: Nufern, 2011):

Table 13. Specifications of Nufern 780-HP optical fiber

Nufern 780-HP	Value	Unit
Nominal operating wavelength	880 ± 100	nm
Cut-off wavelength	730 ± 30	nm
Attenuation	≤ 4.0	dB/km
Cladding diameter	125 ± 1	μm
Core diameter	4.4	μm
Coating diameter	245 ± 15	μm

The first method selected for D-Fiber manufacturing is chemical etching using HF (hydrofluoric acid) solution. Accordingly, fiber jacket on one side of standard fiber was removed using razor blades and thin grinding papers (mechanical etch). Then, HF solutions at varying concentrations were applied to the partially-exposed fiber cladding regions to etch the fiber chemically:

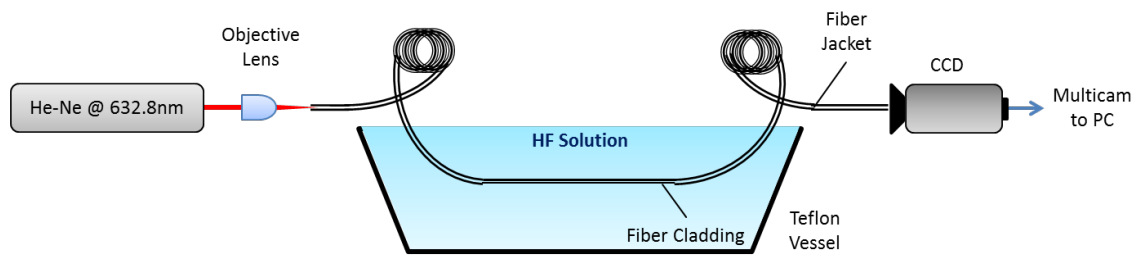


Figure 107. Chemical etch of standard fibers for D-Fiber manufacturing

30% and 48% aqueous HF solutions were used in chemical etch processes. During the chemical etch, the variation of the fiber properties and the occurrence of the chemical process was confirmed by launching the fiber with 632.8nm He-Ne laser and observing the output at the fiber end using a CCD sensor. The chemical etching process was also applied to a very short length of D-Fiber available in the lab at the time of the experiment (see Section 5.2).

An example of the laser output recorded during the chemical etch procedure for the standard fiber is given below. It was determined that the power measurements was in good agreement with the literature (Quero, et.al, 2010), as given in the figure below the measured data.

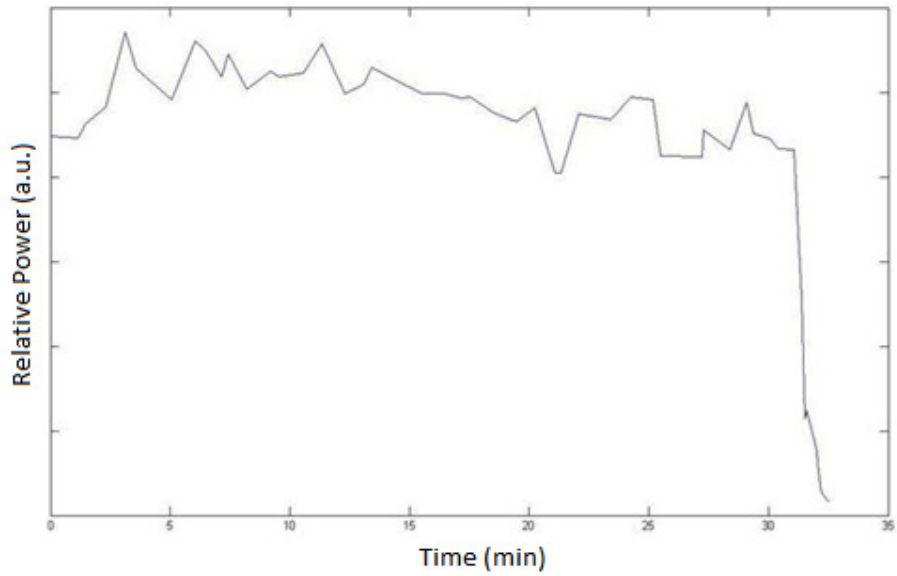


Figure 108. Output power throughout etching for standard fiber

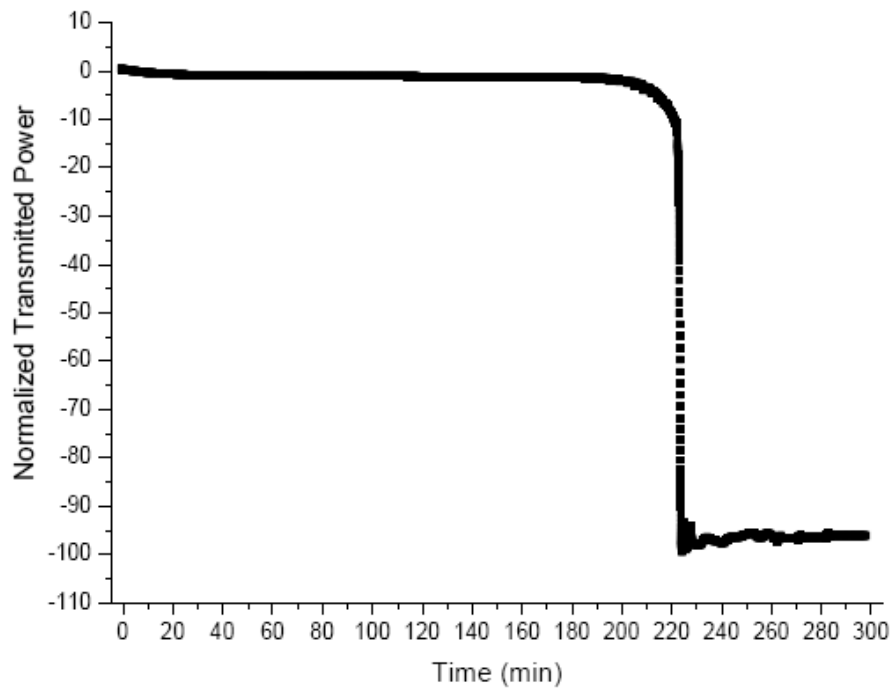


Figure 109. Transmitted power versus the etching time
(Source: Quero, et.al, 2010)

Fibers underwent chemical etching were examined using scanning electron microscope (SEM) and the results obtained are given below. It should be noted that the fibers examined under the SEM had to be cut in order to fit into the microscope apparatus and therefore the fiber ends seen in some of the images are not related to the chemical etch process:

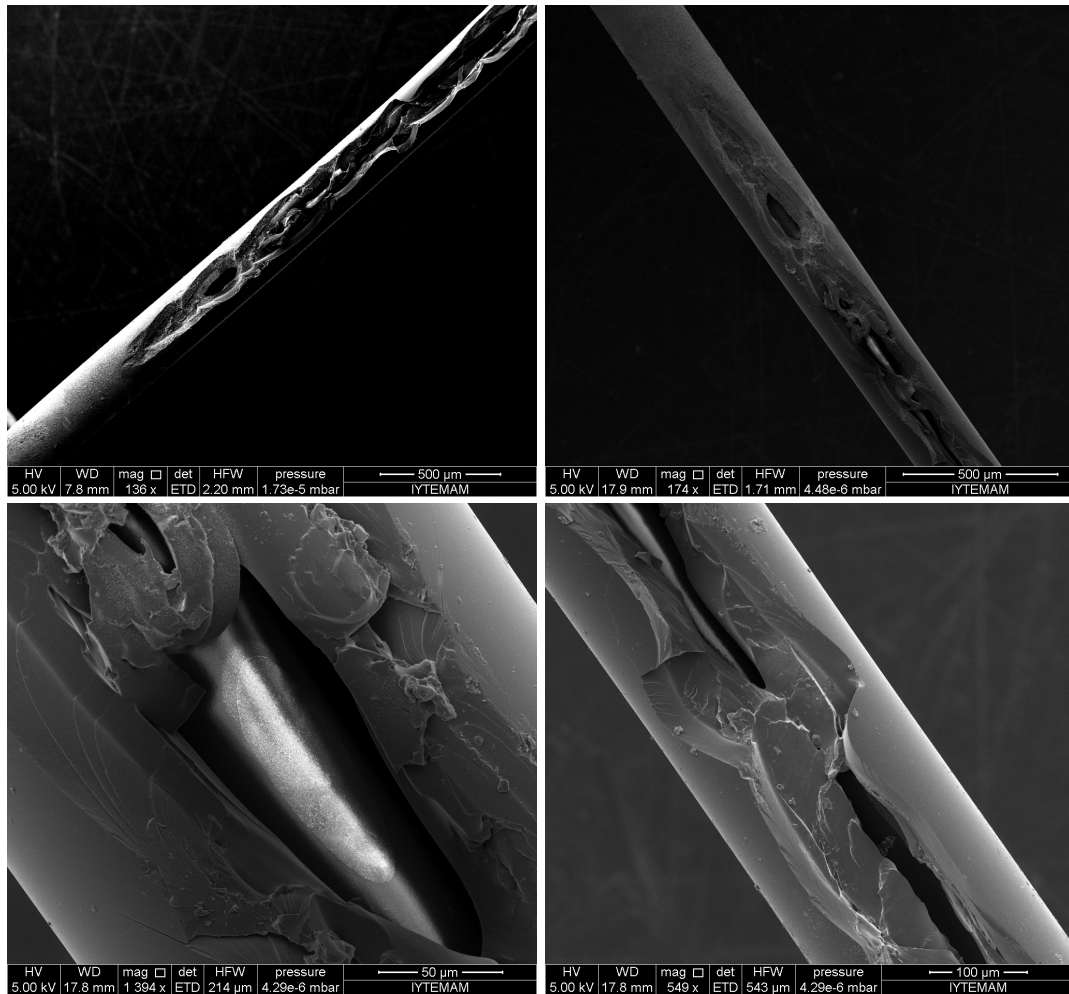


Figure 110. Chemically etched standard fibers

Deformities due to the mechanical etch of the fiber jacket layer can be seen in the above images. These irregularities cause non-uniform diffusion of the etch solution into the fiber jacket and lead to an inhomogeneous variation of the fiber radius throughout the processed region.

It can also be seen that the etching solution dissolves the fiber core and cladding regions in a higher rate than the fiber jacket. As a result, cavities are formed between the jacket and the cladding and the etching solution diffuses into and starts dissolving the undesired surfaces of the structure, i.e., the opposite side of the fiber.

In conclusion of these studies, manufacturing D-Fibers by chemical etching standard fibers were unsuccessful. The results point to the unfeasibility of obtaining usable results using chemical methods.

5.2. D-Fiber HF Etching

The necessity of chemical etching of D-Fibers arises from the need to thin-out the fiber in order to decrease the distance between the outer medium and the fiber core. The components to be fabricated on the flat side of the fiber should be accessible by the evanescent tail of the mode fields propagating in the core.

Chemical etching of standard optical fibers using Hydrofluoric Acid (HF) was presented in the previous section. As for the chemical etching of D-Fibers, the experimental setup was modified and improved prior to these studies.

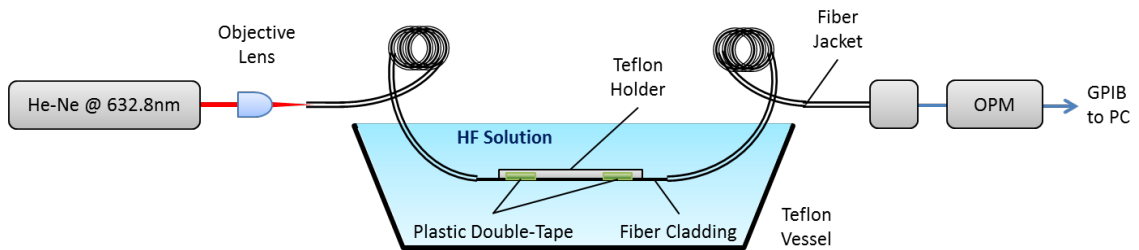


Figure 111. Setup used for HF etching of D-Fibers

First of all, the measurement setup for recording the output of the fiber have been improved; instead of visual observation of the laser output via CCD camera, fiber outputs were coupled into the optical powermeter and the acquired values were recorded and plotted in real-time via the PC running MATLAB software (see Figure 111 and Figure 112).

The upgraded recording/observation setup has proven to be better in resolution in terms of the output power and also in time scales, due to the real-time display. New measurements also enable zooming in time and power axes, allowing for making use of the resolution of the powermeter and sampling rate.

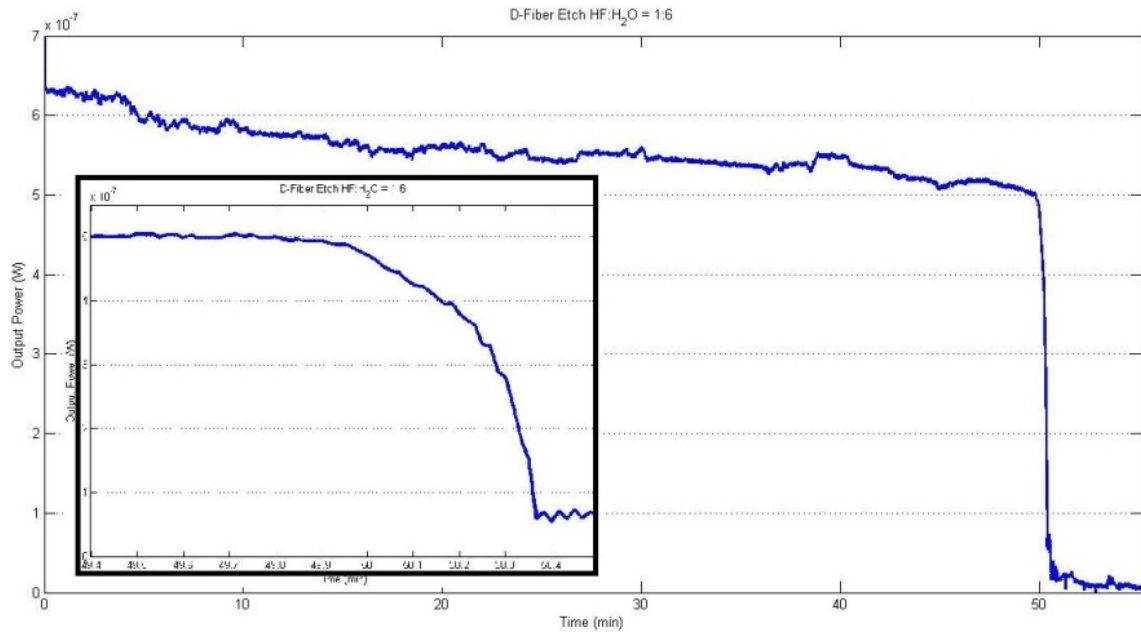


Figure 112. Measurement of the output power throughout HF etching of D-Fiber – updated system, real-time data

The dilution rate of the HF solution used in the process was also changed from 48% to 14%, or in other words, the HF was diluted using pure deionized water (>99.9%) to yield the ratio HF:H₂O = 1:6. With this adjustment, the etching rate of the fiber was slowed down to a more controllable level, in that the problems of being unable to stop the chemical etching reaction were evaded. The reaction takes place yet fast enough so that the desired level of thinning is attained without the reaction time going over to the order of hours. In addition to the HF concentration, the amount of water used to mechanically stop the reaction was increased dramatically. With the current procedure, DI water in the order of few liters is employed in order to be able to stop the etching reaction.

Numerous etching experiments were performed, during which the laser output was observed and recorded. Later, the etched fiber samples were inspected by SEM analysis and both the effects of etching and inherent properties of the fibers were studied.

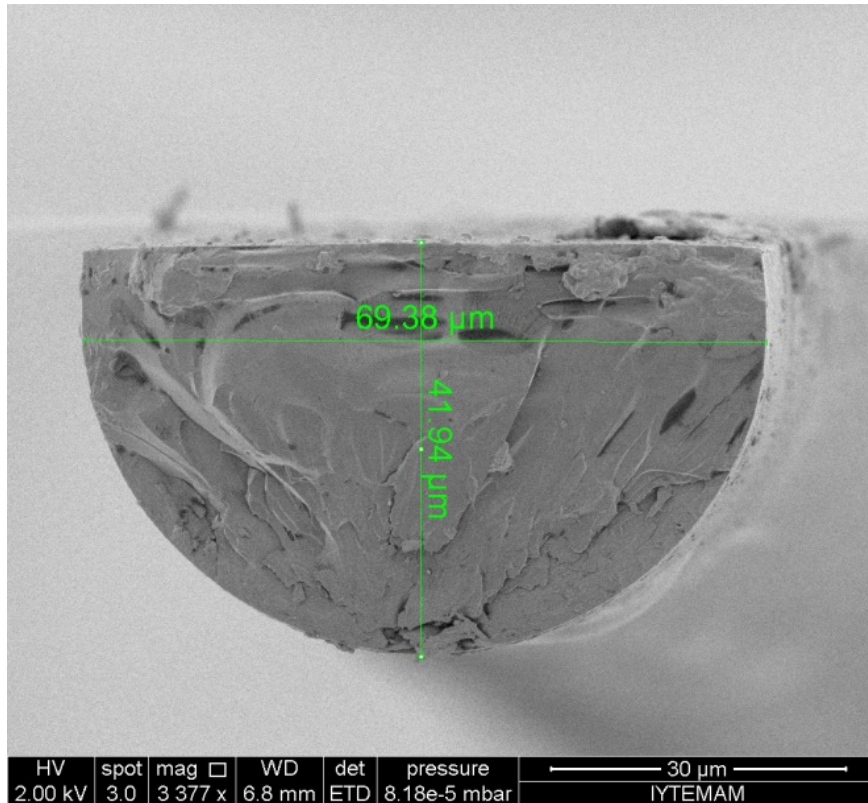


Figure 113. SEM analysis of D-Fiber etched with HF:H₂O=1:6 for 38 min

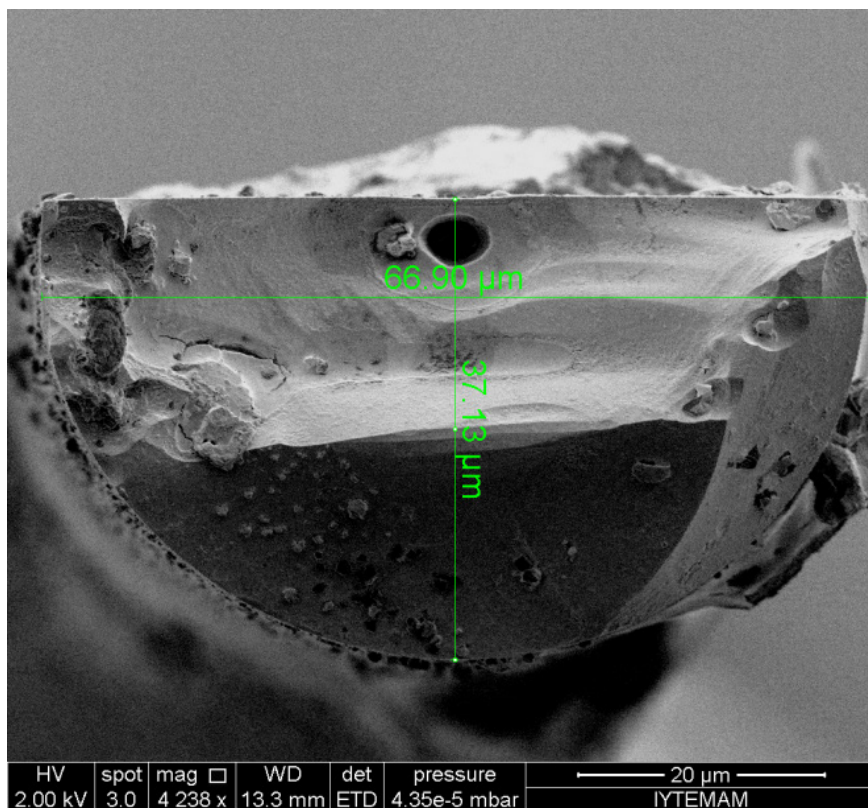


Figure 114. SEM analysis of D-Fiber etched with HF:H₂O=1:6 for 48 min

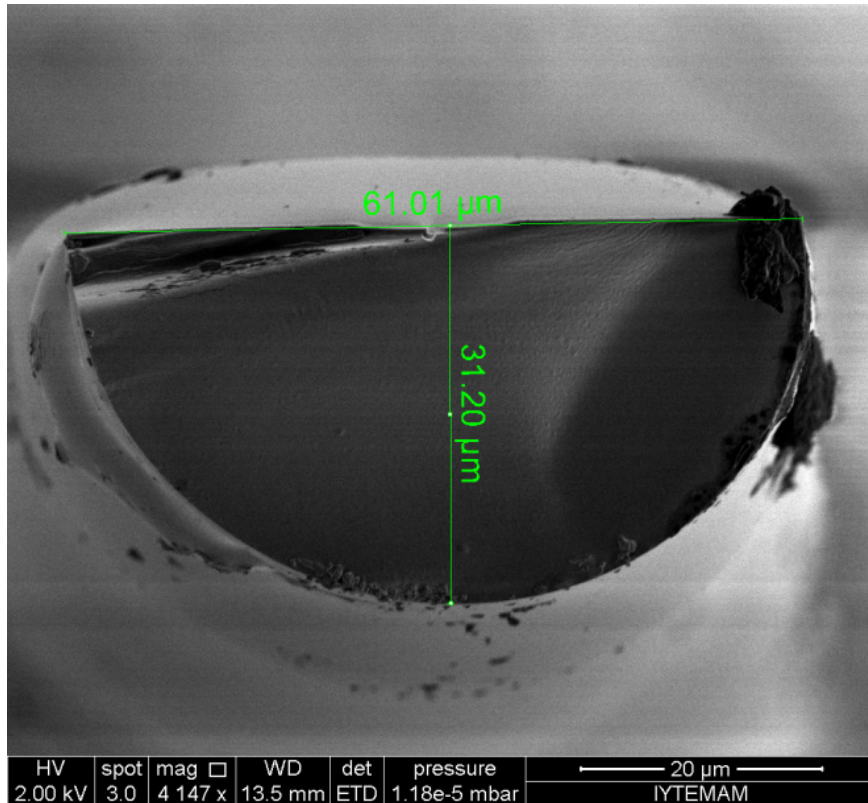


Figure 115. SEM analysis of D-Fiber etched with HF:H₂O=1:6 for 63 min

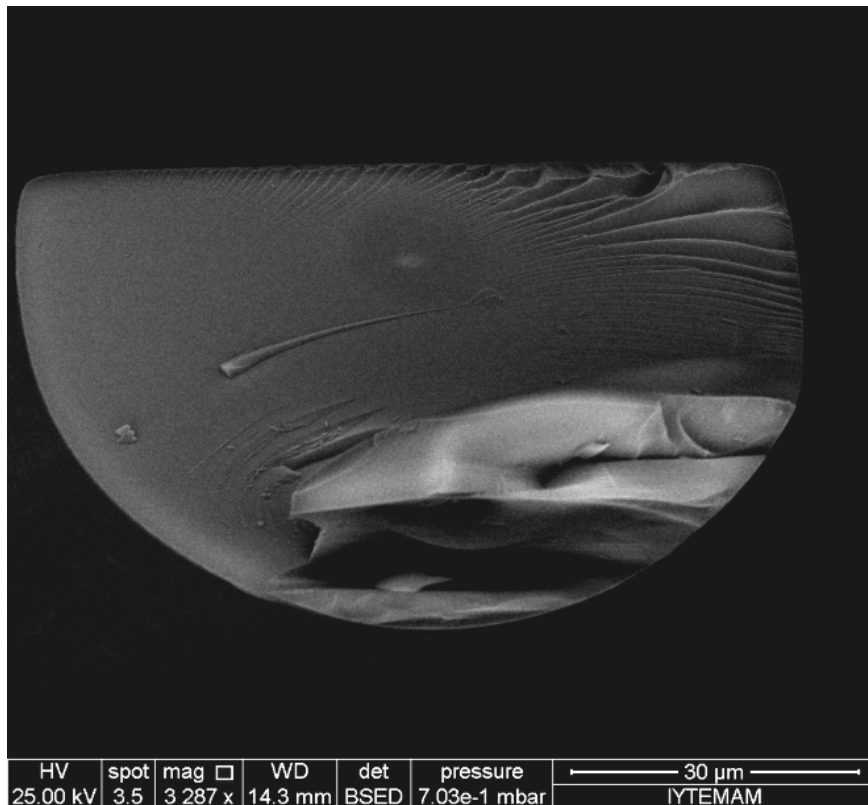


Figure 116. SEM analysis of raw (unprocessed) D-fiber sample

Using the SEM studies and also the fiber specifications previously released by the manufacturer (KVH, 2000), the following model for the D-Fiber was established:

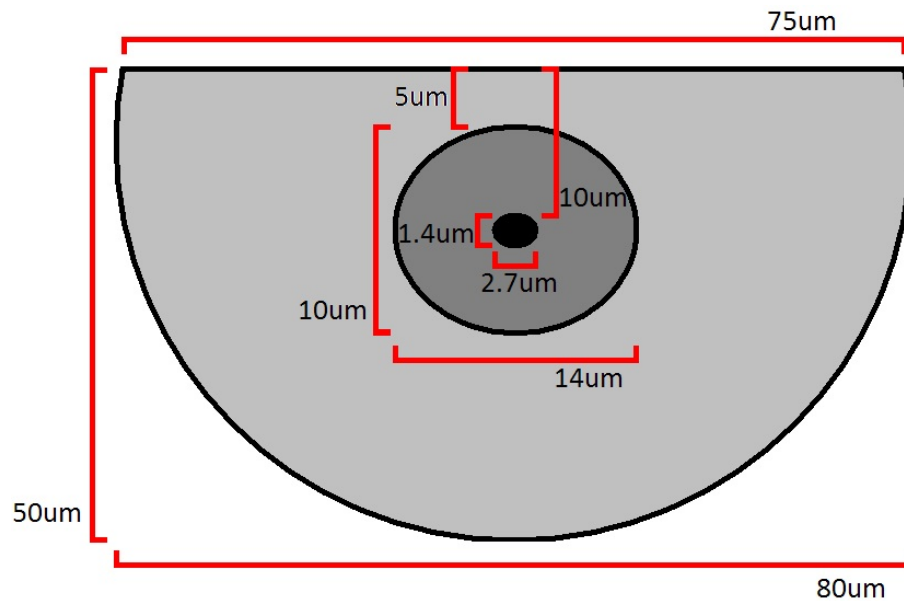


Figure 117. D-Fiber model based on SEM studies and fiber specifications

Results of the etching experiments and measurements show that when the etching solution has the composition $\text{HF}:\text{H}_2\text{O} = 1:6$, the etch rate varies between 118nm/min and 200nm/min depending on the ambient conditions such as temperature, humidity, etc. Etching is uniform in both width and length of the fiber. Accordingly, considering that the maximum target depth to be achieved is 10 μm , the target time-frames for obtaining the desired fiber properties are calculated as follows:

- For etch rate=118nm/min, 10 μm takes 85min06sec.
- For etch rate=200nm/min, 10 μm takes 50min00sec.

HF etching characteristics of the studied optical fibers are summarized in the below chart:

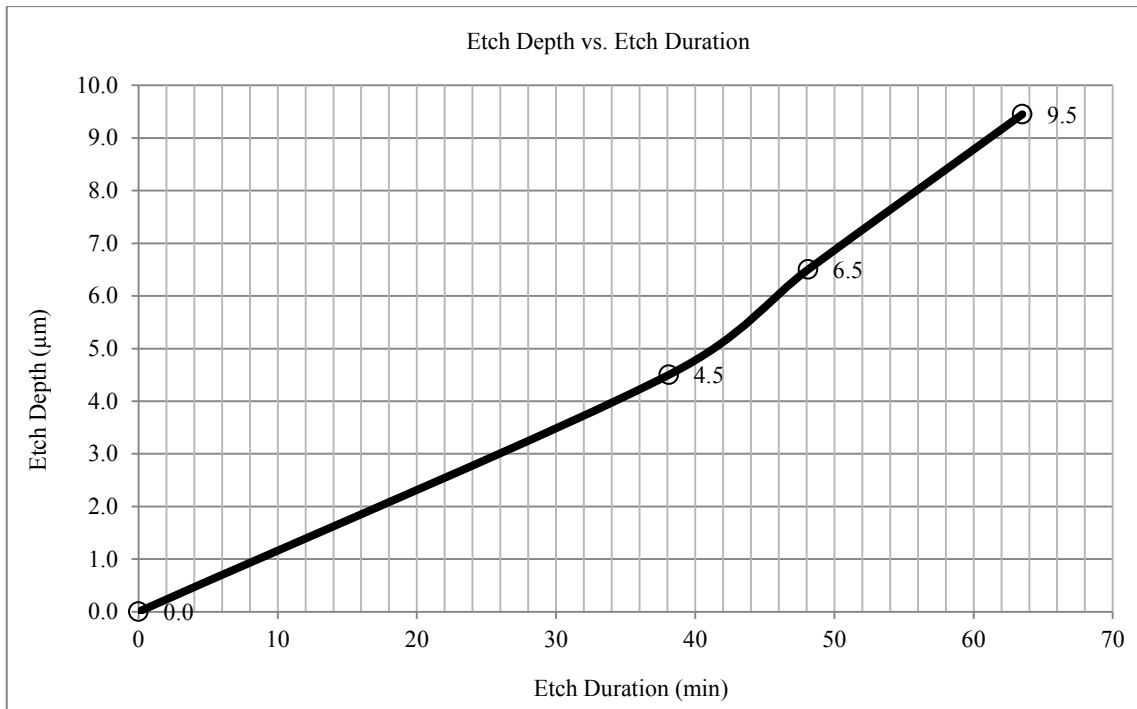


Figure 118. HF-etch depth vs. etch time for D-Fiber (HF:H₂O=1:6)

5.3. Side-Polished Fibers

Following the extensive studies on determining the optimum way of fabricating in-house D-Fibers and applying modifications to such fibers due to supply problems, the solution was established as utilizing the side-polished optical fibers manufactured by Phoenix Photonics, based in UK. The manufacturing method is via partial removal of cladding layer of the optical fiber, where Corning HI1060 optical fibers are employed in the fabrication of the components (Phoenix, 2012):



Figure 119. Side-polished optical fibers manufactured by Phoenix Photonics.

The specifications of the Corning HI1060 optical fiber (Corning, 2010) employed in the side-polished fiber fabrication are given in Table 15. With the fiber supply issue resolved, device fabrication studies were initiated.

Table 14. Specifications of Corning HI1060 optical fiber

Corning HI1060	Value	Unit
Nominal operating wavelength	> 980	nm
Cut-off wavelength	920 ± 50	nm
Cladding diameter	125 ± 0.5	μm
Core diameter	5.3	μm
Coating diameter	245 ± 15	μm

5.4. Final Device Fabrication

5.4.1. Fabrication Steps and Experimental Setup

In light of the previously completed design and optimization studied, device fabrication was commenced. In doing so, previously designed and finalized experimental setup was built. The experimental setup reached its final form by first obtaining photopolymerization on photopolymer thin films cast on glass substrates, defining and measuring the photopolymerization, adapting the process to on-fiber fabrication and inclusion of the utilized measurement systems.

The overall experimental realization process consists of the following steps:

- 1) Polymer synthesis – preparation of the reactant solution
- 2) Preparing the experimental setup, optimization and fine tuning
- 3) Preparing and positioning the optical fiber, alignment and launching the fundamental and second modes
- 4) Polymer casting and curing, simultaneous monitoring of the fiber output mode
- 5) Fabrication of the grating structure via photopolymerization – laser direct-writing
- 6) Monitoring and recording the output power

The schematic representation and an image of the experimental setup are given below. During the photopolymerization process, in addition to the direct-writing 543nm He–Ne laser, a second He–Ne laser operating at 632.8nm was employed to launch the fundamental (LP_{01}) and second (LP_{11}) modes of the fiber. Power output of the fiber was monitored using a powermeter and the output mode fields during different stages of the fabrication process was recorded using a CCD camera with 720 x 640 pixel image

sensor with $11\mu\text{m} \times 11\mu\text{m}$ pixels. Hence, the main principle was to fabricate the device on the fiber while monitoring the power output simultaneously.

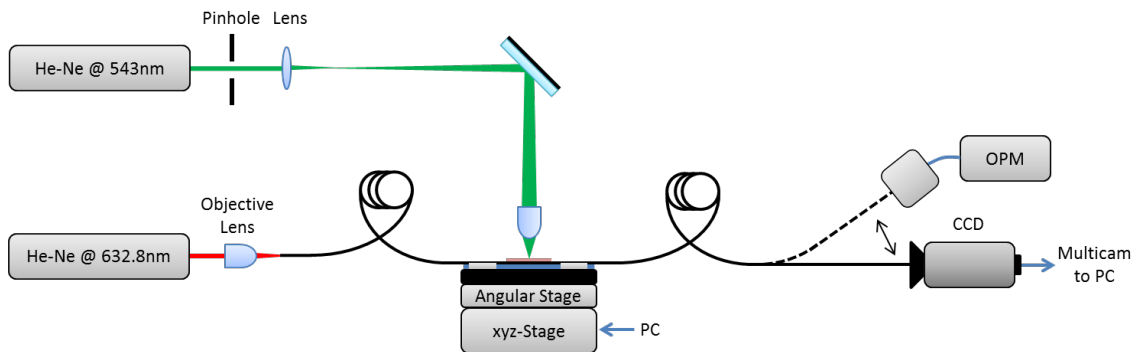


Figure 120. Schematic representation of the experimental setup

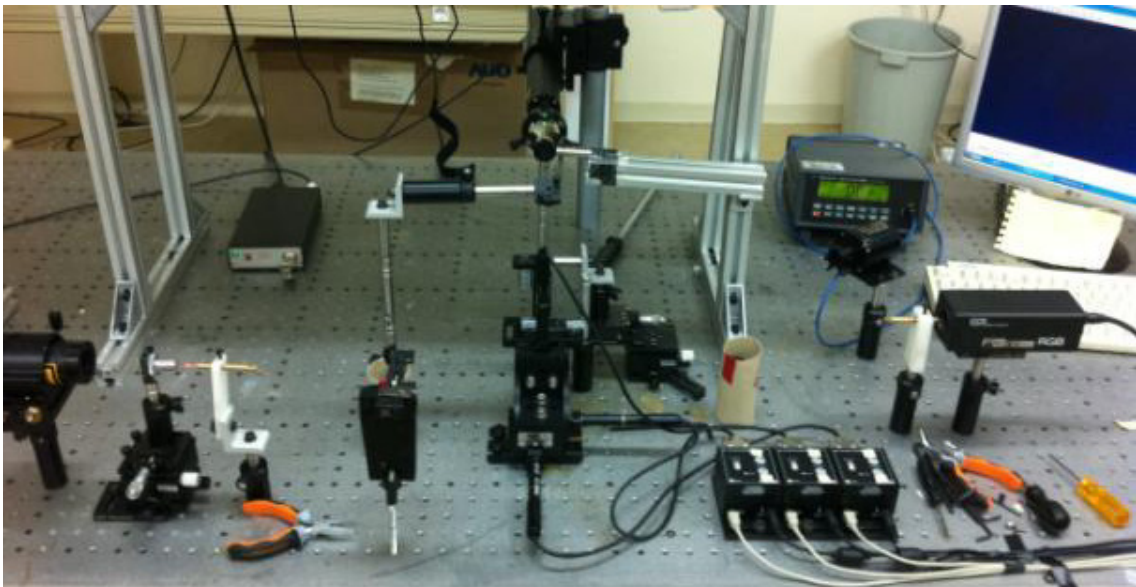


Figure 121. Experimental setup

As mentioned above, Corning HI1060 optical fiber was employed in the experimental studies. Fiber specifications are given below:

- Core refractive index: $n_{\text{core}}=1.4572$
- Cladding refractive index: $n_{\text{clad}}=1.4507$
- Core radius: $a=2.65\mu\text{m}$.

Previous studies had shown that the fiber supports two modes at 632.8nm wavelength, namely LP_{01} and LP_{11} :

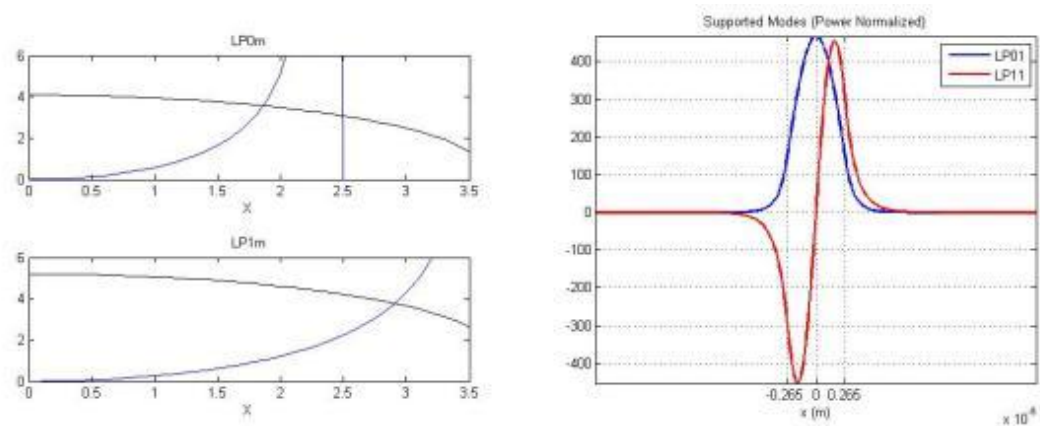


Figure 122. Modes supported by Corning HI1060 fiber excited at 632.8nm

Device fabrication was performed on the flat side surface of the fiber, which was thinned by the fiber vendor and this target area of the fiber had been placed on a glass substrate which provided ease of handling during the studies. The active area was later placed on the motorized xyz-stage which enabled the direct-writing laser beam to scan over the polymer layer in the desired pattern.

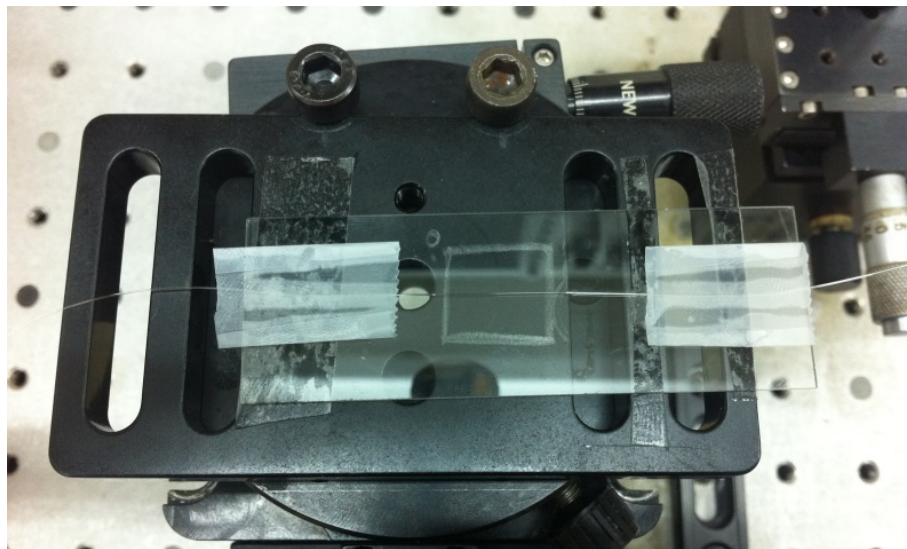


Figure 123. Launched optical fiber mounted on the motorized xyz-stage

5.4.2. Trial 1 – Single-Fiber Device at 632.8nm

The first two modes of the fiber were launched using 632.8nm laser and fiber power output and mode profiles were recorded (Measured power levels at each step of the process are given below).

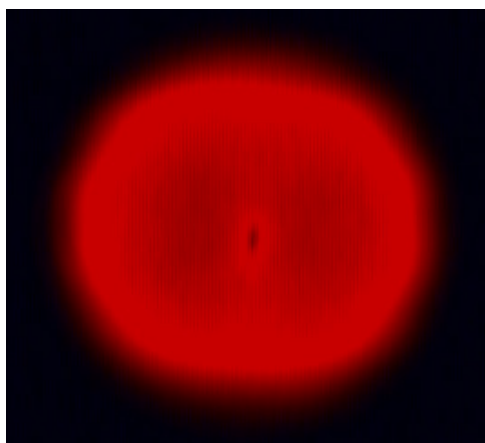


Figure 124. Launching the fiber and exciting the first two modes

Table 15. Output power of bare fiber – Trial 1

Process stage	Output power
Bare fiber	558±10nW

To form the polymer thin film layers, the polymer recipe finalized in the previous stages of the project was used:

Table 16. Polymer recipe constituents and their respective molar ratios

Material	Ratio in the solution	Calculated amount in 15ml aqueous solution	Form
H ₂ O	-	(15g)	Liquid
PVA	10% w/v H ₂ O	1.5g	Powder
TEA	0.199M	0.445g	Liquid
AA	0.446M	0.475g	Powder
YE	2.5x10 ⁻⁴ M	2.4mg	Powder

Prepared solution was cast on the bare fiber and film thickness was reduced using doctor blade method, followed by a 24-hour polymer cure at room temperature and the output power and mode profiles were recorded.

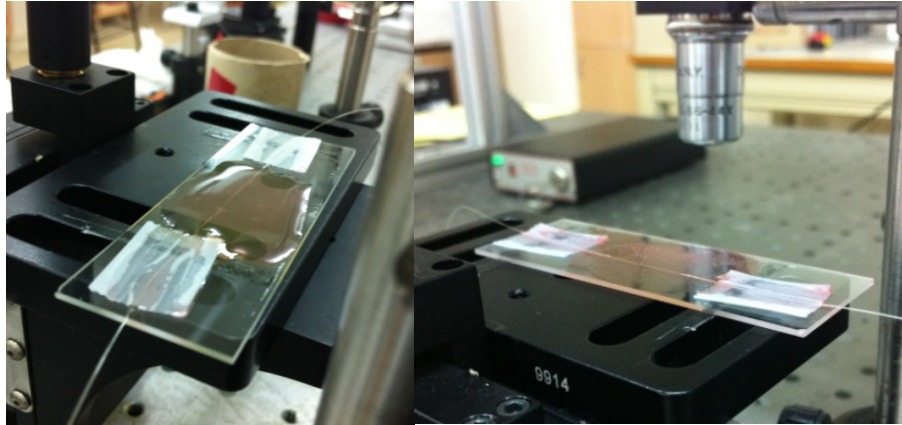


Figure 125. Polymer coating, doctor blade and cure

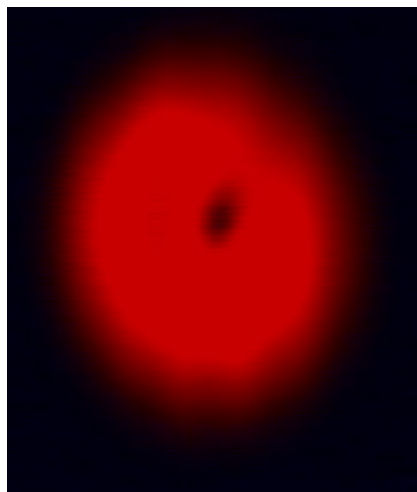


Figure 126. Recording the fiber output post-cure, prior to direct-writing

Table 17. Output power of unprocessed polymer coated fiber – Trial 1

Process stage	Output power
Polymer coated fiber, unprocessed	79.5±10nW

As it had been shown and expected from previous polymer coating studies, coating the fiber with unprocessed (unphotopolymerized) polymer changes the outer refractive index of the waveguide and guiding properties of the fiber change expectedly; this results in the drop of the measured output power. Following the completion of the cure step, direct-writing photopolymerization stage was commenced.

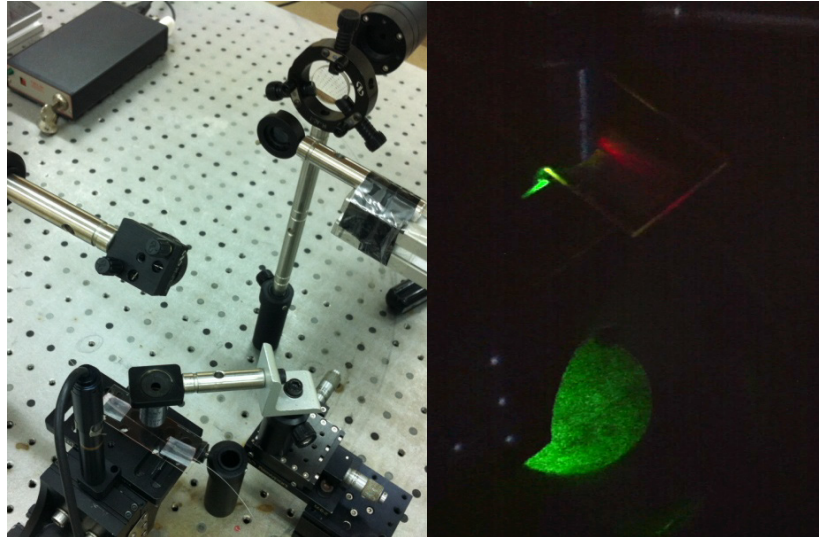


Figure 127. Photopolymerization by direct-writing

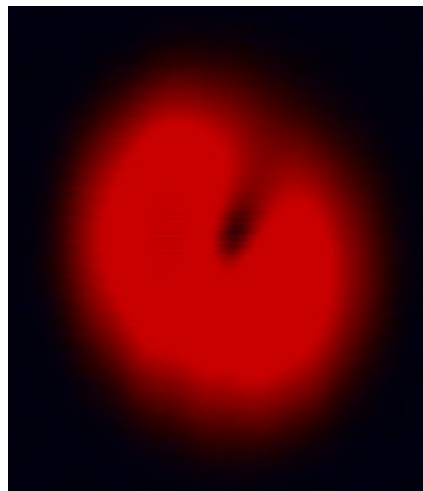


Figure 128. Monitoring the fiber output following the fabrication of grating via direct-writing polymerization

Output power levels measured during and at the end of the stages are presented below:

Table 18. Output power at various process stages – Trial 1

Process stage	Output power
Bare fiber	558±10nW
Polymer coated fiber, unprocessed	79.5±10nW
Grating direct-written fiber	79.5±10nW

As can be seen by the measurements and it had been expected through previous calculations, the effect of the grating on the fiber output is masked by the noise level at

the laser output. That is, the coupling efficiency at the ideal case is expected to be 12% according to the calculations and when calculated according to the output level of 79.5nW prior to direct-writing, the power to be coupled corresponds to 9.5nW, which is lower than the 10nW noise level measured at the output.

In light of these results, it was seen not feasible to be able to measure the experimental coupling efficiency under these experimental conditions and calculation of the coupling efficiency via numerical analysis of the output modes was performed.

Recorded CCD images of the output modes were imported into MATLAB environment and oscillatory noise at the output was filtered using unprocessed-polymer-coated and direct-written-polymer-coated fiber outputs. Using the output modes, total power was calculated for the two stages: prior to and after grating fabrication.

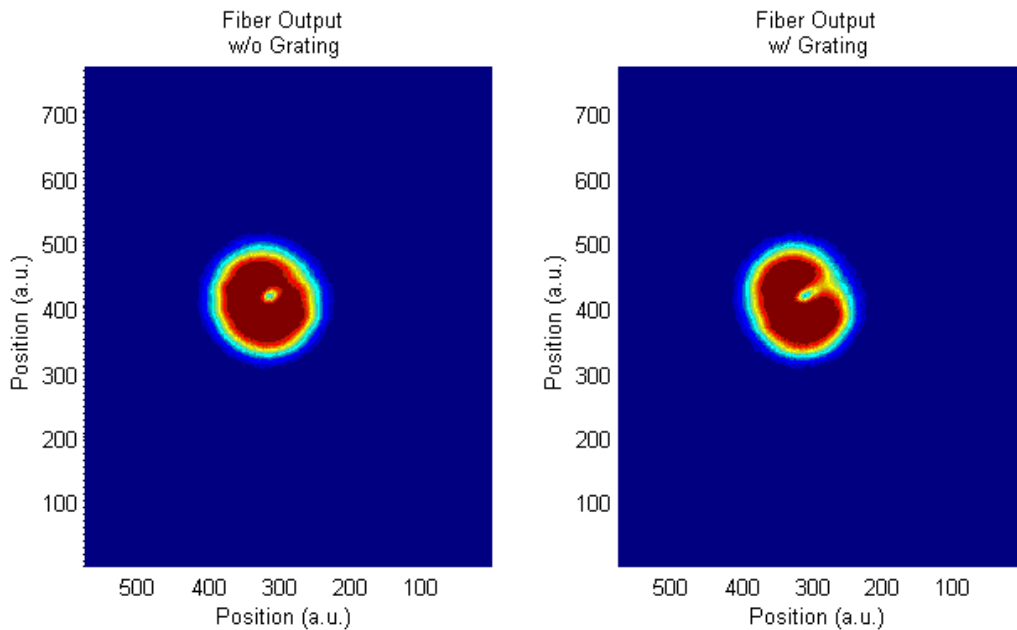


Figure 129. CCD fiber output images of before (left) and after grating direct-writing, normalized in MATLAB environment

The calculations show that the grating induces a difference of **2.2263%** (1.79nW) at the output power. According to this result, the grating structure does actually perturb the light propagating inside the fiber and leads to 2% total coupling efficiency. As can be recalled, theoretical calculations showed an expected efficiency of 12%, which is higher than experimental results.

Further analysis of the CCD output mode profiles had shown an error in the measurements, namely, the saturation of the CCD array due to the power level incident

at the detector. Analysis of the error has shown that this might have led to loss of mode profile information during the recording of the profiles. In light of these findings, it was decided to repeat the experimental process.

5.4.3. Trial 2 – Single-Fiber Device at 632.8nm

As in the first experimental run of the final device fabrication, a new fiber sample placed on a glass substrate with thinned flat side surface was used. The fiber was excited using 632.8nm He-Ne laser and the output profiles and power levels were recorded prior to raw polymer casting.

Table 19. Output power of the bare fiber – Trial 2

Process stage	Output power
Bare fiber	1.057±0.15μW

The exact polymer recipe was used in Trial 2 as in Trial 1. The power levels were recorded once again after the end of the polymer curing stage.

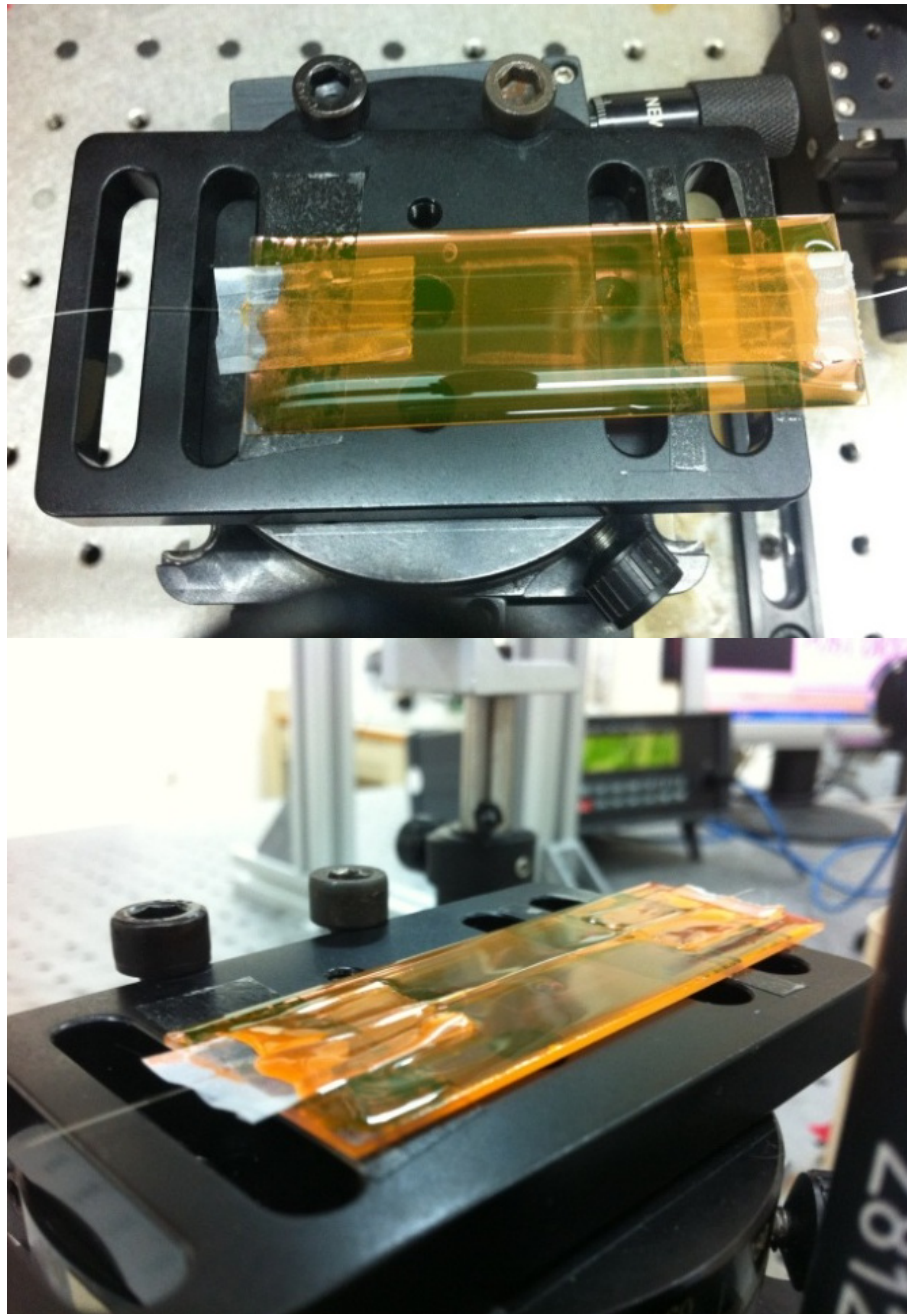


Figure 130. Polymer coating (top) and cure

Table 20. Output power of unprocessed polymer coated fiber – Trial 2

Process stage	Output power
Polymer coated fiber, unprocessed	$0.92 \pm 0.17 \text{ nW}$

As before, following the completion of the cure step, direct-writing photopolymerization stage was commenced and the output mode intensity profiles and

power levels were recorded. Output power levels measured during and at the end of the Trial 2 stages are presented below:

Table 21. Output power at various process stages – Trial 2

Process stage	Output power
Bare fiber	$1.057 \pm 0.15 \mu\text{W}$
Polymer coated fiber, unprocessed	$0.92 \pm 0.17 \text{nW}$
Grating direct-written fiber	$0.92 \pm 0.17 \text{nW}$

As anticipated to be similar to the first trial, the expected effect of the grating is lower than the noise level measured at the output. Therefore, calculation of the coupling efficiency via numerical analysis of the output modes was performed.

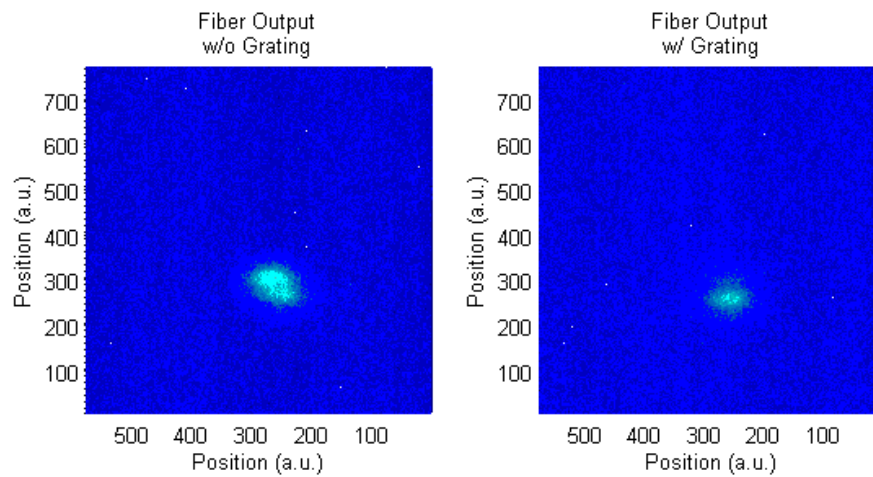


Figure 131. CCD fiber output images of prior to and after grating direct-writing, observed in MATLAB environment (Source: Sümer and Dinleyici, 2013)

Since there was no saturation of the CCD observed in this second fabrication trial, a cross-sectional modal analysis was possible.

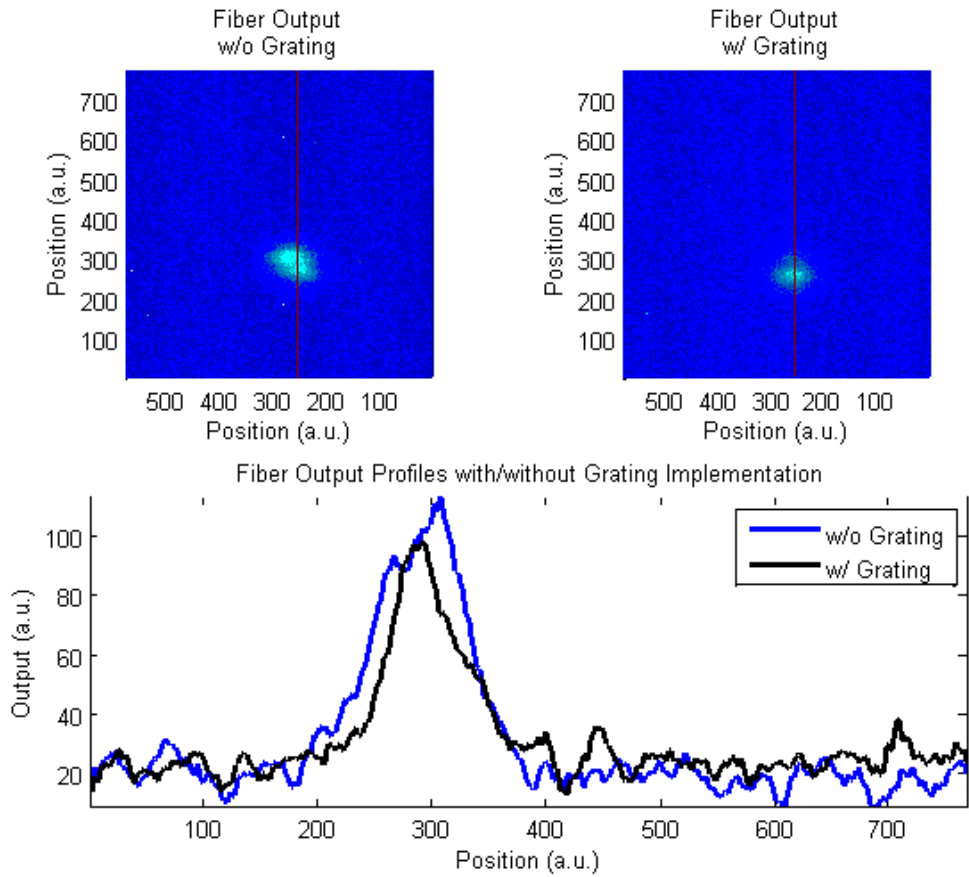


Figure 132. Cross-sectional analysis of the input and output mode profiles

Using the cross-sections, a mode-by-mode fitting was performed on the fiber outputs and power transfer between the modes was calculated.

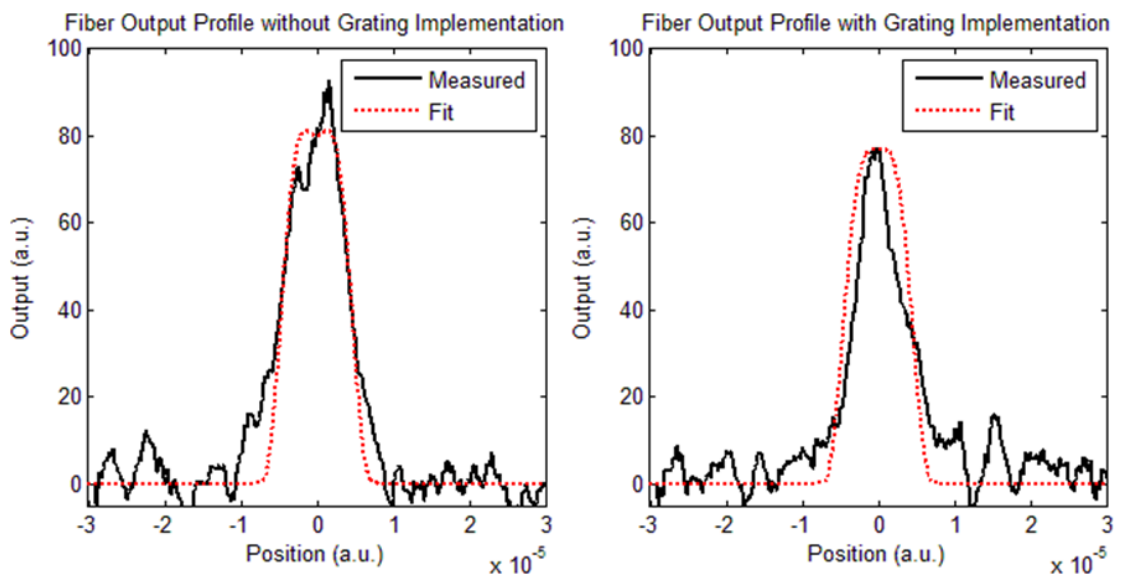


Figure 133. Fiber output profiles without (left) and with grating implementation (Source: Sümer and Dinleyici, 2013)

The analysis has revealed a coupling efficiency of **7.635%** of the input LP₁₁ mode. With these results, the grating structure actually perturbing the light propagating inside the fiber was demonstrated for a second time, which has led to almost 8% coupling efficiency. As can be recalled, theoretical calculations showed an expected efficiency of 12%, which is a bit higher than experimental results; the difference between the theory and the experiment is associated with experimental conditions and measurement tolerances. In addition, during the second fabrication the grating structure formed on the polymer-coated fiber was also documented:



Figure 134. Reflection microscope image of the fiber with the fabricated grating

5.4.4. Trial 3 – Single-Fiber Device at 852nm

The fabrication procedure for the 852nm device basically includes the same experimental steps as the earlier ones, yet the change in the operation wavelength has an impact on the measurement capabilities. In the experimental setup, when the 632.8nm laser source is replaced by the 852nm, the wavelength of the source launching the fiber modes moves out of the visible spectrum. The consequence of this switch is being unable to utilize the CCD detector and therefore monitoring and/or recording of the output fiber mode fields not being possible.

The first fabrication trial of the 852nm device was initially planned to be a complete fabrication of the grating coupler including the assembly of both propagation (input) and coupled (output) fibers. However, a mishap occurring during the procedure prevented the procedure to reach culmination; as a result, the trial resulted in being the reiteration of the previous fabrication processes with the exception of the operation wavelength.

The input fiber was launched via the 852nm laser and the output power level was recorded both prior to and after casting the photopolymer. After an overnight cure of the photopolymer at room temperature in a dark environment, the grating structure was fabricated via direct-writing photopolymerization on the thin film layer. The output power levels prior to and after the grating is induced are recorded and as a result, the perturbing effect of the grating structure was directly observed on the output power (see Table 22).

Table 22. Output power at various process stages – Trial 3

Process stage	Output power
Bare fiber	Input fiber: 25.49±0.15μW
Polymer coated fiber, post-cure	Input fiber: 4.51±0.15μW
Grating direct-written fiber	Input fiber: 3.80±0.15μW

Accordingly, a total coupling efficiency of **15.742%** is achieved in fiber modes prior to the assembly of the coupled (output) fiber. The efficiency obtained at this intermediate stage of device production is lower than the calculated target efficiency of the complete device as expected, while, the obtained value at this stage is higher than that of the 632.8nm device, which is the main reason of incorporating 852nm wavelength.

5.4.5. Trial 4 - Complete Structure at 852nm

The fabrication procedure was attempted once more for the 852nm device, to include the assembly of both input and output fibers to form the complete coupler structure.

Also, in order to increase the polymer surface contact area with the ambient and facilitate efficient polymer curing after the second (output) fiber is mounted, the glass holder which the fiber is attached to was modified prior to assembly. The initial and final structures of the glass fiber holder are shown in Figure 135 and a modified fiber holder sample is shown in Figure 136.

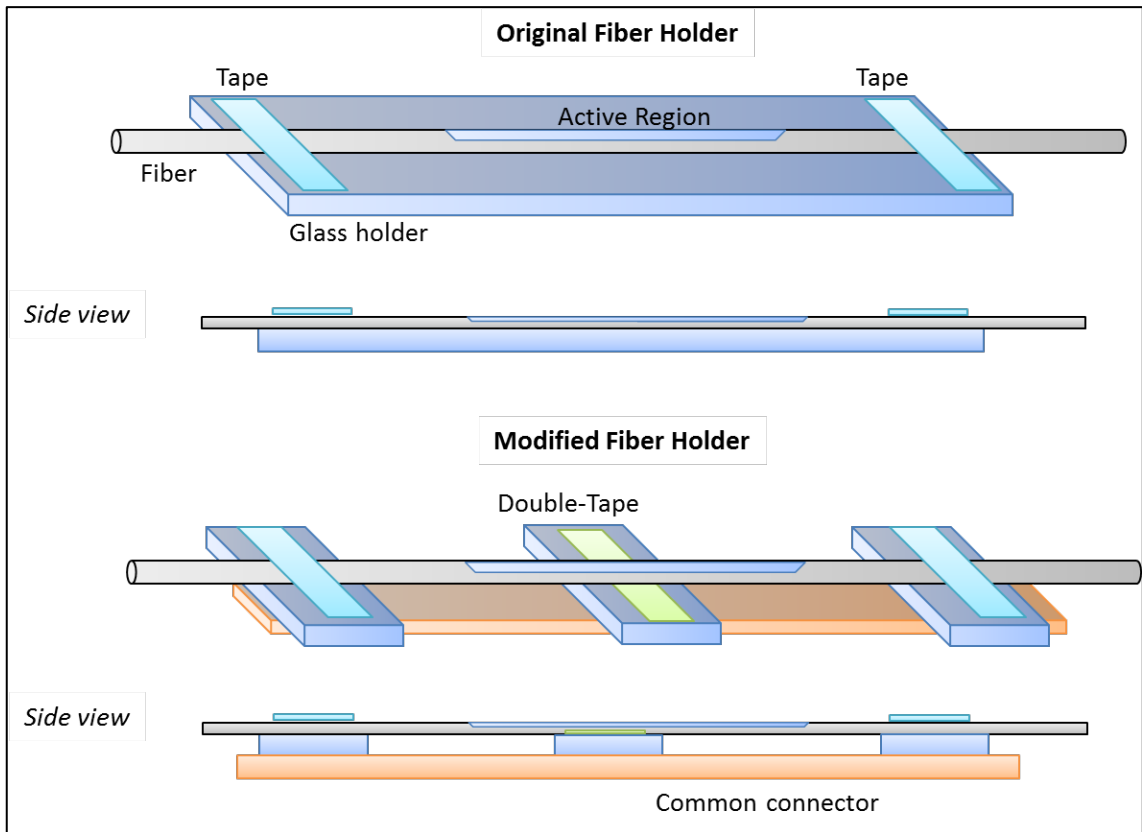


Figure 135. Original and modified structures of the glass fiber holder



Figure 136. Modified fiber holder

The fabrication process was not altered; input fiber was launched via the 852nm laser, followed by the casting of the photopolymer. After an overnight cure, the grating structure was fabricated on the thin film layer. The output power was recorded at each step of the fabrication process. Once more, the perturbing effect of the grating structure is directly observed on the output power of the input fiber (see Table 23).

Consequently, a total coupling efficiency of **13.012%** is obtained prior to the assembly of the second fiber. The efficiency obtained at this stage is lower than the target efficiency as expected, while, it is higher than that of the 632.8nm device similar to the previous fabrication attempt of the 852nm device.

Table 23. Output power at various process stages – Trial 4

Process stage	Output power
Bare fiber	Input fiber: $5.32 \pm 0.15 \mu\text{W}$
Polymer coated fiber, post-cure	Input fiber: $56.1 \pm 0.17 \text{nW}$
Grating direct-written fiber	Input fiber: $48.8 \pm 0.17 \text{nW}$
Upper fiber mount, pre-cure	Input fiber: $49.3 \pm 0.17 \text{nW}$
Post-cure, final device	Input fiber: $3.55 \pm 0.15 \mu\text{W}$
	Output fiber: 0.00W

Device fabrication is resumed with the casting the second polymer layer and mounting the output fiber.

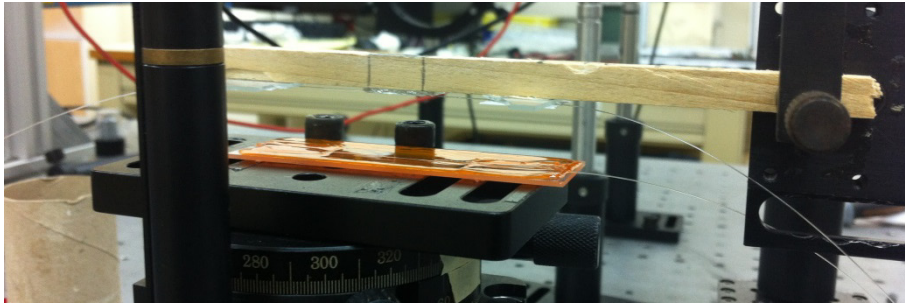


Figure 137. Final device fabrication – mounting the output fiber

The power at the output is recorded both immediately after the fiber assembly for reference and at the end of the overnight cure of the second polymer layer at room temperature in a dark environment. A photograph of the final device is presented in Figure 138.

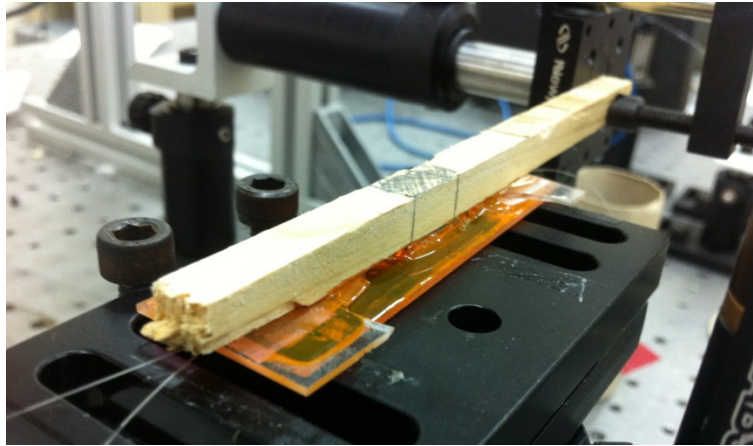


Figure 138. Final device

The output power levels at each step of the fabrication process are presented above in Table 23. As described previously, the intermediate results during the single-fiber stage of the fabrication indicated a total coupling efficiency of 13%, whereas at the end of the overall device fabrication, the power level measured at the output fiber was 0.0nW. As it stands, this result may seem to indicate an experimental error of which the root-cause is yet to be determined.

Being unable to measure the laser power actually coupled into the output fiber makes it difficult to obtain a more comprehensive assessment of the experimental performance of the device. Nevertheless, when only the change in the input fiber power level is taken into account, the overall drop – Bare Fiber vs Final Device – in the power output caused by the grating fabrication points to a total power efficiency of **33.270%**, which is the highest experimental efficiency level obtained throughout this study.

5.4.6. Trial 5 - Complete Structure at 852nm

The next fabrication trial for the complete 852nm device included revisions in the experimental setup. Optical Spectrum Analyzer (OSA) was utilized in the measurement setup to facilitate observation of the fiber modes in the device output and also the fiber holder apparatus for the second fiber was revised. With the addition of the OSA and change of operation wavelength, together with the inclusion of the 632.8nm source for verifying the viability of the second fiber, the final form of the experimental setup was established as depicted in Figure 139 and presented in Figure 140.

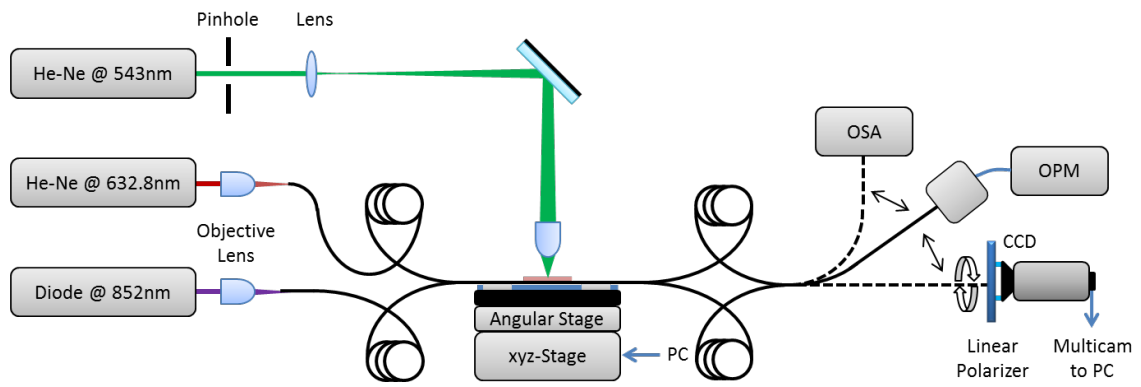


Figure 139. Schematic representation of final form of the experimental setup

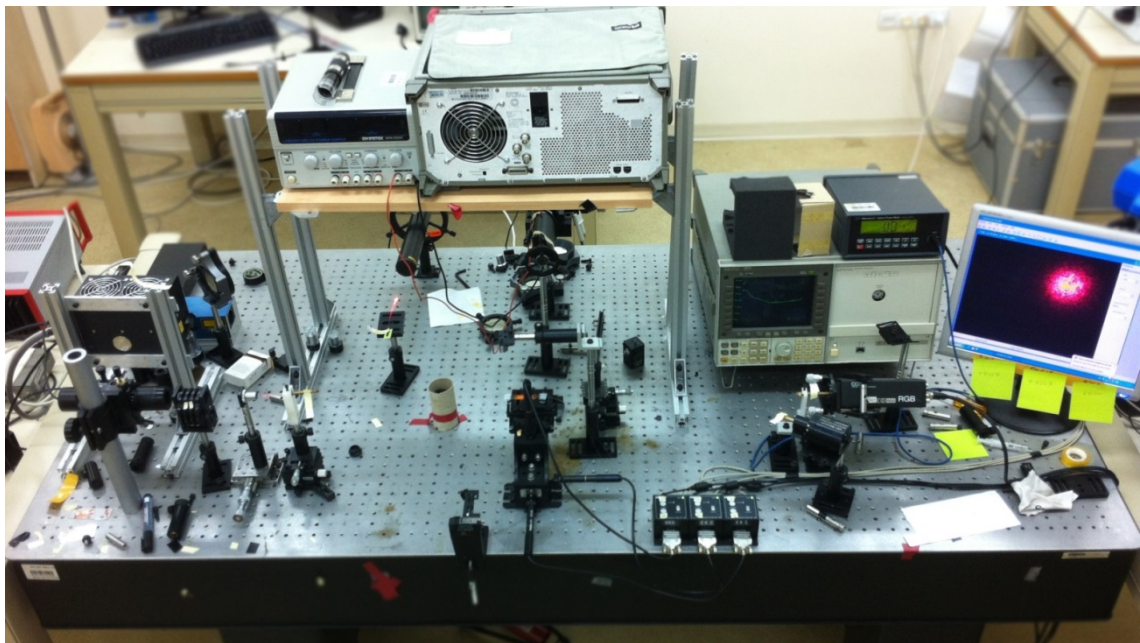


Figure 140. Final form of the experimental setup

As mentioned above, the fiber holder apparatus for the second optical fiber was revised to facilitate a more efficient polymer cure:

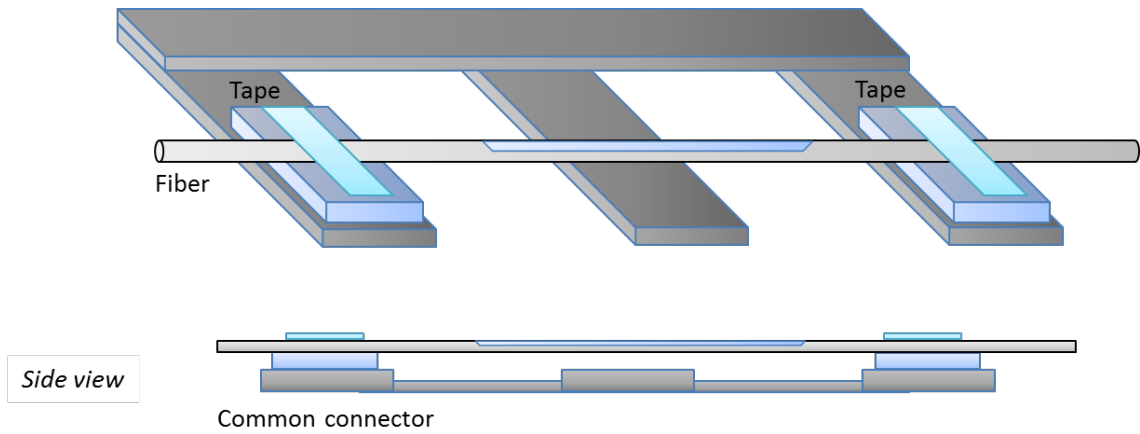


Figure 141. Schematic representation of the revised fiber holder

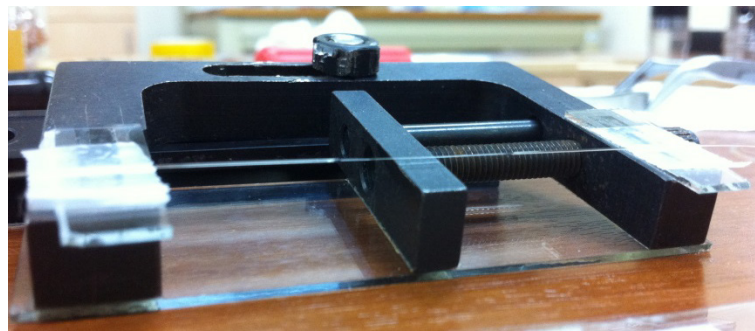


Figure 142. Revised fiber holder

Output power measurements performed throughout several stages of fabrication are presented below:

Table 24. Output power at various process stages – Trial 5

Process stage	Output power
Bare fiber	Input fiber: $2.790 \pm 0.15 \mu\text{W}$
Polymer coated fiber, post-cure	Input fiber: $0.894 \pm 0.15 \mu\text{W}$
Grating direct-written fiber	Input fiber: $0.773 \pm 0.15 \mu\text{W}$
Post-cure, final device	Input fiber: $1.705 \pm 0.15 \mu\text{W}$
	Output fiber: 0.00W

Accordingly, the effect of the grating on the output (before vs. after direct-writing) is recorded as **13.53%**, whereas the overall drop in the device output as a result of the device implementation is calculated to be **38.88%**.

By incorporating the Optical Spectrum Analyzer measurements of the fiber output, individual modes propagating in the fiber were successfully differentiated. In addition, the change in the respective ratios of these modes was recorded and the perturbation caused by the grating was documented. The recorded patterns and calculated changes in the respective ratios of mode powers are presented in the following figures and table.

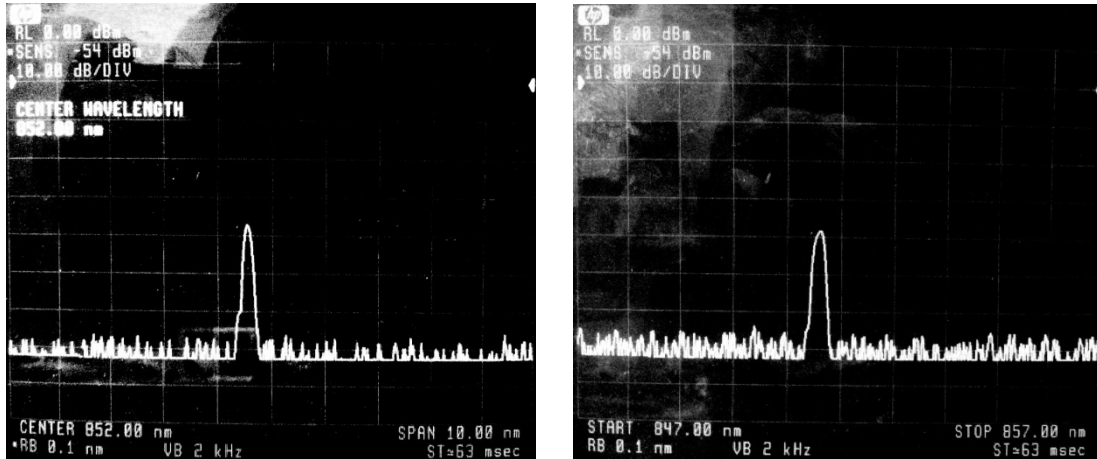


Figure 143. OSA measurements performed before (left) and after direct-writing

Table 25. Relative mode power ratios obtained via OSA measurements

Process stage	LP ₁₁ /LP ₀₁ ratio
Bare fiber	Input fiber: 35.48%
Final device	Input fiber: 26.28%

The results of the measurements performed with the Optical Spectrum Analyzer provide an additional verification of mode perturbation caused by the direct-written grating.

5.4.7. Trial 6 – Single-Film Device at 852nm

An intermediate fabrication trial was also performed involving the assembly of a device composed of two fibers and a single film layer in between, i.e., without the grating or the second polymer layer. The results obtained are presented in the table below:

Table 26. Output power at various process stages – Trial 6

Process stage	Output power
Bare fiber	Input fiber: 0.583±0.15μW
Post-cure, final device	Input fiber: 1.140±0.15μW
	Output fiber: 0.00W

In addition, the measurements obtained via the Optical Spectrum Analyzer and the resulting relative modal amplitude ratios are presented in the following.

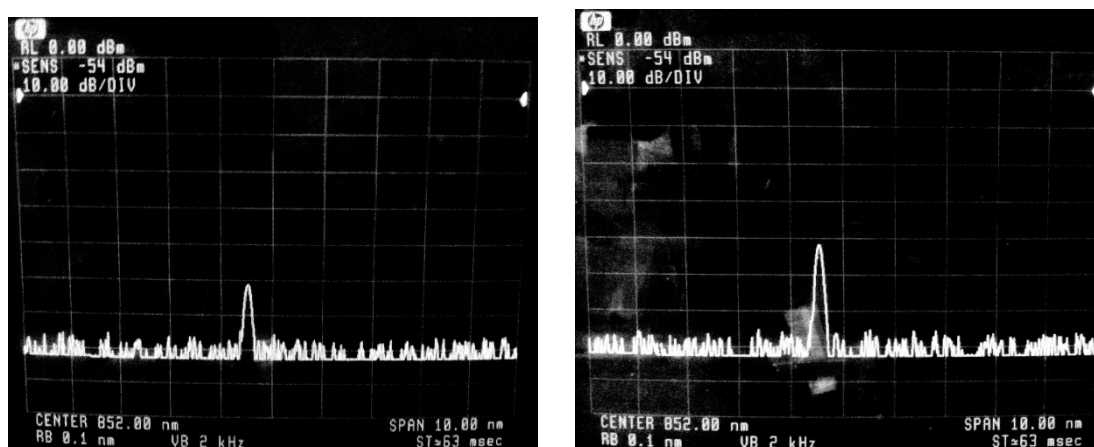


Figure 144. OSA measurements performed before (left) and after device fabrication

Table 27. Relative mode power ratios obtained via OSA measurements

Process stage	LP ₁₁ /LP ₀₁ ratio
Bare fiber	Input fiber: 37.79%
Final device	Input fiber: 31.27%

5.4.8. Trial 7 – Complete Structure with Polarization Analysis

In order to enable polarization measurements of the fiber modes and to provide a well-rounded analysis of the experimental device performance, the final fabrication of the device was performed to operate at 632.8nm. The main reason for using the aforementioned wavelength is to provide an ease of alignment and observability of the polarized fiber outputs via the CCD detector.

Accordingly, the CCD Camera in the experimental setup –depicted in Figure 139 was equipped with a linear sheet polarizer in the front section of the CCD sensor. Due to the mechanical design of the CCD camera and in order not to lose light output at the fiber exit, the sheet linear polarizer had to be attached directly in front of the CCD sensor and angular scanning of the fiber output was performed by rotating the entire polarizer+CCD camera system around the propagation axis (See figure below).

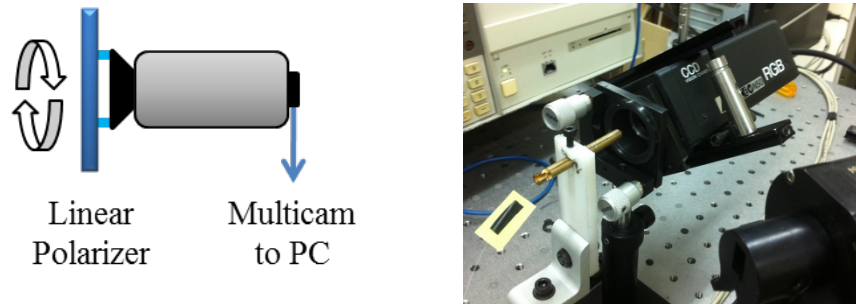


Figure 145. Representation (left) and photograph of the rotating polarizer+CCD system

The analysis of the measured field intensity patterns was performed by taking individual recordings at varying angles and/or by performing a frame-by-frame analysis of the video captures recorded during full rotations of the system around the center axis; where the related results and analyses are presented in the next chapter.

In addition, as for the previous devices, the power measurements at various process stages are presented below, where the results indicate a recorded effect of the grating on the output (before vs. after direct-writing) of **7.446%**:

Table 28. Output power at various process stages – Final Trial

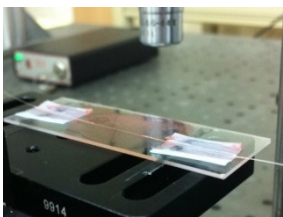
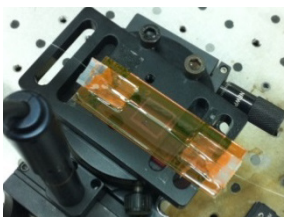

Process stage	Output power
Bare fiber	Input fiber: $4.88 \pm 0.15 \mu\text{W}$
Polymer coated fiber, post-cure	Input fiber: $4.70 \pm 0.15 \mu\text{W}$
Grating direct-written fiber	Input fiber: $4.35 \pm 0.17 \mu\text{W}$
Post-cure, final device	Input fiber: $3.94 \pm 0.15 \mu\text{W}$
	Output fiber: 0.00W

CHAPTER 6

RESULTS AND DISCUSSION

The experimental results regarding the fabricated devices' coupling performance were obtained via optical power measurements at the output of the propagation fiber. For wavelengths of operation within the range of the CCD sensor, modal fit of the recorded output intensity with calculated mixed mode patterns were also performed. Hence, an assessment of the total power coupling as well as an evaluation of the mode-selectivity of the fabricated structures has been obtained. For a thorough analysis of the mode-selectivity of the fabricated devices, polarization measurements, results of which will be discussed later in this chapter, were incorporated. A compilation of the overall device performances is presented in the tables below.

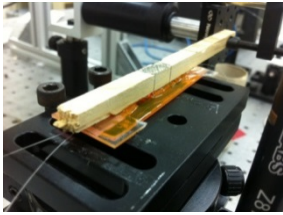
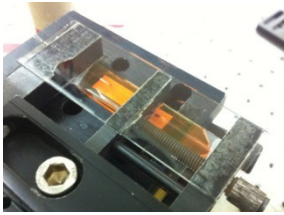
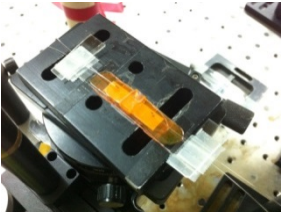
Table 29. Single-fiber devices fabricated throughout the study

#	Trial 1	Trial 2	Trial 3
Device			
Operation wavelength	632.8nm	632.8nm	852nm
Calculated efficiency	12.70%	12.70%	68.64%
Measured efficiency	2.23%	7.64%	15.74%
Measurement techniques	CCD, OPM	CCD, OPM, modal fit	OPM

As described in the previous chapter, the measured efficiency of Trial 1 with operation wavelength of 632.8nm is accounted for by the CCD saturation during the measurements. On the other hand, the results of Trial 2 are in good agreement with the efficiency level calculated during device design. As for Trial 3 with operation wavelength of 852nm, while the achieved level was below the expected efficiency, the

overall efficiency of the device was measured to be higher than its predecessors, which validated the change of operation wavelength in order to increase the achievable performance.

Table 30. Complete devices fabricated throughout the study

#	Trial 4	Trial 5	Trial 7
Device			
Operation wavelength	852nm	852nm	632.8nm
Calculated efficiency	68.64%	68.64%	12.70%
Measured efficiency	33.27%	38.88%	7.45%
Measurement techniques	OPM	OPM, OSA	OPM, OSA, polarizer+CCD

The results obtained for the operation wavelength of 852nm where the complete structure was fabricated show an expected increase in the measured efficiencies. In fact, the efficiency is measured as 38.88%, more than double the previous value of 15%.

Apart from the optical power measurements, in order to be able to achieve a quantitative analysis of the experimental mode-selectivity performance and also to differentiate the modes propagating in the device, Trial 7 was performed. As described in the previous chapter, to be able to utilize the CCD sensor in measuring the fiber output through the linear polarizer, the wavelength of operation was set as 632.8nm. In terms of power measurements, the obtained value of 7.45% has been in good agreement with the previous results obtained for the same wavelength.

Polarization-dependent measurements of the device output were utilized to evaluate the performance of the fabricated device using a sheet linear polarizer attached in the front section of the CCD detector (See Figure 145). Angular measurements involving 360-degree rotations around the propagation axis were achieved by the unison rotation of the polarizer-CCD detector pair. After the measurements, individual images recorded at distinct polarizer angles and captured frames of rotational video recordings

were run through noise cancellation, which was followed by the fitting of recorded fiber mode field intensity distributions with patterns calculated based on fiber parameters and the wavelength of operation.

As previously discussed, Corning HI1060 optical fiber was launched at 632.8nm wavelength for this set of measurements. Using the fiber parameters and the wavelength of operation, calculated intensities of the mode fields supported by the fiber are presented in the following figure.

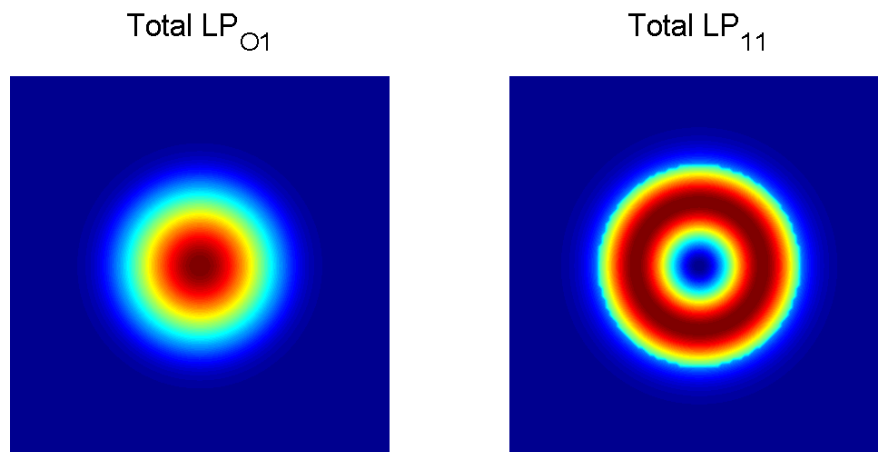


Figure 146. Fundamental mode (left) and second-order mode supported by the device

The physical structure of the optical fibers utilized in the study, as described in Chapter 5, include a side-polished region on which the photopolymer film casting and laser direct-writing processes are performed (See Figure 119). The original geometry of the fibers presented in Table 14 exhibit a circular symmetry. The presence of the side-polished region breaks this symmetry and therefore allows for the existence of degenerate modes within the fiber (See Figure 147). In the experimental studies, a laser source with a known linearly polarized output was used and therefore the fiber input was solely linearly polarized.

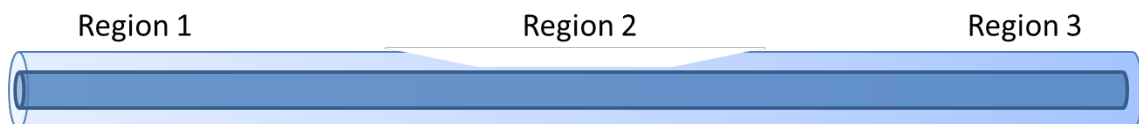


Figure 147. Structure of the optical fiber used in the experiments

With reference to the above figure, Region 1 exhibits circular symmetry, whereas the side-polished area in Region 2 breaks this symmetry and modes are degenerated. The two-fold degeneracy of the LP_{01} mode and the four-fold degeneracy of the LP_{11} mode result in a total of 8 independent modes theoretically possible to exist within the fiber simultaneously (Ghatak and Thyagarajan, 1998). In Region 3 the circular symmetry of the fiber geometry is restored and it is once again theoretically possible for all the guided modes to propagate within the fiber.

Accordingly, the degenerate LP_{01} and LP_{11} modes supported by the HI1060 fiber at the operation wavelength of 632.8nm in Region 1 were calculated as presented below, where the arrows shown in the figures represent the direction of the electric field.

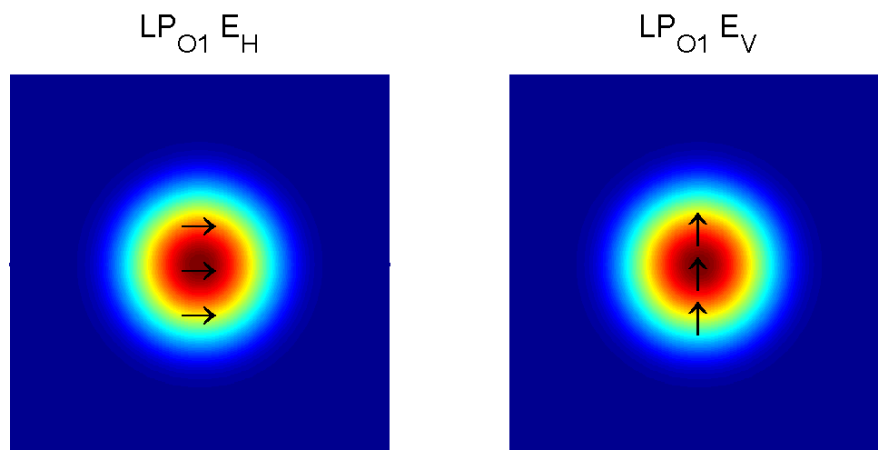


Figure 148. Degenerate LP_{01} modes supported by HI1060 at 632.8nm

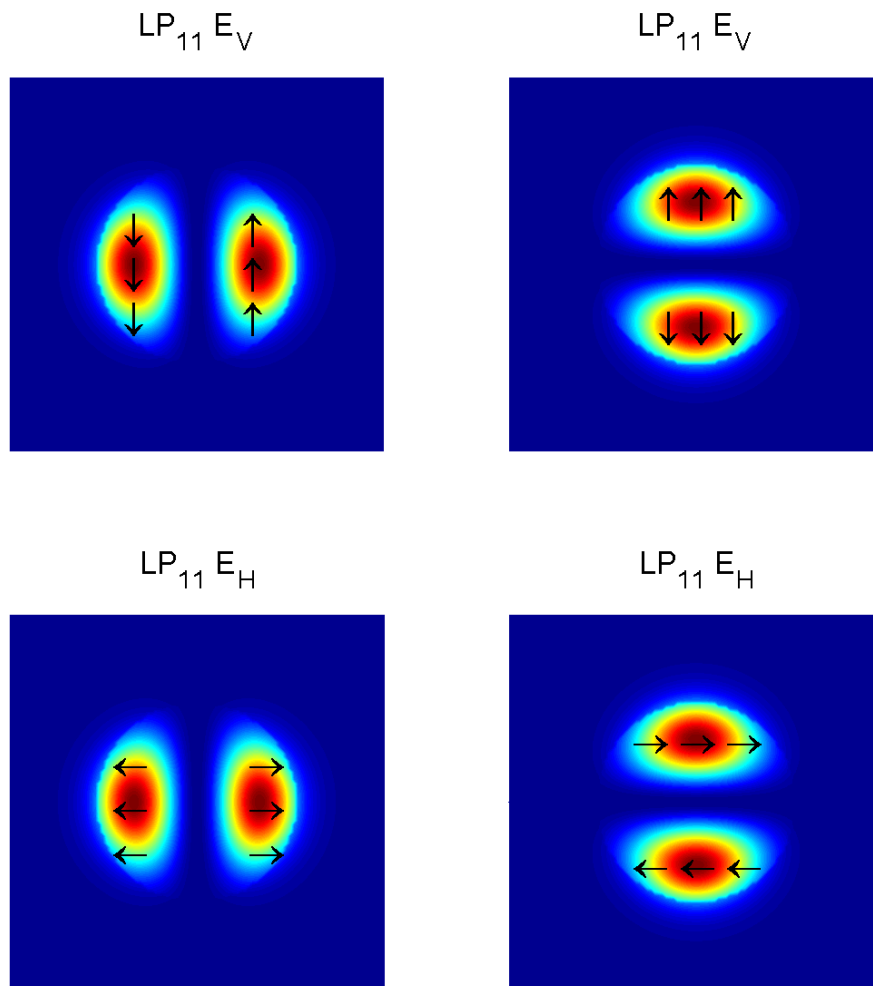


Figure 149. Degenerate LP_{11} modes supported by HI1060 at 632.8nm

Since the resulting modes are independent, degeneracy of the LP_{01} and LP_{11} modes lead to a total of 8 modes supported by the structure, which are calculated for the HI1060 fiber at 632.8nm as depicted in the figures below.

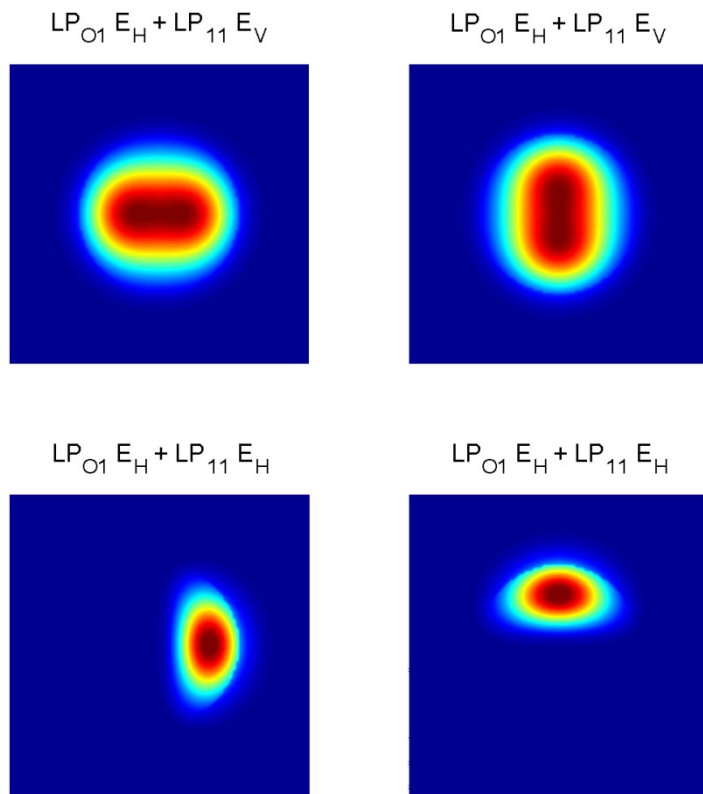


Figure 150. Degenerate $LP_{01}E_H$ + degenerate LP_{11} combinations

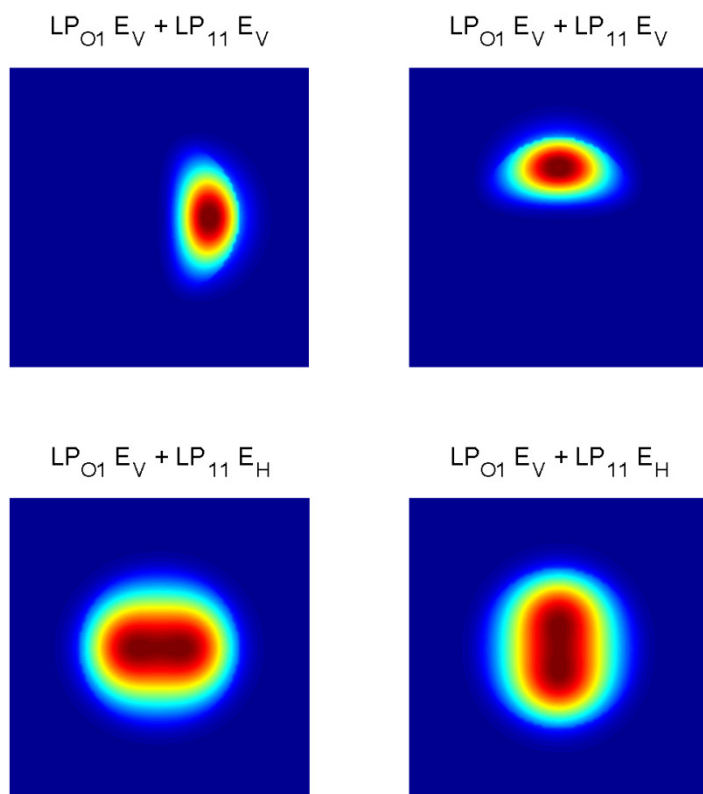
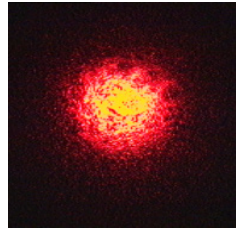
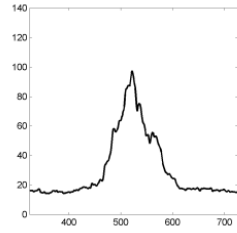
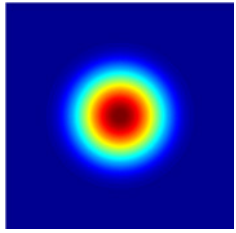
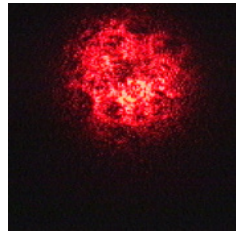
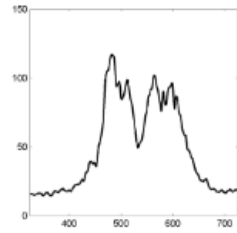
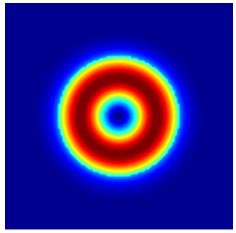
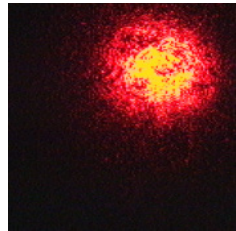
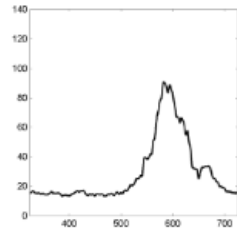
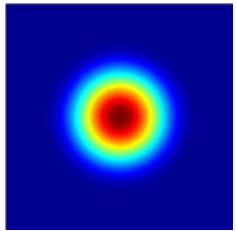
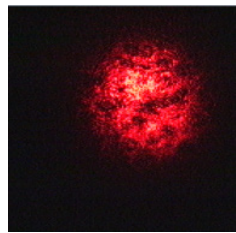
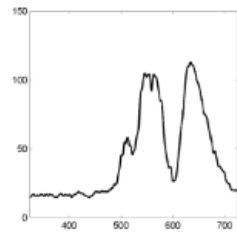
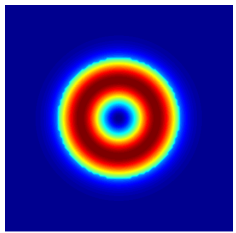


Figure 151. Degenerate $LP_{01}E_V$ + degenerate LP_{11} combinations

Using the experimental setup and procedure described in Chapter 5, the output mode field intensity of the unetched fibers were measured and results are presented in Table 31. It should be noted that although the recorded patterns were run through noise cancellation, it was not possible to completely clear out the artifacts caused by the surface deformities of the linear sheet polarizer used in the measurements.

Table 31. Measured and calculated degenerate modes of unetched fiber

Polarizer angle	Measured	Cross-section	Calculated	Mode
0°				LP ₀₁
90°				LP ₁₁
180°				LP ₀₁
270°				LP ₁₁

To obtain a quantitative analysis of the mode-selectivity of the fabricated device, the output measurements were performed on the device both prior to and after the grating fabrication. Hence, the perturbation induced by the direct-written grating on each of the propagating modes was successfully observed. It should be noted here that the intensity profiles of the modes propagating through the device are overlapped at the

device output and the output is observed using the rotating linear polarizer to differentiate the polarized modes at the device output.

Because of the fiber structure with the side-polished region, not all of the degenerate modes necessarily propagate through to the device output, as some of these modes may not exist within the structure. To determine the exact modes propagating in the device, results of the polarization measurements was analyzed.

Measurements show that after fiber launch followed by the side-polished region, $LP_{01} E_H$, $LP_{11} E_H$ (2 degenerate combinations) and $LP_{11} E_V$ modes exist within the optical fiber, propagate through Region 3 and are observed at the output. Modes propagating through the device to the fiber output are depicted in the below figure.

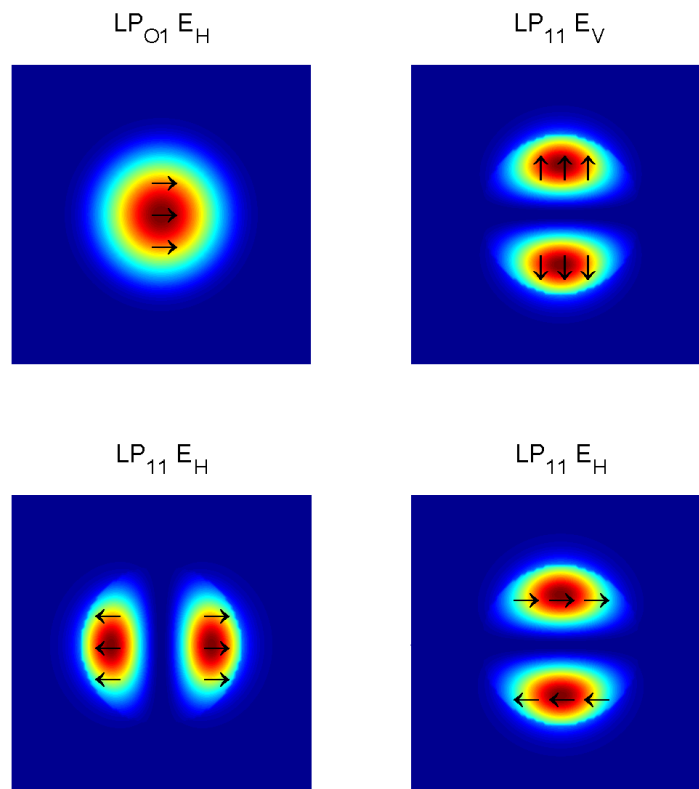


Figure 152. Degenerate modes propagating through the device output

Accordingly, the measurements obtained prior to grating implementation are presented in Table 32 below, where $LP_{01} E_H$ and $LP_{11} E_V$ modes are observed as a combined intensity distribution due to the polarized nature of the intensity measurements.

Table 32. Measured and pattern-fitted degenerate modes before grating fabrication

Polarizer angle	Measured	Cross-section	Calculated	Mode
0°				LP ₁₁ E _V
45°				LP ₀₁ E _H + LP ₁₁ E _V
90°				LP ₁₁ E _H
135°				LP ₁₁ E _V + LP ₁₁ E _H
180°				LP ₁₁ E _V
225°				LP ₀₁ E _H + LP ₁₁ E _V
270°				LP ₁₁ E _H
315°				LP ₁₁ E _V + LP ₁₁ E _H

Besides providing information about the guided modes of the device, the measurements above also verify degenerate modes being formed within side-polished fibers.

Using the above measurements, the polarization-independent total mode field intensity at the device output without the grating implementation was studied. Accordingly, with the combination of modes propagating through the device the total intensity pattern obtained at the output is calculated as depicted in Figure 153.

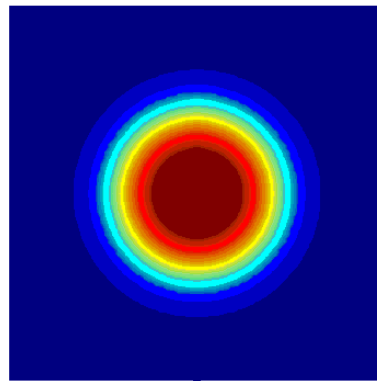


Figure 153. Total output field pattern before grating implementation

Moreover, measurements obtained *after* the direct-writing of the grating structure are presented in Table 33.

Table 33. Measured and pattern-fitted degenerate modes after grating fabrication

Polarizer angle	Measured	Cross-section	Calculated	Mode
0°				LP ₁₁ E _V
180°				LP ₁₁ E _V

Measurements indicate that only a single degenerate higher-order mode, namely, $LP_{11} E_V$ mode propagates through the device after the implementation of the grating. In other words, it is shown by the measurement results that the grating blocks the propagation of fundamental $LP_{01} E_H$ and secondary $LP_{11} E_H$ modes and selectively allows for the propagation of secondary $LP_{11} E_V$ mode.

These results provide a definitive experimental verification of the mode-selective behavior of the designed device. While the LP_{01} mode is allowed to propagate through without the existence of the grating coupler, the fundamental mode is completely blocked and only a single higher-order mode component is allowed at the output of the complete device.

Moreover, the polarization analysis reveals that the mode-selectivity of the device is achieved as a direct result of the polarization-selective behavior of the grating coupler.

CHAPTER 7

CONCLUSION

The main aim of this thesis was to design and fabricate a fiber-integrated grating coupler capable of selectively coupling out higher-order modes propagating in an optical fiber. Although neither photopolymer direct-writing nor fiber grating couplers are novel concepts, realization of an on-fiber grating by photopolymerization is the first application of the method to create a fiber-integrated device.

To establish a theoretical basis, it was shown by the theoretical analysis that it is possible to design a mode-selective device based on a grating coupler. Moreover, it was suggested by the simulation and design optimization studies that a coupling efficiency as high as 68% was achievable. In addition, it was also shown by the photopolymerization experiments and characterization studies that it is possible to fabricate the suggested structure by direct-writing of the AA/PVA based photopolymer.

Volumetric characterization studies indicated a refractive index difference of 0.0013 induced in the polymer films, where the volumetric refractive index profile was modelled using a piece-wise Gaussian based function. Moreover, surface characterization studies revealed that the physical structure of the surface relief caused by direct-writing can be modelled as a combination of two Gaussian functions.

Using the theoretical model based on coupled-mode theory and the know-how acquired throughout the studies, several devices were fabricated. The performance analyses of the devices were carried out using output power measurements, optical spectrum analyses, device output mode-field fitting and degenerate mode polarization measurements.

Measurements revealed a maximum coupling efficiency of 38.88% reached through experimental studies. It was also verified via polarization measurements that mode-selectivity is achieved by the fabricated devices. Furthermore, experimental results indicated that the device exhibits a polarization-selective coupling behavior by selectively blocking degenerate modes at the output.

In terms of coupling efficiency, even though the experimental results are lower than the expected theoretical figures, the results are highly acceptable considering that

this has been the very first study of the device concept and it is imperative that there is much room for improvement. Follow-up studies of the coupler could lead to novel grating structures with improved coupling efficiency and enhanced mode-selectivity.

The significance of this study is that it was theoretically shown and experimentally verified that it is possible to design and fabricate fiber-integrated devices using direct-writing photopolymerization. By applying the device concept to communication wavelengths, prospective studies arising from the described findings could pave the way for a new array of fiber-integrated switching nodes, which would act as the building blocks of countless all-optical devices and network components.

BIBLIOGRAPHY

- Abeles, F., 1963. "VI Methods for Determining Optical Parameters of Thin Films," In: E. Wolf, Editor(s), *Progress in Optics*, Elsevier, Volume 2, Pages 249-288, 1963. doi:10.1016/S0079-6638(08)70561-4.
- Babeva, T., Mackey, D., Naydenova, I., Martin, S., and Toal, V. 2010. "Study of the photoinduced surface relief modulation in photopolymers caused by illumination with a Gaussian beam of light." *Journal of Optics*, 12(12), 124011.
- Born, M. and Wolf, E. 1999 "Principles of Optics," Cambridge University.
- Callister Jr., W.D., 2003. "Material Science and Engineering, An Introduction", John Wiley and Sons, Inc.
- Corning Inc., 2010. "Corning® HI 1060 & RC HI 1060 Specialty Optical Fibers," Technical Specifications, Revision M0100008.
- Das, B., Joseph, J., Singh, K., 2009. "Material saturation in photopolymer holographic data recording and its effects on bit-error-rate and content-addressable search," *Optics Communications*, Volume 282, Issue 2, 15 January 2009, Pages 177-184.
- Dhar, L., 2006. "High-performance polymer recording materials for holographic data storage," *MRS Bull.* 31, 324-328.
- Dinleyici, M.S. and Sümer, C., 2011. "Characterization and estimation of refractive index profile of laser-written photopolymer optical waveguides," *Optics Communications*, 284, no.21, pp. 5067-5071. doi: 10.1016/j.optcom.2011.07.038.
- Eldada, L., Yin, S., Poga, C., Glass, C., Blomquist, R., and Nonwood, R.A., 1998. "Integrated multichannel OADMS using polymer Bragg grating MZIS," *Photonics Technology Letters IEEE*, 10(10), 1416-1418.
- Gallego, S., Ortuño, M., Neipp, C., Márquez, A., Beléndez, A., and Pascual, I., 2005. "Characterization of polyvinyl alcohol/acrylamide holographic memories with a first-harmonic diffusion model." *Applied optics*, 44 (29), 6205-6210.
- Garcia, C., Pascual, I., Costela, A., Garcia-Moreno, I., Gomez, C., Fimia, A. and Sastre, R., 2002. "Hologram Recording in Polyvinyl Alcohol/Acrylamide Photopolymers by Means of Pulsed Laser Exposure", *Appl. Opt.* 41, 2613-2620. doi:10.1364/AO.41.002613.
- Ghatak, A. and Thyagarajan, K., 1998. "An Introduction to Fiber Optics," Cambridge University Press.

- Gleeson, M. and Sheridan, J., 2009. "Nonlocal photopolymerization kinetics including multiple termination mechanisms and dark reactions. Part I. Modeling," J. Opt. Soc. Am. B 26, 1736-1745.
- Gülgün, M.A., 2011. "SEM/AFM Polymer Measurement," [email] Personal Communication, 27 May 2011.
- Hesselink, L., Orlov, S.S. and Bashaw, M.C., 2004. "Holographic data storage systems," Proc. IEEE 92, 1231-1280.
- Huang, W. P., and Haus, H. A. ,1989. "Power exchange in grating-assisted couplers," Journal of Lightwave Technology, 7(6), 920-924.
- Jeong, Y.C., Lee, S. and Park, J.-K..2007. "Holographic diffraction gratings with enhanced sensitivity based on epoxy-resin photopolymers", Optics Express, Vol.15, No.4.
- Jia, B., Gan, X., Gu, M., 2004. "Height/width aspect ratio controllable two-dimensional sub-micron arrays fabricated with two-photon photopolymerization", Optik - International Journal for Light and Electron Optics, Volume 115, Issue 8, Pages 358-362. doi:10.1078/0030-4026-00370.
- Keil, N., Yao, H.H., Zawadzki, C., Beyer, F., Radmer, O., Bauer, M. and Dreyer., C., 2005. "Super compact optical add-drop multiplexer for FTTH applications based on low-loss polymer waveguide materials," Electronics Letters, 41(4), 186-188.
- Kim, W.S., Jeong,Y.-C. and Park, J.-K., 2005. "Organic-inorganic hybrid photopolymer with reduced volume shrinkage", Appl. Phys. Lett. 87, 012106. doi:10.1063/1.1954884.
- KVH Industries, 2000. "KVH E-Core™ Polarization Maintaining Fiber Options and Price List," Technical Specifications, Revision 6/13/00.
- Lawrence, J.R., O'Neill, F.T. and Sheridan, J.T., 2001. "Photopolymer holographic recording material", Optik 112, 449-463.
- Leng, Y., Yun, V., Lucas, L., Herman, W.N., Lee, C.H. and Goldhar, J., 2005."Non-lithographic fabrication of polymer waveguides and grating couplers," Quantum Electronics and Laser Science Conference QELS'05 (Vol.3, pp. 1588-1590).
- Li, D., Yang, J., DeMasi, R., Ke, X., & Wang, M. R., 2004. "Holographic data storage on azobenzene photopolymer film using nanosecond laser pulses," Optics communications, 235(4), 275-279.
- Liu, Z., Srisanit, N., Ke, X., Wu, P., Song, S., Yang, J. J., and Wang, M. R. 2007. "An azobenzene functionalized polymer for laser direct writing waveguide fabrication." Optics Communications, 273(1), 94-98.

- Lowder, T. L. .2008. “*Surface relief D-fiber bragg gratings for sensing applications,*” PhD Thesis, Brigham Young University.
- Ma, H.,Jen, A.K.Y. and Dalton, L.R. 2002. “*Polymer–Based Optical Waveguides: Materials, Processing, and Devices*”, Adv. Mater. 2002, 14, No.19.
- Martin, S., Feely, C.A. and Toal, V., 1997. “*Holographic recording characteristics of an acrylamide-based photopolymer*”, Appl. Opt. 36, 5757-5768.
- Neipp, C., Gallego, S., Ortuño, M., Márquez, A., Beléndez, A., Pascual, I., 2003. “*Characterization of a PVA/acrylamide photopolymer. Influence of a cross-linking monomer in the final characteristics of the hologram,*” Optics Communications, Volume 224, Issues 1–3, 15 August 2003, Pages 27-34.
- Nufern Corp., 2011. “*780-HP Standard Specifications and Design Parameters,*” Technical Specifications, Revision NU0016-12/16/2011.
- Pawluczyk, R.,“*Modified Brewster angle technique for the measurement of the refractive index of a DCG Layer,*” Applied Optics, Vol. 29, No. 4, 1990.
- Phoenix Photonics Limited, 2012. “*Side-polished optical fibers,*” Technical Specifications, Revision 01202.
- Quero, G., Crescitelli, A., Paladino, D., Consales, M., Buosciolo, A., Giordano, M., Cutolo, A., and Cusano, A., 2010. “*Evanescence wave long-period fiber grating within D-shaped optical fibers for high sensitivity refractive index detection*”, Sensors and Actuators B: Chemical (2010).
- Sabatyan, A. and Tavassoly, M.T., 2007. “*Application of Fresnel diffraction to nondestructive measurement of the refractive index of optical fibers*”, Optical Engineering, Volume 46, Issue 12.
- Sabatyan, A. and Tavassoly, M.T., 2009. “*Determination of refractive indices of liquids by Fresnel Diffraction*”, Optics and Laser Technology, Volume 41, Issue 7.
- Sabel, T., Orlic, S., Pfeiffer, K., Ostrzinski, U. and Grützner, G., 2013., “*Free-surface photopolymerizable recording material for volume holography,*” Opt. Mater. Express 3, 329-338.
- Saleh, B.E.A. and Teich, M.C. 2007. “*Fundamentals of Photonics,*” John Wiley and Sons Inc.
- Sanchez, M.O., 2011. “*PVA/AA,*” [email] Personal Communication, 14 December 2011.
- Schilling, M. L., Colvin, V. L., Dhar, L., Harris, A. L., Schilling, F. C., Katz, H. E. and Boyd, C., 1999. “*Acrylate oligomer-based photopolymers for optical storage applications*”. Chemistry of materials, 11(2), 247-254.
- Schutzmann, S., Casalboni, M., Matteis, F.D., Proposito, P., 2005. “*Refractive index measurements of thin films using both Brewster and m-line technique: A*

- combined experimental setup*,” Journal of Non-Crystalline Solids, Volume 351, Issues 21-23, SiO₂, Advanced Dielectrics and Related Devices 5, p. 1814-1818. doi:10.1016/j.jnoncrysol.2005.04.022.
- Smith, K. H. (2005). “*In-fiber optical devices based on D-fiber*,” PhD Thesis, Brigham Young University.
- Sullivan, A.C., Grabowski, M.W. and McLeod, R.R., 2007. “*Three-dimensional direct-write lithography into photopolymer*,” Applied optics, 46(3), 295-301.
- Sun, N.-H.m et al., 1997. “*Analysis of Grating-Assisted Directional Couplers Using the Floquet–Bloch Theory*,” J. Lightwave. Tech., Vol.15, No.12, Dec 1997.
- Surdutovich, G. I., R. Z. Vitlina, and V. Baranauskas. “*Simple reflectometric method for measurement of weakly absorbing films*,” Thin Solid Films 355 (1999): 446-450.
- Surdutovich, Gregory, Ritta Vitlina, and Vitor Baranauskas. “*Anisotropic protective coating for Brewster angle Windows*,” Applied Optics 38.19 (1999): 4172-4176.
- Sümer, C. and Dinleyici, M.S., 2013. “*A fiber-integrated optical component fabricated via photopolymerization: Mode-selective grating coupler*”, Optics Communications, Vol.308, p.36-42, Nov. 2013.
- Torres, V.M., 2011. “*AA/PVA Film Solubility*,” [email] Personal Communication, 15 November 2011.
- Trentler, T.J., Boyd, J.E. and Colvin, V.L., 2000. “*Epoxy Resin–Photopolymer Composites for Volume Holography*,” Chemistry of Materials, 12(5), 1431-1438. doi:10.1021/cm9908062.
- Verhoeven, J.W., 1996 “*Glossary of Terms Used in Photochemistry (IUPAC Recommendations 1996)*”, Pure Appl. Chem., Vol. 68, No. 12, pp. 2223-2286. doi:10.1351/pac199668122223.
- Wang, D. and Elisseff, J. H.. 2004. “Photopolymerization”. Encyclopedia of Biomaterials and Biomedical Engineering 1212-1225. doi:10.1081/E-EBBE-120007372.
- Yariv, A. and Yeh, P., 2006. “*Photonics: Optical Electronics in Modern Communications*,” (The Oxford Series in Electrical and Computer Engineering). New York: Oxford Univ. Press.
- Yesayan, A., and Piche, M., 2004. “*Grating-assisted coupler used as a narrow bandwidth channel-dropping filter*”. Optical and quantum electronics, 36(14), 1221-1225.
- Yokota, H., Kobayashi, M., Mineo, H., Kagawa, N., Kanbe, H. and Sasaki, Y., 2008. “*Demonstration of an all-optical switching operation using an optical fiber grating coupler*,” Optics Communications, Volume 281, Issue 19, 1 October 2008, Pages 4893-4898.

Zammit, M.D., Davis, T.P. and Willett, G.D., 1997. “*Visible Light Pulsed-Laser Polymerization at 532 nm Employing a Julolidine Dye Photosensitizer Initiation System*”, *Macromolecules* 30 (19), 5655-5659. doi:10.1021/ma970440j.

APPENDIX A

POLYMER BATCHES

Complete list of polymer batches prepared throughout the experimental studies.

Label & date	Material	Target amount	Weighed amount	Note	Batch purpose
A 25.06 2009	TEA	2180mg	2190mg	-	Fabrication test, photopolymerization test, diffraction methods
	PEI	2400mg	3800mg	PEI dissolved partially (Acetone solution)	
	PPGDGE	6drp	6drp	-	
	AA	2180mg	2170mg	-	
	YE	4.4mg	100mg	Unclear reading on YE	
B 04.08 2009	TEA	2180mg	2260mg	-	Fabrication test, photopolymerization test, diffraction methods
	PEI	2400mg	2400mg	Partial acetone spill (Acetone solution)	
	PPGDGE	6drp	6drp	-	
	AA	2180mg	2190mg	-	
	YE	4.4mg	19mg	-	
C 05.08 2009	PEI	2400mg	3740mg	(Acetone solution)	Spin-coat test, photopolymerization test, diffraction methods
	TEA	2180mg	2190mg	-	
	PPGDGE	6drp	6drp	-	
	AA	2180mg	2200mg	-	
	YE	4.4mg	8.3mg	-	
D 12.03 2010	PEI	2400mg	4000mg	(Acetone solution)	Contaminated, not used
	TEA	2180mg	2182mg	-	
	PPGDGE	6drp	6drp	-	
	AA	2180mg	2181mg	-	
	YE	4.4mg	8.1mg	-	
E 16.03 2010	PEI	1500mg	1700mg	(Acetone solution)	Switched to thick glass substrate; photopolymerization test, Brewster methods
	TEA	1362mg	1400mg	PEI ran out; recipe targets down-scaled to meet the ratios	
	PPGDGE	4drp	4drp		
	AA	1362mg	1430mg		
	YE	2.75mg	5.5mg		
F 28.04 2010	H ₂ O	4.0g	39.746g	(40ml aqueous solution)	Spin-coat test, spacer test, SEM analysis, diffraction methods, Brewster methods
	PVA	4.0g	4.032g		
	TEA	1.187g	2.072g		
	AA	1.268g	1.264g		
	YE	6.5mg	7.2mg		

Label & date	Material	Target amount	Weighed amount	Note	Batch purpose
G1 11.05 2010	H ₂ O	15.0g	16.8g	(15ml aqueous solution)	Not used
	PVA	1.5g	1.55g		
	TEA	0.445g	0.886g	*Overshoot	
	AA	0.475g	0.597g	*Overshoot	
	YE	2.4mg	9.8mg	*Overshoot	
G2 14.05 2010	H ₂ O	15.0g	15.277g	(15ml aqueous solution)	SEM analysis, diffraction methods, Brewster methods
	PVA	1.5g	1.69g		
	TEA	0.445g	1.01g		
	AA	0.475g	0.473g		
	YE	2.4mg	2.4mg		
H1 22.11 2010	H ₂ O	10.0g	10.32g	(10ml aqueous solution)	Diffraction methods
	PVA	1.0g	1.056g		
H2 22.11 2010	H ₂ O	20.0g	20.0g	(20ml aqueous solution)	Diffraction methods
	PVA	2.0g	2.0g		
I 14.02 2011	H ₂ O	15.0g	15.62g	(15ml aqueous solution)	Fabrication test, diffraction methods
	PVA	1.5g	1.535g		
	TEA	0.445g	0.682g		
	AA	0.475g	0.486g		
	YE	2.4mg	3.3mg		
J 28.02 2011	H ₂ O	15.0g	14.995g	(15ml aqueous solution)	Diffraction methods
	PVA	1.5g	1.5121g		
	TEA	0.445g	0.462g		
	AA	0.475g	0.477g		
	YE	2.4mg	2.5mg		
K 04.06 2011	H ₂ O	15.0g	16.06g	(15ml aqueous solution)	Fabrication test, diffraction methods
	PVA	1.5g	1.509g		
	TEA	0.445g	0.451g		
	AA	0.475g	0.486g		
	YE	2.4mg	3.2mg		
L 06.06 2011	H ₂ O	15.0g	15.02g	(15ml aqueous solution)	AFM / SEM / Stylus, solubility / staining tests, grating fabrication, diffraction methods
	PVA	1.5g	1.528g		
	TEA	0.445g	0.477g		
	AA	0.475g	0.489g		
	YE	2.4mg	2.7mg		
M 28.07 2012	H ₂ O	15.0g	15.138g	(15ml aqueous solution)	Trial 1: Single-fiber device at 632.8nm
	PVA	1.5g	1.507g		
	TEA	0.445g	0.456g		
	AA	0.475g	0.478g		
	YE	2.4mg	2.5mg		

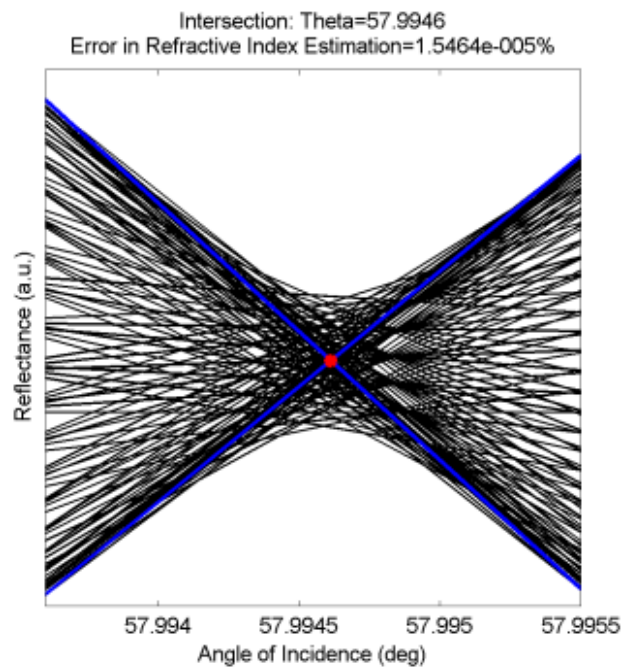
Label & date	Material	Target amount	Weighed amount	Note	Batch purpose
N 12.01 2013	H ₂ O	15.0g	15.07g	(15ml aqueous solution)	Trial 2: Single-fiber device at 632.8nm
	PVA	1.5g	1.508g		
	TEA	0.445g	0.473g		
	AA	0.475g	0.476g		
	YE	2.4mg	2.4mg		
O 26.09 2013	H ₂ O	7.5g	7.5g	(7.5ml aqueous solution)	Trial 3: Single-fiber device at 852nm
	PVA	1.5g	1.507g		
	TEA	0.445g	0.469g		Trial 4: Complete structure at 852nm
	AA	0.475g	0.477g		
	YE	2.4mg	2.8mg		
P 14.06 2014	H ₂ O	5.0g	5.033g	(5ml aqueous solution)	Trial 5: Complete structure at 852nm
	PVA	1.5g	1.530g		
	TEA	0.445g	0.469g		Trial 6: Single-film device at 852nm
	AA	0.475g	0.479g		
	YE	2.4mg	2.6mg		
Q 14.06 2014	H ₂ O	5.0g	5.05g	(5ml aqueous solution)	Trial 7: Complete structure at 632.8nm with polarization analysis
	PVA	1.5g	1.528g		
	TEA	0.445g	0.603g		
	AA	0.475g	0.506g		
	YE	2.4mg	2.5mg		

APPENDIX B

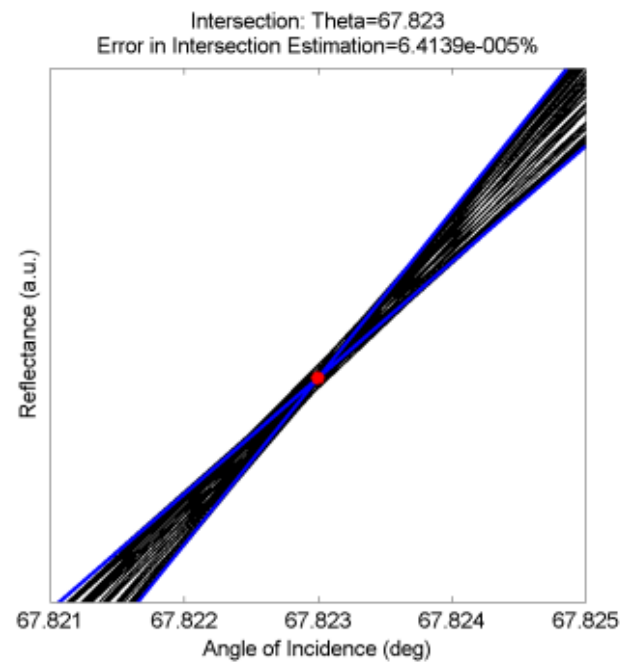
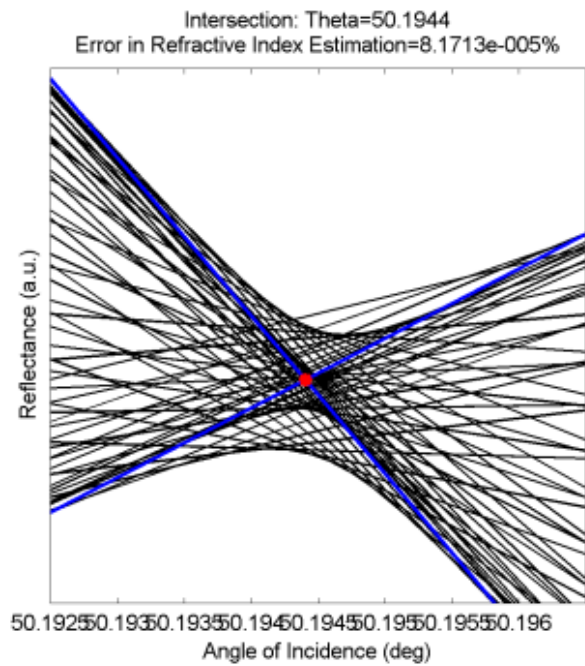
IMPROVED BREWSTER METHOD CONFIGURATIONS

Complete set of configurations employed in the sensitivity and accuracy calculations presented in Section 3.1.3.4.

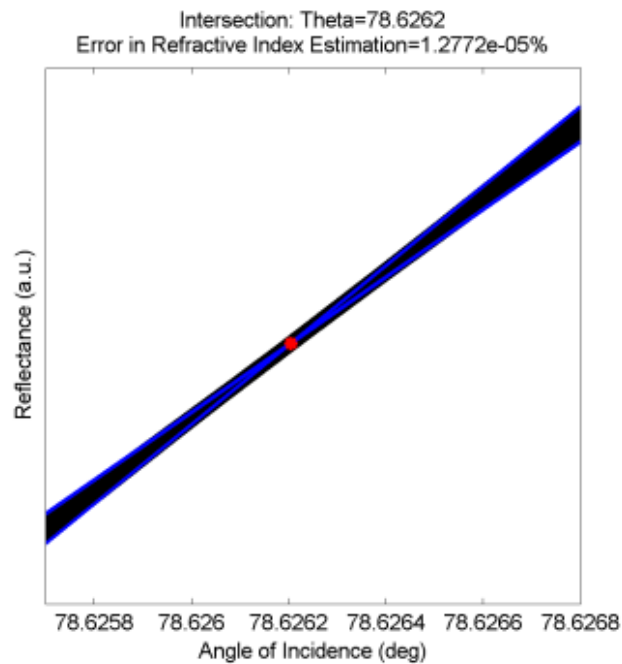
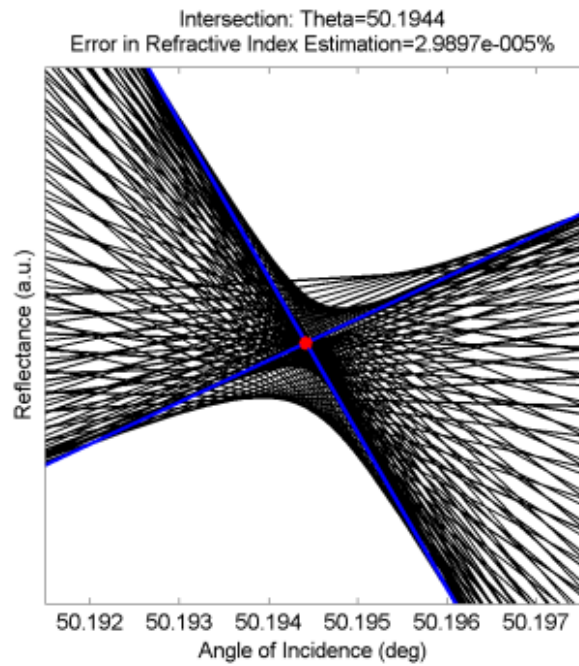
Configuration 1	n_0	1.000
	n_1	1.600
	n_2	1.456
Intersection #1	Angle of intersection (°)	57.9946128099173
	Calculated n_1	1.59999975258359
	Error rate of index estimation (%)	0.0000154635248911239
Intersection #2	Does not exist	



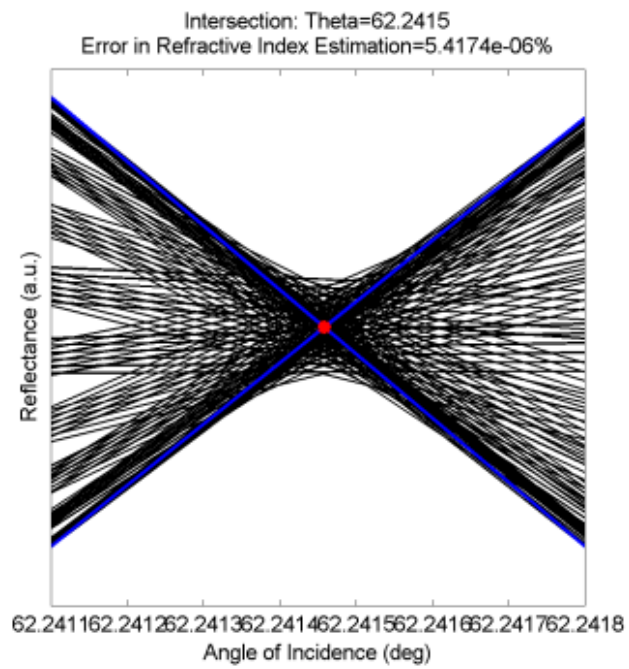
Configuration 2	n_0	1.000
	n_1	1.200
	n_2	1.456
Intersection #1	Angle of intersection ($^\circ$)	50.1944058823529
	Calculated n_1	1.1999901944078
	Error rate of index estimation (%)	0.0000817132680038431
Intersection #2	Angle of intersection ($^\circ$)	67.8229999999999
	Error rate of intersection estimation (%)	0.0000641390828304056
	Calculated n_2	1.45600063753711
	Error rate of substrate index (%)	0.0000437868894836075



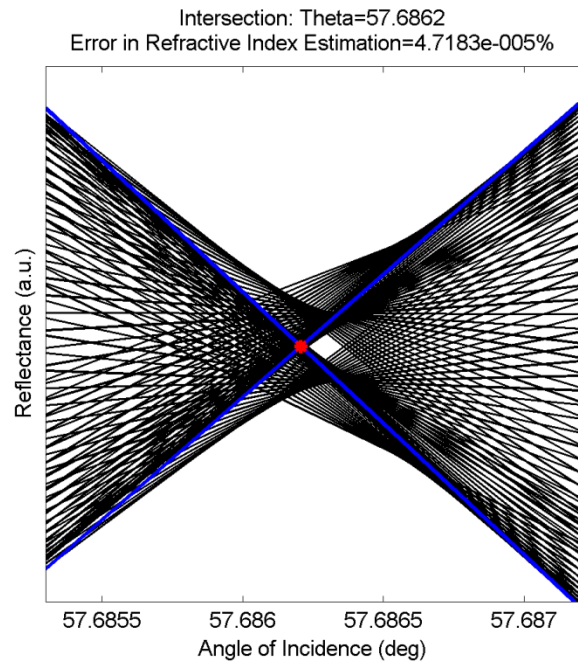
Configuration 3	n_0	1.000
	n_1	1.200
	n_2	1.700
Intersection #1	Angle of intersection ($^\circ$)	50.1944204832713
	Calculated n_1	1.1999964123558
	Error rate of index estimation (%)	0.0000298970350328294
Intersection #2	Angle of intersection ($^\circ$)	78.6262041666666
	Error rate of intersection estimation (%)	0.0000127719375302104
	Calculated n_2	1.700001200256
	Error rate of substrate index (%)	0.0000706032944788065



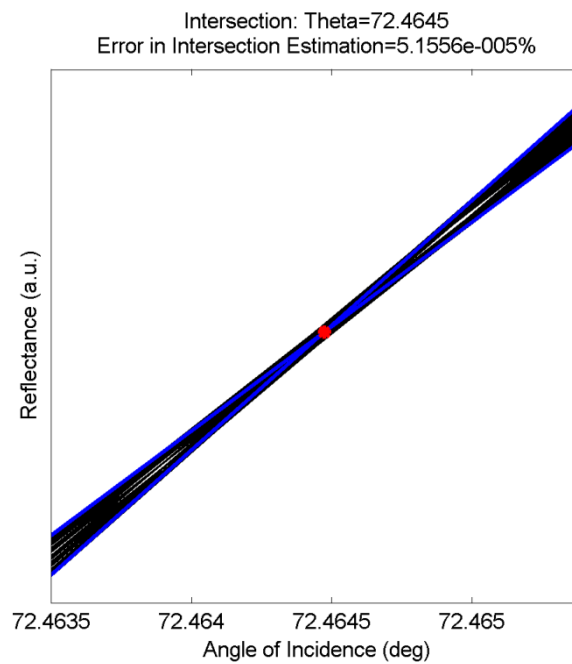
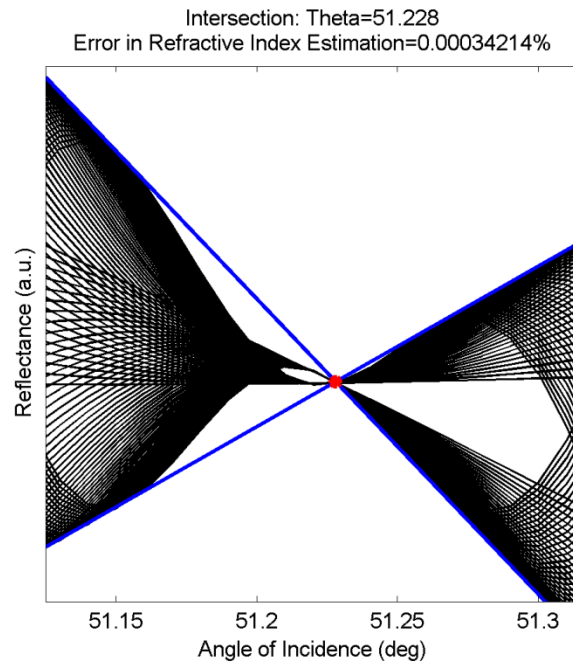
Configuration 4	n_0	1.000
	n_1	1.900
	n_2	1.700
Intersection #1	Angle of intersection (°)	62.2414581196581
	Calculated n_1	1.89999989706939
	Error rate of index estimation (%)	5.41740021263667E-06
Intersection #2	Does not exist	



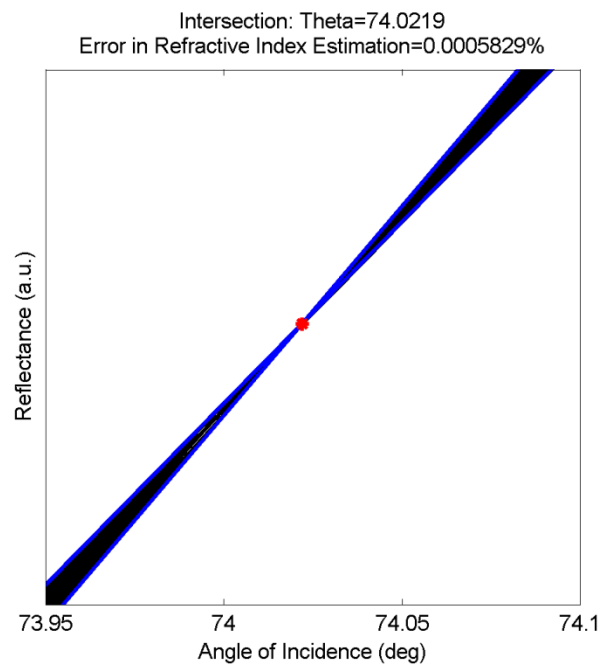
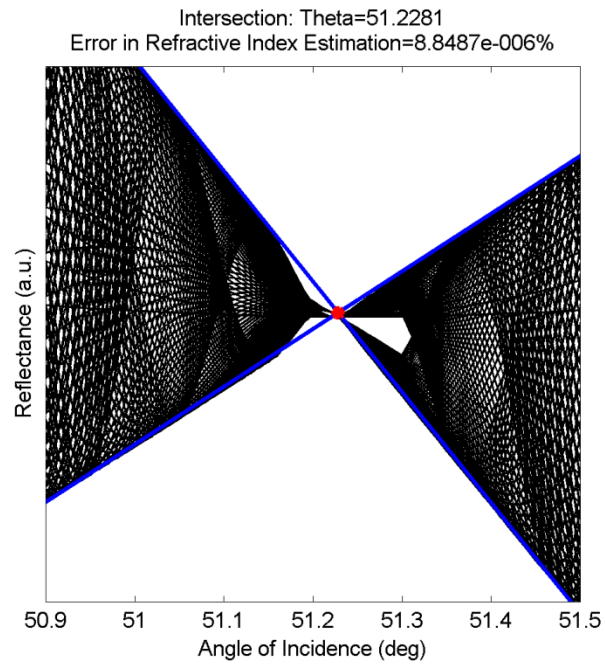
Configuration 5	n_0	1.000
	n_1	1.581
	n_2	1.483
Intersection #1	Angle of intersection (°)	57.686206153846129
	Calculated n_1	1.581000745969315
	Error rate of index estimation (%)	4.718338485399994e-005
Intersection #2	Does not exist	



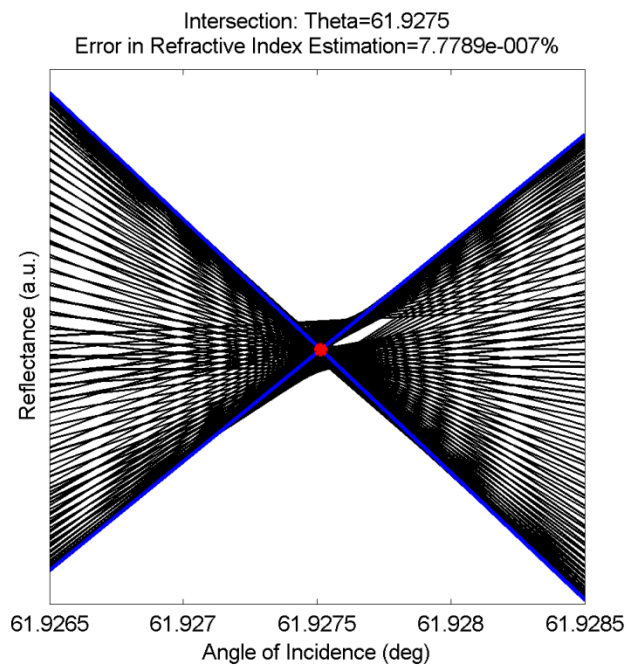
Configuration 6	n_0	1.000
	n_1	1.245
	n_2	1.483
Intersection #1	Angle of intersection ($^\circ$)	51.228026196928639
	Calculated n_1	1.244995740417905
	Error rate of index estimation (%)	3.421351080714360e-004
Intersection #2	Angle of intersection ($^\circ$)	72.464474358974257
	Calculated n_2	1.483006460157213
	Error rate of substrate index (%)	4.356141073841336e-004



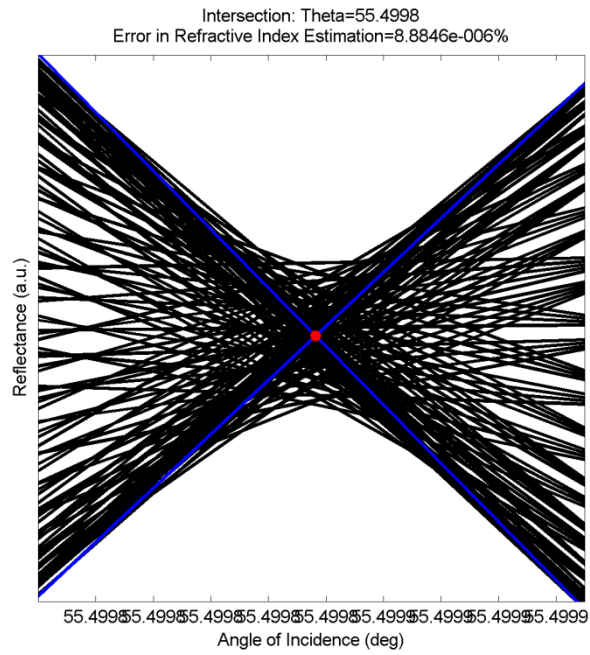
Configuration 7	n_0	1.000
	n_1	1.245
	n_2	1.513
Intersection #1	Angle of intersection ($^\circ$)	51.228124379755229
	Calculated n_1	1.245000110166555
	Error rate of index estimation (%)	8.848719240605883e-006
Intersection #2	Angle of intersection ($^\circ$)	74.021892925430194
	Calculated n_2	1.513008080716784
	Error rate of substrate index (%)	5.340857094615633e-004



Configuration 8	n_0	1.000
	n_1	1.875
	n_2	1.513
Intersection #1	Angle of intersection (°)	61.927513249211351
	Calculated n_1	1.875000014585385
	Error rate of index estimation (%)	7.778871946584330e-007
Intersection #2	Does not exist	



Configuration 9	n_0	1.000
	n_1	1.455
	n_2	1.522
Intersection #1	Angle of intersection (°)	55.499836415833741
	Calculated n_1	1.455000129271478
	Error rate of index estimation (%)	8.884637676195305e-006
Intersection #2	Does not exist	

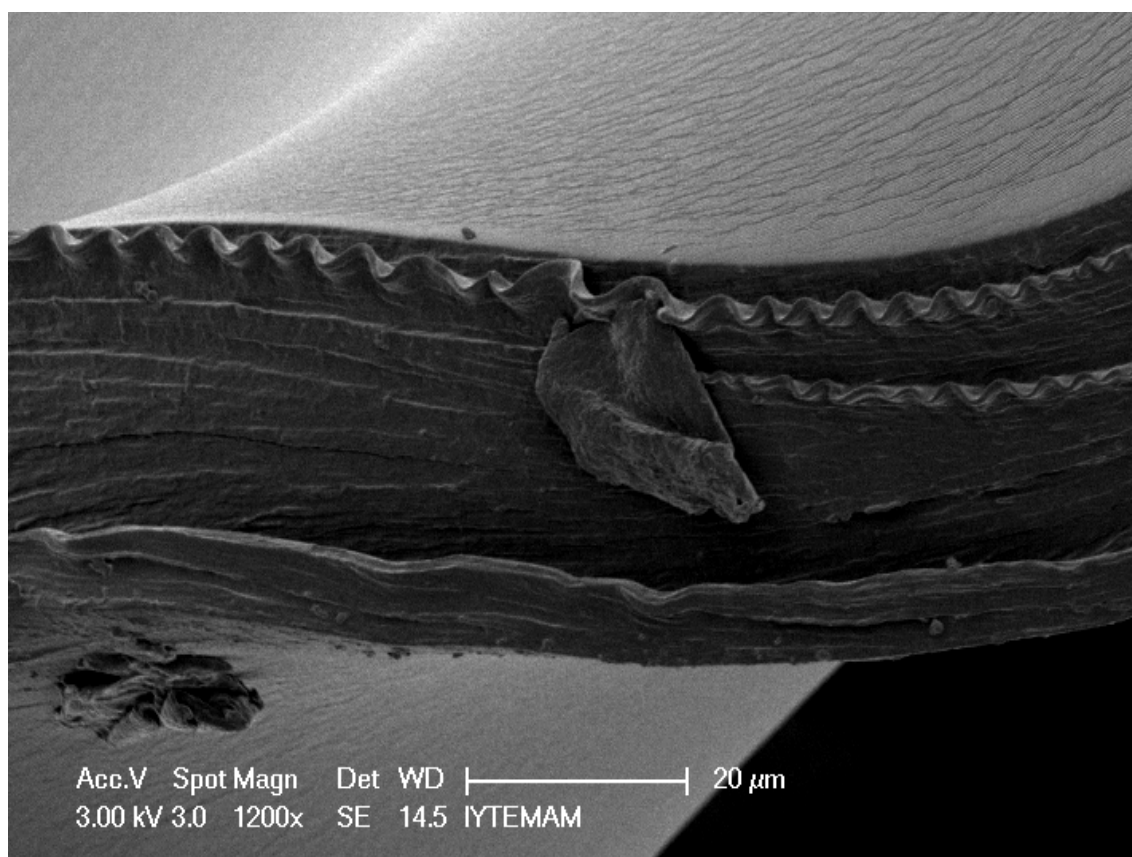


APPENDIX C

SEM IMAGES

“Polymer Lasagna”

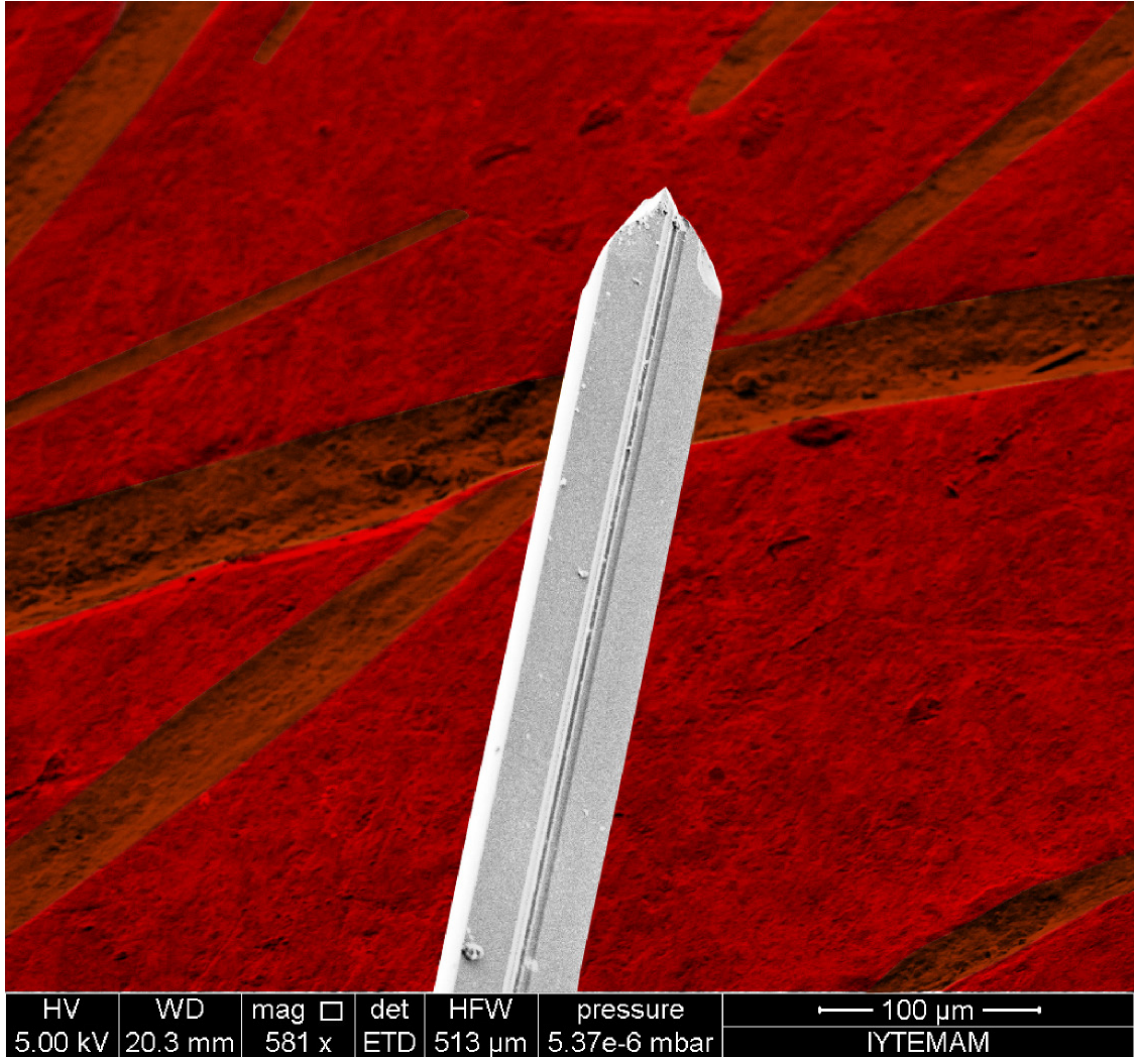
Runner-Up in 2011 Scanning Electron Microscopy Image Contest held by Izmir Institute of Technology – Center for Materials Research (IYTE-MAM).



Photopolymer thin films prepared by embedding Acrylamide monomers in Polyvinyl Alcohol polymer matrix were analyzed with Scanning Electron Microscopy, which enabled film thickness measurements, surface quality inspection and cross-section analyses. In certain regions where the thin film had separated from the substrate, observations revealed rupture warping on the film layer.

“Narsil”

Contestant in 2011 Scanning Electron Microscopy Image Contest held by Izmir Institute of Technology – Center for Materials Research (IYTE-MAM).



Optical D-Fibers were stripped off their jacket layers and chemically etched via hydrofluoric acid (HF) solution in order to thin-out the cladding layer. Fibers are later employed in the fabrication of integrated optical components by casting an Acrylamide/Polyvinyl Alcohol based photopolymer on the planar surface of the fiber. The photopolymer is exposed to focused laser light in repetitive linear patterns to form a volumetric grating, where controlling the exact distance between the fiber core and polymer layer is crucial.

SEM analyses of the etched samples revealed apparent thinning of the cladding layer, in addition to partial etching of the core layer depending on the concentration of the HF solution. Total vanishing of the core layers was observed in extreme cases, where the etching time was extended well over the optimal duration. Such an example of total etching of the core is seen in this SEM image, in which the trace of the position where the core layer was located is clearly seen in the middle section of the fiber.

The image was colored by Bertan Kılıçcioğlu with inspiration from “Narsil”, the legendary broken sword in the book Lord of the Rings by J.R.R. Tolkien.

VITA

Can Sümer received B.Sc. degree from Bilkent University in 2003, M.Sc. degree from Sabancı University in 2005, and Ph.D. degree from Izmir Institute of Technology in 2014. He has been working as a Senior Optical Design Engineer at Vestel Electronics - Lead Technologies Group since 2012.

Publications

Sümer, C., Kuştepe, A., Dinleyici, M.S., “*Improved Brewster Angle Method with Analytical Approach for Determining Refractive Indices of Thin Films*”, Thin Solid Films (*In Review*).

Sümer, C., Dinleyici, M.S., “*A fiber-integrated optical component fabricated via photopolymerization: Mode-selective grating coupler*”, Optics Communications, Vol.308, p.36-42, Nov. 2013.

Dinleyici, M.S., **Sümer C.**, “*Characterization and estimation of refractive index profile of laser-written photopolymer optical waveguides*,” Optics Communications, Vol.284 (21) p.5067-5071, Oct. 2011.

Sümer C., Öztürk C., “*A highly asymmetric, hybrid, directional-coupler sensor*,” Fotonik’05 - 7. Ulusal Optik, Elektro-Optik ve Fotonik Çalışma Toplantısı, Ankara, Turkey, Dec. 2005.